NATURE OF MAGNETIC ORDERING IN DOPED HEXAGONAL AND ORTHORHOMBIC MANGANITES

By

NEETIKA

Enrolment No. PHYS01201004020

Bhabha Atomic Research Centre, Mumbai, India

A thesis submitted to the
Board of Studies in Physical Sciences

In partial fulfillment of requirements
for the Degree of

DOCTOR OF PHILOSOPHY
of
HOMI BHABHA NATIONAL INSTITUTE

OCTOBER, 2015

STATEMENT BY AUTHOR

This dissertation has been submitted in partial fulfillment of requirements for an advanced degree at Homi Bhabha National Institute (HBNI) and is deposited in the Library to be made available to borrowers under rules of the HBNI.

Brief quotations from this dissertation are allowable without special permission, provided that accurate acknowledgement of source is made. Requests for permission for extended quotation from or reproduction of this manuscript in whole or in part may be granted by the Competent Authority of HBNI when in his or her judgment the proposed use of the material is in the interests of scholarship. In all other instances, however, permission must be obtained from the author.

(Neetika)

DECLARATION

I, hereby declare that the investigation presented in the thesis has been carried out by me. The work is original and has not been submitted earlier as a whole or in part for a degree / diploma at this or any other Institution/University.

(Neetika)

DECLARATION

I, hereby declare that the minor suggestions of the examiners have been incorporated in the thesis.

Dr. Amitabh Das

(Guide)

List of Publications

In Refereed Journal:

Related to Thesis

1. *Transport and magnetic properties of Fe doped $CaMnO_3$*
   Neetika, A. Das, I. Dhiman, A.K. Nigam, A.K.Yadav, D. Bhattacharyya, and S. S. Meena
   J. Appl. Phys., **112**, 123913 (2012).

2. *Spin reorientation behavior in $YMn_{1-x}M_xO_3$ (M = Ti, Fe, Ga; x = 0, 0.1)*
   Neetika Sharma, A. Das, C. L. Prajapat, and S. S. Meena
   J. Magn. Magn.Mater.**348**, 120 (2013).

3. *Magnetic and dielectric behaviour in $YMn_{1-x}Fe_xO_3$ ($x \leq 0.5$)*
   Neetika Sharma, A. Das, S. K. Mishra, C. L. Prajapat, M. R. Singh, and S. S. Meena
   J. Appl. Phys.**115**, 213911 (2014).

4. *Phase separated behavior in Yttrium doped $CaMnO_3$*
   Neetika Sharma, A. Das, C. L. Prajapat, Amit Kumar, and M. R. Singh
   Mater. Res. Bull. 77, 284 (2016).

5. *Effect of rare-earth dopants on the magnetic ordering of frustrated h-$YMnO_3$*
   Neetika Sharma, A. Das, C. L. Prajapat, and M. R. Singh
   J. Magn. Magn. Mater. (doi/ 10.1016/j.jmmm.2016.07.043).

In Other Areas:

1. *Jahn-Teller assisted polaron hopping and associated dielectric response of $PrFe_{0.5}Mn_{0.5}O_{2.9}$*
   C.Ganeshraj, S. Kavita, R. Mahendiran, **Neetika Sharma**, A.Das, and P.N.Santhosh
   Appl. Phys. Lett. **103**, 112909 (2013).

2. *Cation distribution and magnetic properties of Co-Zr doped $BaCo_xZr_xFe_{(12-2x)}O_{19}$ prepared via citrate precursor sol-gel route*
   R.K.Mudsainiyan, S. K. Chawla, S.S. Meena, **Neetika Sharma**, Ripandeep Singh, A. Das
   Ceram.Int. **40**, 16617 (2014).

3. *Transport, magnetic and structural properties of Mott insulator MnV_2O_4 at the boundary between localized and itinerant electron limit*
   Prashant Shahi, Saurabh Kumar, **Neetika Sharma**, Ripandeep Singh, P.U. Sastry, A.Das, A Kumar, K. K. Shukla, A. K.Ghosh, A. K. Nigam, Sandip Chatterjee.
   J. Mater. Sci. **49**, 7317 (2014).

4. *Spin-Phonon Coupling and High temperature Phase transition in Multiferroic Material $YMnO_3$*
   Mayank gupta, Ranjan Mittal, Mohamed Zbiri, **Neetika Sharma**, Stéphane Rols, Helmut

Schober, S.L. Chaplot
J. Mater. Chem. C 3, 11717, 2015.

5. *Magnetic and Optical properties of Fe doped crednerite* $CuMnO_2$
K.K. Shukla, P. Shahi, Gopal S, A. Kumar, A. K. Ghosh, Ripandeep Singh, **Neetika Sharma**, A. Das, A. K. Sinha, Amish G. Joshi, A. K. Nigam, and Sandip Chatterjee
RSC Adv. **5**, 83504 (2015).

Papers presented in Conferences

1. *The effect of Fe Doping on the Magnetic structure of* $CaMnO_3$
Neetika, A. Das
DAE Solid State Physics Symposium**56** 280 (2011).

2. *Magnetic Structure Of Multiferroic Manganites,* $YMn_{1-x}M_xO_3$ *(M = Ga, Ti; x = 0, 0.1)*
NeetikaSharma, C. L. Prajapat and A. Das
DAE Solid State Physics Symposium**57** 228 (2012).

3. *Magnetic Structure Of Multiferroic Manganites,* $YMn_{1-x}M_xO_3$ *(M = Ga, Ti; x = 0, 0.1)*
NeetikaSharma and A. Das
International Symposium on Neutron Scattering **2** 39 (2013).

4. *Neutron diffraction studies of hexagonal manganites.*
NeetikaSharma and A. Das
International Conference on Magnetic Materials and Applications (MagMA-2013), December 5-7, 2013, Department of Physics, IIT Guwahati.

5. *Effect of Fe doping on the Structural, Magnetic, and Dielectric Properties of* $YMnO_3$
Neetika, A. Das, S. K. Mishra, C. L. Prajapat
DAE Solid State Physics Symposium **58** 239 (2013).

6. *Phase separated behavior in Yttrium doped* $CaMnO_3$
Neetika Sharma, A. Das, Amit Kumar, C. L. Prajapat, , and M. R. Singh
5th Conference on Neutron Scattering **5** 49 (2015).

(Neetika)

To My Parents

ACKNOWLEDGEMENTS

I would like to thank all the people who helped me during my PhD and in one way or the other, made this thesis possible.

First, I want to thank my advisor Dr. Amitabh Das for his guidance, constant support, constructive criticism and valuable advices. I am greatly indebted to him more than he knows. I am also thankful to Dr. S. Basu, Head, Solid State Physics Division, BARC for his support and encouragement. I also thank Prof. S. L. Chaplot, Prof. D. K. Aswal and Prof K.G. Suresh whose useful suggestions as doctoral committee members have been very helpful. I am grateful to Prof. Chaplot for providing me an opportunity to work in SSPD under the guidance of Dr. Amitabh Das.

I also wish to thank Dr. C. L. Prajapat, Dr. Amit Kumar and Dr. S. K. Mishra, for magnetization, neutron depolarization, and dielectric measurements. I am grateful to Mayank Gupta for guiding me through Quantum Espresso. I am also thankful to Dr. V. K. Aswal, Dr. D. Sen, Dr. R. Mittal, Dr. P.U. Sastry, and Dr. J. Bahadur for their constructive support during the period of my thesis work. I take the opportunity to thank all the members of Solid State Physics Division who directly or indirectly have helped me in these five years.

I specially thank Sugam Kumar, Debes Ray, Tista Basak, Indu Dhiman, Akshay Chinchalikar, Ripandeep Singh, Rohan Phatak, Anup Bera, and Mitali Swain for their help and advices.

Thanks to Pallavi for being a caring roommate and for your motivation. I thank Priyanka for being a wonderful friend and making the last hectic months of my PhD enjoyable. It has been a pleasure to meet so many talented and friendly people during my time at BARC, I want to say thank you to Ashok, Sanjay, Nirmal, Avik, Sumit, Indresh, and Pulkit for all your help and the nice memories.

Thanks to Nandan for not hesitating to point out my bad habits/attitudes so that I could fix them.

Finally, I thank my parents, my brother and sister who have constantly supported and encouraged me all my life, and making me what I am today.

I am sure that I have forgotten to thank some people. Thanks to everyone who contributed to make my years in BARC enjoyable.

CONTENTS

Page No.

SYNOPSIS **xv**

LIST OF FIGURES **xxvi**

LIST OF TABLES **xxxv**

1. INTRODUCTION **1-35**

1.1 Manganites 1

1.2 Orthorhombic Manganites 2

1.2.1 Crystal Structure 4

1.2.2 Crystal – field splitting and Jahn –Teller Theorem 6

1.2.3 Magnetic Interactions 7

1.2.3.1 Double exchange 8

1.2.3.2 Super exchange 9

1.2.4 Magnetic properties of manganites 10

1.2.5 Phase separated behavior in manganites 14

1.2.6 Orthorhombic calcium manganite ($CaMnO_3$) 15

1.3 Hexagonal Manganite 17

1.3.1 Crystal structure and Crystal – field splitting 18

1.3.2 Magnetism in Hexagonal $RMnO_3$ 20

1.3.3 Ferroelectricity in Hexagonal $RMnO_3$ 28

1.3.4 Multiferroic properties in hexagonal $RMnO_3$ 28

1.3.4.1 Magnetolectric effects in hexagonal $RMnO_3$ 29

1.3.4.2 Magnetoelastic effects in hexagonal $RMnO_3$ 31

1.3.5 Hexagonal $YMnO_3$ 31

1.4 Issues 33

1.5 Plan of the thesis 35

2. EXPERIMENTAL TECHNIQUES 36-67

2.1 Sample preparation 36

2.2 Scattering theory 38

2.3 Bragg’s formulation for diffraction 40

2.4 Powder diffraction method 42

2.5 X-ray scattering 43

2.5.1 X-ray diffractometer 45

2.6 Neutron scattering 46

2.6.1 Magnetic diffraction 49

2.6.2 Neutron powder Diffractometer 53

2.7 Data Analysis : Rietveld Method 56

2.8 Polarized neutron spectrometer for depolarization studies 58

2.9 Four probe resistivity set up 61

2.10 Magnetization measurements 62

2.11 X-ray absorption spectroscopy 63

2.12 Mössbauer spectroscopy 65

2.13 Dielectric Measurement 67

3. EFFECT OF A-SITE AND B-SITE DOPING ON THE MAGNETIC PROPERTIES OF HEXAGONAL YMNO$_3$. 68-153

3.1 Effect of A-site doping on the magnetic properties of YMnO$_3$ 71

3.1.1 Effect of rare earth dopants on the magnetic structure of YMnO$_3$ 71

3.1.1.1 Crystal structure 71

3.1.1.2 Magnetic properties 78

3.1.1.3 Magnetic Structure 83

3.1.1.4 Short range correlations 93

3.2 Effect of B-site doping on the magnetic properties of YMnO$_3$ 97

3.2.1 Effect of Mn site substitution on the structural and magnetic properties of YMn$_{1-x}$M$_x$O$_3$ (M=Ti, Fe, Ga; x=0,0.1). 97

3.2.1.1 Crystal structure 97

3.2.1.2 Magnetic properties 100

3.2.1.3 Mössbauer spectrometry 105

3.2.1.4 Magnetic structure 107

3.2.1.5 Temperature dependent X-ray absorption spectroscopy 112

3.2.2 Magnetic and dielectric behavior in YMn$_{1-x}$Fe$_x$O$_3$(x≤0.5) 124

3.2.2.1 Crystal structure 125

3.2.2.2 Magnetic properties 128

3.2.2.3 Mössbauer spectrometry 131

3.2.2.4 Magnetic structure and phase diagram 133

3.2.2.5 Dielectric properties 140

3.2.2.6 X-ray absorption spectroscopy 144

3.3 Computational results for $YMnO_3$ 149

3.4 Conclusion 153

4. **EFFECT OF A-SITE AND B-SITE DOPING ON THE MAGNETIC PROPERTIES OF OTHORHOMBIC CAMNO$_3$. 156-193**

4.1 Effect of A-site doping on the magnetic properties of $CaMnO_3$ 158

4.1.1 Studies on Yttrium doped $CaMnO_3$ 158

4.1.1.1 Crystal structure 158

4.1.1.2 Transport and magnetic properties 161

4.1.1.3 Magnetic structure 166

4.1.1.4 Neutron depolarization studies 171

4.2 Effect of Mn site doping on the magnetic properties of $CaMnO_3$ 173

4.2.1 Effect of Fe doping on the transport and magnetic properties of $CaMnO_3$

4.2.1.1 Crystal structure 174

4.2.1.2 XANES study 176

4.2.1.3 Mössbauer spectrometry 178

4.2.1.4 Transport and magnetic properties 180

4.2.1.5 Magnetic structure 184

4.2.1.6 Dielectric study 186

4.3 Computational results for $CaMnO_3$ 190

4.4 Conclusion 193

5. **SUMMARY AND CONCLUSIONS 194-202**

5.1 Effect of A-site and B-site doping on the magnetic properties of hexagonal $YMnO_3$ 195

5.1.1 Effect of A-site doping on the magnetic properties of $YMnO_3$ 195

5.1.2 Effect of B-site doping on the magnetic properties of $YMnO_3$ 196

5.2 Effect of A-ste and B-site doping on the magnetic properties of orthorhombic $CaMnO_3$ 199

5.2.1 Effect of A-site doping on the magnetic properties of $CaMnO_3$ 200

5.2.2 Effect of B-site doping on the magnetic properties of $CaMnO_3$ 200

5.3 Scope of the work 202

REFERENCES **203**

Homi Bhabha National Institute

Ph. D. PROGRAMME

1. Name of the Student: Neetika

2. Name of the Constituent Institution: Bhabha Atomic Research Centre

3. Enrolment No.: PHYS01201004020

4. Title of the Thesis: Nature of Magnetic Ordering in Doped Hexagonal and Orthorhombic Manganites

5. Board of Studies: Physical Sciences

SYNOPSIS

The interest in the study of manganites ($RMnO_3$) is because of their unique electronic and magnetic properties. Intrinsic correlation of the crystal structure, magnetic and electronic properties leads to various phases and transitions in these manganites. Two different crystal structures are found in manganites according to the ionic radius of the R-site ions. The $RMnO_3$ compounds with smaller R^{3+} ionic radius (R = Ho to Lu and Y) crystallize in the non-centrosymmetric hexagonal space group $P6_3cm$, while the orthorhombic structure with *Pnma* space group is found for R^{3+} ions with a larger ionic radius (R = La, Ce, Pr, Nd, Sm, Eu, Gd, Tb or Dy).The hexagonal building block is fundamentally different from the orthorhombic building block, resulting in different physical properties. The orthorhombic manganites, $RMnO_3$ with R = La–Gd does not show any ferroelectricity, whereas for rare earths smaller than Dy, hexagonal

$RMnO_3$ exhibits multiferroic behaviour. Since the electronic and magnetic properties are governed by the interplay of charge, spin and orbital degrees of freedom, chemical substitutions play a dominant role in their physical properties.

In orthorhombic doped manganites there is overwhelming evidence that these oxides with high chemical homogeneity do show spatially inhomogeneous structures, i.e. regions showing different electronic and magnetic orders. This phenomenon is called as phase separation (PS) and is observed in both hole doped and electron doped manganites. However, in contrast with the hole-doped systems, there have been very few attempts to understand the electron-doped systems theoretically as well as experimentally. The presence of ferromagnetic component in some of the electron doped manganites (Mn^{4+} rich) raises an important question whether there is a canting of the G-type AFM structure, as originally proposed by deGennes, or a coexistence of magnetic phase separation to form domains of AFM and FM ordering. Some attempts have been made to understand the origin of ferromagnetic component in Mn^{4+} -rich compounds. In $CaMnO_3$, the Ca-site as well as in Mn-site substituted studies both phase separation and canted behavior has been observed. The debate over phase separation versus canted magnetic structure continues to be of interest.

Multiferroic hexagonal manganites have attracted special attention because of the coexistence of ferroelectric (FE) and magnetic ordering. In these hexagonal manganites geometry (crystal structure) plays an important role for the ferroelectric as well as for the magnetic properties. Recently, considerable attention has been paid to investigate the mechanism of the coupling in hexagonal manganites. Single phase multiferroic materials are of great interest due to its application in memory devices. The magnetic order of Mn^{3+} is mainly dominated by AFM in-plane Mn-O-Mn superexchange interaction, while the Mn–O–O–Mn superexchange between neighboring planes is approximately two orders of magnitude weaker. In a recent theoretical study it has been shown that the value of ferroelectric polarization can be controlled by changing the magnetic ground state. The role of possible changes in magnetic structure leading to large magnetocapacitance has been raised in some of the doping studies.

In the present thesis, the effect of the A-site and B-site doping on the magnetic and electronic properties of orthorhombic $CaMnO_3$ and hexagonal $YMnO_3$ manganites have been investigated. Neutron diffraction experiments allow us to study both chemical and magnetic structure and thereby to study their influence on various physical properties.

The thesis consists of five Chapters.

Chapter1: Introduction

In this Chapter a general introduction to the orthorhombic and hexagonal manganites and the various intriguing phenomena exhibited by these manganites is given. The crystal structures for both orthorhombic and hexagonal managnites, as well as their different crystal field splitting have been discussed. This structural difference makes the physics of the hexagonal manganite distinctly different from that of the orthorhombic one. A brief overview of the some of the important features of both the hexagonal and orthorhombic manganites has been discussed.

Chapter 2: Experimental Techniques

This Chapter includes a brief description about the sample preparation techniques and working principles of the various experimental techniques (x-ray diffraction, neutron diffraction, dc magnetization, resistivity set-up, neutron depolarization, Mössbauer spectroscopy, X-ray absorption, and dielectric spectroscopy) employed to investigate the structural and magnetic properties of the compounds. The polycrystalline compounds were synthesized by conventional solid state reaction route and initial phase identification of these samples was done by x-ray powder diffraction. The crystal and magnetic structure as a function of temperature are investigated by neutron diffraction technique. The neutron diffraction patterns were recorded on the PD2 powder diffractometer ($\lambda = 1.2443$Å) at the Dhruva reactor, Bhabha Atomic Research Centre, Mumbai between 6K and 300K in the angular range $5^o \leq 2\theta \leq 140^o$. A brief description about the Rietveld method to refine the crystal structures and to determine the magnetic structures from the powder diffraction data, is also given. The representation theory analysis for determining magnetic structures has been carried out using the BASIREPS and the SARAH programs. The magnetization measurements were carried out using the superconducting quantum interference design (SQUID) magnetometer. The resistivity as a function of temperature was measured using four - probe set up. To study the magnetic inhomogeneity in some of the selected samples, neutron depolarization measurements ($\lambda = 1.205$Å) were carried out on the polarized neutron spectrometer at Dhruva reactor, Bhabha Atomic Research Centre, Mumbai, India, with Cu_2MnAl (1 1 1) as polarizer and $Co_{0.92}Fe_{0.08}$ (2 0 0) as analyzer. To study the magnetoelectric coupling in hexagonal manganites, low-temperature dielectric measurements were carried out using a frequency-response analyzer (Novocontrol *TB*-Analyzer). In some of the Fe doped samples Mössbauer spectroscopy measurements have been done to know the oxidation states of Fe ions. XANES and EXAFS measurements on powder samples of $YMn_{1-x}M_xO_3$ (for x=0.1 and M = Ti, Fe, and Ga) were performed to probe the local structure surrounding the Mn sites.

Chapter 3: Effect of A-site and B-site doping on the magnetic properties of hexagonal $YMnO_3$

In this Chapter 3, the effect of doping on the magnetic structure and frustrated nature of hexagonal $YMnO_3$ has been studied. In hexagonal frustrated systems, $YMnO_3$ is preferred for the study of magnetic ordering of Mn ions, as there is no influence from the magnetism due to the rare earth 4*f* electrons. This chapter broadly consists of three parts viz., (1) Effect of A-site doping on the magnetic properties of $YMnO_3$, which consists of studies on $Y_{1-x}R_xMnO_3$ (R= Yb, Er, Tb, Ho; $x \leq 0.2$)) (2) Effect of B-site doping on the magnetic properties of $YMnO_3$, which consists of studies on (i) $YMn_{1-x}M_xO_3$ (M = Ti, Fe, Ga; x = 0, 0.1), and (ii) $YMn_{1-x}Fe_xO_3$ ($x \leq 0.5$), and (3) Computational studies on $YMnO_3$.The compounds are isostructural and crystallize with hexagonal structure in $P6_3cm$ space group. The magnetic structure of $YMnO_3$ is modelled by Γ_3 irreducible representation (IR) below T_N ~ 75K. By substituting Y with 20% of Er and Yb, the magnetic structure changes gradually from $\Gamma_3 + \Gamma_4$ to Γ_4 IR, while the moments remain almost unchanged with doping. With Ho doping at Y site, the magnetic structure is explained by taking Γ_3 alone for $5K \leq T < 35K$ and a mixture of Γ_3 and Γ_4 IR for $T \geq 35K$. However, in Tb doped sample, the magnetic structure has been explained by Γ_4 IR. The moment on Tb has been observed at 6K and the magnetic structure at 6K has been explained by Γ_4 IR with moments on Tb. The frustration parameter ($f=|\theta_{CW}| / T_N$) reduces with doping at Y-site. It is also noticeable that the intensity of the diffuse scattering becomes gradually weakened with doping of magnetic ions at the Y-site. The short range correlations in these doped samples have also been studied by Fourier transforming the diffuse part of the magnetic neutron diffraction data. The magnetic coupling between the magnetic R ion and Mn moments plays an important role here and relieves the frustration effects inherent to the quasi-two dimensional Mn moment ordering. We find the results can be explained by combining the effect of R-Mn interactions and ionic size of the dopants [1]. These studies conclude that the partial substitution of Y by magnetic ions, not only change the long range Mn order but also effect the short range magnetic correlations, along with the frustrated behavior of the compounds.

In the second par twe report the effects of Ti^{4+} (d^0), Fe^{3+} (d^5) and Ga^{3+} (d^{10}), doping at Mn-site on the structural and magnetic structure of $YMnO_3$. The dopants have been chosen to study the effect of interaction of the filled and unfilled orbital on the magnetic structure. The compositions were limited to 10% doping to remain in the isostructural phase. The polycrystalline compounds of $YMn_{1-x}M_xO_3$ (M = Ti, Fe, Ga; x = 0, 0.1) crystallize with hexagonal structure in $P6_3cm$ space group. Doping with these three ions, Ti^{4+} (d^0), Fe^{3+} (d^5) and Ga^{3+} (d^{10}) affect the magnetic structure of this compound in contrasting manner. The magnetic structure remains same with nonmagnetic Ga doping. However it is modified on doping with nonmagnetic ion Ti^{4+} (d^0). It is described by the basis vectors of the Γ_2 IR with moment $2.3\mu_B$ at 6K. On doping with Fe^{3+} (d^5) the magnetic structure immediately below T_N is explained by considering the Γ_3 IR. On further lowering of temperature, a spin reorientation at ~ 35K is observed. Below this temperature, the magnetic structure of $YMn_{0.9}Fe_{0.1}O_3$ is explained by considering mixed Γ_3 and Γ_4 representations. The ordered moments are found to be reduced from the expected value for a Mn^{3+} ion in all these compounds indicating the frustrated nature of these compounds. However, the frustration parameter, f is significantly reduced in the case of Ti doped compound with Γ_2 IR [2].

Further, to study the local structure of hexagonal $YMn_{1-x}M_xO_3$ (M = Ti, Fe, Ga; x = 0, 0.1) compounds x-ray absorption spectroscopy measurements have been performed. The x-ray absorption near edge spectra (XANES) show that the valence state of Mn atom remain essentially unaltered on doping. The dopants substitute at the Mn-site preserving the trigonal bipyramidal geometry. XANES spectra of $YMn_{0.9}Ti_{0.1}O_3$ at Ti K-edge,$YMn_{0.9}Ga_{0.1}O_3$ at Ga K-edge, indicates Ti is in +4 oxidation state and Ga is in +3 oxidation state, respectively. XANES measurements together with Mössbauer and magnetization measurements indicate the presence of Fe in +3 oxidation state. No appreciable change is observed in the XANES spectra of the samples with temperature. This indicates that structure as well as the oxidation states of Mnremains same with temperature for all doped samples. The EXAFS measurements indicate the presence of a double peak or shoulder for all studied samples all studied temperatures. The presence of double peak is indication of different Mn-O coordination shells having large difference in the bond lengths between the Mn-O_A and Mn-O_P bonds, where O_A and O_P denote the two apical and three planar oxygen atoms, respectively. This difference in Mn-O_A and Mn-O_P bonds is also observed in neutron diffraction data. The temperature dependent behavior of bond lengths obtained from EXAFS measurements is in agreement with the neutron diffraction data in all studied samples.

In the second part of the Mn-site doping studies, we describe the influence of Fe^{3+} substitution on the $YMn_{1-x}Fe_xO_3$ ($x \leq 0.5$) series. The substitution of Fe by Mn is interesting because of the same ionic radii of Fe^{3+} and Mn^{3+} yet different magnetic moment values. Because of the presence of an electron in d_z^2 orbital in case of Fe^{3+}, substitution of Fe^{3+} allow us to study the effect of electron doping in the $YMnO_3$. The substitution with Fe at Mn site leads to progressive changes in chemical and magnetic structure as a function of temperature and composition. A hexagonal phase for $x \leq 0.2$ and for $0.3 \leq x \leq 0.5$ a mixed hexagonal (characteristic to $YMnO_3$) and orthorhombic phase (characteristic to $YFeO_3$) is observed. With increase in Fe doping, there is a progressive increase of the orthorhombic phase fraction. All the compounds are antiferromagnetic and the magnetic structure is described as a mixture of Γ_3 and Γ_4 IR in the hexagonal phase. The ratio of these two IRs is found to vary with Fe doping ($x \leq 0.2$). The angle (φ) the spin makes with the a-axis changes from 28° for $YMn_{0.9}Fe_{0.1}O_3$ to 55° for $YMn_{0.8}Fe_{0.2}O_3$ at 6K. The magnetic ground state in the orthorhombic phase of the higher doped samples (x

≥0.3) is explained by taking $\Gamma_1(G_xC_yA_z)$ representation of *Pnma* setting. In $YMnO_3$ suppression of dielectric constant ε′ is observed below T_N indicative of magnetoelctric coupling. This anomalous behavior reduces in Fe doped samples. The dielectric constant is found to be correlated with the magnetic moment (M) obtained from neutron diffraction experiments and follows a M^2 behavior close to T_N in agreement with the Landau theory [3].

Further, the local structure of these doped hexagonal compounds has been studied by x-ray absorption spectroscopy measurements. The XANES at Mn K-edge demonstrate that the valence state of Mn atom remain essentially unaltered by doping. The dopants substitute the Mn-site, preserving the trigonal bipyramidal geometry for $x \leq 0.2$. For higher doping region ($0.3 \leq x \leq 0.5$), a second orthorhombic phase appears where Mn is coordinated by six oxygen atoms (hexagonal coordination). These observations are in agreement with our earlier x-ray diffraction and neutron diffraction studies.

First principle calculations were performed on hexagonal-$YMnO_3$ using DFT technique as implemented in Quantum Espresso (QE) code. The exchange-correlation potential utilized in these calculations was the Perdew-Zunger (PZ) version of the local density approximation (LDA). These calculations were performed incorporating the Hubbard correction. In hexagonal $YMnO_3$, calculations were performed with a grid of 12×12×12 reciprocal lattice points. In these calculations, the electronic self-consistent cycles were made to converge until the variation of the total energy was less than 10^{-8}eV. In our calculations, we imposed an A-type antiferromagnetic order and did the structural relaxation. The relaxed structural parameters obtained by QE code are reported. They are in agreement with the experimental as well as with the simulations results of VASP.

Chapter 4: Effect of A-site and B-site doping on the magnetic properties of orthorhombic $CaMnO_3$

In this Chapter, we have investigated the effect of Ca-site and Mn-site doping on the magnetic structure of $CaMnO_3$. $CaMnO_3$ is the end member of the $(La,Ca)MnO_3$ system. It has the perovskite related $GdFeO_3$-type orthorhombic structure and exhibits a G-type antiferromagnetic (AFM) structure (T_N ~125 K) with a weak ferromagnetic component in its ground state. Doping with trivalent ions at Ca^{2+} site or tetravalent or pentavalent substitution at Mn^{3+} site is found to give rise to ferromagnetic (FM) behavior in these compounds. The role of spin canting and/or phase separation leading to FM behavior in these compounds has been a subject of discussion in literature. To take this discussion further we have studied doping effects at the Ca^{2+} and Mn^{3+} sites in this compound. This chapter broadly consists of three sections viz., studies on (1) $Ca_{1-x}Y_xMnO_3$ ($0 \leq x \leq 0.2$), (2) $CaMn_{1-x}Fe_xO_{3-\delta}$ ($x \leq 0.3$), and (3) Computational studies on $CaMnO_3$. The first part of this chapter comprises of the effect of Y^{3+} doping in $Ca_{1-x}Y_xMnO_3$ ($0 \leq x \leq 0.2$) series. The compounds crystallize in orthorhombic structure for $x \leq 0.1$ while a coexistence of monoclinic and orthorhombic phase is observed at low temperatures in the case of $x=0.2$. The temperature dependence of the resistivity exhibits a semiconducting behavior and is described by small polaron model. The activation energy exhibits a minimum at $x=0.1$ and is ascribed to presence of ferromagnetic clusters in this sample. The magnetic structure for $x=0.1$ sample, at 6K is found to be G_Z type, similar to the parent compound. The rapid increase in magnetization and decrease in flipping ratio below 110K indicates the presence of ferromagnetic correlations (~7μm). These studies together indicate a phase separated state with FM clusters embedded in the AFM matrix in $x=0.1$ sample. The transition to the long-range magnetically ordered state in this sample is preceded by a Griffith's phase. Neutron diffraction and neutron depolarization studies rule out the presence of ferromagnetic correlations in x=0.2 sample. The ferromagnetic behavior in this case is suppressed and the antiferromagnetic ordering is described by coexisting C-type and G-type magnetic structures. For x=0.2, the orthorhombic phase partially transforms to a monoclinic phase. An antiferromagnetic ordering of the type G_z for the orthorhombic phase and C-type ordering for the monoclinic phase is observed in x=0.2 sample. The T_N (C-type) is found to be higher (125K <T_N(C) <150K) than T_N (G-type) (~100K) [4].

The effect of doping with Fe at Mn-site is studied in $CaMn_{1-x}Fe_xO_{3-\delta}$ ($x \leq 0.5$) series of compounds and these are discussed in second part of this chapter. The compounds of the series $CaMn_{1-x}Fe_xO_{3-\delta}$ ($x \leq 0.3$) are found to be isostructural and crystallize in $GdFeO_3$-type orthorhombic structure (space group *Pnma*). With Fe doping, no change in structure is observed although it induces lattice expansion. Mössbauer and paramagnetic susceptibility measurements show that Fe substitutes in 4+ valence state and XANES measurements indicate the presence of mixed oxidation states of Mn in the studied compounds. An increase in resistivity is observed with Fe doping, and this is explained by taking into consideration the band structure of Fe^{4+} and Mn^{4+}. The temperature dependence of resistivity is found to be described by small polaron model for x = 0 and variable range hopping model for x = 0.1. For higher x values, it follows a parallel combination resistance model. Instead of phase separated state, canted behavior has been observed for Mn-site doping. A small reduction in T_N from 120K (x = 0) to 100K (x = 0.2) with increase in x is found. The magnetic structure changes from G_z-type collinear AFM structure for x= 0 to canted AFM structure G_ZF_Y-type for Fe doped compounds. The AFM component of the moment progressively decreases with x while FM component exhibits a maximum at x = 0.2 [5].

First principle calculations on orthorhombic-$CaMnO_3$ were performed using the QE code to establish the magnetic ground state of this compound. The PZ version of the LDA for the exchange-correlation potential was utilized in these calculations. The Hubbard corrections were incorporated. For orthorhombic $CaMnO_3$, the calculations were performed with a grid of 8×4×8 reciprocal lattice points. In this study, A-type, G-type, C-type antiferromagnetic states were considered. The relative stabilities of these magnetic states were determined by comparing their total energies (or enthalpy). These calculations show that for $CaMnO_3$, G-type magnetic structure is the most stable among the three antiferromagnetic configurations, which is in agreement with the experimental results.

Chapter 5: Summary and Conclusion

A summary of the research work carried out and conclusions in this thesis is described in Chapter 5. The list of bibliographic references used in this thesis has been given after this chapter.

References:

1. Neetika Sharma, A. Das, Amit Kumar, C. L. Prajapat, , and M. R. Singh. J. Magn. Magn. Mater. (doi/ 10.1016/j.jmmm.2016.07.043).
2. Neetika Sharma, A. Das, C. L. Prajapat, and S. S. Meena, J. Magn. Magn. Mater. **348**, 120 (2013).
3. Neetika Sharma, A. Das, S. K. Mishra, C. L. Prajapat, M. R. Singh, and S. S. Meena. J. Appl. Phys.**115**, 213911 (2014).
4. Phase separated behavior in Yttrium doped $CaMnO_3$. Neetika Sharma, A. Das, Amit Kumar, C. L. Prajapat, , and M. R. Singh, Mater. Res. Bull. **77**, 284 (2016).
5. Neetika, A. Das, I. Dhiman, A.K. Nigam, A.K.Yadav, D. Bhattacharyya, and S. S. Meena, J. Appl. Phys., **112**, 123913 (2012).

LIST OF FIGURES

1.1 (a) Structure of the ideal cubic perovskite unit cell. (b) Sketch of the perovskite Pnma structure. 4

1.2 A schematic showing the relative energy levels of Mn 3d orbitals in ideal conditions, under the influence of crystal field, and after going a Jahn-Teller distortion. 6

1.3 Illustration of double-exchange mechanism for Mn ions with different valence state. 8

1.4 Schematic arrangement of spins in super exchnage interactions. The orbitals involved are the Mn eg and O 2p, and arrows show the virtual transfer of electrons between these orbitals. The transfer results in (a) antiferromagnetic, (b) antiferromagnetic, and (c) ferromagnetic arrangement of the Mn spins, respectively. 10

1.5 Different type of magnetic spin configuration in perovskite manganites. 12

1.6 The crystal structure of hexagonal $RMnO_3$ compounds (a) in paraelectric $P6_3/mmc$ (High temperature phase) phase, (b) in ferroelectric $P6_3cm$(Low temperature phase) phase. 18

1.7 A schematic showing the relative energy levels of Mn 3d orbitals in trigonal bypiramidal geometry. 19

1.8 The one dimensional magnetic spin arrangement of Mn^{3+} ions in hexagonal $RMnO_3$ compounds. 22

1.9 The irreducible representations Γ_1 to Γ_6 for R^{3+} in hexagonal $RMnO_3$ compound. 23

2.1 Schematic diagram of the scattering geometry. 39

2.2 A schematic diagram depicting the Bragg's law. 40

2.3 Direction of unit vectors ε, k, λ described in the text towards magnetic scattering in addition to scattering angle α, θ. The q lies in the plane of ε, k and is perpendicular to ε and magnitude of sinα. 52

2.4 A schematic and the corresponding instrument parameters of neutron powder diffractometer installed at Dhruva 55

2.5 Position detection system. 55

2.6 A schematic diagram of neutron depolarization spectrometer. 61

2.7 Diagram of sample positioning within the pick-up coils of the SQUID magnetometer. 63

2.8 A typical x-ray absorption spectrum for FeO at Fe edge. 65

2.9 The effect of isomer shift, quadrupole splitting, and nuclear Zeeman interaction on the nuclear energy levels of 57Fe (adapted from Ref. 198). 67

3.1 The schematic picture of the crystal structure of $YMnO_3$ in $P6_3cm$ space group. 68

3.2 Room temperaturepowder X- ray diffraction patterns of $Y_{0.8}R_{0.2}MnO_3$ (R= Yb, Er, Ho, Tb). Open circles are observed data points. The solid line represents the Rietveld refinement. Inset (a) shows the variation of unit cell volume (V) as a function of average A-site ionic radius, $<r_A>$. 72

3.3 Room temperaturepowder neutron diffraction patterns of $YMnO_3$. Open circles are observed data points. The solid line represents the Rietveld refinement. The tick marks indicates the position of nuclear Bragg peaks corresponding to space group $P6_3cm$. 73

3.4 Variation of planar bond lengths (Mn-O3 and Mn-O4) as a function of volume at 300K. (b) Variation of planar bond lengths (Mn-O3 and Mn-O4) as a function of volume at 6K. 74

3.5 Temperature variation of (a) lattice parameters a and c for $YMnO_3$, (b) unit cell volume and solid line represent a fit to Debye - Grüneisen equation at high temperature above T_N, and then this extrapolated to the lowest temperature below T_N. 75

3.6 Temperature variation of (a) lattice parameters a and c for $Y_{0.8}Ho_{0.2}MnO_3$, (b) unit cell volume and solid line represent a fit to Debye - Grüneisen equation at high temperature above T_N, and then this extrapolated to the lowest temperature below T_N. 75

3.7 Linear plot of the ΔV versus the square of the ordered magnetic moments of Mn ions. 76

3.8 (a) Tilting angle for $Y_{0.8}R_{0.2}MnO_3$ (R= Yb, Er, Ho, Tb) samples at 6K. The line is a guide to the eye (b) Buckling angle of MnO_5 trigonal bypiramids for all doped samples at 6K. 78

3.9 (a) The zero field-cooled (ZFC) magnetization (M) versus temperature (T) in field of H=0.1T for $Y_{0.8}R_{0.2}MnO_3$ (R= Yb, Er, Ho, Tb). Inset shows the enlarged picture of low temperature part of ZFC and FC magnetization (M) versus temperature (T).(b) Shows the inverse of susceptibility as a function of temperature and Curie- Weiss fit (solid line). 82

3.10 Evolution of the selected portion ($12° \leq 2\theta \leq 20°$) of neutron diffraction patterns with temperature for $YMnO_3$ in the temperature range 6K - 75K. 84

3.11 One-dimensional irreducible representations for the $YMnO_3$. 85

3.12 The observed (symbols) and calculated (line) neutron diffraction pattern for $YMnO_3$ compound at T = 6K and 300K. Lower solid line is the difference between observed and calculated pattern. The first row of tick marks indicates the position of nuclear Bragg peaks and second row indicate the position of magnetic Bragg peaks. Inset shows the variation of magnetic moment as a function of temperature. 86

3.13 The observed (symbols) and calculated (line) neutron diffraction pattern for $YMnO_3$, $Y_{0.8}Er_{0.2}MnO_3$, and $Y_{0.8}Yb_{0.2}MnO_3$ compounds at T = 6K. The first row of tick marks indicates the position of nuclear Bragg peaks and second row indicate the position of magnetic Bragg peaks. Inset (a) shows the variation of tilting angle (φ) as a function of ionic radius and magnetic structures for $Y_{0.8}Er_{0.2}MnO_3$, and $Y_{0.8}Yb_{0.2}MnO_3$. 88

3.14 The observed (symbols) and calculated (line) neutron diffraction pattern for $Y_{0.8}Ho_{0.2}MnO_3$ compound at T = 6K. Lower solid line is the difference between observed and calculated pattern. The first row of tick marks indicates the position of nuclear Bragg peaks and second row indicate the position of magnetic Bragg peaks. Inset shows the variation of tilting angle (φ) as a function of temperature for $Y_{0.8}Ho_{0.2}MnO_3$, and magnetic structure of $Y_{0.8}Ho_{0.2}MnO_3$. 89

3.15 The observed (symbols) and calculated (line) neutron diffraction pattern for $Y_{0.8}Tb_{0.2}MnO_3$ compound at T = 6K. Lower solid line is the difference between observed and calculated pattern. The first row of tick marks indicates the position of nuclear Bragg peaks and second row indicate the position of magnetic Bragg peaks. Inset shows the variation of magnetic moment as a function of temperature and 91 magnetic structure at 6K.

3.16 The magnetic diffusing scattering for $Y_{0.8}R_{0.2}MnO_3$ (R= Yb, Er, Ho, Tb) and $YMnO_3$, at (a) 75K, (b) 100K. The solid line corresponds to the 2D Warren function fitting results. 96

3.17 Radial correlation function g(r) for $Y_{0.8}R_{0.2}MnO_3$ (R= Yb, Er, Ho, Tb) and $YMnO_3$ at 75K. Arrows indicate the nearest-neighbour bond distances for Mn sublattice. 97

3.18 Room temperaturepowder X- ray diffraction patterns of $YMn_{1-x}M_xO_3$ (M = Ti, Fe, Ga; x = 0, 0.1). Open circles are observed data points. The solid line represents the Rietveld refinement. 98

3.19 Tilting angle for all doped sample at 6K. The dashed line denotes the tilting of $YMnO_3$ (4.5°). (b) Buckling angle of MnO_5 trigonal bypiramids for all doped samples at 6K. The dashed line denotes the buckling in $YMnO_3$. 99

3.20 The zero field-cooled (ZFC) magnetization (M) versus temperature (T) in field of H = 0.1T for $YMn_{1-x}M_xO_3$ (M = Ti, Fe, Ga; x = 0, 0.1). (b) Shows the inverse of susceptibility as a function of temperature and modified Curie- Weiss fit (solid line). 103

3.21 Room temperature Mössbauer spectrum of $YMn_{0.9}Fe_{0.1}O_3$. 105

3.22 Integrated intensity of (100) magnetic reflection for $YMn_{1-x}M_xO_3$ (M = Ga, Fe; x= 0, 0.1) as a function of temperature. (b) Integrated intensity of (101) magnetic reflection for $YMn_{1-x}M_xO_3$ (M = Ti, Fe, Ga; x = 0, 0.1) as a function of temperature. 108

3.23 The observed (symbols) and calculated (line) neutron diffraction pattern for $YMn_{0.9}Ti_{0.1}O_3$ compound at T=6K. Lower solid line is the difference between observed and calculated pattern. The first row of tick marks indicates the position of nuclear Bragg peaks and second row indicate the position of magnetic Bragg peaks. Inset (a) shows the M-H curve at T = 5K. Inset (b) shows the variation of magnetic moment as a function of temperature. 109

3.24 The observed (symbols) and calculated (line) neutron diffraction pattern for $YMn_{0.9}Fe_{0.1}$ O_3 compound at T = 55K. Lower solid line is the difference between observed and calculated pattern. The first row of tick marks indicates the position of nuclear Bragg peaks and second row indicate the position of magnetic Bragg peaks. 110

3.25 The observed (symbols) and calculated (line) neutron diffraction pattern for $YMn_{0.9}Fe_{0.1}O_3$ compound at T=6K. Lower solid line is the difference between observed and calculated pattern. The first row of tick marks indicates the position of nuclear Bragg peaks and second row indicate the position of magnetic Bragg peaks. Inset (a) shows the variation of tilting angle (φ) as a function of temperature. Inset (b) shows the variation of magnetic moment as a function of temperature. 111

3.26 Magnetic structures of $YMn_{0.9}Fe_{0.1}O_3$ and $YMn_{0.9}Ti_{0.1}O_3$. 112

3.27 Normalised XANES spectra of $YMn_{1-x}M_xO_3$ (for x=0.1 and M=Ga, Ti and Fe) at Mn K-edge with along with reference Mn metal, $MnCl_2$ and Mn_2O_3 sample. 113

3.28 Normalised XANES spectra of $YMn_{1-x}M_xO_3$ (for x=0.1 and M=Ga, Ti and Fe) at (a) Ti K-edge with reference Ti metal and TiO_2 (b) Fe K-edge with reference Fe metal and Fe_2O_3, (c) Ga K-edge with reference Ga_2O_3. 114

3.29 Normalised XANES spectra at Mn K-edge for (a) $YMnO_3$, (b) $YMn_{0.9}Ti_{0.1}O_3$, (c) $YMn_{0.9}Fe_{0.1}O_3$ at different temperatures. 116

3.30 Fourier transformed EXAFS spectra of (a) $YMn_{1-x}M_xO_3$ (for x=0.1 and M=Ga, Ti and Fe) at Mn K-edge, (a) $YMn_{0.9}Ti_{0.1}O_3$ Ti K-edge (b) $YMn_{0.9}Fe_{0.1}O_3$ Fe K-edge and (c) $YMn_{0.9}Ga_{0.1}O_3$ Ga K-edge. 117

3.31 Fourier transformed EXAFS spectra of $YMnO_3$ for temperature 300K, 200K, 100K, 50K, 35K and 10K at Mn K-edge (Scatter points) and theoretical fit (Solid line). 118

3.32 Fourier transformed EXAFS spectra of $YMn_{0.9}Ti_{0.1}O_3$ for temperature 300K, 200K, 100K, 35K, and 10K at Mn K-edge (Scatter points) and theoretical fit (Solid line). 119

3.33 Fourier transformed EXAFS spectra of $YMn_{0.9}Fe_{0.1}O_3$ for temperature 300K, 200K, 100K, 35K, and 10K at Mn K-edge (Scatter points) and theoretical fit (Solid line). 120

3.34 Variation of bond length with temperature for (a) $YMnO_3$, (b) $YMn_{0.9}Ti_{0.1}O_3$ and (c) $YMn_{0.9}Fe_{0.1}O_3$. 121

3.35 Variation of bond lengths (obtained from neutron diffraction) for $YMnO_3$. 122

3.36 Variation of bond lengths (obtained from neutron diffraction) for $YMn_{0.9}Ti_{0.1}O_3$. 122

3.37 Variation of bond lengths for (a) $YMnO_3$, (b) $YMn_{0.9}Ti_{0.1}O_3$. 123

3.38 The variation of volume fraction of hexagonal and orthorhombic phases of $YMn_{1-x}Fe_xO_3$ with the Fe content x. 125

3.39 Temperature variation of the (a) lattice parameters a and c, (b) unit cell volume for $YMn_{0.8}Fe_{0.2}O_3$. Inset shows the tilting and buckling angles at 6 K and 300K. 126

3.40 Temperature variation of unit cell volume for $YMn_{0.6}Fe_{0.4}O_3$. The solid line is a fit to the Debye - Grüneisen equation. 127

3.41 The zero field-cooled (ZFC) magnetization (M) versus temperature (T) in field of H=0.1T for $YMn_{1-x}Fe_xO_3$ (x = 0, 0.1, 0.2, 0.3, 0.4, 0.5). Inset shows the inverse of susceptibility as a function of temperature and modified Curie- Weiss fit (solid line). 130

3.42 The plot of Mössbauer spectrum of (a) $YMn_{0.8}Fe_{0.2}O_3$, (b) $YMn_{0.5}Fe_{0.5}O_3$ at 300K. 132

3.43 The observed (symbol) and calculated (line) neutron diffraction pattern for $YMn_{0.8}Fe_{0.2}O_3$ compound at T = 6K and 300K. Lower solid line is the difference between observed and calculated pattern. The first row of tick marks indicates the position of nuclear Bragg peaks and second row indicate the position of magnetic Bragg peaks. Inset (a) shows the variation magnetic moment as a function of temperature. Inset (b) shows the raw neutron data for x= 0, 0.1 and 0.2 samples at 6K. 134

3.44 The variation of tilting angle (φ) as a function of Fe content at 6K. Inset shows the variation of tilting angle (φ) as a function of temperature for $YMn_{0.8}Fe_{0.2}O_3$. 135

3.45 The magnetic structure for $YMn_{0.8}Fe_{0.2}O_3$ at 6K. 136

3.46 The observed (symbol) and calculated (line) neutron diffraction pattern for $YMn_{0.7}Fe_{0.3}O_3$ compound at T = 6K and 300K. Lower solid line is the difference between observed and calculated pattern. The first and second row of tick marks indicates the position of nuclear Bragg peaks for hexagonal and orthorhombic phase respectively. The third and fourth rows indicate the position of magnetic Bragg peaks. Inset shows the variation of tilting angle (φ) as a function of temperature for $YMn_{0.7}Fe_{0.3}O_3$. 137

3.47 The observed (symbol) and calculated (line) neutron diffraction pattern for $YMn_{0.5}Fe_{0.5}O_3$ compound at T=6K and 300K. Lower solid line is the difference between observed and calculated pattern. The first row of tick marks indicates the position of nuclear Bragg peaks and second row indicate the position of magnetic Bragg peaks. Inset shows the magnetic structure of the compound at 6K and variation of T_{SR} and T_N as a function of Fe concentration (x) 138

3.48 Phase diagram of $YMn_{1-x}Fe_xO_3$ ($0.0 \leq x \leq 0.5$). 139

3.49 The variation of dielectric constant (ε') with temperature (T) for (a) $YMnO_3$ (b) $YMn_{0.8}Fe_{0.2}O_3$ and (c) $YMn_{0.5}Fe_{0.5}O_3$. Inset shows the complex impedance (Z'') plane plot versus real part of impedance (Z'). Dielectric loss (tan(δ)) versus temperature (T) is shown in the inset of a. 141

3.50 The variation of Δε (ε'(T) - ε'(0)) as a function of $M^2(T)$ for (a) YMnO3 and (b) $YMn_{0.8}Fe_{0.2}O_3$. Inset shows the thermal variation of Δε for $YMnO_3$ (x=0), $YMn_{0.8}Fe_{0.2}O_3$ (x=0.2), and for $YMn_{0.5}Fe_{0.5}O_3$ (x=0.5). 143

3.51 Normalised XANES spectra of $YMn_{1-x}Fe_xO_3$ ($0.0 \leq x \leq 0.5$) at Mn K-edge. 145

3.52 Normalised XANES spectra of $YMn_{1-x}Fe_xO_3$ ($0.0 \leq x \leq 0.5$) at Fe K-edge. 146

3.53 Fourier transformed EXAFS spectra of $YMn_{1-x}Fe_xO_3$ at Mn K-edge (Scatter points) and theoretical fit (Solid line). 148

3.54 Fourier transformed EXAFS spectra of $YMn_{1-x}Fe_xO_3$ at Fe K-edge (Scatter points) and theoretical fit (Solid line). 149

4.1 Room temperaturepowder X- ray diffraction patterns of $Ca_{1-x}Y_xMnO_3$ ($0 \leq x \leq 0.2$). Open circles are observed data points. The solid line represents the Rietveld refinement. The tick marks indicates the position of nuclear Bragg peaks. The plots for x=0.1 and 0.2 are offset vertically for clarity. Inset shows the temperature variation of the monoclinic and orthorhombic phase fraction for x=0.2. The solid lines are the guide to the eye. 159

4.2 (a) Electrical resistivity (*ρ*) versus temperature (*T*) for $Ca_{1-x}Y_xMnO_3$(x = 0.0, 0.1, 0.2). (b) The variation of ln (*ρ/T)* with inverse of temperature. The solid line through the data is the fit to the small polaron model 162

4.3 The variation of activation energy (W) and resistivity at 50K (ρ_{50K}) as a function of composition. The solid line is a guide to the eye 164

4.4 The temperature variation of the magnetic susceptibility for $Ca_{1-x}Y_xMnO_3$ ($0 \le x \le 0.2$). Inset (a) shows the variation of M with magnetic field at T=5K. Inset (b) shows the inverse of susceptibility as a function of temperature and fit to Griffiths model (x=0.1) and Curie- Weiss law (x=0.2). 165

4.5 The observed (symbols) and calculated (line) neutron diffraction pattern for $Ca_{0.9}Y_{0.1}MnO_3$ compound at T = 6K. Lower solid line is the difference between observed and calculated pattern. The first row of tick marks indicates the position of nuclear Bragg peaks and second row indicate the position of magnetic Bragg peaks. Inset shows the thermal variation of magnetic moments. The obtained magnetic structure is drawn in the inset. 167

4.6 The observed (symbols) and calculated (line) neutron diffraction pattern for $Ca_{0.8}Y_{0.2}MnO_3$ compound at T = 6K and 300K. Lower solid line is the difference between observed and calculated pattern. The first and second row of tick marks indicates the position of nuclear Bragg peaks for *P2₁/m* and *Pnma* space group, respectively. The third and fourth row indicates the position of magnetic Bragg peaks for C-type and G-type AFM, respectively. Inset shows the thermal variation of magnetic moments. The obtained magnetic structures are drawn in the inset. 170

4.7 The flipping ratio (R) versus temperature for $Ca_{1-x}Y_xMnO_3$ (x=0.1, 0.2). 172

4.8 Room temperature powder X- ray diffraction patterns of $CaMn_{1-x}Fe_xO_3$ ($0 \le x \le 0.3$). Open circles are observed data points. The solid line represents the Rietveld refinement. The tick marks indicates the position of nuclear Bragg peaks. The plots for x=0.1, 0.2 and 0.3 are offset vertically for clarity. 175

4.9 Room temperaturepowder X- ray diffraction patterns of $CaMn_{1-x}Fe_xO_3$ ($0 \le x \le 0.3$). Open circles are observed data points. The solid line represents the Rietveld refinement. The tick marks indicates the position of nuclear Bragg peaks. The plots for x=0.1, 0.2 and 0.3 are offset vertically for clarity. 175

4.10 XANES spectra of the $CaFe_xMn_{1-x}O_{3-\delta}$ samples for x = 0, 0.1 and 0.2 at Mn K-edge along with that of reference compounds Mn_2O_3 and MnO_2. 177

4.11 Room temperature Mössbauer spectra of $CaMn_{1-x}Fe_xO_3$ for x = 0.1 and 0.2 samples. 179

4.12 (a) Electrical resistivity (ρ) versus temperature (T) for $CaMn_{1-x}Fe_xO_{3-\delta}$(x = 0.0, 0.1, 0.2, 0.3) . (b) The variation of 1/ ρ with temperature. The continuous line through the data is the fit (discussed in the text) 180

4.13 The zero field-cooled (ZFC) magnetization (M) versus temperature (T) in field of H = 1T for $CaMn_{1-x}Fe_xO_{3-\delta}$(x = 0.0,0.1,0.2,0.3) .Inset shows the inverse of susceptibility as a function of temperature. 183

4.14 The observed (symbols) and calculated (line) neutron diffraction pattern for $CaMn_{0.8}Fe_{0.2}O_3$ compound at T = 6K and 300K. Lower solid line is the difference between observed and calculated pattern. The first and second row of tick marks indicates the position of nuclear Bragg peaks and magnetic Bragg peaks for *Pnma* space group, respectively.The obtained magnetic structures are drawn in the inset. 185

4.15 Real part of dielectric permittivity ε' as a function of temperature at different frequencies for $CaMnO_3$. Inset shows the variation of loss (tanδ) with temperature. 188

4.16 Real part of dielectric permittivity ε' as a function of temperature at different frequencies for $CaMn_{0.9}Fe_{0.1}O_3$. Inset shows the variation of loss (tanδ) with temperature. 188

4.17 Real part of dielectric permittivity ε' as a function of temperature at different frequencies for $CaMn_{0.8}Fe_{0.2}O_3$. Inset shows the variation of loss (tanδ) with temperature. 189

4.18 Arrheniuos plot of relaxation times for (a) $CaMnO_3$ (b) $CaMn_{0.9}Fe_{0.1}O_3$ (c) $CaMn_{0.8}Fe_{0.2}O_3$. 190

LIST OF TABLES

3.1 Lattice parameters and selected bond lengths at 6K and 300K, Curie-Weiss fit parameters, geometrical frustration parameter (*f*), tilting angle (α), buckling angle (β) and correlation length (ξ) for $Y_{0.8x}R_{0.2}MnO_3$ (R= Yb, Er, Tb, Ho). 79

3.2 Results of Rietveld refinement of neutron diffraction pattern at 6K and 300K, Curie – Weiss fit parameters, geometrical frustration parameter, and transition temperature for $YMn_{1-x}M_xO_3$ (M = Ti, Fe, Ga; x = 0, 0.1). 102

3.3 Mössbauer parameters at room temperature for $YMn_{0.9}Fe_{0.1}O_3$. 106

3.4 Results of Rietveld refinement of neutron diffraction pattern at 6K, transition temperature, Curie – Weiss fit parameters, geometrical frustration parameter for $YMn_{1-x}Fe_xO_3$ ($0.1 \leq x \leq 0.5$). 129

3.5 Mössbauer parameters for $YMn_{1-x}Fe_xO_3$ (x = 0.2, & 0.5) at 300K. 132

3.6 Fe K-edge energy of reference (Fe_2O_3) and $YMn_{1-x}Fe_xO_3$ samples. 147

3.7 Comparison between the calculated and experimental (6K) structural parameters of $YMnO_3$ (Hexagonal phase, space group $P6_3cm$). The experimental structure (space group $P6_3cm$) consists of Y1 and O3 atoms at the position 2a(x,y,z), Y2 and O4 at 4b(x,y,z), and Mn, O1, and O2 at 6c(x,y,z) Wyckoff site. 152

3.8 Comparison between the calculated and experimental bond lengths in $YMnO_3$ (Hexagonal phase, space group $P6_3cm$). 153

4.1 Results of Rietveld refinement of neutron diffraction pattern at 6 K, resistivity values, Curie – Weiss fit parameters, and variance (σ^2) for $Ca_{1-x}Y_xMnO_3$. 163

4.2 Results of Rietveld refinement of neutron diffraction pattern at 6K, resistivity values at room temperature, Curie – Weiss fit parameters, exchange integral values, ferromagnetic component (F_Y) and antiferromagnetic component (G_Z) of moment for $CaMn_{1-x}Fe_xO_{3-\delta}$. 176

4.3 Mössbauer parameters at room temperature for $CaMn_{1-x}Fe_xO_{3-\delta}$. 179

4.4 The parameters obtained from fitting the resistivity data for $CaMn_{1-x}Fe_xO_{3-\delta}$ in the paramagnetic region. 182

4.5 Structural parameters for $CaMnO_3$ obtained for three different values of 192

Hubbard corrections compared with our experimental results.

4.6 Values of total enthalpy for $CaMnO_3$ calculated for three different values of Hubbard corrections (U). 192

Chapter 1

Introduction

1.1 Manganites

Manganites refer to a family of manganese oxides, which shows a very rich phase diagram and fascinating properties. The name “manganites” was first given by Jonker and Van Santen [1, 2] and they were first to crystallize and study the magnetic properties of the mixed-valence manganites such as $LaMnO_3$-$CaMnO_3$, $LaMnO_3$-$SrMnO_3$, and $LaMnO_3$-$BaMnO_3$. End-members of these series are usually antiferromagnetic insulators, while compounds with intermediate compositions may be ferromagnetic and conducting. The term manganites should only apply to compounds containing tetravalent Mn only. However, Jonker and van Santen adopted this term to refer to mixed valent compounds. These compounds belong to the strongly correlated electron systems, since many properties and transitions in these cannot be described by simple one electron models. Manganites have attracted continuous interest for their strong correlation among the charge, spin, and orbital degrees of freedom which makes these systems particularly sensitive to external perturbations, such as temperature, application of magnetic field or high pressure, and A-site ionic radius. This correlation creates multiple ground states, *viz.* ferromagnetic insulator, ferromagnetic metal, antiferromagnetic charge ordered insulator, and paramagnetic insulator [3]. Recently, another characteristic behavior in manganites, *viz.*, multiferroicity, has been highlighted due to the revival of interest in magnetoelectric effects [4-6], where magnetic (electric) polarization is controlled by electric (magnetic) fields.

The manganites have the chemical formula $RMnO_3$, where the R site is usually occupied by rare earth ions. Two different crystal structures are found in manganites according to the ionic radius of the R-site ions. The $RMnO_3$ with large ionic radii (R = La, Ce, Pr, Nd, Sm, Eu, Gd, Tb or Dy), crystallize with the perovskite structure having orthorhombic *Pnma* symmetry [7]. For smaller rare-earths ions (R = Ho to Lu and Y, Sc), the orthorhombic perovskite structure is no longer stable under ordinary synthesis conditions and the hexagonal non-perovskite phase becomes more stable [8]. However, it is possible to transform the crystal structures of these two families from hexagonal to orthorhombic (or vice versa) under high temperatures and high pressure [9] or by means of special synthesis methods such as, chemical solution deposition [10], low temperature soft chemistry or epitaxial thin-film growth [11, 12]. The hexagonal building block is fundamentally different from the orthorhombic building block, resulting in different physical properties. The magnetic ordering of Mn ions in both these phases occurs by the superexchnage interactions between Mn ions via oxygen. Regardless, of the similar size of Fe^{3+} and Mn^{3+} ion, in $RFeO_3$, the perovskite structure is found to be stable for all the R ionic sizes, i.e. from La to Lu, in contrast with $RMnO_3$ manganites [13, 14]. The rare earth orthochromites $RCrO_3$ [13], and $RCoO_3$ (except for $LaCoO_3$) where R is a rare earth element or yttrium, all crystallize in an orthorhombically distorted perovskite structure [15]. Therefore, the instability of the perovskite structure for small R ions in manganites is considered to be a consequence of the interplay of geometric and Jahn-Teller (JT) distortion.

1.2 Orthorhombic Manganites

The perovskite manganites are fascinating due to their several interesting properties such as colossal magnetoresistance (CMR), charge, spin and orbital coupling, and mesoscopic phase separation tendencies. As a function of doping or average size of A-site cations, they show a rich and interesting magnetic phase diagram. These properties of doped manganites are regulated by the influence of the Jahn-Teller distortion and the electron-phonon interactions in addition with magnetic exchange interactions [16-26]. The full Hamiltonian model which regulates the physics of the manganites and describes the various competing magnetic ground states, including charge and orbital degrees of freedom, consists of five terms;

$$H = H_{kin} + H_{Hund} + H_{AFM} + H_{el-ph} + H_{el-el} \,;$$

where, the first term is the kinetic energy of the e_g electron, H_{Hund} is the Hund coupling between the e_g electron spin and the localized t_{2g} spin, and expressed as,

$$H_{Hund} = -J_H \sum_i s_i . S_i$$

These two terms in the above expression describes the double exchange Hamiltonian. In above two terms role of e_g electrons has been discussed. But the antiferromagnetic exchange between t_{2g} electrons has been not taken into consideration. The third term in the above expression is the Heisenberg exchange term given as;

$$H_{AFM} = -J_{AF} \sum_{\langle i\, j \rangle} S_i . S_j \;;$$

where J_{AF} is the antiferromagnetic exchange coupling between nearest neighbor t_{2g} spins. This term accounts for the appearance of the G-type antiferromagnetic phase for the system with no e_g electrons, such as $CaMnO_3$. The fourth is the electron-phonon coupling, combines the JT and the breathing mode distortions and is summarized as,

$$H_{el-ph} = g \sum_i \left(Q_{1i} n_i + Q_{2i} \tau_{xi} + Q_{3i} \tau_{zi} \right) + k_{JT} \sum_i (Q_{2i}^2 + Q_{3i}^2)/2 + k_{br} \sum_i Q_{1i}^2 / 2 \,;$$

where g is the coupling constant between the e_g electrons and distortions of the MnO_6 octahedron, Q_{1i} is the breathing-mode distortion. Q_{2i} and Q_{3i} are the respective (x^2-y^2) and ($3z^2$-r^2) type JT distortions. The electron phonon coupling term depends on the $\beta = k_{br} / k_{JT}$, which regulates which distortion, the JT or breathing mode, plays a more important role. The Coulomb interaction between e_g electrons is given by last term H_{el-el}. The total Hamiltonian described above includes several competing tendencies and couplings, but, it is quite difficult to solve such a complicated Hamiltonian. Therefore, to investigate further the properties some simple models are requires as discussed by Dagotto et al.[27] and Hotta et al.[28].

1.2.1 Crystal Structure

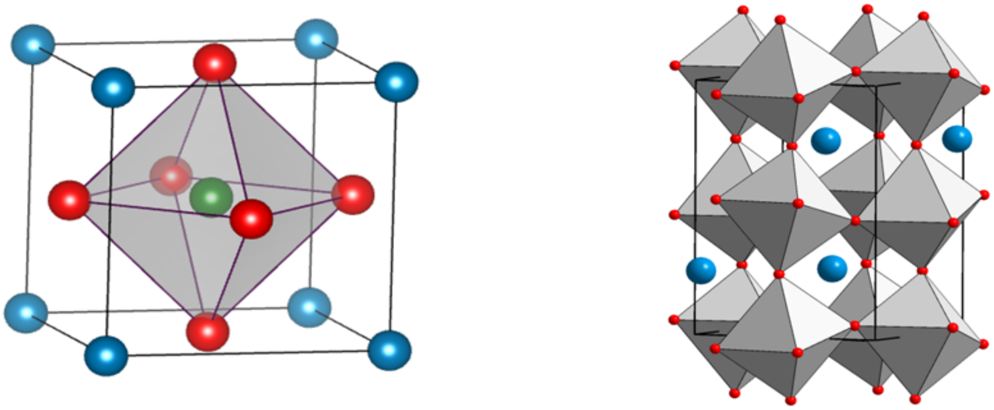

Figure 1.1: Structure of the (a) ideal cubic perovskite unit cell, (b) Orthorhombic structure

The manganites with general formula $RMnO_3$ having structure similar to that of perovskite mineral $CaTiO_3$ are named as perovskites [29]. In an ideal perovskite structure, the A cations are surrounded by twelve oxygen ions and the Mn ions are surrounded by six oxygen ions in octahedral coordination. The perovskite crystal structure can be regarded as a three dimensional network of corner sharing MnO_6 octahedra, with the Mn ions in the middle of the octahedra. The real perovskite structures are nearly never perfectly cubic.The reason is that it is hard to fulfill the relation between the radii of R and B ions, which is required for the perfect cubic lattice. The tolerance factor, $t=(r_R+r_O)/\sqrt{2}(r_{Mn}+r_O)$ where r_R, r_{Mn} and r_O represents the average ionic radius of the element at site A,B or O, is a measure of the deviations from the ideal cubic perovskite structure [30]. Tolerance factor is ideally 1 in a cubic structure with an angle of 180° between Mn-O-Mn bonds. But if the R–site cation is smaller than the ideal value, the tolerance factor t would be < 1. As t decreases, the lattice structure transforms to the rhombohedral and then to the orthorhombic structures, in which the bending of the Mn–O–Mn bond and its deviation from an angle of 180° increases.These compounds possess a stable perovskite structure when $0.75 < t < 1$[31]. The smaller ionic radius of A-ions in comparison to voids between the octahedra results in geometrical distortions in the form of cooperative buckling and tilting of the corner shared octahedra. Therefore, the transformation to orthorhombic structure from a cubic structure occurs by rotations of the octahedra in antiphase about the pseudocubic a and c axis and in-phase about the pseudocubic b axis. The in-phase and anti-phase rotations are denoted with the superscripts $+$ and $-$ respectively, such that the Glazer's notaion associated with the *Pnma* space group is $a^- b^+ a^-$[32]. This is known as the *GdFeO*$_3$ rotation and yields the space group *Pnma*. The orthorhombic cell parameters are related to those of the ideal cubic cell as $a \approx c \approx \sqrt{2}a_c$ and $b \approx 2a_c$ (lattice parameters of orthorhombic unit cell denoted by a, b, and c). The undistorted ideal cubic structure and orthorhombic structure for $RMnO_3$ is depicted in figure 1.1. There are two substructures related to the orthorhombic symmetry, denoted as O and O'orthorhombic structure, respectively. The O- orthorhombic structure is due to cooperative buckling of the corner shared octahedra and is purely due to the rotation of octahedral whereas the O'- orthorhombic structure is attributed to the superimposition of JT distortion on O-orthorhombic structure. The two substructures are distinguished by comparing the unit cell parameters, where $b/\sqrt{2} > c$ and $a > c$ for O-orthorhombic and $a > c > b/\sqrt{2}$ for O'-orthorhombic structure [33, 34].

1.2.2 Crystal – field splitting and Jahn –Teller Theorem

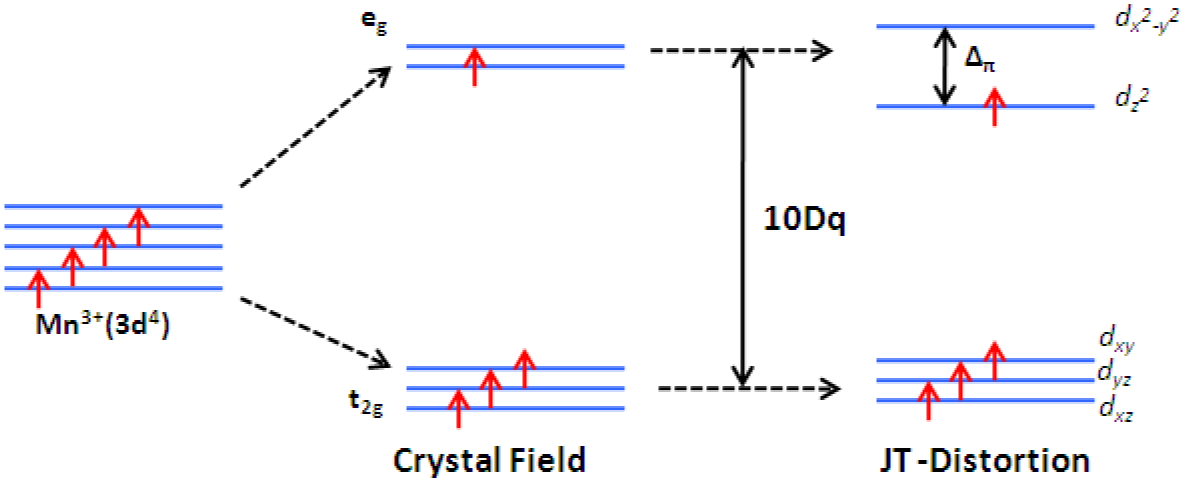

Figure 1.2: A schematic showing the relative energy levels of Mn 3d orbitals in ideal conditions, under the influence of crystal field, and after going a Jahn-Teller distortion.

Crystal field theory describes the effect a local environment has on the energy-levels of an ion. In an isolated atom or ion, the d orbitals are all degenerate, i.e. they have identical orbital energies. The ground state of Mn ions comprises of five-fold degenerate $3d$ orbitals, shown in figure 1.2. In perovskite manganites, the Mn ions are located in the centre of MnO_6 octahedra, surrounded by the six nearest-neighbor oxygen ions. In octahedral symmetry, the d levels split into $t_{2g}\left(d_{xy}, d_{xz}, and\ d_{yz}\right)$ and $e_g\left(d_{x^2-y^2}, d_{z^2}\right)$ and the orbitals which lie along these axes $\left(i.e.\ x^2-y^2, z^2\right)$ will be (raised in energy) destabilized more that the orbitals which lie in-between the axes $\left(i.e.\ xy, xz, yz\right)$. Therefore, the $d_{x^2-y^2}$ and d_{z^2} orbitals occupy the higher energy states while the d_{xy}, d_{xz}, d_{yz} occupy the lower energy state. Similarly, in the case of Mn ions situated in a tetrahedral site lead to a splitting such that e_g level lies lower in energy and a triplet state t_{2g} at higher energy level. The difference in energy of the t_{2g} and e_g energy levels is dependent on the type of transition metal, ligand bond, and the geometry of the molecule. These two states have an energy gap of $\Delta_{CF} = 10Dq \approx 1eV$ where the energy of e_g states are $6Dq$ higher than the ground state energy. D is the crystal parameter related to geometry and q is the charge on an atom and is ~ $<r^4>$, where r is the average atomic distance.

Besides the crystal field splitting effects, the Jahn-Teller (JT) effect also causes splitting of t_{2g} or e_g orbitals, provided either of these is partially occupied. In the perovskite manganites *RMnO*$_3$ the Mn^{3+} ion has a d^4 configuration. The Mn^{3+} ion has high-spin configuration, with three electrons occupying the three t_{2g} orbitals and one electron occupying the doubly degenerate e_g orbitals as $t_{2g}^3 e_g^1$. The Jahn-Teller theorem states that such an electronic configuration is unstable and that the degeneracy has to be lifted by a (local) distortion of the octahedral [25]. The JT effect originates from the degenerate Mn^{3+} d^4 ion in an octahedral crystal field and induces elongation of the crystal within the xy plane and shrinking along the z -axis. This results in a further removal of the t_{2g} and e_g degeneracy. The Jahn-Teller effect is typically an order of magnitude smaller than the crystal field splitting energy. In the presence of the Jahn-Teller distortion the e_g orbitals have different energies, which lead to many interesting phenomena like orbital ordering in manganese perovskites.

1.2.3 Magnetic Interactions

The long range ordering of the magnetic moments, exhibited by magnetic materials arises because of the different type of exchange interactions present in these materials. In manganites the stabilization of several coexisting magnetic ground states have been ascribed to competition between ferromagnetic double exchange and antiferromagnetic super exchange interactions. Both of them are indirect exchange interactions mediated by the oxygen, which is located between the two Mn cations. The double exchange and superexchnage interactions between Mn ions have been elaborated below.

1.2.3.1 Double Exchange

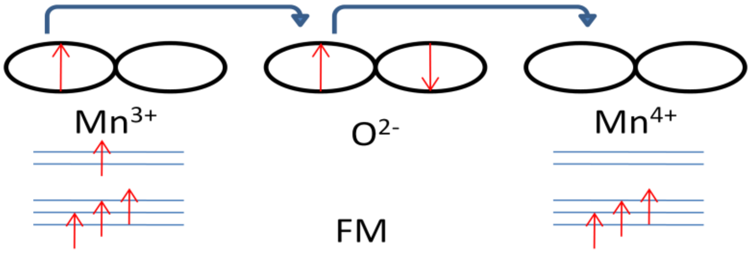

Figure 1.3: Illustration of double-exchange mechanism for Mn ions with different valence state.

The theory of double exchange was introduced by Zener [35], which gives a qualitative understanding of the origin of ferromagnetism in doped manganites. Double exchange takes its name from the fact that it results from a combination of Coulomb and kinetic-exchange.The double-exchange mechanism was subsequently reformulated and studied in two classic papers by Anderson and Hasegawa [36] and by de Gennes [37]. According to this mechanism, both ferromagnetism and conduction are linked to the mobility of the manganese conduction electrons. This is the interaction between pairs of Mn^{3+} and Mn^{4+} ions in mixed-valent perovskites through an oxygen atom. In this mechanism, the concurrent transfer of an electron from Mn^{3+} (3d e_g) orbital to an O (2p) orbital and from the same O (2p) to Mn^{4+} (3d e_g) orbital on an adjacent ion take place. According to this process, the hopping depends on the orientation of the magnetic moment of the t_{2g} state. The Hund's rule coupling makes it favorable for the spin of the core electrons to align with the spin of the itinerant electron and thus this electron transfer scheme makes ferromagnetic alignment energetically favorable. An important aspect is that double exchange is spin polarized conduction and occurs only when the spins of the adjacent Mn ions are aligned parallel or are ferromagnetically ordered.

1.2.3.2 Superexchange

The mechanism of superexchange (SE) interaction was first introduced by Kramer in 1934 [38]. SE interaction is an indirect interaction between magnetic ions, too far apart to be connected by direct exchange, but coupled through a non-magnetic material. SE interaction is a virtual exchange between electrons of magnetic ions with electrons from the same 2p orbital of oxygen, which have antiparallel spins according to Pauli's exclusion principle. The superexchange can be ferromagnetic or antiferromagnetic. For instance in thecase of Mn^{3+}- O -Mn^{4+}, it depends on the orientation of the Mn^{3+} orbital. This model was further developed by Anderson and in the same year Goodenough [39] and Kanamori [40] proposed some rules which described the main features of the superexchnage intaeractions. The rules are:

(1) The superexchange interactions are antiferromagnetic where the virtual electron transfer is between overlapping orbitals that are each half-filled.

(2) These interactions are ferromagnetic where the virtual electron transfer is from a half-filled to an empty orbital or from a filled to a half-filled orbital.

Goodenough (1955) proposed a concept of semi covalent exchange, which a refinement of the superexchange that takes account of the degree of covalency (or the sharing time of valence electrons of $O2p$ orbital with the electrons of the partially filled Mn $3d$orbitals which depends on the spin - spin interaction between $3d$ and $2p$ valence electrons) and orbital symmetry.The nature of the exchange varies with the degree of overlap of the empty $Mn\ 3d$ level and the filled $O2p$ level. However, the Goodenough-Kanamori rules are same for both superexchange and semicovalent exchange interactions.

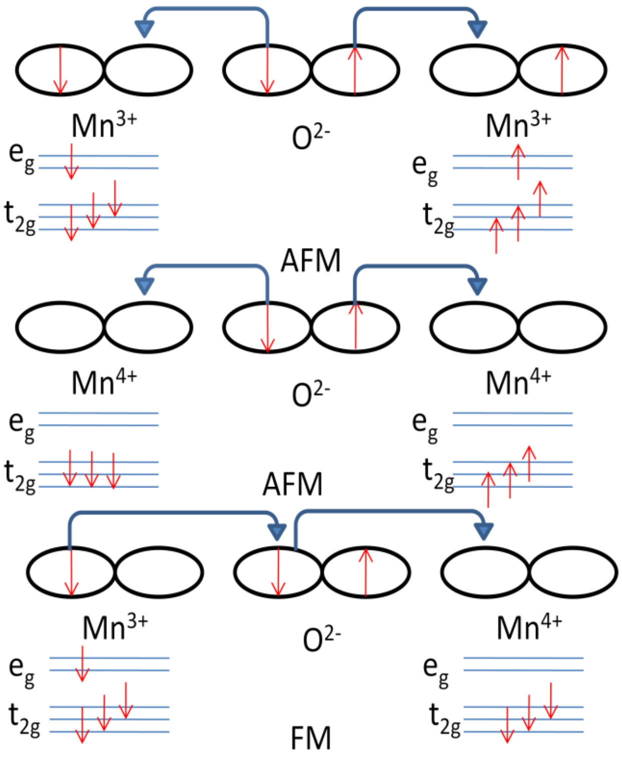

Figure 1.4: Schematic arrangement of spins in super exchnage interactions. The orbitals involved are the Mn eg and O 2p, and arrows show the virtual transfer of electrons between these orbitals. The transfer results in (a) antiferromagnetic, (b) antiferromagnetic, and (c) ferromagnetic arrangement of the Mn spins, respectively.

1.2.4 Magnetic properties of manganites

The competition between DE and SE interactions in manganites results in different types of magnetic structures in doped manganites. Seven possible spin arrangements in perovskites located on the Mn ions, A, B, C, D, E, F, and G are shown in figure 1.5. Perovskite manganites of the type $R_{1-x}A_xMnO_3$ (R=La, Pr, Sm etc, A=Ca, Ba, Sr etc) have been studied intensively in view of their rich magnetic phase diagram, which display a variety of magnetic structures as a function of doping. Depending upon doping and average A-site ionic radii, these compounds exhibit various ground states such as ferromagnetic metallic, ferromagnetic insulating, antiferromagnetic insulating, in addition to charge and orbital ordering.

In doped manganites, $La_{1-x}Ca_xMnO_3$ is the most studied mixed valent system, which exhibits varied electronic and magnetic phase transitions. Jonker and van Santen [1], as well as Wollan and Koehler [41] have investigated the rich magnetic phase diagram of Ca-doped $La_{1-x}Ca_xMnO_3$ using neutron diffraction techniques. They found the existence of different antiferromagnetic (A, C-E, C, and G types) as well as ferromagnetic configuration. The various magnetic structures displayed by the (La, Ca)MnO_3 as a function of doping depends on the different proportion of the Mn^{3+} and Mn^{4+} ions. For $x = 0$; i.e. for $LaMnO_3$ (only Mn^{3+} ions), an A-type antiferromagnetic structure has been observed below $T_N = 140K$. The A-type structure has ferromagnetic layers that are coupled antiferromagnetically. The substitution with Ca^{2+} ions leads to the simultaneous occurrence of Mn^{3+} and Mn^{4+} ions in the system. For low Mn^{4+} concentration ($x < 0.08$) the system evolves from an AFM to canted state. The model of a homogeneous canted phase was developed by de Gennes [37]. However, an alternative hypothesis of existence of inhomogeneous mixture of FM and AF phases has been shown in many studies [42-46]. The coexistence of the ferromagnetic and insulating phases have been observed for x between 0.08 and 0.17 ($0.08<x<0.17$). Further increase in Mn^{4+} concentration, a ferromagnetic component starts to grow and it changes completely from AFM to FM for $x{\sim}0.3$. The metallic phase only exists over a narrow range of $0.17 < x < 0.50$, where the CMR effect is also observed [47]. Near $x=0.5$, a new AF phase consisting of a regular stacking of the C and E types called the CE type, has been observed. With further increase in x (or Mn^{4+} concentration), the CE structure progressively transform to C-type structure. The end compound at x=1, $CaMnO_3$ exhibits a G-type antiferromagnetic (AFM) structure (T_N ~125 K) with a weak ferromagnetic component in its ground state [48]. In this configuration each Mn moment is oriented antiparallel to its nearest Mn neighbors.

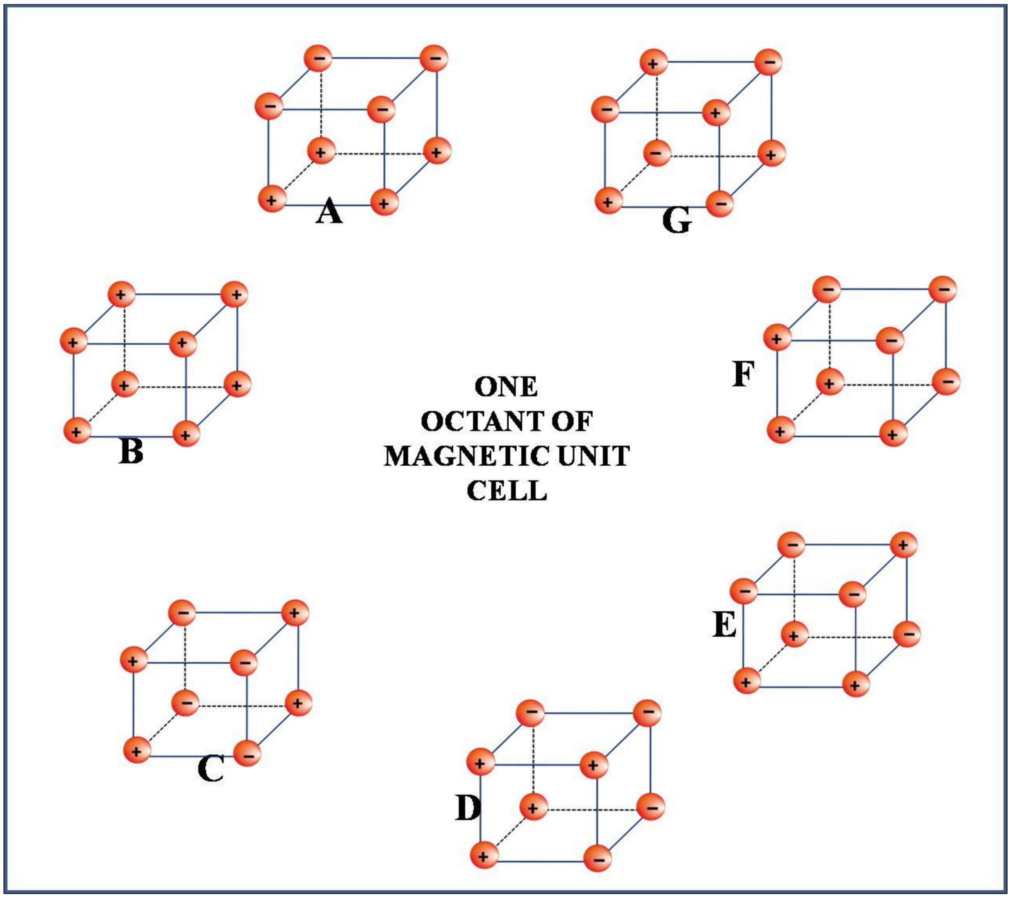

Figure 1.5: Different type of magnetic spin configuration in perovskite manganites [41]

These doped manganites with x<0.5 are so-called hole-doped (Mn^{3+} rich); those with x>0.5, are electron doped manganites (Mn^{4+} rich). The existence of ferromagnetism for both electron doped and hole doped systems has motivated new investigations of the magnetoresistive properties [49]. In contrast with the hole-doped systems, there have been very few attempts to understand the electron-doped systems theoretically as well as experimentally. Recently the electron-doped region of manganites has attracted a great deal of interestin view of their rich phase diagram [50-57]. In the study of the electric and magnetic properties of some of the Ca based electron doped manganites $Ca_{1-x}A_xMnO_3$ (A= Pr, Nd, Eu, Gd, Ho, Sm, Ce , Th) Maignan et. al.[53] and Martin et. al.[54] have shown that the electron concentration is the dominating effect influencing the physical properties as against the average ionic radii in the case of hole doped manganites. They also have found a ferromagnetic metallic phase in a very small region around x~0.12. The presence of ferromagnetic component in some of these electron doped manganites raises an important question whether there is a canting of the G-type AFM structure, as originally proposed by deGennes [37], or a coexistence of magnetic phase separation to form domains of AFM and FM ordering. According to deGennes, in lightly doped systems a small concentration of doped carriers into the e_g band (which is fully polarized due to the strong Hund's coupling of localized t_{2g} electrons) gives rise to ferromagnetic double-exchange interactions, which competes with AFM super-exchange to produce a spin canted G-AFM state. For many years this canted state was assumed to be correct, and many experiments were explained by using the canted state proposed by deGennes. Note also that a canted state is not easy to distinguish experimentally from a mixed or a phase separated AF-FM state. However, in a number of theoretical studies it has been found that the spin canted state is not energetically stable, suggesting a tendency toward phase separation magnetic state in both hole and electron doped manganites [58-63]. It has been also shown that the existence of a canted ground state depends on the relative magnitudes of the various electronic parameters, such as Hund's rule exchange energy and Coulomb repulsion. Canting is unstable in the systems when the Hund's rule- exchange energy $J_H<\infty$ and Coulomb repulsion is considered [64]. Not only the theoretical studies but, a number of experimental evidences also suggest the existence of inhomogeneities in manganites either in macroscopic form or, through the presence of clusters of one phase embedded into another [65-68].

1.2.5 Phase separated behavior in manganites

The interesting thing about manganites is that they are intrinsically electronically inhomogeneous, consisting of different spatial regions with different electronic and magnetic order though with high chemical homogeneity. These regions with different electronic and magnetic orders have been observed even in purest form of single crystals [69-73]. These regions can be static or dynamic and their size can be tuned by the application of external magnetic field [74]. Furthermore, the size scale of these spatial inhomogeneities can vary from nanometres to as large as micrometres. This phenomenon is called as phase separation (PS) in which different phases having different electronic and magnetic properties coexist in a single phase material. This sort of phase-separation behavior is a common characteristic of many manganites, resulting from the strong coupling between lattice, electronic and magnetic degrees of freedom. Phase separation effect is observed in both the hole doped and the electron doped manganites. Phase separation has also been suggested to occur in the cuprates [75] and nickelates [76]. Phase separation behavior results from the competition among double exchange, the AFM super exchange, and the Coulomb interaction. On the basis of theoretical calculations, Dagotto et al. [71] have argued that the phase separation and phase coexistence occurs on a wide range of length scales from sub-nanometers to few micrometers throughout the doping range. Its presence at different length scales in doped manganites has been also discussed by Shenoy et al. [73]. Different techniques, depending on the length scale, can be used to study the phase separation in the systems. Inhomogeneity of larger length scale can be probed by neutron and x-ray scattering techniques, whereas NMR and Mossbauer can be used for smaller length scales

[71]. First instance of phase coexistence in manganites was observed in neutron diffraction experiments in 1950. The presence of heterogeneous admixture of FM and AFM phases was discussed by Wollan and Koehler in the analysis of their data for $La_{1-x}Ca_xMnO_3$ series [41]. Two types of phase separation scenario have been observed in doped managnites. One is based on the electronic inhomogeneity (electronic phase separation) and other one is driven by the disorder induced in the system by chemical substitution [71]. Monte Carlo simulations on the manganites have shown the existence of large FM clusters in the antiferromagnetic phase, when the densities of ferromagnetic and antiferromagnetic phases are equal [77]. The variation in the size of clusters has been explained by Moreo et al. [77] on the basis of disorder in the system.They find that introducing disorder into AFM matrix leads to growth of FM clusters. The electronic phase separation as suggested by Dagotto et al. is caused by the presence of competing states with different electron density and Coulomb effects, leading to nanometer sized cluster coexistence [71]. However, the disorder-driven phase separation behavior leads to the formation of large coexisting clusters [78].

1.2.6 Orthorhombic Calcium Manganite ($CaMnO_3$)

$CaMnO_3$ is the end member of the (La,Ca)MnO_3 system. It has the perovskite related $GdFeO_3$-type orthorhombic structure and has a G-type antiferromagnetic (AFM) structure (T_N ~125 K) with an additional weak ferromagnetic component in its ground state. The weak ferromagnetism observed in pure $CaMnO_3$ is presumably resulting from the anisotropy imposed by orthorhombic distortion [79]. The magnetic interactions between the Mn ions are superexchange interactions. Because of Mn^{+4} configuration, there is no tendency for Jahn-Teller distortion. However, the substitution of Ca^{2+} by trivalent or tetravalent ions leads to the simultaneous occurrence of Mn^{3+} and Mn^{4+} ions in the system and that significantly modifies the structural and transport properties of $CaMnO_3$, making magnetic phase diagram complex. The electrical and magnetic properties of Mn perovskites are critically dependent on the Mn oxidation state. This compound generates scientific interest because of mainly for the following reasons (i) the absence of Jahn – Teller active Mn^{3+} ions in the stochiometric compound and (ii) the deficiency of oxygen in this phase which produces electron doping and thus leads to strong increase in conductivity in these oxygen deficient compounds [80] (iii) The thermoelectric properties of $CaMnO_3$ with partial substitution of transition metal cation have been studied and it is observed that its thermoelectric performance can be improved by doping at Ca-site and doping Mn site with cations having more than +4 valency [81]. Additionally, phase separation effect in the Ca-rich end of the series is much less studied than the La-rich end and half doped manganites, both theoretically and experimentally [82]. The debate over phase separation versus canted magnetic structure has not been resolved, yet. In the Ca-site as well as in Mn-site substitution studies both the phase separation and the canted behavior has been observed as shown in following studies. Phase separation behavior has been reported for Sm [54] and Pr [65] doped $CaMnO_3$ whereas for Ho [66] doped the magnetic ground state has been identified as a spin canted antiferromagnet. A more detailed magnetic study on the $Ca_{1-x}Sm_xMnO_3$ system, in the region $0<x<0.1$, points toward a cluster glass metallic state, and a lack of long-range FM order. Similar studies on Mn site substituted $CaMnO_3$ show phase separated FM+AFM ground state for Ru substituted samples [67]. However, the magnetic structure of Mo doped $CaMnO_3$ is found to be $A_XF_yG_Z$ type and a clear distinction between phase separation and spin canting behavior in this compound could not be made [68]. The nature of the ferromagnetic component is far from being clear—it has been explained as due to the canted antiferromagnetism,or by ferromagnetic domains embedded in the antiferromagnetic matrix. Phase separation (coexistence of FM and AFM) behavior has been observed experimentally in single electron doped systems such as $Ca_{1-x}La_xMnO_3$ for $0<x\leq0.09$, $Ca_{1-x}Pr_xMnO_3$ for $x\leq0.1$, and $Ca_{0.9}Tb_{0.1}MnO_3$ [83]. However, in two electron doped $Ca_{1-x}Ce_xMnO_3$ for $0<x\leq0.075$ system, the magnetic ground state is better described by canted AFM model [84].

1.3 Hexagonal Manganite

The $RMnO_3$ compounds with smaller rare-earthions (R = Ho to Lu and Y) crystallize in the non-centrosymmetric hexagonal space group $P6_3cm$ [85]. These hexagonal manganites belong to the class of multiferroic materials [86, 87]. Multiferroics are materials in which two or all three of the properties viz., ferroelectricity, magnetism and ferroelasticity co-exist simultaneously in a single phase [88]. Depending on the microscopic mechanism of the onset of ferroelectricity and magnetic ordering, multiferroics can be classified into two types. In the first group of multiferroics (Type-1), ferroelectricity and magnetism originate from different sources and the ferroelectricity is usually established at much higher temperature (often above room temperature) and the magnetic order appears at low temperatures. In the second group (Type-2 multiferroics), the transition into the magnetic and ferroelectric states happens at the same temperature. The second group of multiferroics includes all materials with a magnetically ordered structure that breaks the spatial inversion symmetry and induces simultaneously a ferroelectric state [89, 90]. The ferroelectric polarization in these materials is caused by magnetic ordering and this leads to a strong coupling between the magnetic and ferroelectric properties. Hexagonal manganites are member of type-1 multiferroic compound in which the ferroelectric transition temperature (T_{FE} ~ 600K-1000K) and Néel temperature (T_N ~ 75K-130K) are well separated from each other indicative of a weak coupling between the two ordering [91-94]. These materials are interesting to study not only because of their multiferroic nature but also because of their quasi-2D magnetic ordering, as they have a triangular magnetic structure with easy plane anisotropy in the ab plane.

In these hexagonal manganites geometry (crystal structure) plays an important role for the ferroelectric as well as for the magnetic properties.

1.3.1 Crystal structure and Crystal – field splitting

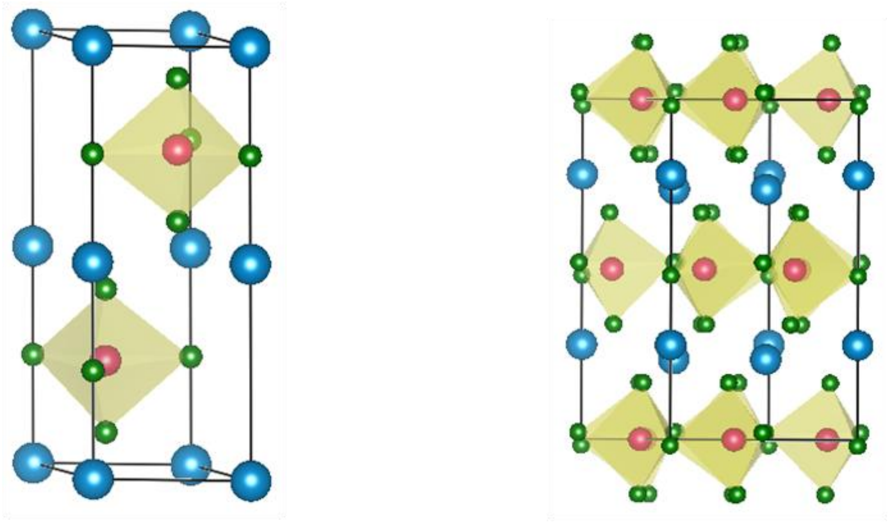

$P6_3/mmc$ (High temperature phase) $P6_3cm$(Low temperature phase)

Figure 1.6: The crystal structure of hexagonal $RMnO_3$ compounds (a) in paraelectric $P6_3/mmc$ (High temperature phase) phase, (b) in ferroelectric $P6_3cm$ (Low temperature phase) phase.

In this section we introduce the high and low-temperature structures of the hexagonal manganites. Hexagonal manganites crystallize in hexagonal structure with space group ($P6_3/mmc$) at high temperature but they undergo a structural transition to ferroelectric phase (space group $P6_3cm$) below T ~ 1000 K [95-97]. The phase transition of the hexagonal $RMnO_3$ from centrosymmetric space group $P6_3/mmc$ (high temperature phase) to non-centrosymmteric space group $P6_3cm$ (low temp phase) occurs by loss of mirror symmetry (plane) perpendicular to the c-axis, resulting in tilted MnO_5 bipyramids, with unequal apical Y–O bond lengths, and a larger unit cell, with three times the $P6_3/mmc$ unit-cell volume.The group theoretical analysis proposed [98-99] that there are three symmetry-allowed paths from a high-temperature paraelectric (PE) *P6$_3$/mmc* to a low temperature ferroelectric (FE) *P6$_3$cm* phase of $YMnO_3$. However it was not observed in the high resolution neutron diffraction measurements, in which a clear transition at 1258±14 K corresponding to a unit-cell tripling and a change in space group from *P6$_3$/mmc* to polar *P6$_3$cm* has been observed [100]. The main difference in symmetry between the two space groups is that in the high temperature phase all atoms are constrained to planes, parallel to the ab plane, whereas in the low temperature phase only the Mn ions are confined in the plane. For the *P6$_3$/mmc* phase, there are only two formula units in its unit cell. A schematic of crystal structure of $YMnO_3$ in paraelectric and ferroelectric phases is presented in figure 1.6. The *P6$_3$cm* space group contains six formula units in its primitive unit cell. The Mn atoms occupies 6c site whereas A ion occupies two inequivalent crystallographic 2a and 4b sites. Each Mn atom in these compounds is surrounded by three in-plane and two apical oxygen atoms, thus forming the MnO_5 trigonal bypiramid. These MnO_5 bipyramids form a layered structure on the ab plane and, they are well separated from one another along the c axis by the rare-earth-element layers, leading to a natural two-dimensional network of the magnetic Mn ions. A measure of such frustration is defined as a ratio of $\frac{|\theta_{CW}|}{T_N}$(where θ_{CW} is the Curie-Weiss temperature) [101]. Each Mn atom occupies the center of a triangular bipyramid whose vertices are oxygen atoms.

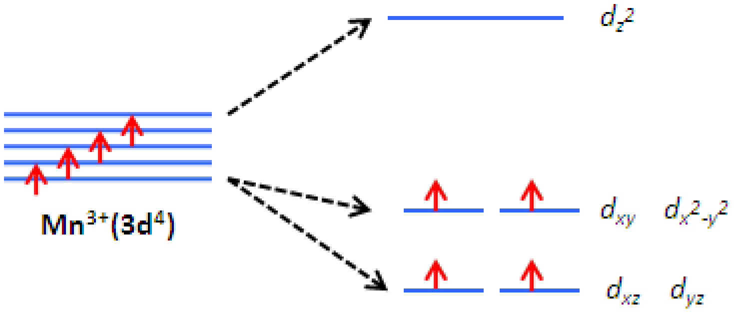

Figure 1.7: A schematic showing the relative energy levels of Mn 3d orbitals in trigonal bypiramidal geometry.

As discussed above, the environment around Mn ion in hexagonal manganites is different from the usual one in an orthorhombic phase. The rare-earth ion or Y, Sc ions are in seven-fold coordination in hexagonal phase. If the Mn ion is in any coordination other than octahedral (such as tetrahedral, hexagonalor cubic), the d orbitals experience a different splitting [85 102]. Instead of a triplet t_{2g} and a doublet e_g, here d-levels are split into two doublets (d_{xz}, d_{yz} and d_{xy}, $d_{x^2-y^2}$) and an upper singlet (d_{z^2}), as shown in figure 1.7. Therefore, the four d electrons of Mn^{+3} ions in the hexagonal manganites occupy two lowest-lying doublets and so there is no orbital degeneracy left, unlike in the MnO_6 octahedron of the orthorhombic manganites. The Mn^{+3} ion is not Jahn-Teller active in hexagonal manganite. This structural difference makes the physics of the hexagonal manganite distinctly different from that of the orthorhombic one.

1.3.2 Magnetism in Hexagonal $RMnO_3$

The magnetic structure of hexagonal $RMnO_3$ and the details of the long range order of Mn spins were first investigated using neutron diffraction experiments in the middle of the 1960's by Bertaut, Mercier [93] and Koehler et al. [103]. All hexagonal manganites show antiferromagnetic (AFM) order of the Mn^{3+} spins below their respective Néel temperatures. The magnetic properties arise from the Mn^{3+} ($3d^4$) ions with spin $S = 2$. With magnetic R- ions (Ho, Er, Tm, and Yb), the magnetic nature of these compounds are likely to be influenced due to the R-R and R-Mn interactions [104-111]. The interaction of the rare earth moments may cause another magnetic phase transition at low temperature involving mainly the rare earth moments with a possible effect on the Mn^{3+} spins. The magnetic order of Mn^{3+} network is mainly dominated by AFM in-plane Mn-O-Mn superexchange interaction, while the Mn–O–O–Mn superexchange between neighbouring planes is approximately two orders of magnitude weaker [93]. Due to antiferromagnetic interaction between the spins of the close-packed Mn^{3+}ions, located in the z =0 and z = ½ planes, the moments get aligned into a 120° structure in the ab plane.

Representation theory has been applied to find all possible magnetic structures compatible with space group $P6_3cm$. Altogether six different irreducible representations (IR) ($\Gamma_1 - \Gamma_6$) are possible with propagation vector, $\vec{k} = 0$ for Mn ion with four of them being 1D representations [112, 113]. The one- dimensional representations Γ_1, Γ_2, Γ_3, and Γ_4 correspond to the magnetic space groups $P6_3cm$, $P6_3\underline{cm}$, $P\underline{6}_3c\underline{m}$, and $P\underline{6}_3\underline{c}m$, respectively (in the international notations, each underlined symbol means that given symmetry operation is combined with the time inversion). In Γ_1 representation, the magnetic moment has a component in the xy plane and the spins are oriented perpendicular to the x-axis. The z = 0 and z = ½ layers are antiferromagnetically coupled in Γ_1. However, in Γ_3 representation, the magnetic moment has an additional component along the z axis. The coupling is ferromagnetic for both, the component in xy plane and for the component along the z axis. In Γ_2 representation, the magnetic moment has a component in xy plane and a component along the z axis. The coupling is antiferromagnetic for the component in xy plane and ferromagnetic for the component along the z axis. In Γ_4 representation the spins are in the xy plane and are oriented perpendicular to the x-axis. The z = 0 and z = ½ layers are ferromagnetically coupled in Γ_4. The one-dimensional representations Γ_1, Γ_2, Γ_3, and Γ_4 are shown in figure 1.8. It should also be noted that combinations of different IRs are possible and they describe a magnetic structure with an angle φ between 0° and 90° (φ is the angle between a axis and Mn moment).

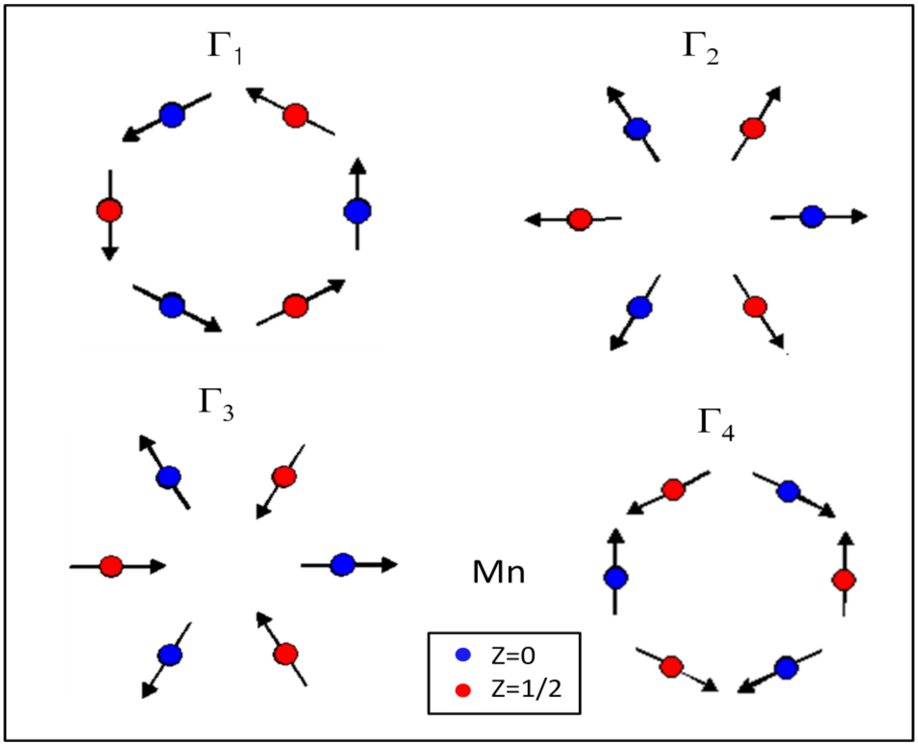

Figure 1.8: The one dimensional magnetic spin arrangement of Mn^{3+} ions in hexagonal $RMnO_3$ compounds.

In the case when R is a magnetic ion, in addition to Mn, there would be possible magnetic representation for R^{3+} ions also. For magnetic R^{3+} ions, symmetry analysis yields six different irreducible representations [112]. The one-dimensional representations Γ_1 to Γ_4 correspond to R^{3+} moments aligned parallel/antiparallel to the crystallographic c axis, and the two dimensional irreducible representations Γ_5 and Γ_6 represent magnetic states with R^{3+} moments in the ab plane. The irreducible representations Γ_1 to Γ_6 for R^{3+} moments are shown in figure 1.9.

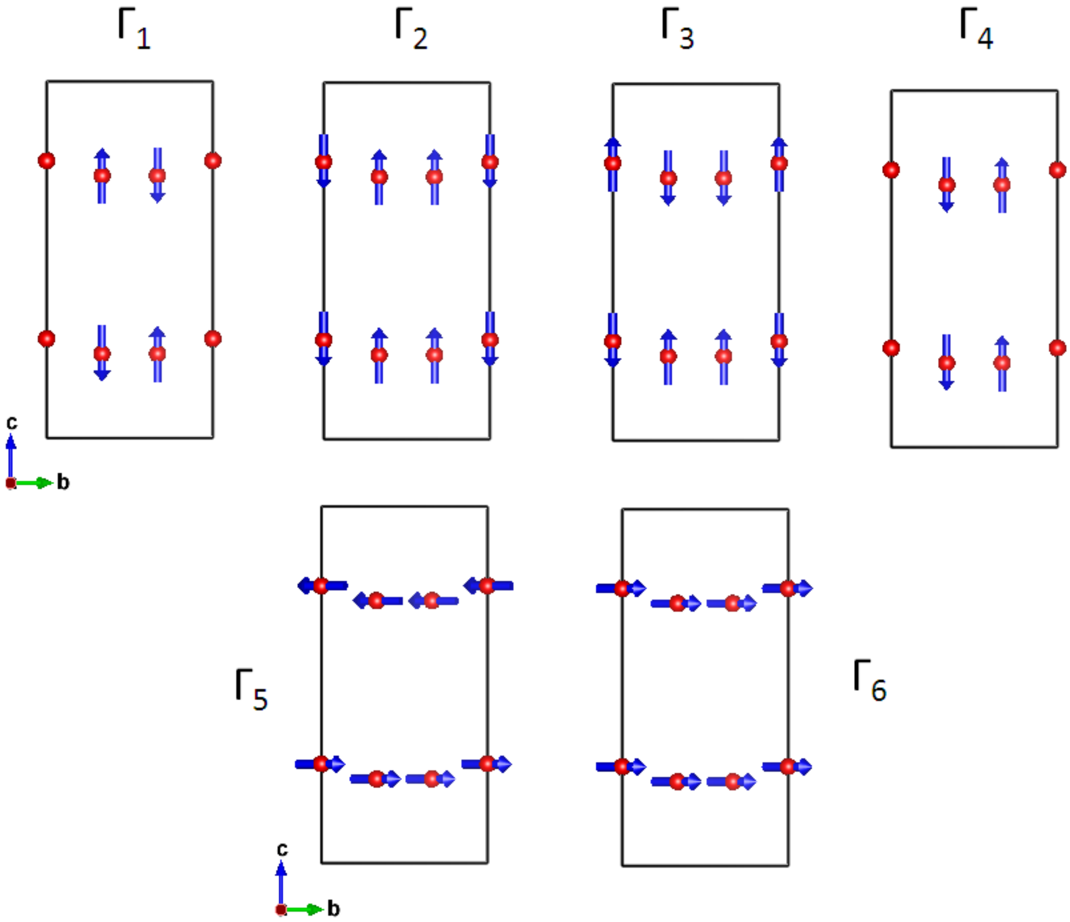

Figure 1.9: The irreducible representations Γ_1 to Γ_6 for R^{3+} moments in hexagonal $RMnO_3$ compounds.

For a perfect triangular spin arrangement in the basal plane of the hexagonal $RMnO_3$ compounds, the neutron diffraction patterns would be indistinguishable if the moments were rotated by 90° in the basal plane and the coupling between the $z = 0$ and $z = 1/2$ layers were changed in sign (from AFM to FM and vice versa). This means, that the magnetic modes Γ_1 (Γ_3) and Γ_2 (Γ_4) would be indistinguishable if the atomic positions for the Mn atoms were $x \approx 1/3$ [112]. The magnetic structures which are indistinguishable by neutron diffraction can be distinguished by non-linear optical spectroscopy due to the non centrosymmetric structure of hexagonal manganites [114, 115]. Second Harmonic Generation (SHG) is a nonlinear optical method which illuminates nonlinear crystal surfaces with an optical wave and measures the second harmonic response function [116]. The magnetic symmetries of hexagonal $RMnO_3$ have been studied extensively by Fiebig et al. [107] using the SHG spectroscopy. The different Mn orderings in hexagonal manganites depend upon the ionic radius of the R ion and the magnetic R (4f) – Mn (3d) interactions.

The origin of magnetism in hexagonal manganites for R non-magnetic (Y^{3+}, Sc^{3+}, Lu^{3+}) is from Mn^{3+} ions only. Two magnetic structures, α-type (the Γ_3 representation of space group $P6_3cm$) and β type (the Γ_1 representation of space group $P6_3cm$) have been suggested for $YMnO_3$ by Bertaut et. al [93]. According to Munoz et. al [113], the β - type structure better describes the magnetic structure of $YMnO_3$,but in first principle calculation, it has been shown that the ground state of $YMnO_3$ should be Γ_3 IR ($P\underline{6}_3c\underline{m}$) and not Γ_1. This is because in $P6_3cm$ structure there are two types of interactions, between nearest neighbor (NN) and next nearest neighbor (next-NN), but the behavior of NN interactions and next-NN interactions obey different rules. The strength of exchange coupling between nearest neighbour is directly related to bond lengths but in the case of next-NN interactions a simple analysis of bond lengths is not applicable since these interactions involve intermediate paths. For the next-NN interactions between planes, there are two equivalent strong bonds and one weak bond. So to minimize the energy of the system, there should be a FM coupling in the weak bond and this FM coupling is present only in Γ_3 and not in Γ_1. By taking into account these next- NN interactions, it has been theoretically shown that Γ_3 irreducible representation is stabilized in $YMnO_3$ [117]. According to recent neutron scattering experiments the magnetic ground state of $YMnO_3$ is best described by linear combination of Γ_3 and Γ_4 IR of space group $P6_3cm$ [118, 119]. In the mixed model of Γ_3 and Γ_4 IR, the moments are in the a-b plane and tilted away from the principal crystallographic axis by a tilting angle(Φ).

In $YMnO_3$, tilting angle (Φ) between the moments and the principal crystallographic axis in the ab plane is reported 10.3° by Park et al.[118], 11.1° by Brown and Chatterji [119].

Both Lu^{3+} ($LuMnO_3$) and Sc^{3+} ($ScMnO_3$) do not carry any magnetic moment, similar to Y^{3+}, but the magnetic ground state in both of these manganites is different from $YMnO_3$. The ionic radii of Lu^{3+} and Sc^{3+} are significantly smaller than Y^{3+} resulting in a compression of the in-plane lattice constant and stronger magnetic exchange interactions within the ab-plane as well as along the c-axis. As a consequence, the Néel temperatures increase from $YMnO_3$ (~75 K) to $LuMnO_3$ (~90 K) and to $ScMnO_3$ (~130 K) [120-122]. According to the neutron diffraction experiments the nature of magnetic ordering in $LuMnO_3$ is different from $YMnO_3$. Based on these studies, two spin configurations have been suggested for $LuMnO_3$: Γ_2 ($P6_3\underline{cm}$) or Γ_4 ($P\underline{6}_3\underline{c}m$) [96, 103,123, 124]. Spin reorientation in $LuMnO_3$ has not been observed in neutron scattering experiments in contrast to SHG optical experiments, where it was observed that $LuMnO_3$ apparently exhibits a spin reorientation from Γ_4 ($P\underline{6}_3\underline{c}m$) to Γ_3 ($P\underline{6}_3\underline{c}m$) magnetic symmetry with an intermediate phase ($P\underline{6}_3$) coexisting with the two other phases below 60 K [107]. However, spin reorientation behavior has been seen in $ScMnO_3$ in neutron diffraction experiments. In early neutron diffraction experiments, it has been observed that the magnetic symmetry changes from $P\underline{6}_3$ (Γ_4+ Γ_3) with a angle of 80° (close to Γ_4) to low temperature phase with an angle of 15° (close to Γ_3) [125-126]. Similar kind of magnetic symmetry has been observed by SHG optical experiments, in which the magnetic symmetry changes from Γ_4 to a linear mixture of Γ_4 and Γ_3 [107, 109, 127]. Munoz et al., however described the magnetic structure by Γ_2 IR with a spin angle of 0° in the temperature range 75K<T<130K which changes to a mixed representation of Γ_1 and Γ_2 [113].

In hexagonal $RMnO_3$ with magnetic R-ion (Ho^{3+}, Er^{3+}, Yb^{3+}, Tm^{3+}), a complex magnetic diagram emerges from the R (4f) – Mn (3d) and R (4f) –R (4f) interactions. Because of the very similar size of the Y^{3+} (1.019Å) and Ho^{3+} (1.015 Å) ions, structures of $YMnO_3$ and $HoMnO_3$ are quite similar. However, in $HoMnO_3$, three distinct anomalies have been observed around T_N~75K, T_{SR}~33K, and T_{Ho}~5K [128-133]. All transitions are also accompanied by distinct anomalies of the heat capacity and dielectric constant [128-133]. These sharp and distinct anomalies correspond to spin reorientation behaviour as a function of temperature. In $RMnO_3$ (R- magnetic) compounds, it has been observed that the 4b and 2a sites order independently. Moreover, the magnetic moments on these two sites (4b and 2a) can be considered to be independent and do not have to be of the same size. The ordered Ho moments on 4b sites are observed below 33K with different magnetic symmetry, whereas Ho (2a) sites remain paramagnetic down to 5K [134-136]. Different magnetic symmetries above and below T_{SR} (~ 33K) have been proposed by different authors. Munoz et al. [134] proposed a transition from Γ_2 to Γ_1 IR upon decreasing temperature. However, according to later neutron scattering [108, 110, 137] and SHG optical experiments an abrupt spin reorientation (Mn spins undergo an in-plane 90° rotation) takes place at about 33K where themagnetic symmetry changes from Γ_4 to Γ_3 followed by another spin orientation below 5K, where the Mn spins rotate into the Γ_1 ($P6_3cm$) magnetic symmetry. In $ErMnO_3$ (T_N~75K), magnetic symmetry Γ_2 or Γ_4 has been proposed by neutron diffraction measurements [138-141]. However, Γ_4 magnetic symmetry has been identified by SHG optical measurements at all temperatures below T_N (~ 80K) [106]. Recently, the magnetic phase diagram of $ErMnO_3$ has been revised by D. Meier et al. [111] using optical SHG technique and neutron diffraction experiments. In the temperature range $10K<T<T_N$, the magnetic order of Mn^{3+} ions belongs to Γ_4 IR, which triggers the magnetic order of the Er^{3+}(4b)

according to the same representation (Γ_4). Below 10K, the magnetic symmetry is dominated by 4f exchange interactions of Er^{3+} on 2a site, resulting in changing the magnetic symmetry from Γ_4 to Γ_2 IR. The magnetic exchange interactions between rare earth ions and Mn spins, results in a complex phase diagram for both $ErMnO_3$ and $HoMnO_3$ at low temperature. Neutron diffraction and SHG optical experiments measurements indicate to the Γ_4 magnetic symmetry in $YbMnO_3$. The nature of magnetic ordering of Mn moments and Yb^{3+} moments on 4(b) and 2(b) site was first proposed by Fabrèges et al, by combining neutron diffraction and Mössbauer spectroscopy [104]. According to molecular field analysis, the ordering of Yb(4b) moments occurs below T_N~85K (well above the T_N^{Yb}) and is driven by the exchange interactions of Mn-Yb spins and ordering of Yb(2a) occurs below 5K through Yb-Yb exchange interactions.

The effect of magnetic field on the magnetic structures of hexagonal manganites results in different structures. It is found that the phase diagrams for compounds with non magnetic ions in the A-site are not modified by magnetic fields thus indicating an active role for the rare earth cation magnetism in these hexagonal manganites [122].

The magnetic symmetries observed in these hexagonal managnites can be divided in two groups. In the first group (Γ_1, Γ_2 and, Γ_6) the magnetic moments in z= 0 and ½ can be transformed by simple rotations only whereas in second group (Γ_3, Γ_4, and Γ_5) rotations should be combined with the time inversion symmetry. Recent theoretical studies revealed that each group has nearly equal values of polarization (P). But, transition from one group to another would change the polarization of the system [117]. Thus, in principle, the value of the ferroelectric polarization can be controlled by changing the magnetic ground state.

1.3.3 Ferroelectricity in Hexagonal $RMnO_3$

The hexagonal manganites undergo ferroelectric transition far above the magnetic ordering temperature of Mn^{3+} ions. These are paraelectric with centrosymmetric space group ($P6_3/mmc$) at high temperature but they undergo a structural transition to ferroelectric phase (space group $P6_3cm$) below T ~ 1000 K. Ferroelectricity (FE) in hexagonal manganites $AMnO_3$, with A = Y, Dy, Ho, Er, Tm, Yb, Lu, or Sc, was discovered as early as 1963 by Bertaut et al [142] but the origin of the ferroelectricity has recently been revised [143]. The lack of d^0 or lone pair, in these compounds, makes the origin of ferrolectricity a topic of discussion [144]. It has been shown that the ferroelectricity is not due to the off centre displacement of Mn^{3+} ions as originally claimed by Yakel et al. [85], but rather is due to the cooperative buckling of MnO_5 bypiramids which leads to relative displacement of A^{3+} and O^{2-} ions along the c-axis. The displacement of A^{3+} and O^{2-} leads to the formation of local antiparallel electric dipoles with different magnitudes, resulting in net polarization. A detailed analysis of the origin of ferrolectricity in these hexagonal manganites has been done by Van Aken et al. by first principle calculations [143] and has concluded that the ferroelectricity in $YMnO_3$ is due to electrostatic and size effects. The A-site ions are not directly responsible for FE in these compounds but the geometric effect. Hence, the hexagonal manganites are also known as the geometric ferroelectrics.

1.3.4 Multiferroic coupling in hexagonal $RMnO_3$

Multiferroic behaviour corresponds to the presence of more than one ferroic order in single phase crystal. These ferroic order parameters canbe ferromagnetism (antiferromagnetism), ferroelectricity, ferroelasticity, and ferrotoroidicity. In case of hexagonal manganites, both magnetoelastic and magnetoelctric coupling has been observed. Magnetoelctric and magnetoelastic effects for hexagonal manganites have been elaborated below.

1.3.4.1 Magnetoelectric Effects in hexagonal RMnO$_3$

The magnetoelectric (ME) effect in its most general definition denominates the coupling between electric and magnetic fields in matter. This coupling results in change in magnetization (electric polarization) by electric (magnetic) fields. The ME effects in single phase crystals, in external fields are described in the Landau theory by writing the expansion of the free energy. Only terms which are invariant with respect to all symmetry operations are included [145-148].

$$F(E,H) = F_0 - P_i^s E_i - M_i^s H_i - \frac{1}{2}\varepsilon_0\varepsilon_{ij}E_iE_j - \frac{1}{2}\mu_0\mu_{ij}H_iH_j - \alpha_{ij}E_iH_j - \frac{1}{2}\beta_{ijk}E_iH_jH_k - \frac{1}{2}\gamma_{ijk}H_iE_jE_k + ..$$

where, F$_0$ is the free energy in the absence of any external field, P_i^s, M_i^s are the spontaneous polarization and magnetization, respectively. ε, μ are the dielectric permittivity and magnetic permeability, α is the linear magnetoelectric susceptibility tensor, β and γ are the high order terms describing the non-linear ME effects.The polarization is given by taking the derivative of free energy with respect to electric field,

$$P_i(E,H) = \frac{-\partial F}{\partial E_i} = P_i^s + \varepsilon_0\varepsilon_{ij}E_j + \alpha_{ij}H_j + \frac{1}{2}\beta_{ijk}H_jH_k + \gamma_{ijk}H_iE_j$$

The magnetization is obtained by taking the derivative of free energy with respect to magnetic field,

$$M_i(E,H) = \frac{-\partial F}{\partial H_i} = M_i^s + \mu_0\mu_{ij}H_j + \alpha_{ij}E_i + \beta_{ijk}E_iH_j + \frac{1}{2}\gamma_{ijk}E_jE_k$$

The linear ME effect can be expressed as,

$$P_i = \alpha_{ij} H_j$$

$$M_i = \alpha_{ji} E_i$$

where, α_{ij} is designated as the linear magnetoelectric effect and corresponds to the induction of polarization by a magnetic field or a magnetization by an electric field. In hexagonal manganites, the linear ME effect is forbidden because of the symmetry. However, the higher order couplings mediated through the strong spin-lattice interaction may result in anomalies in dielectric constant at the magnetic phase transitions [149-152]. Magnetoelectric coupling can be measured indirectly by simply recording changes in either the magnetization near a ferroelectric transition temperature or the dielectric constant near a magnetic transition temperature. The first signature of magnetoelectric coupling in hexagonal managites was observed in case of $YMnO_3$ [149]. However, single-crystal measurements revealed that this anomaly in the dielectric constant of $YMnO_3$ exists only in the a-b plane, and not along the direction of the ferroelectric polarization, which is along the c axis [153-155]. Later on, anomalies in the in-plane dielectric constant have been reported for (Y, Ho, Yb, Lu) MnO_3 at the onset of T_N indicating coupling between the electric polarization and magnetic ordering [120]. A large and sharp decrease of the dielectric constant below T_N has been observed and is attributed to charge-transfer excitation in the geometrical frustrated system [153]. The explanation for the origin of this magnetoelectric effect has been suggested to be the interaction between ferroelectric (FE) and antiferromagnetic (AFM) domain walls. Non linear optical measurements have shown that, these ferroelectric (FE) and antiferromagnetic (AFM) domain walls are not independent of each other but, instead, a clamping mechanism was shown to exist between these domain walls [156-158]. Proposal for the clamping feature includes strain at the ferroelectric domain wall and modification of spin interactions at ferroelectric walls [159-160]. This behavior indicates the strong interaction of ferroelectric and magnetic orders and novel physical phenomena happening in between the different domains.

1.3.4.2 Magnetoelastic Effects in $RMnO_3$

When the hexagonal manganites undergo antiferromagnetic transition, there are also distinct anomalies in the structural parameters. For example, both the lattice parameters as well as the unit cell volume exhibit an anomalous contraction below T_N. They exhibit an anomalous behavior in the magnetically ordered state which might be attributed to the magnetoelastic coupling in these hexagonal compounds. The magnetoelastic coupling, in hexagonal manganites has been shown to arise due to the large atomic displacement of almost every atom within the unit cell, first reported by Lee et al [150], from their high resolution neutron and synchrotron powder diffraction experiments. However, as pointed out by Chatterji et al [161], no explanation was given as to how correlations between structural and magnetic parameters were avoided. Later on, the magnetoleastic effect in $YMnO_3$ has been reported by Chatterji et al [161] using high Q data. In hexagonal manganites, this magnetoelastic effect is two orders of magnitude larger than those appearing in other magnetic materials. Therefore, the gigantic magnetoelastic coupling plays a significant role in dominating many physical properties in hexagonal manganites. In addition, there are many studies showing the anomaly around transition temperature, such as the dielectric constant, heat capacity measurements, and the lattice constant measurements, which are attributed to the indirect coupling via lattice strain [120, 162].

1.3.5 Hexagonal $YMnO_3$

Now, we focus on the properties of hexagonal Yttrium manganite ($YMnO_3$) which has interesting magnetic and structural properties. $YMnO_3$, a hexagonal manganite, shows an antiferromagnetic transition at T_N~75K and a ferroelectric transition at T_C~950K. In spite of the large difference between the antiferromagnetic transition temperature and ferroelectric transition temperature this compound exhibit anomaly in the in-plane dielectric constant indicative of a coupling between the two orderings. Non linear optical measurements on $YMnO_3$ also find clear evidence for coupling between the ferroelectric and antiferromagnetic domain walls [156-158]. The microscopic origin of the spin-charge coupling in $YMnO_3$ has also been investigated in detail using Raman studies [163-164] and magnetoelastic measurements [161]. From Raman studies spin phonon coupling has been observed in this compound below T_N [163-164].

All the hexagonal manganites (Ho, Er, Yb, Lu, Sc, In, Tm) have almost similar transition temperature, and basically shares all the physical properties of $YMnO_3$, except for the magnetic structure. $YMnO_3$ is favored for the study of magnetic ordering of Mn ions, as there is no perturbation from the rare earth *f* electrons. Therefore, $YMnO_3$ has been studied extensively, compared to other hexagonal manganites. The magnetic structure of $YMnO_3$ has been discussed above in detail. Inelastic measurement on the $YMnO_3$ shows evidence for both spin liquid and spin ordered phases with a small easy-plane anisotropy which makes the magnetic symmetry even more complicated [165]. The results seem to be consistent with a quasi two-dimensional frustrated magnetic system with weak interplane coupling. The evidence of geometric frustration has been also seen in thermal conductivity and heat capacity measurements [120, 130, 153]. The frustrated behavior in $YMnO_3$ has been also found to be influenced by doping at Y-site and Mn site [166-168]. Both doping and external pressure evidently modify the magnetic properties of $YMnO_3$, indicating a strong correlation between the magnetic ordering and the crystal structure in such a spin frustrated system. In addition to the change in long range magnetic symmetry, the formation of spin-liquid phase in $YMnO_3$ occurs through the symmetrization of triangular network of Mn ions at high pressures. However, the temperature dependence of the spin-liquid phase fraction at high pressures is different from that of at ambient pressure. The fraction of spin-liquid phase increases with decrease in temperature at high pressure [169-171].

The bond lengths and bond angles play a crucial role in stabilization of the magnetic structure in hexagonal manganites. The role of possible changes in magnetic structure leading to large magnetocapacitance has been raised [172-173]. It is also possible to change the ferroelectric properties of the system by changing the magnetic ground state.

1.4 Issues

The coexistence of ferroelectric and magnetic orders in $YMnO_3$ below the transition temperature raises the question of how the two order parameters mutually interact with one another and how different physical properties might be affected by their coupling. To see the effect of their coupling and its effect on the physical properties we have investigated the effect of the A-site and B-site doping on the structural, magnetic and electronic properties of hexagonal $YMnO_3$. Though fully doped compounds have been investigated in a number of studies, the effect of partially doping $YMnO_3$ with isovalent magnetic ions is much less studied, particularly using neutron diffraction technique in exploring the crystal and magnetic structure. The origin of magnetism in hexagonal $YMnO_3$ is from Mn^{3+} ions only. The different Mn orderings in hexagonal manganites depend upon the ionic radius of the R ion and the magnetic R (4f) – Mn (3d) interactions. Partial substitution of magnetic ions at Y-site is expected to introduce out of plane R-Mn interactions, significantly influencing the magnetic structure and frustrated behaviour. Further, we can alter the magnetic exchange interactions by varying structural parameters. We implement this structural variation by doping with ions (Yb^{3+}, Er^{3+}, Ho^{3+}, Tb^{3+}) of different ionic radius. Since the magnetic properties of $YMnO_3$ are most strongly influenced by Mn-Mn interactions, we have studied the effects of Ti^{4+} (d^0), Fe^{3+} (d^5) and Ga^{3+} (d^{10}) doping on the structural and magnetic structure of $YMnO_3$ by directly influencing the B-site interactions. The dopants have been chosen to study the effect of interaction of the filled (d^{10}), partially filled (d^5) and unfilled orbital (d^0) on the magnetic structure. We find that these three dopants affect the magnetic structure of this compound in contrasting manner. Our neutron scattering studies on both Y-site doping and Mn-site doping on $YMnO_3$ have shown different magnetic ground states. Neutron scattering showed that the phase transition from one magnetic phase to other is much more complicated than we had assumed previously. Our neutron scattering studies provided new insights into this family of $RMnO_3$.

Compound $CaMnO_3$ is of interest due to disputable phase separation/canted antiferromagnetism behavior shown in some of the Mn (IV) –rich doped compounds. The role of spin canting and/or phase separation leading to FM behavior in these compounds has been a subject of discussion in literature. Phase separation effect in the Ca-rich end of the series is much less studied than in the case of La-rich end and half doped manganites, both theoretically and experimentally. Hole doped manganites $La_{1-x}Ca_xMnO_3$ exhibit a complex magnetic phase diagram. By doping $CaMnO_3$ with Y^{3+} ion which is non magnetic and similar to La^{3+}, albeit with lower ionic radii, it was expected, that an equally complex magnetic phase diagram would emerge. We have found phase separated magnetic ground state for $Ca_{1-x}Y_xMnO_3$. We find that as against Ca-site doping, the Mn site substitution ($CaMn_{1-x}Fe_xO_{3-\delta}$) favors canted G-type structure. As a result of the identical electronic configuration of Mn^{3+} and Fe^{4+}, it's doping in effect results in electron doping. The debate over phase separation versus canted magnetic structure continues to be of interest. The $Ca_{1-x}Y_xMnO_3$ and $CaMn_{1-x}Fe_xO_3$ are not conclusive of the whole magnetic phase diagram of the electron doped system.

1.5 Plan of the thesis

The main objective of the present thesis is to investigate the effect of the A-site and B-site doping on the structural, magnetic and electronic properties of hexagonal $YMnO_3$ and orthorhombic $CaMnO_3$ manganites. The present thesis comprises of five chapters. After giving an overall introduction in Chapter 1, Chapter 2 gives a brief description about the sample preparation technique and working principles of the various experimental techniques (x-ray diffraction, neutron diffraction,dc magnetization, and Mössbauer spectroscopy) employed to investigate the structural and magnetic properties of the compounds. A brief description about the Rietveld method, employed to refine the crystal structures and to determine the magnetic structures from the powder diffraction data, is also given in Chapter 2. The Chapters 3 and 4 constitute results on the doped hexagonal $YMnO_3$ and doped orthorhombic $CaMnO_3$, respectively. The results of the thesis are summarized in chapter 5.

Chapter 2

Experimental Techniques

This chapter discusses the method of synthesis and various experimental techniques used for the characterization of the compounds studied in the present work. All the samples studied in the framework of this thesis were prepared in polycrystalline form by conventional solid-state reaction method. The phase purity of the studied samples was checked by X-ray diffraction technique. Subsequently, neutron diffraction technique was used to extract the crystal and magnetic structures. For analyzing the X-ray and neutron diffraction data, the Rietveld refinement method was used. Neutron depolarization measurements were carried out to study magnetic inhomogenities in some of the selected samples. In addition, resisitivity, dc magnetization, X-ray absoption spectroscopy, Mössbauer spectroscopy, and dielectric measurement were carried out. A brief description of these techniques is given below.

2.1 Sample preparation

The synthesis of homogenous and stoichiometric material is imperative to obtain the desired physical properties. The polycrystalline samples studied in this thesis have been prepared by solid state reaction method [174]. In the solid state reaction, for the reaction to take place homogeneously, it is very important to mix and grind the powders thoroughly for long duration to obtain homogeneous distribution of the desired stoichiometric compound. This method involves the diffusion of ions across the solid interfaces, which is a slow process. Therefore, the typical reaction time in a solid state reaction ranges from few days to few weeks at high temperatures. We have used high purity compounds as precursors for the synthesis of all the samples studied here. In the present thesis, we have studied two sets of samples viz. hexagonal and orthorhombic crystals. The procedure followed were the same for both set of samples, only the heating temperatures and the reaction/sample prep time were different. The hexagonal compounds of $YMn_{1-x}M_xO_3$ (M = Ti, Fe, Ga; x = 0, 0.1), $YMn_{1-x}Fe_xO_3$ ($x \leq 0.5$), and $Y_{1-x}R_xMnO_3$ (R= Yb, Er, Tb, Ho; $x \leq 0.2$) were made using the following steps:

i. The starting materials Y_2O_3, Yb_2O_3, Er_2O_3, Tb_4O_7, Ho_2O_3 and MnO_2 for $Y_{1-x}R_xMnO_3$ (R= Yb, Er, Tb, Ho; $x \leq 0.2$) were heated to ~ 500°C for 10hrs to remove the low temperature volatile impurities. Powders were then weighed in proper stoichiometric ratio, and grounded using agate mortar and pestle.

ii. This powdered mixture was then calcined at 1100°C for approximately 36 hrs, and then slowly cooled down to room temperature. Calcination is the process which usually takes place at or above the thermal decomposition temperature. It is mainly employed to convert precursors into their respective oxide forms.

iii. These compounds were grounded several times in order to get homogeneous mixture. Many intermediate grindings and heatings are required to get appropriate phase formation and phase purity. After the calcinations, the compounds were reground, and then again calcined at 1200°C for 48 hours.

iv. Final sintering of Yb, Er, Ho doped samples was done at 1250°C for 90 hours with several intermediate grindings. For Tb doped samples, final sintering was done at 1350°C for 60 hours.

v. After the calcinations, the compounds were reground, and then pressed into pellets. Samples were pelletized into pellets of diameter 16 mm using hydraulic pressure of ~ 3 ton/cm^2. These pellets were then again sintered for a longer time (~60 hours) in the temperature range of 1100°C - 1350°C, and then slowly cooled down to room temperature.

The orthorhombic samples were using the following procedure:

i. The high purity starting materials ($CaCO_3$, MnO_2 and Fe_2O_3, for the compounds $CaMn_{1-x}Fe_xO_{3-\delta}$) were heated to ~ 500°C for 10 hrs to remove the low temperature volatile impurities. Powders were then weighed in proper stoichiometric ratio, and intimately mixed using an agate mortar and pestle.

ii. This powdered mixture was heated in air at 1100^{o}C for 20h, 1150^{o}C for 20h, 1250^{o}C for 20hand 1300^{o}C for 46h, successively with intermediate grindings. These compounds were grounded several times in order to get homogeneous mixture.

iii. Finally, the samples were pressed into pellets of diameter 16 mm using hydraulic pressure of ~ 3 ton/cm^{2}and heat treated at 1300^{o}C for 24 h.

The heating and cooling programs are determined by the form and reactivity of reactants. The obtained final compositions are initially characterized by powder x-ray diffraction measurements.

2.2 Scattering theory

Many experimental techniques in condensed matter are based on interaction between the probe particles (they may be x-ray photons, neutrons or electrons etc.) and the sample. In an ideal scattering experiment, an incident beam of radiation with definite energy E_i (wave vector k_i) is scattered by a target into a radiation of energy E_f (wave vector k_f) as shown in figure 2.1. For simplicity, we will only consider elastic scattering, in which there is no interchange of energy (or momentum) between the scattered radiation and the target (i.e. E_i=E_f). The scattering vector from figure 2.1 is given as, $\Delta k = \vec{k}_f - \vec{k}_i = \vec{Q}$, which measures the change in two wave vectors, whose magnitude is $4\pi\sin\theta/\lambda$. Scattering experiments comprise the measurement of the intensity distribution as a function of the scattering vector. The quantity directly measured in an elastic scattering experiment is the partial differential cross section $\frac{d\sigma}{d\Omega}$, which describes the number of incident particles scattered into a volume element of solid angle $d\Omega$. The magnitude of the $\frac{d\sigma}{d\Omega}$ is related to the structure factor, F(Q), which further gives us the arrangement of the atoms in the sample. The crystal structure can be studied by diffracting neutrons, x-rays and electrons whose wavelength is comparable to the interplanar spacing. In case of neutrons, the interaction is described in terms of a scattering length, (b) and for x-rays a form factor, f_i, directly related to the electron density of the material. Bragg's law provides a simplistic model to understand the conditions which are required for the diffraction to occur [175-177].

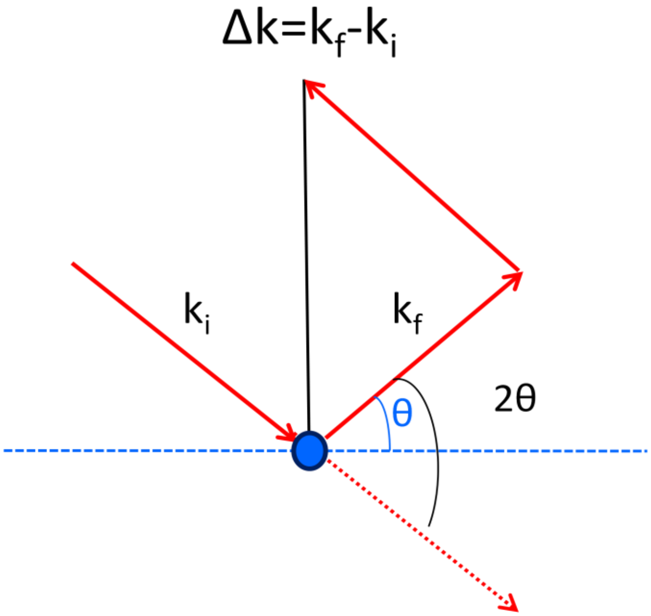

Figure 2.1: Schematic diagram of the scattering geometry.

2.3 Bragg's formulation for diffraction

The structure of crystalline materials can be considered as a regular arrangement of atoms in a unit cell, which being a repeating unit constitutes the crystal. The wavelength of the probe particles being approximately equal to this interplanar spacing is the necessary condition for diffraction to occur.

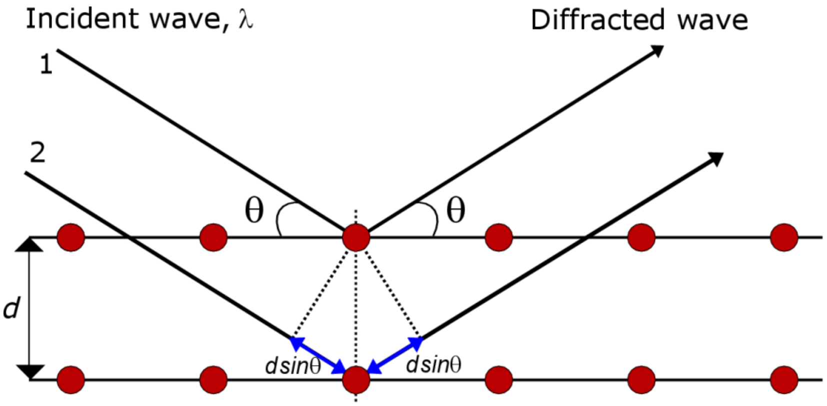

Figure 2.2: A schematic diagram depicting the Bragg's law

Consider an arbitrary family of parallel lattice planes spaced d apart and irradiated at an angle θ with a monochromatic beam of radiation, as shown in figure 2.1. The path difference for rays reflected by two adjacent planes is $2d\sin\theta$, where θ is the grazing angle. The constructive interference of the radiation from successive planes occurs when the path difference is an integral number n of wavelength λ, such that, $n\lambda = 2d\sin\theta$. This is the Bragg's law and the corresponding Bragg reflections would occur only for $\lambda \leq 2d$. When Bragg's law is satisfied, the reflected beams will be in phase, leading to constructive interference, otherwise destructive interference occurs. There is a reciprocal relationship between the Bragg angle θ and the spacing between the reflecting planes(d). This means that larger spacing of repeating units in a crystal results in smaller diffraction angles.

Later von Laue proposed an alternate formulation for x-ray diffraction in which he considered the scattering from individual atoms rather than planes. The phase of the incident radiation does not change after scattering from atoms and hence they can interfere coherently with each other. Consider two identical atoms, separated by $\vec{R}$, which are diffracting x-rays with initial wave vector $\vec{k}_i$ which scatter to wave vector $\vec{k}_f$. For the constructive interference, the path difference ($\left(\hat{k}_i - \hat{k}_f\right).\vec{R}$) between the scattered wave vectors from these two atoms should be an integral multiple of incident wavelength. After substituting in the magnitude of the wave vectors ($\vec{k} = \frac{2\pi}{\lambda}\hat{k}$), this condition can be written as $\left(\vec{k}_i - \vec{k}_f\right).\vec{R} = 2\pi m$, or, equivalently, $e^{i(\vec{k}_f - \vec{k}_i).\vec{R}} = 1$. For the orderly arrangement of atoms in a crystal, the following condition is satisfied, $e^{i\vec{G}.\vec{R}} = 1$ where $\vec{G}$ is the reciprocal lattice vector and $\vec{R}$ is the displacement vector between two atoms in the real space. Thus, the diffraction condition can thus be derived as follows:

$$\begin{aligned}
&\left(\vec{k}_f - \vec{k}_i\right) = \left(\vec{G}_i\right) \\
&\left(\vec{k}_i + \vec{G}_i\right)^2 = \left(\vec{k}_f\right)^2 \\
&\left|\vec{k}_i\right|^2 + 2\vec{k}_i.\vec{G} + \left|\vec{G}\right|^2 = \left|\vec{k}_f\right|^2
\end{aligned}$$

For an elastic scattering, we have: $\left|\vec{k}_i\right|^2 = \left|\vec{k}_f\right|^2$. Therefore, the above equation can be rewritten as $2\vec{k}_i.\vec{G} = \left|\vec{G}\right|^2$, which further reduces to Bragg's law $n\lambda = 2d\sin\theta$. In a diffraction experiment,the Bragg condition provides a direct determination of the crystal symmetry and of the lattice constants.

Three different methods have been devised for making diffraction measurements. These are (i) Laue method, (ii) Rotating-Crystal method, and (iii) powder method. In practise, powder diffraction method is the most useful technique for the identification of unknown materials or mixtures of phases in a single material. Since, for some materials, the growth of single crystals can be difficult, thus diffraction from a powder sample is an attractive alternative. Now we will discuss powder diffraction method.

2.4 Powder diffraction method

Diffraction of X-rays or neutrons by polycrystalline samples is one of the most important, powerful and widely used analytical techniques for crystal structure analysis. The most common use of powder diffraction is chemical analysis. Powder diffraction measurements are generally simple to carry out and quick. In powder diffraction method, a finely powdered sample is placed in a monochromatic x-ray/neutron beam. An ideal polycrystalline powder sample consists of a very large number (e.g.~ 10^9mm^{-3}) of very small crystals (ideally ~1μm) that are randomly oriented with respect to each other. The number, position and intensity of reflections in a diffraction pattern depend primarily on the symmetry and size of the unit cell and the arrangement of atoms within it, but are also influenced by the nature and wavelength of the radiation used. The hkl reflection from polycrystalline sample has the form of a cone of diffracted radiation, wherein a separate cone is formed for each set of differently spaced lattice planes. The basic equation for the integrated intensity I of the reflection hkl for a random powder sample illuminated by a primary beam of intensity I_P is

$$I = I_P K \lambda^3 V^{-2} m_{hkl} PL \left| F(Q) \right|^2 v$$

where K depends on whether X-rays or neutrons are used to collect the data, V is the volume of the unit cell, m_{hkl} is the multiplicity of the hkl reflection, P is the polarization factor, L the so-called Lorentz factor that is defined by the geometry of the diffraction, $F(Q)$ is the structure factor, taking into account thermal effects, and v is the effective diffracting volume of the sample, including the effects of absorption [178].

Diffraction from polycrystalline materials with monochromatic radiation requires the Debye–Scherrer diffractometer to provide only one degree of freedom in changing the diffraction conditions, corresponding to changing the 2θ angle. On the other hand, two additional degrees of freedom for specimen orientation are required for single crystal diffraction experiments with monochromatic radiation.

2.5 X-ray scattering

X-rays are electromagnetic waves with a much shorter wavelength than the visible light. X-rays used in diffraction have wavelength approximately in the range of 0.5-2.5Å. X-rays to be used for diffraction experiments are generated by a cathode ray tube by heating a filament to produce electrons. These electrons are then accelerated with the help of an applied voltage towards the target material. X-rays are then emitted because of the rapid deceleration of the electrons striking the target. There are two types of x-ray spectrum depending upon how accelerated electron interacts with target material, and those are characteristic spectra and continuous spectra. Only the K lines of characteristic spectra are useful in X-ray diffraction because many diffraction experiments require the use of monochromatic radiation. X-ray photons interact with the electrons of the atoms, primarily through its electric field. Both coherent and incoherent scattering of X-rays from these electrons are possible. The coherent part gives rise to Bragg scattering and the incoherent part contributes to the background in a powder diffraction experiment. The scattering of x-rays from a crystal lattice produces a diffraction pattern which contains information about the atomic arrangements within the crystal. The intensity of a diffracted beam is given by, $I \alpha |F(Q)|^2$, where $|F(Q)|$ is defined as,

$$F(Q) = \sum_i f_i e^{-2\pi i(hx_i + ky_i + lz_i)} e^{-B(\frac{\sin\theta}{\lambda})^2} \tag{2.1}$$

Here f_i is atomic scattering factor (also called *form factor*) and is proportional to the Fourier transform of the electronic charge distribution of the corresponding atom, $f_i = \int \rho(r) e^{iQ.r} d^3r$. The atomic scattering factor depends on the type of scattering, which in turn depends on the nature of the incident radiation. The summation is over all the atoms in the unit cell, f_i is the atomic scattering factor for X-rays, which is replaced by scattering length, b for neutrons, hkl are the Miller indices of the particular plane and x_i, y_i, z_i are the fractional coordinates of the atoms in the unit cell. The second exponential term is the well known Debye–Waller factor which arises due to the thermal motion of the atoms and provides the thermal average of the structure factor, where $B = 8\pi^2 U$. In this expression U is the isotropic temperature factor, which is equal to the square of mean displacement of the atom from its equilibrium position. Therefore, the intensity of a diffracted beam decreases as the temperature is raised, and at a given temperature, thermal vibration causes a larger damping of the diffraction peaks at higher angles. If the wave scattered by an atom is in the forward direction (2θ = 0), then waves scattered by all the electrons of the atom are in phase and the amplitudes of all the scattered waves can be added directly. Hence, the atomic form factor f_i is directly proportional to the atomic number Z or number of electrons in the atom. It is for this reason that it is difficult to locate light elements such as carbon, oxygen and hydrogen in presence of heavy atoms. As the scattering angle

2θ increases, the atomic form factor f_i decreases. The decrease of f_i is due to the comparable dimensions of the electronic cloud and X-ray wavelengths. Therefore, the net effect is that the atomic form factor (ratio of the amplitude scattered by an atom to that scattered by a single electron) fall off with $(\sin\theta)/\lambda$. As a consequence, the Bragg peaks at higher angles will generally exhibit a lower intensity compared to those at lower angle [177,179].

2.5.1 X-ray diffractometer

In a diffractometer, a monochromatic X-ray beam is allowed to fall on the powdered specimen and then the diffracted beam falls on a detector which is placed on the circumference of a circle centered on the powdered specimen. The intensity of the diffracted beam is measured directly either by ionization it produces in a gas or the fluorescence it produces in a solid. The diffraction pattern of the sample is recorded continuously with the diffractometer in $\theta – \theta$ mode or θ - 2θ mode. For the θ - 2θ mode, the X-ray tube is stationary, the sample moves by the angle θ and the detector simultaneously moves by angle 2θ. The counter is then driven at a constant angular velocity through increasing values of 2θ. The apparatus used in our experiments is X-ray diffractometer system, Geiger flex (RU 200 Rigaku generator/max-A). It consists of an X-ray tube, a goniometer with divergence soller slit, protector, sample holder and receiving soller slit mounted on it and a counter to detect the diffracted rays. X-ray monochromator placed in diffracted beams is made up of pyrolytic graphite. The X-ray source is rotating anode type with the target material as Copper. The scintillation detector is of Sodium Iodide (NaI) doped with Thallium (Th).

For x-rays, the cross section depends on the square of the number of electrons and thus varies in a monotonic fashion throughout the periodic table. Clearly it will be difficult to determine the lighter atoms (e.g. hydrogen) positions with x-rays in the presence of heavy elements such as metal ions. Also, it is difficult to distinguish between the neighboring elements in the periodic table from X-ray diffraction studies. These problems can be overcome in neutron diffraction experiments.

2.6 Neutron scattering

Neutron scattering provides information that is complementary to that from other scattering techniques [180, 181]. There are a number of properties of neutrons that make it a useful probe for scattering experiments. The relevant properties of neutrons are given below:

- The wavelength of thermal neutrons is comparable to interatomic spacing in solids, and hence thermal neutron diffraction is suitable to study the crystal structure of solids.
- Unlike X-ray, in case of neutron scattering the fundamental scattering body is not the electron cloud but the nucleus. Since the size of the nucleus is very small as compared to the wavelength of the incident neutrons, the form factor is absent in the neutron nuclei scattering. The atomic scattering factor increases with increasing atomic number (Z) in X-rays, but for neutrons the scattering is not strongly dependent on the atomic number of an atom. This has major advantages, such as to be able to see light atoms (e.g. hydrogen) in the presence of heavier ones, and to distinguish neighboring elements more easily.
- Even though neutrons do not have an electric charge, they do posses a magnetic moment ($-\gamma\mu_N$ where $\gamma = 1.913$ and μ_N is the nuclear magneton) and can scatter from magnetic moments in a sample. This makes them an excellent candidate for probing static and dynamic magnetic properties such as spin waves and magnetic ordering.Thus neutron scattering can yield valuable information about themagnetic structure and spin dynamics of magnetic materials.

- Additionally, the energy of the neutrons is comparable to the energy of elementary excitations in matter, making it suitable for the study of dynamic processes.

Currently, there are two methods for producing neutron beams of sufficient intensity for powder diffraction namely, a nuclear reactor and a spallation source. The neutrons emerging from reactor and spallation neutron sourcehave very high energies (epithermal neutrons) and are therefore moderated to have useful energy ranges. The neutrons are called thermal, cold or hot depending on the temperature T of the moderator. The neutrons emerging from reactor are in thermal equilibrium with the moderator and their spectrum is approximately Maxwellian, with the temperature of the moderator. The neutron spectrum, having Maxwellian probability distribution between λ and $\lambda + d\lambda$ is defined as,

$$\phi(\lambda) = \frac{\text{constant}}{\lambda^5} \exp\left(-\frac{h^2}{2mk_B T \lambda^2} \right)$$

and the peak of this distribution occurs at $\lambda = \frac{h}{\sqrt{(5mk_B T)}}$. Since the thermal neutrons emerging from the moderator form a divergent beam with a continuous wavelength distribution, whereas diffraction studies require parallel beams of neutrons with a well-defined single wavelength, the thermal neutrons have to be monochromatized and collimated first before they can be allowed to fall on the specimen under study. It is important to choose the monochromator such that to get a minimum contribution from second order wavelength. For this purpose, the monochromator is chosen such that the structure factor amplitude from a suitable set of its atomic planes is zero or very small, for second order diffraction. The Germanium crystal has diamond structure, hence the second order reflections from lattice planes whose Miller indices (hkl) are all odd are systematically absent. Hence using the (111), (311) or (331) reflecting planes of a germanium monochromator, there will be no λ/2 contamination in the monochromate beam. Further, monochromatic beam intensity I_M and the angular spread $(\Delta 2\theta)$ of neutrons beyond the sample will depend upon the inpile collimation α_0, secondary collimation α_1 and the mosaic spread β of the monochromator crystal. Therefore, I_M and $\Delta 2\theta$ is given as [182-183]

$$I_M = \phi(\lambda)\frac{2\pi P_M \beta \alpha_0 \alpha_1}{\left(\alpha_0^2+\alpha_1^2+4\beta^2\right)^{1/2}}\cot\theta_M\,;$$

and

$$\Delta 2\theta = \frac{\dfrac{4(a+1)^2}{\alpha_0^2}+\dfrac{(2a+1)^2}{\beta^2}+\dfrac{4a^2}{\alpha_1^2}}{\dfrac{4}{\alpha_0^2\alpha_1^2}+\dfrac{1}{\alpha_0^2\beta^2}+\dfrac{1}{\alpha_1^2\beta^2}}$$

In these expressions, $\phi(\lambda)$ is the incident neutron flux on the monochromator for wavelength (λ), θ_M is the Bragg angle, P_M isthe peak reflectivity of monochromator. The quantity a is the dispersion parameter given as $\frac{\tan\theta_{sample}}{\tan\theta_M}$. The dispersion parameter compares the dispersion produced by the sample and the monochromator for a given spread of the wavelength in the incident beam.

The wavelength of the thermal neutrons, used in the scattering, is much larger than the nuclear radius, which makes the nuclei point-like scatterers. The scattering in such a case is spherically symmetric (isotropic) and has the character of an *s* wave (l=0). The potential for neutron-nucleus interaction for a nucleus ata fixed position R_j is described by Fermi pseudo potential, $V(r)=\frac{2\pi\hbar^2}{m_n}\sum_j b_j\delta(r-R_j)$ and therefore, the differential scattering cross section in this case is

$\frac{d\sigma}{d\pi} = \left(\frac{m_n}{2\pi\hbar}\right)^2 \left|\int V(r)e^{-iQ.r}\right|^2 = \left|\sum_j b_j e^{iQ.R_j}\right|^2$, where, b_j is the neutron scattering length and it depends upon the isotope and spin state of nucleus. If we consider that isotopes and spin states are randomly distributed in a solid, with no correlations among the different lattice positions, Then the differential scattering cross section can be written as $\frac{d\sigma}{d\Omega} = \left(\frac{d\sigma}{d\Omega}\right)_{coh} + \left(\frac{d\sigma}{d\Omega}\right)_{inc}$.The incoherent scattering cross section has no Q dependence and gives an isotropic background in the data. The coherent scattering cross section part for the crystal structures, having more than one atom per unit cell is given as, $\left(\frac{d\sigma}{d\Omega}\right)_{coh} = N\frac{(2\pi)^2}{V}\langle b\rangle^2 \sum_G \delta\left(Q-G\right)\left|F(Q)\right|^2$, here N is the number of unit cell, V is the volume of the unit cell and $F(Q)$ is the nuclear structure factor. The presence of δ-function in coherent scattering part implies that the coherent elastic scattering in crystals only occurs when the scattering vector (Q) is equal to a reciprocal lattice vector (G), as this is the requirement for constructive interference in the scattering. The nuclear structure factor is similar to x-ray where f_i (Q dependent) is the atomic scattering factor for X-rays, which is replaced by scattering length, b for neutrons. Unlike X-rays, the neutron scattering lengths depend on the details of the nucleus-neutron strong-interactions and therefore, the sign and the magnitude of the b vary random across the periodic table. X-ray and neutron diffraction are complimentary probes and should be used judiciously.

2.6.1 Magnetic diffraction

Neutron has a spin quantum number of ½ and a magnetic moment of 1.9μ_N due to which it interacts with magnetic moments of the unpaired electrons of the magnetic atoms thus producing neutron scattering in addition to scattering produced by nucleus. The corresponding neutron scattering is called magnetic neutron scattering and nuclear neutron scattering, respectively. The magnetic scattering is dependent on the spin–spin correlation function. In the paramagnetic state, the magnetic moments of atoms are completely uncoupled to each other and are randomly oriented. According to Halpen and Johnson [184], for paramagnetic ion the differential magnetic scattering cross section per unit solid angle per atom is given as

$$d\sigma_{pm} = \frac{2}{3} S(S+1)\left(\frac{e^2\gamma}{mc^2}\right)^2 f(Q)^2$$

Here S is the spin quantum number, γ is the magnetic moment expressed in nuclear magneton and $f(Q)$ is magnetic form factor (Fourier transformation of the spin density in an atom), given by, $f(Q) = \int \rho(r) e^{iQ.r} d^3r$. For a perfect paramagnet, in which there exist no interactions and no correlations between the atomic spins, the magnetic scattering is spatially isotropic, elastic and is independent of temperature. Paramagnetic material scatter neutron incoherently, as the magnetic spins are oriented randomly, providing no contribution to the Bragg’s peak. Compared to nuclear scattering (no Q-dependence, then so-called constant form factor), magnetic neutron scattering arises from the outer electrons in open shells only, which gives rise to the form factor in the case of magnetic scattering. This form factor is somewhat similar to the X-ray form factor. However for neutrons, it is only a few outer orbit unpaired electrons which contribute to the magnetic moment and hence the form factor for the magnetic scattering falls off more rapidly as a function of scattering angle as compared to the X-ray form factor. This restricts the range of theta over which significant intensities can be detected. Antiferromagnetic **(**AFM) and ferromagnetic (FM) have distinct features in the neutron diffraction. In case of a ferromagnetic or ferrimagnetic material, additional Bragg intensity to the lower angle fundamental nuclear peaks is observed. In case of an antiferromagnetic material, where the magnetic unit cell could be larger than the crystallographic unit cell, additional Bragg peaks appear corresponding to the magnetic unit cell.

Scattering by antiferromagnetic and ferromagnetic materials

In case of antiferromagnetic and ferromagnetic materials, the magnetic moments of individual ions are oriented in a defined manner, in contrast with their random orientation in space for paramagnetic materials. In ferromagnetic materials the moments are all parallel to each other while in antiferromagnetic materials the moments are antiparallel to each other. The differential magnetic cross section in these cases can be expressed as

$$d\sigma_m = q^2 S^2 \left(\frac{e^2 \gamma}{mc^2} \right)^2 f(Q)^2$$

where q is the magnetic interaction vector defined as $q = \vec{\varepsilon}\left(\vec{\varepsilon}.\vec{K}\right) - \vec{K}$, where $\vec{K}$ is a unit vector in the direction of the atomic magnetic moment and $\vec{\varepsilon}$ is the scattering vector. In general for an atom in which both spin and orbital moments are present, the spin quantum number is replaced by the total angular momentum J.

If the chemical and the magnetic unit cells are of the same size, then the coherent magnetic peaks will be superimposed on the nuclear Bragg peaks. In ferromagnetic systems, the coincidence of magnetic and nuclear peaks leads to an enhancement in intensities of low angle nuclear Bragg reflection. While in antiferromagnetic compounds, the magnetic unit cell may have dimensions different from the chemical one, causing the appearance of super lattice reflections at new positions.

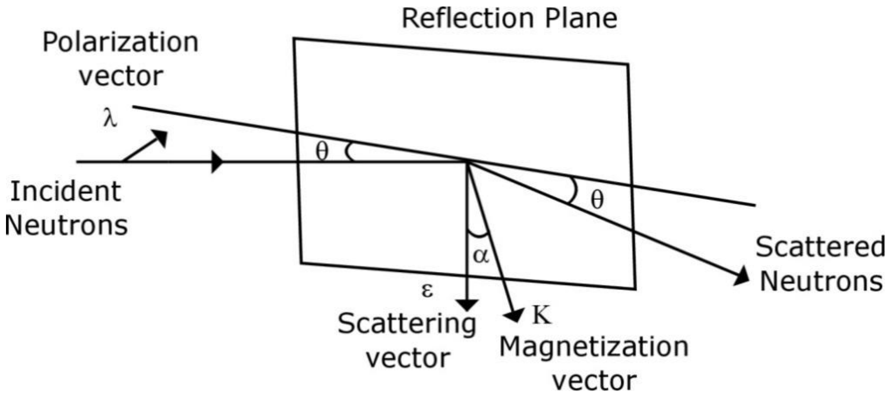

Figure 2.3: Direction of unit vectors ε, k, λ described in the text towards magnetic scattering in addition to scattering angle α, θ. The q lies in the plane of ε, k and is perpendicular to ε and magnitude of sinα.

According to Halpen and Johnson, differential scattering cross section of an atom, allowing for both nuclear and magnetic scattering is

$$\frac{d\sigma}{d\Omega} = F_N^2 + 2F_N F_{mag}(P.q) + F_{mag}^2 \qquad 2.2$$

Where ***P*** is the unit vector in the direction of polarization of the incident neutrons. When neutron beam is unpolarized, the average value of Pq will be zero; therefore, resultant structure factor is given as $F^2 = F_N^2 + q^2 F_{mag}^2$. In this expression, F_N^2 is the nuclear structure factor defined in eq 2.1 , while F_{magn}^2 is the magnetic structure factor defined as

$$F_{magn}^2 = \left| \sum_i p_i \exp\left(2\pi i\right)\left(hx_i + ky_i + lz_i\right) \right|^2 ;$$

and

$$q^2 = 1 - \left(\varepsilon.K^2\right) = \sin^2\alpha$$

where, $p = \left({e^2\gamma}\big/{2mc^2} \right) gJf$. Here g is the lande splitting factor, J is the total angular momentum f is the magnetic form factor and α is the angle between magnetization and scattering vector. The occurrence of this form factor in magnetic scattering in contrast to the nuclear scattering arises due to the unpaired electron distribution which determines the magnetic moment. The distribution of these electrons is over a volume of space having spatial dimensions which are comparable to the neutrons wavelength. In order to determine the value of q^2, we have to know the relative orientation of the aligned magnetic moments and the scattering vector. Therefore if the magnetic moments are parallel to the reflecting plane as shown in figure 2.2, then $\alpha = 90^\circ$ and $q = 1$. On the other hand if magnetic moment is perpendicular to the reflecting plane then $\alpha = 0^\circ$ and $q = 0$.

2.6.2 Neutron powder diffractometer

The neutron powder diffractometer PD2, which has been used mostly in this study, uses the tangential beam port T-1013 in the Dhruva reactor hall at Bhabha Atomic Research Centre, Mumbai, India [185]. The powder diffractometer is multi linear position sensitive detectors (PSDs) based, covering wide angular range from $4° < 2\theta < 140°$. It employs Ge (331) monochromator crystal at a take off angle of 60° to obtain monochromatic neutron beam of wavelength λ=1.2443Å. A schematic diagram of this instrument and the parameters is shown in figure 2.4. The powdered samples are packed in a cylindrical Vanadium container, attached to a cold finger of closed cycle refrigerator for temperature dependent measurements between 5 and 300K. The use of Vanadium container is advantageous because it has negligible coherent scattering cross-section; therefore, does not produce diffraction peaks. The detection system consists of 5 linear PSDs. The PSDs have been developed using 10 μm diameter Ni-Cr alloy wire having specific resistance of $9\Omega/mm$. The sensitive length of the PSD is 875 mm and the diameter of the outer brass tube is 36.5 mm. The filling gas is constituted of ^{3}He at 10 atm pressure and krypton (Kr) at 2 atm pressure. The neutrons collide with ^{3}He and produce ${}_1^1H$ and ${}_1^3T$. The reaction is as follows, ${}_2^3He + {}_0^1n = {}_1^1H + {}_1^3T + 0.765\ MeV$. The range of ${}_1^1H$ and ${}_1^3T$ is very large and in order to reduce it, a small amount of krypton is added, which acts as a stopping gas. The interactions of these charged particles with a gas lead to ionized (electron-ion pair) and excited molecules along the path. Many electrons reach the anode for each primary ion pair produced in the gas. The energy of these electrons increases and collisions with other gas atoms cause further ionisation producing more electrons. These secondary electrons themselves drift and acquire enough energy to cause further ionisation (and electrons), and so a large cloud of electrons arrives at the anode in a process known as an avalanche. The avalanche is localized and it covers a small portion of the length of the anode.

The PSDs work on the principle of charge division method. This typically uses a resistive anode and determines the position of the avalanche by sensing either the amplitudes or the rise times of the signals received at either end. Let the neutron hits at a distance x from the A side and Q charge is released. This charge is divided into two parts in the inverse ratio of the resistance of the wire from the point of capture to the end of the detector as shown in the figure below. The data acquisition system, having input from all 5 PSDs, is done with the help of a computer.

$$V_a \ \alpha \ \rho x$$

$$V_b \ \alpha \ \rho(L-x)$$

$$\frac{V_a}{V_a + V_b} = \frac{x}{L}$$

Here ρ is the resistance per unit length of the wire and L is the length of the wire. Thus by measuring the voltages V_a and V_b the position where the neutron hit the chamber can be calculated.

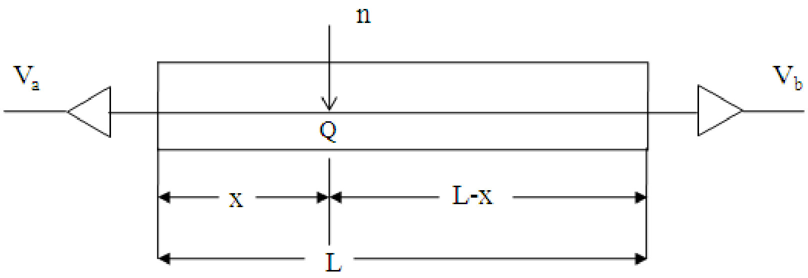

Figure 2.5: Position detection system

Beam hole no.	T1013
Monochromator	Ge (331)
Wavelength	1.244 Å
Beam size	4.0cm× 1.5 cm
Flux at sample	8.5×10^{5} n/cm^{2}/sec
Scattering angle	$4^{o} < 2\theta < 140^{o}$
Q range	0.4 – 9.4 Å^{-1}
$\Delta d/d$	~ 0.8 %
Detector	5 (1d-PSD)
Sample environment	5 – 300K

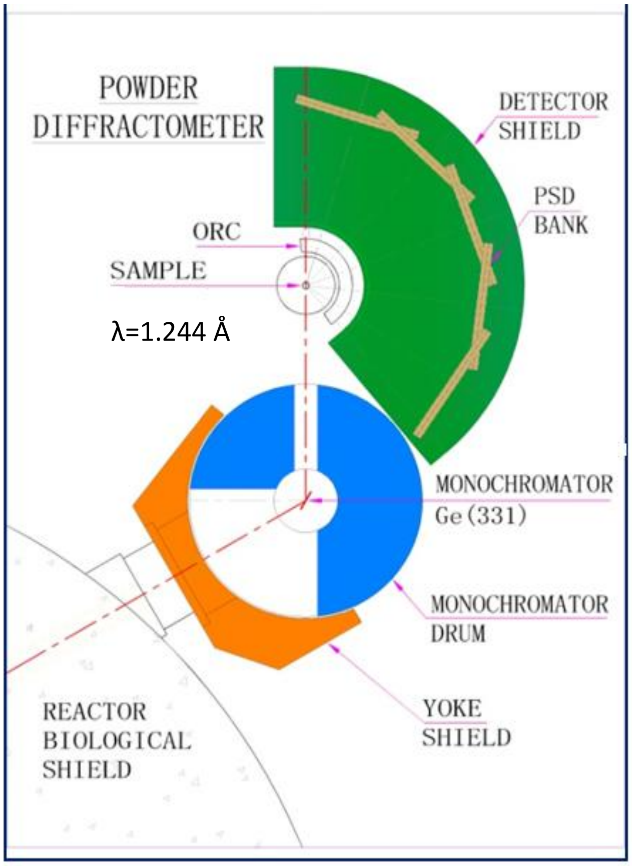

2.7 Data Analysis: Rietveld Method

Rietveld refinement/analysis is a technique devised by Hugo Rietveld for use in the characterization of crystalline materials [186-187]. Rietveld method is a least squares refinement method to refine x-ray and neutron diffraction patterns. For the refinement, a good initial guess, or at least knowledge of, the structure is required. The parameters such as lattice parameters, atomic positions, site occupancies, magnetic moments and experimental factors that affect peak shape and background are varied, until the agreement between the calculated and measured diffraction profiles are optimized.

The intensity of the Bragg peak is determined from $|F_k|^2$ values calculated by summing the contributions from the neighboring Bragg reflections and the background as follows

$$y_{ci} = s\sum_{k} L_k \left|F_k\right|^2 \Phi(2\theta_i - 2\theta_k) P_k A + y_{bi}$$

where s is the scale factor, k represents Millar indices (h, k, l), L_k contains the Lorentz polarization and multiplicity factor, ϕ is the reflection profile function, $|F_k|$ is the structure factor and is given as $\sum_i f_i e^{-2\pi i(hx_i + ky_i + lz_i)} e^{-B(\frac{\sin\theta}{\lambda})^2}$, Here, A is the absorption factor, P_K is the preferred orientation and y_{bi} is the background intensity at the i^{th}step. The background intensity in the i^{th} step is obtained either from manually inserting the table of background intensities or from refinable background polynomial functions. The measured profile of a single, well resolved, powder diffraction peak is dependent on two intrinsic parameters: (i) an instrumental parameter including the spectral distribution, and (ii) the sample contribution based on the crystal structure and the crystallinity of the sample. The powder diffraction peak recorded on constant wavelength neutron diffractometer can be described by Pseudo-Voigt function. This function utilizes a combination of pure Lorenzian (L) to pure Gaussian (G) by the parameter η, given as, $V = \eta L + (1-\eta)G$ for $0 \le \eta \le 1$.The peak width, defined as full width at half maximum (FWHM), is in general given as, $H^2 = U\tan^2\theta + V\tan\theta + W$, where U, V, and W are refinable parameters. The quality of the agreement between the observed and the calculated profiles can be evaluated from the residual R- values.

Profile factor	$R_p = 100\dfrac{\sum_{i=1,n}\lvert y_i - y_{ci}\rvert}{\sum_{i=1,n} y_i}$;
Weighted profile factor	$R_{wp} = 100\left[\dfrac{\sum_{i=1,n} w_i \lvert y_i - y_{ci}\rvert^2}{\sum_{i=1,n} w_i {y_i}^2}\right]^{1/2}$;
Expected weighted profile factor	$\mathrm{R}_{\exp} = 100\left[\dfrac{n-p}{\sum_i w_i {y_i}^2}\right]^{1/2}$;
Goodness of fit indicator	$S = \dfrac{R_{wp}}{R_{\exp}}$;
Reduced chi-square	$\chi^2 = \left[\dfrac{R_{wp}}{R_{\exp}}\right]^2 = S^2$;
Bragg factor,	$R_B = 100\dfrac{\sum_h \lvert I_{obs,k} - I_{cal,k}\rvert}{\sum_h \lvert I_{obs,k}\rvert}$;

where $I_{obs,k}$ and $I_{cal,,k}$ are the observed and calculated intensities assigned to k^{th} Bragg reflection at the end of refinement cycle, n and p are the number of observations and refined parameters, respectively. Notably, in addition to having low values of these R factors, the refined model has to be physically correct. Both structural and magnetic refinements are carried out by Rietveld method using FULLPROF program [188]. The representation theory analysis for determining magnetic structures has been performed using the BASIREPS [188] and the SARAH [189] programs. The identification of magnetic reflections is usually accomplished by a careful comparison of powder patterns recorded below and above the magnetic phase transition temperatures. The simultaneous Rietveld refinement combines both neutron and x-ray powder diffraction data is an effective technique taking advantage of the different contrast mechanisms for x-rays and neutrons. Editing a proper input file is the critical point. The successful practical operation of this program, which depends on the sequence of the model parameters, is primarily dependent on the experience and the ability of the user. Parameters are usually refined sequentially, but it is typical to first perform a refinement of scale factor and background of the corresponding diffraction patterns.

2.8 Polarized neutron spectrometer for depolarization studies

The beam of neutrons obtained from the neutron sources is unpolarized. These neutrons can be polarized by using one of the three following methods, (i) Transmission though polarizing filters (e.g. preferential absorption by polarized ^{3}He nuclei), (ii) Reflection from polarizing mirrors and supermirrors (using preferential reflection), and (iii) Bragg reflection from magnetetized single crystals (e.g. Crystals of $Co_{0.92}Fe_{0.08}$, Heusler alloy (Cu_2MnAl)). In the case of polarized beam the term $2F_N F_{mag} P.q \neq 0$ in equation 2.2. From equation 2.2, it follows that scattering amplitude for the up and down pointing spins will be $(F_N + F_{mag})$ and $(F_N - F_{mag})$, while the corresponding intensities are $I_1 = (F_N + F_{mag})^2$ and $I_2 = (F_N - F_{mag})^2$. The polarization of the neutron beam (incident beam polarization) is defined as,

$$P = (I_1 - I_2)/(I_1 + I_2)$$

This indicates that there is coherence between nuclear and magnetic and scattering amplitude and if we can find a material for which a particular reflection has $|F_N| = |F_{mag}|$ (Nuclear structure factor=Magnetic structure factor) then we shall obtain a completely polarized beam. In this instrument the neutrons are polarized by using a polarizing crystals $Co_{0.92}Fe_{0.08}$ (analyzer), Heuslar crystal Cu_2MnAl (monochromator-cum-polarizer). A schematic diagram of neutron depolarization spectrometer is shown in figure 2.6. It consists of polarizer, guide field, dc flipper, analyzer and BF_3 detector. The Cu_2MnAl (111) crystal is mounted between the pole pieces of $SmCo_5$ permanent magnet assembly which provides a vertical uniform field of 2.8kOe. The polarization efficiency of the monochromatic beam obtained from this polarizer is 98.83±0.01%. A polarization sensitive analyzer single crystal $Co_{0.92}Fe_{0.08}$ (200) is inserted in the pole gap of a $SmCo_5$ magnet assembly. The purpose of the analyzer crystal is to analyze the spin state of neutrons scattered from the sample. Above described set up is used for the measurement of depolarization of incident polarized neutron beam. This depolarization measurement is advantageous to study the ferromagnetic behavior in samples with coexisting ferromagnetic and antiferromagnetic phases. This technique measures spatial magnetic inhomogeneities on a length scale from 1000Å to several micrometers. In neutron depolarization measurements, we measure flipping ratio R (ratio of transmitted intensities for two spin states of the incident neutron spin) which is a measure of the transmitted beam polarization. The flipping ratio can be expressed in the form, $R = \frac{1 - P_i D P_A}{1 + (2f - 1) P_i D P_A}$; where, P_i is the incident beam polarization, P_A is the efficiency of the analyzer crystal, f is the efficiency of the DC flipper and D is the depolarization coefficient (due to the sample under investigation). In the absence of any depolarization in sample, D = 1, and, when there is total depolarization D = 0. Unlike M(H) measurements, where the sample is subjected to high field, depolarization measurements provide information about the presence of ferromagnetic domains in low magnetic fields and therefore, does not influence the magnetic ground state. An estimate of the domain size of the ferromagnetic region is obtained using the expression $P_f = P_i \exp[-\alpha(d/\delta)\langle\phi_\delta\rangle^2]$, where P_f and P_i are the transmitted beam and incident beam polarization, respectively, α is a dimensionless parameter (=1/3), d is the sample thickness, δ is a typical domain length and the precession angle $\phi_\delta = (4.63\times10^{-10} Oe^{-1} A^{-2})\lambda\delta B$ [190]. The domain magnetization, $B = 4\pi M_s$ is obtained from the bulk magnetization, where M_S is the spontaneous magnetization. This expression is valid in the limit where domains are

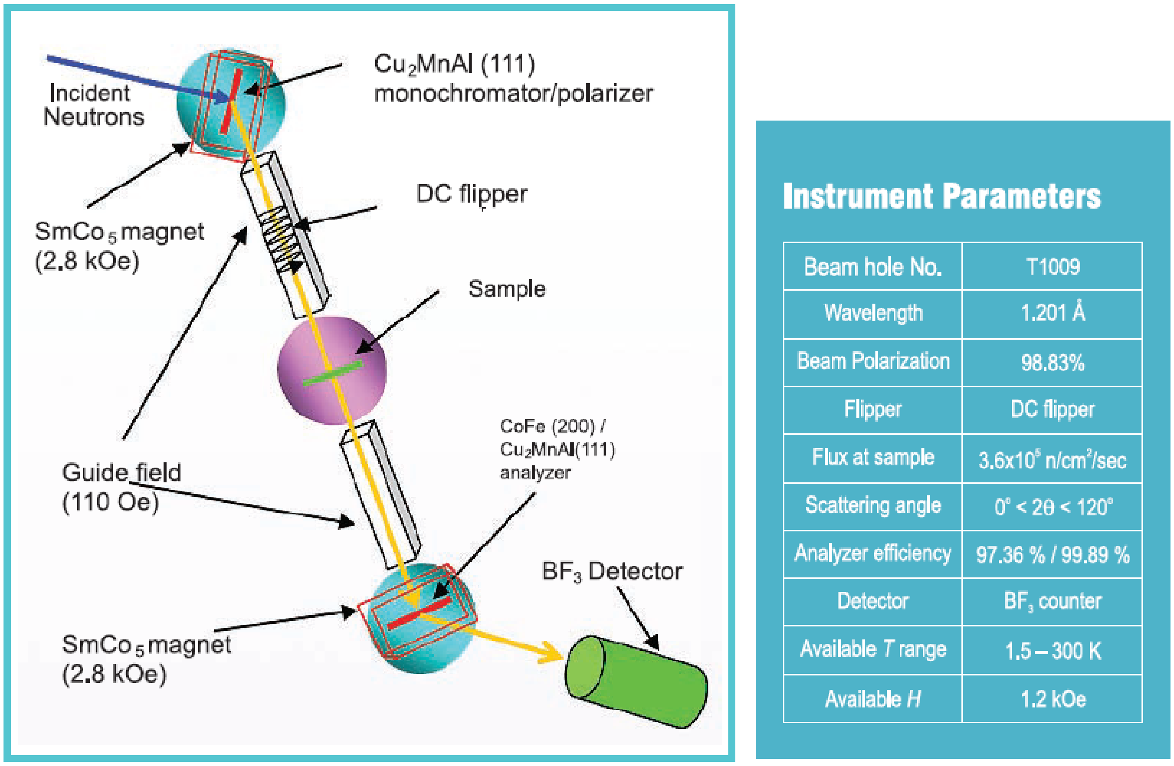

Instrument Parameters

Beam hole No.	T1009
Wavelength	1.201 Å
Beam Polarization	98.83%
Flipper	DC flipper
Flux at sample	$3.6\text{x}10^5$ n/cm^2/sec
Scattering angle	0° < 2θ < 120°
Analyzer efficiency	97.36 % / 99.89 %
Detector	BF_3 counter
Available *T* range	1.5 – 300 K
Available *H*	1.2 kOe

Figure 2.6: A schematic and the corresponding instrument parameters of neutron neutron depolarization

randomly oriented and the Larmor precession of the neutron spin due to the internal magnetic field of sample is a small fraction of 2π over the typical domain length scale. Neutron depolarization measurements (λ = 1.201Å) were carried out on the polarized neutron spectrometer at Dhruva reactor, Bhabha Atomic Research Centre, Mumbai, India. Powdered samples studied here were packed in an aluminium can of 5mm diameter. Data acquisition and control of the spectrometer are accomplished through a computer.

2.9 Four probe resistivity set up

To study the transport behavior of our samples, resistivity measurements have been carried out using the four point probe technique in the temperature range of 5K to 300K. Four-point probes method is an electrical impedance measuring technique that uses separate pairs of current-carrying and voltage-sensing electrodes to make more accurate measurements than traditional two-terminal (2T) sensing.

In four probe set up, current I is applied to outer two probes, while the corresponding voltage V is measured across the two inner probes. The measured resistance R(= $\frac{V}{I}$) is converted into resistivity ρ valuesby $\rho = \frac{(RA)}{l}$ where, A is the cross-sectional area that the current flows through and l is the distance between the current contacts. This technique allows the effects of contact resistance to be minimized, leading to greater accuracy for the samples showing low resistivity values. For resistivity measurements the samples are prepared in rectangular form. Four contact points are made by applying silver paste on the measuring surface of the sample. To dry the silver paste we keep it for sometime in air. In order to measure the temperature dependence of resistivity, sample is cooled using closed cycle refrigerator. The entire measurement system comprises of a nanovoltmeter (2182 Keithley), a constant current source (Calibrator SN 8310

AOIP) and a temperature controller (LTC 21 Oxford Instrument), which were interfaced with a computer for automatic data acquisition.

2.10 Magnetization measurements

Magnetization measurements were performed using a Quantum Design SQUID (Superconducting Quantum Interference Device) magnetometer. SQUID provides high resolution (10^{-14}T) for field measurements, enabling the measurements of very small changes in the magnetic flux [193]. This device works on the principal of quantum interference produced using Josephson junctions. These junctions are tunnel junctions comprised of two superconductors separated by thin insulating layer between them. The SQUID functions as a linear current-to-voltage convertor, so that variations in the current in the detection coil circuit produce corresponding variations in the SQUID output voltage.

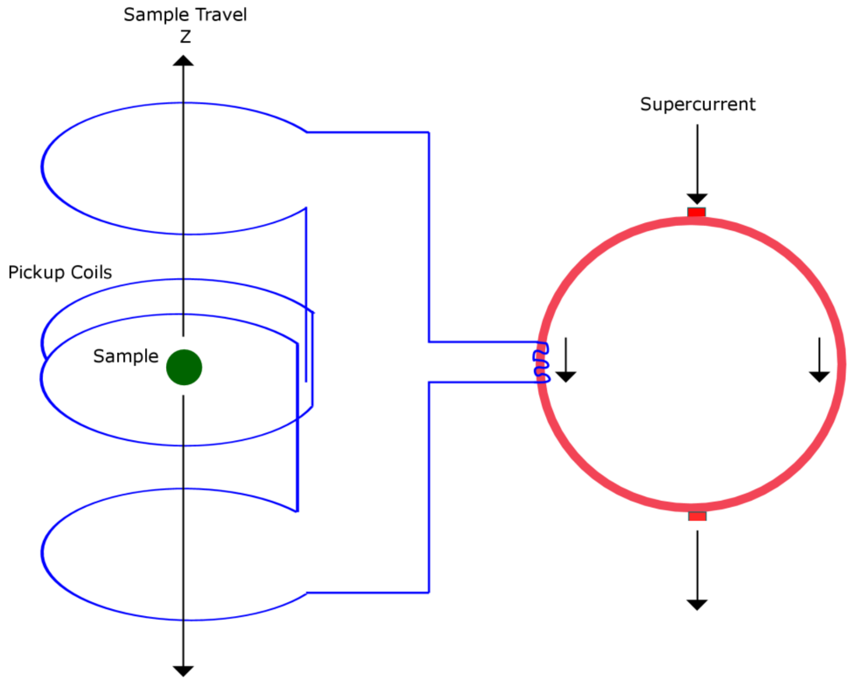

Figure 2.7: Diagram of sample positioning within the pick-up coils of the SQUID magnetometer.

Measurement in SQUID is performed by moving the sample through the superconducting pick-up coils which are located at the center of the magnet. Movement of the magnetised sample through these coils induces a current proportional to the sample magnetization. The greater the magnetization of a sample, the more magnetic flux through the coils changes, which, in turn, generates current in the coils. Properly weighed sample is mounted on the inside of a straw and secured by additional inner straws to prevent movement. Typical magnetization measurements are magnetization as a function of temperature M (T) in fixed applied field and magnetization as a function of magnetic fields at fixed temperatures M(H). To carry out zero field cooled (ZFC) measurements, initially sample is cooled to low temperature (5K) in zero magnetic field. At low temperature, field is applied and measurement is performed upto 300K. For FC measurements, sample is cooled in the presence of same magnetic field from 300K to 5K. Then data is recorded while heating.

2.11 X-ray absorption spectroscopy (XAS)

X-ray absorption spectroscopy (XAS) is a technique that generally deals with measurement of absorption coefficient as a function of X-ray photon energy around an X-ray absorption edge of an element in a material. X-ray absorption spectrum consists of two parts: (i) The spectrum near the absorption edge (viz., the X-ray near edge structure or the XANES part) gives information about the external perturbations in the valence states to which electrons make transitions from core levels upon absorption of X-ray photon energy. X-ray absorption near edge structure (XANES) has been used to probe the electronic structure of these compounds because of its sensitivity to local structural arrangement of the atoms surrounding the absorbing atom, formal oxidation state of the absorbing atom. (ii) The second part of the spectrum which extends from 50eV to ~700eV above the absorption edge is generally called the Extended X-ray Absorption

Fine Structure (EXAFS) part which is characterized by the presence of fine structure oscillations arising due to back scattering of outgoing photo-electron by neighboring atoms, and can give precise information regarding the short range order and local structure around the particular atomic species in the material. EXAFS (Extended X-ray Absorption Fine Structure) is a spectroscopic method providing local structural information about sample by means of the analysis of X-ray absorption spectrum. A typical x-ray absorption spectrum for FeO at Fe edge is shown in figure 2.8. The analysis of XANES and EXAFS can provide fine details of the local structure around the absorbing atom, contributing to the full understanding of the properties of these materials.

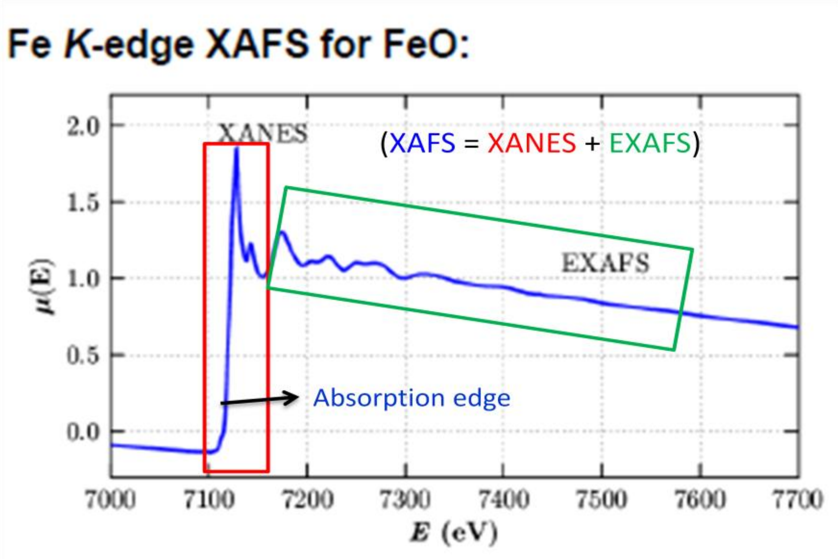

Figure 2.8: A typical x-ray absorption spectrum for FeO at Fe edge.

Samples of appropriate weight, estimated to obtain a reasonable edge jump were taken in powder form and mixed thoroughly with cellulose powder to obtain total weight of 100 mg. Homogenous pellets of 15 mm diameter were prepared using an electrically operated hydraulic press. The EXAFS measurements have been carried out at the dispersive EXAFS beamline (BL-8) and Energy-Scanning EXAFS beamline (BL-9) in transmission mode at the INDUS-2

Synchrotron Source (2.5 GeV, 100 mA) at Raja Ramanna Centre for Advanced Technology (RRCAT), Indore, India [195]. This beamline operates in x-ray energy range of 4 KeV to 25 KeV.

2.12 Mössbauer spectroscopy

Mössbauer spectroscopy, also known as nuclear gamma resonance spectroscopy, is based on the quantum mechanical Mössbauer effect [196]. The recoilless emission and resonant absorption of the γ -rays is known as Mössbauer effect. In order to observe the resonance absorption, γ ray energy is changed over a small range employing Doppler motion. Mössbauer effect has been observed in many isotopes such as ^{57}Fe, ^{99}Ru, ^{119}Sn, ^{121}Sb, ^{151}Eu, ^{155}Gd, ^{193}Ir, and ^{197}Au. ^{57}Fe is the most studied Mössbauer nucleus because it fits these requirements and is the fourth most abundant element in nature. Mössbauer spectra are described using three parameters: (i) isomer shift (δ), which arises due to the electrostatic Coulomb interaction between the nuclear charge and the inner electrons of the atom. The density of *s* electron which are closest to the nucleus, are the main contributors to the isomer shift. Therefore, the difference in the s electron density of the resonant atom, in the source and the absorber, produces a shift in the resonance energy. (ii) Quadrupole splitting (Δ) which is a shift in nuclear energy levels that is induced by an electric field gradient caused by nearby electrons. The quadrupole splitting occurs only in nuclear states with $I>1/2$ (I is nuclear spin quantum number). Therefore, the ground state of ^{57}Fe ($I=1/2$) nucleus cannot exhibit quadrupole splitting, however, the excited state (I = 3/2) has a finite quadrupole moment. In the presence of an electric field gradient, or non-uniform electric field, nuclear energy levels of excited state of ^{57}Fe splited in the doublet as shown in figure 2.9 and (3) hyperfine splitting (for magnetic materials only), arises due to the interaction between magnetic moment of the nucleus and local magnetic field [197].

Iron atoms in different local environments and those having different oxidation states absorb at different energies. The combination of isomer shift and quadrupole splitting parameters (along with the hyperfine field, in the case of magnetically ordered phases) is usually sufficient to identify the valence state and site occupancy of Fe in a given site. A typical Mössbauer spectrum thus consists of sets of peaks (singlet, doublet, or sextets) is shown in figure 2.9. The room temperature Mössbauer spectra of the Fe substituted orthorhombic calcium manganite and hexagonal yttrium manganite samples in the present work were obtained using a Mössbauer spectrometer (Nucleonix Systems Pvt. Ltd., Hyderabad, India) operated in constant acceleration mode (triangular wave) in transmission geometry at room temperature. The source employed was Co-57 in Rh matrix of strength 50 mCi. The calibration of the velocity scale was done by

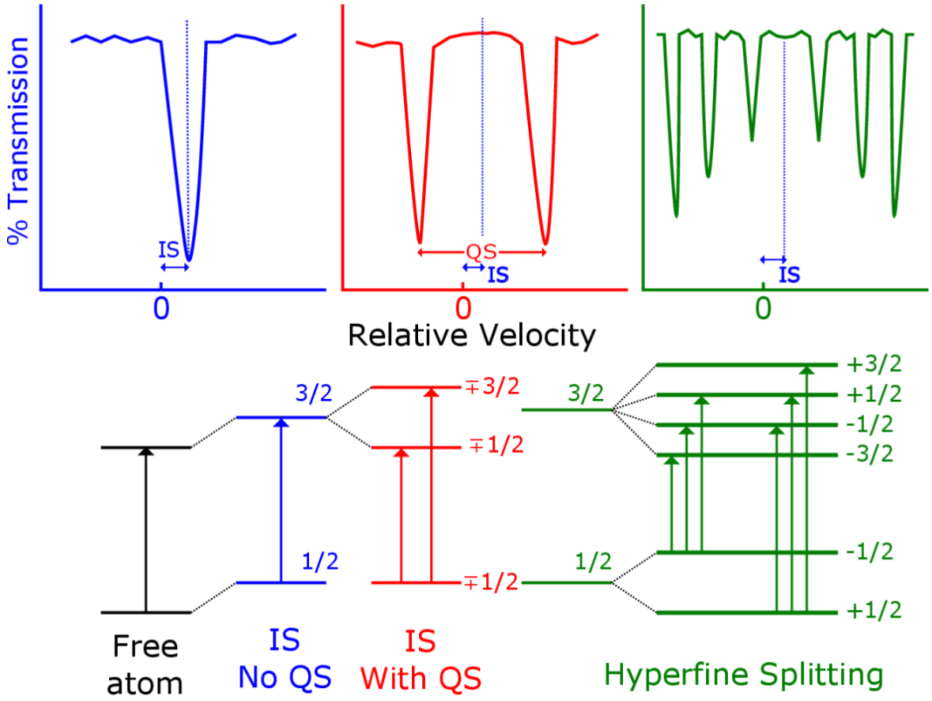

Figure 2.9: The effect of isomer shift, quadrupole splitting, and nuclear Zeeman interaction on the nuclear energy levels of 57Fe (adapted from Ref 198).

using an enriched α-^{57}Fe metal foil. The line width (inner) of calibration spectra was 0.23 mm/s. The Mössbauer spectrum was fitted with a least square fit (MOSFIT) program assuming Lorentzian line shape.

2.13 Dielectric Measurement

The coupling between electrical polarization and magnetic ordering can be studied by measuring the change in electrical polarization (magnetization) upon the application of a magnetic field (electric field) and indirectly by measuring the change of the capacitance (dielectric constant) at magnetic ordering temperature or upon the application of a magnetic field. In the present thesis, the magnetoelectric coupling (ME) in some of the selected samples has been studied by measuring the capacitance as a function of temperature. A dielectric material located between two parallel conducting plates comprises a capacitor. The capacitance of a dielectric medium with a relative permittivity ε_r, in parallel plate geometry is given as, $C = \varepsilon_0 \varepsilon_r \frac{A}{d}$, where, ε_0 is the permittivity of the free space, d is the thickness of pellet (sample), and A is the area of contacts.

For dielectric measurements, disk-shaped pellets of approximately16 mm in diameter and 1–2 mm in thickness were prepared using a uniaxial isostatic press. Then these pellets were sandwiched between the electrodes of the sample cell and the contacts were made by applying silver paste on both surfaces of the pellet. Low-temperature dielectric measurements were carried out using a frequency-response analyzer (Novocontrol *TB*-Analyzer). For cooling the sample down to 5K, a closed-cycle refrigerator with He-gas exchange attachment was used. Temperature-dependent capacitance data was measured in the frequency range 1Hz–1MHz with a heating rate of 0.8K/min in the range from 5 to 300K.

Chapter 3

Effect of A-site and B-site doping on the magnetic properties of hexagonal $YMnO_3$

Hexagonal manganites have been studied extensively because of their multiferroic properties. $YMnO_3$, a hexagonal manganite, shows an antiferromagnetic transition at T_N~75K and a ferroelectric transition at T_C~950K. The noncollinear magnetic order in $YMnO_3$ originates from the strong in-plane AFM superexchnage interactions of the Mn^{3+} spins. The strong superexchnage interactions gives rise to a 120º arrangement of the Mn^{3+} spins in the ab plane. The structural and magnetic properties of $YMnO_3$ in detail are already discussed in introduction part (Chapter 1). Figure 3.1 shows the schematic picture of the crystal structure of hexagonal $YMnO_3$. In this compound Mn^{3+} is in 5- fold coordination forming MnO_5 trigonal bypiramids which forms a quasi - 2D triangular network separated along the *c* axis by a noncoplanar layer of Y atoms. The distance between the nearest Mn atoms is 3.50Å and 6.06Å for the *ab* plane and *c* axis, respectively.

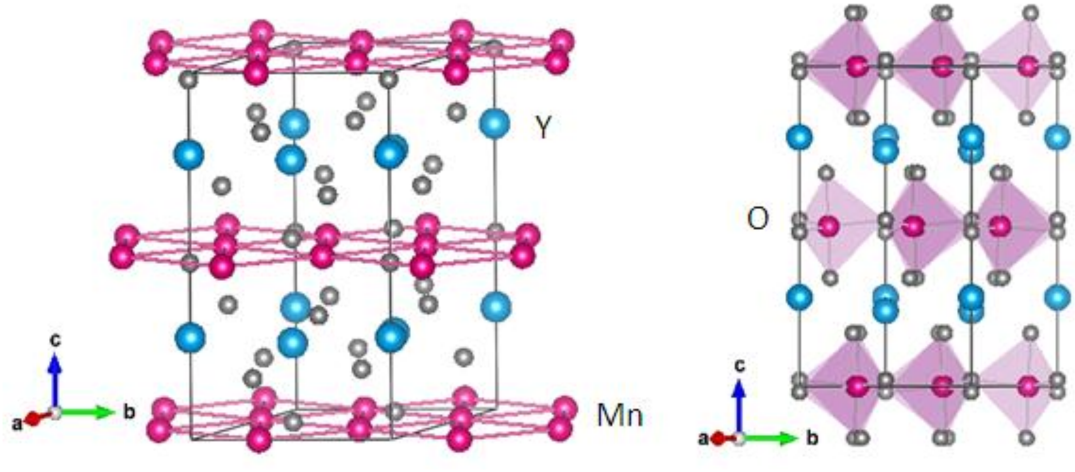

Figure 3.1: The schematic picture of the crystalstructure of hexagonal $YMnO_3$.

The magnetic structure of this compound is found to be strongly influenced by chemical substitution or under the influence of external pressure [166-169]. Divalent substitutions (Ca, Sr) at the Y site show a variety of structural and magnetic phases over a wide composition regime[199-202]. However, only a few studies of doping at the rare-earth site have been reported earlier [166-168, 203]. By doping magnetic Er^{3+} ion at Y site, the magnetic structure changes from Γ_1 representation in $YMnO_3$ to Γ_2 representation in $ErMnO_3$ and the system becomes less frustrated [166]. While, in the case of doping with non-magnetic Lu the frustration parameter remains constant, the magnetic structure varies continuously with Lu doping [168]. The substitution of magnetic ions at Y–site is found to relieve the frustration, while it remains unchanged with non magnetic ion substitution. The reduction in geometrical frustration effects in Er doped samples has been attributed to the magnetic coupling along the c axis between Er and Mn moments [166]. Based on magnetization measurements on single crystals of $Y_{0.8}Tb_{0.2}MnO_3$, a transition at T ~ 23K is observed in addition to AFM ordering of the Mn^{3+} ions at T ~ 71K which has been ascribed to the Mn spin reorientation [203].

The magnetic and frustrated behavior in $YMnO_3$ is also found to be influenced by doping at the Mn site. Spin glass state has been reported in Mn rich hexagonal manganite $YMn_{1+x}O_3$ ($0 \leq x \leq 0.15$) [204] and in $YMn_{1-x}Cr_xO_3$ ($0 \leq x \leq 0.1$) [205]. With Fe doping at the Mn site in $YMnO_3$ a single phase has been obtained for $x \leq 0.3$ [206]. The transition temperature decreases to 60K with 20% Fe doping and reduction in effective moments has also been observed [207]. In $YMn_{1-x}Ti_xO_3$, a structural phase transition from hexagonal ($P6_3cm$) to rhombohedral ($R3c$) is observed around $x = 0.2$ and the Curie-Weiss temperature is found to decrease with increase in Ti concentration indicating the suppression of average antiferromagnetic interactions [208]. By wet chemistry techniques single-phase hexagonal type solid solution has been formed for Cu doping at Mn site in $YMnO_3$ and self doping at the Y-site [209]. Cu^{2+} doping results in partial transformation of the Mn^{3+} into Mn^{4+}, and this introduces weak ferromagnetic interactions Mn^{3+}-Mn^{4+}. Doping with 10% Al, Ru, and Zn leads to a decrease in Mn moment and a slight decrease in T_N has been observed. In this study the magnetic structure of $YMnO_3$ has been explained by taking a mixture of Γ_3 and 18% of Γ_4 and with doping of 10% Al, Ru, Zn the mixing ratio of Γ_3& Γ_4 is found to be modified [168].

In $YMnO_3$, a spin reorientation leading to change in the magnetic ground state from Γ_1 to $\Gamma_1+\Gamma_2$ representation and reduction in order moment have been observed, under external pressure up to 5 GPa. Additionally, the external pressure leads to lowering of the difference between Mn-O3 and Mn-O4 bond lengths leading to enhancing frustration effects. Doping with a magnetic ion and application of external pressure both individually are found to modify the magnetic properties of $YMnO_3$, indicating a strong correlation between the magnetic ordering and the crystal structure in such a spin frustrated system. In addition to the change in long range magnetic symmetry, the formation of spin-liquid phase in $YMnO_3$ occurs through the symmetrization of triangular network of Mn ions at high pressures [169-171]. Though fully doped compounds have been investigated in a number of studies, the effect of partially doping $YMnO_3$ with isovalent magnetic ions is very less, particularly using neutron diffraction technique in exploring the crystal and magnetic structure.

Several attempts have been made to understand these unusual properties of the hexagonal manganites, theoretically as well as experimentally. In this chapter we discuss the influence of A-site and B-site substitution on the crystal and magnetic structure of polycrystalline $YMnO_3$. The doping experiments at the Y-site and Mn-site and external pressure experiments suggest that the magnetic structure of $YMnO_3$ is subject to alterations by these.

This chapter broadly consists of two parts *viz.*, (1) Effect of A-site doping on the magnetic properties of $YMnO_3$, which consists of studies on $Y_{1-x}R_xMnO_3$ (R= Yb, Er, Tb, Ho; $x \leq 0.2$)) (2) Effect of B-site doping on the magnetic properties of $YMnO_3$, which consists of studies on (i) $YMn_{1-x}M_xO_3$ (M = Ti, Fe, Ga; x = 0, 0.1), and (ii) $YMn_{1-x}Fe_xO_3$ ($x \leq 0.5$).

3.1 Effect of A-site doping on the magnetic properties of $YMnO_3$

3.1.1 Effect of rare earth dopants on the magnetic ordering of frustrated *h*-$YMnO_3$

In this study we have partially doped $YMnO_3$ with magnetic ions (Yb, Er, Ho, Tb) and studied its effect on the long range and short range magnetic behavior of these compounds. These doping studies offer a possibility to study the change in magnetic ground state and frustrated behavior via tuning the A-site ionic radii as well as the A-site moment. We have observed that even a small amount of doping induces significant changes in the magnetic structure and frustration behavior of $YMnO_3$.We find the results can be explained by combining the effect of R-Mn interactions and ionic size of the dopants.

3.1.1.1 Crystal structure

The A-site doped compounds studied in the series $Y_{0.8}R_{0.2}MnO_3$ (R= Yb, Er, Ho, Tb) are isostructural and crystallize with hexagonal structure (space group $P6_3cm$). In this structure, Mn occupies 6c (x, 0, 0) site, O occupies 6c (x, 0, z), 2a (0, 0, z) and 4b (1/3, 2/3, z) sites, and Y occupies 2a (0, 0, z) and 4b (1/3, 2/3, z) sites. Figure 3.2 shows the x-ray diffraction pattern of all the samples. All the reflections were indexed and no impurity reflections were observed. The Rietveld refinement of x-ray diffraction data yielded the initial starting parameters for refinement of the neutron diffraction patterns. Figure 3.3 shows a typical neutron diffraction pattern at

300K. We obtain the cell parameters, position parameters, occupancies, thermal parameters (B_{iso}) and magnetic moment from the refinement of the neutron diffraction patterns at various temperatures. The variation of the unit-cell volume as a function of doping shows a systematic behavior. The volume increases with Ho and Tb doping, while it reduces with Er and Yb doping

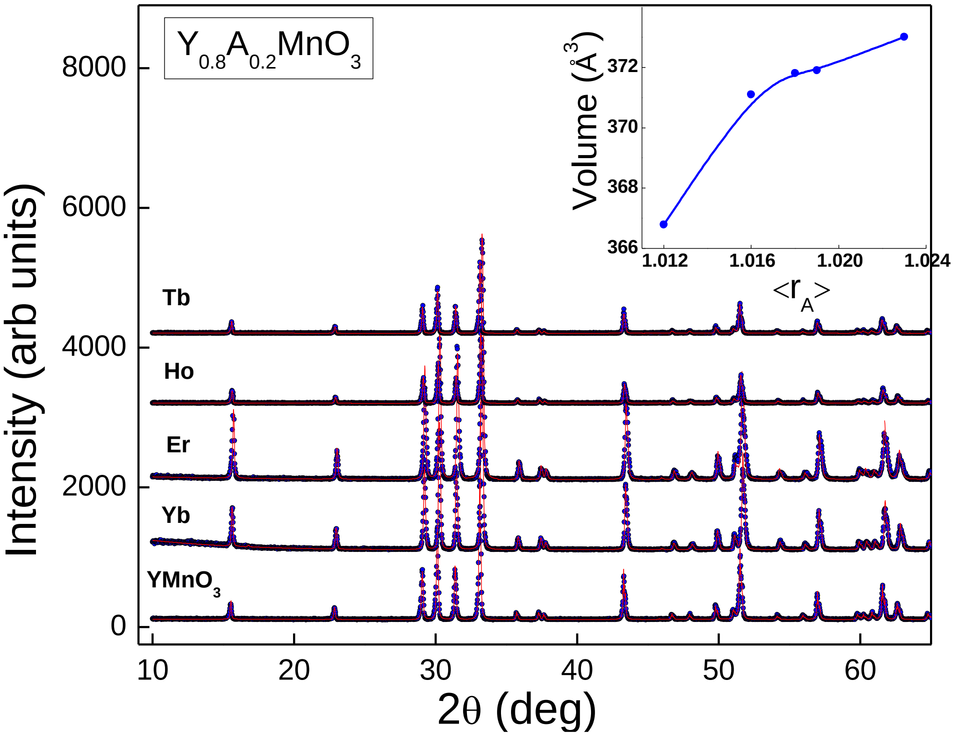

Figure 3.2: Room temperaturepowder X- ray diffraction patterns of $Y_{0.8}R_{0.2}MnO_3$ (R= Yb, Er, Ho, Tb). Open circles are observed data points. The solid line represents the Rietveld refinement. Inset (a) shows the variation of unit cell volume (V) as a function of average A-site ionic radius, $<r_A>$.

which is consistent with the difference in the ionic radii [210] of the dopants as shown in inset of figure 3.2. The cell parameters, unit cell volume, selected bond lengths, and agreement factors obtained from Rietveld refinement of the neutron diffraction data at 300K and 6K are given in Table 3.1. The Mn-O3-Mn and Mn-O4-Mn bond angles are close to 120°, and they change only slightly with doping. However, with doping the splitting in planar bond lengths (Mn-O3, Mn-O4)

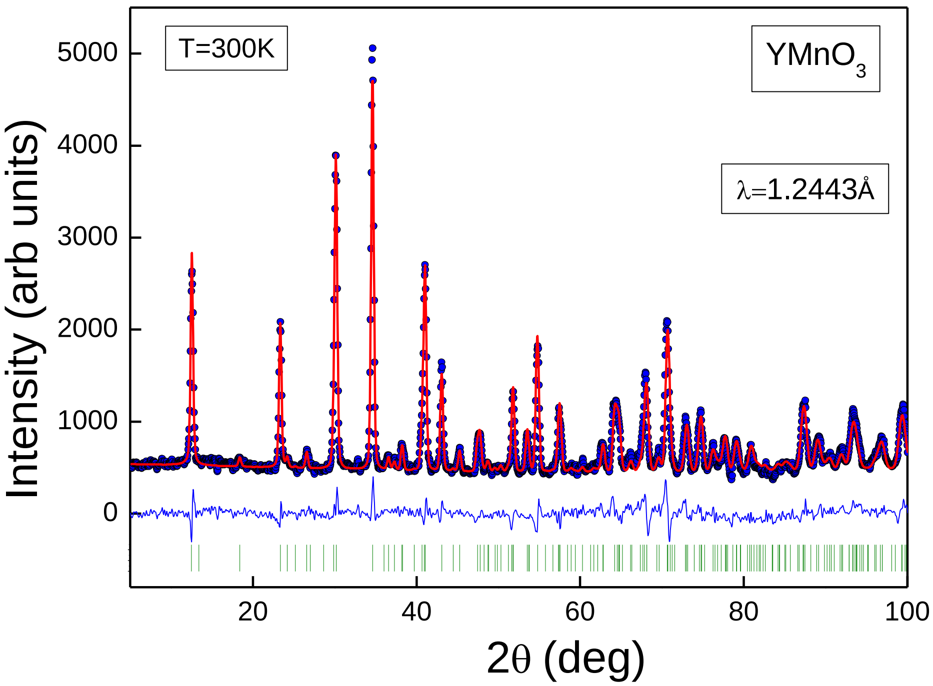

Figure 3.3: Room temperaturepowder neutron diffraction patterns of $YMnO_3$. Open circles are observed data points. The solid line represents the Rietveld refinement. The tick marks indicates the position of nuclear Bragg peaks corresponding to space group $P6_3cm$.

increases. Figure 3.4(a) and 3.4(b) shows the variation of the planar bond lengths (Mn-O3 and Mn-O4) at 300K and 6K, respectively. The difference in Mn-O3 and Mn-O4 bond length remain constant with increase in volume at room temperature. However, at 6K the splitting in planar bond lengths (Mn-O3, Mn-O4) increases with increase in volume. This enhancement in the splitting of Mn-O3 and Mn-O4 bond lengths leads to a less symmetric triangular network of Mn ions, which reduces the frustration in the system [171]. External pressure dependent studies on $YMnO_3$, previously reported [169], show a similar reduction in all the bond lengths with increase in external pressure. Therefore, the similarity of the two results (and magnetic structure discussed later) indicates that the reduction in the size of the dopants leads to chemical pressure effect.

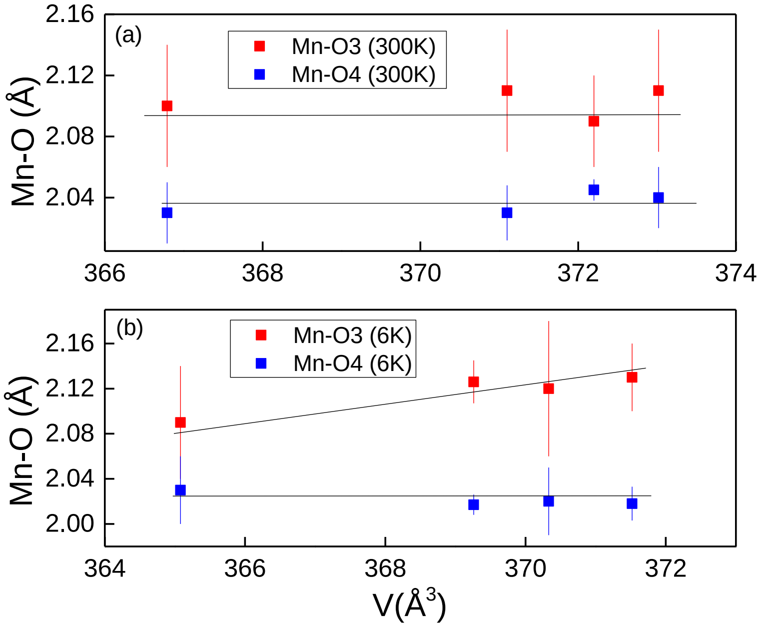

Figure 3.4 (a): Variation of planar bond lengths (Mn-O3 and Mn-O4) as a function of volume at 300K. (b) Variation of planar bond lengths (Mn-O3 and Mn-O4) as a function of volume at 6K.

Variation of cell parameters for YMnO$_3$ with temperature is shown in figure 3.5 (a). The lattice parameter a increases and c decreases with increase in temperature for all the studied samples. This behavior is found to persist up to 1270K in hexagonal manganites [100]. The negative thermal expansion of cparameter is caused by the tilting of MnO$_5$ bypiramids along with the buckling of the Y-planes [96]. The lattice parameters and unit cell volume obtained from x-ray diffraction of YMnO$_3$ agrees with the earlier reported values [113]. A distinct anomaly is observed at the magnetic transition temperature indicating the presence of a magnetoelastic coupling in these samples. Similar behavior has been reported before in similar samples [152, 161]. We find that the anomalous reduction in volume below T$_N$ correlates with the antiferromagnetic moment in these compounds. To obtain this correlation we have fitted the temperature variation of volume above the magnetic ordering temperature to Debye model using

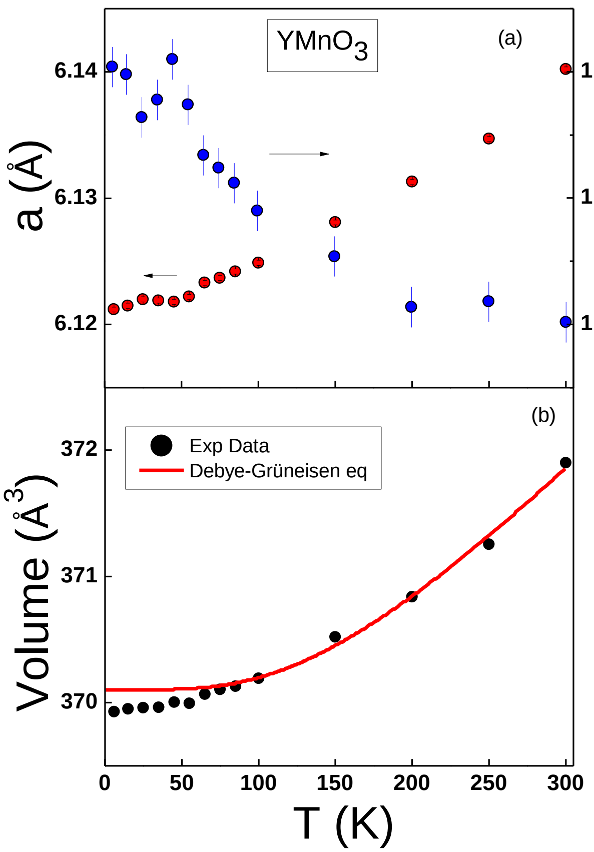

Figure 3.5

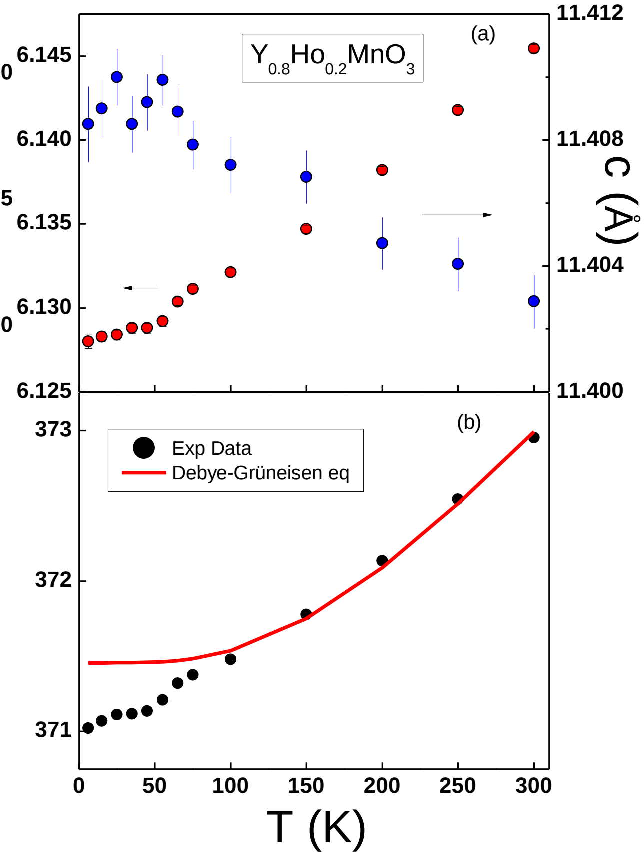

Figure 3.6

Figure 3.5: Temperature variation of (a) lattice parameters a and c for YMnO$_3$, (b) unit cell volume and solid line represent a fit to Debye - Grüneisen equation at high temperature above T$_N$, and then this extrapolated to the lowest temperature below T$_N$.

Figure 3.6: Temperature variation of (a) lattice parameters a and c for Y$_{0.8}$Ho$_{0.2}$MnO$_3$, (b) unit cell volume and solid line represent a fit to Debye - Grüneisen equation at high temperature above T$_N$, and then this extrapolated to the lowest temperature below T$_N$.

Grüneisen approximation and then extrapolated to lower temperature region [119, 211-212]. In the Grüneisen approximation, the temperature dependence of volume is given by, $V(T) = \gamma U(T)/B_0 + V_0$, where γ, B_0, and V_0 are the Grüneisen parameter, bulk modulus and volume, respectively, at T = 0K. In the Debye approximation, internal energy U(T) is given by,

$U(T)=9Nk_BT\left(\frac{T}{\theta_D}\right)^3\int_0^{\frac{\theta_D}{T}}\frac{x^3}{e^x-1}dx$, where $x=\frac{h\nu}{k_BT}$, N is the number of atoms in the unit cell, k_B is the Boltzmann's constant, and θ_D is the Debye temperature in the range 500K-600K. Figure 3.5 (b) shows the temperature variation of unit cell volume of $YMnO_3$ and the corresponding fit to the Debye - Grüneisen equation (Grüneisen approximation is considered by using Debye model). Similar behavior of these parameters has been observed in all the studied samples. The temperature variation of cell parameters and unit cell volume for $Y_{0.8}Ho_{0.2}MnO_3$ is shown in figure 3.6(a)-3.6(b) which is representative for all the doped studied samples. The unit cell volume contracts and below T_N the fit shows a clear deviation from the behavior expected from

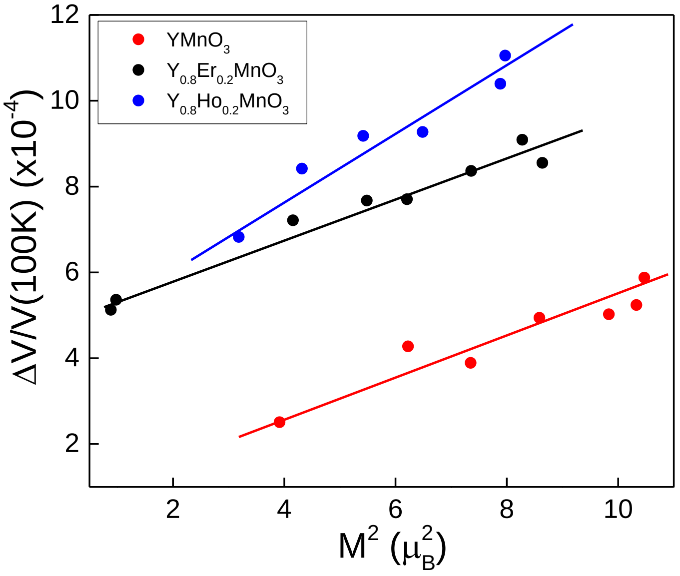

Figure 3.7: Linear plot of the ΔV versus the square of the ordered magnetic moments of Mn ions.

the temperature dependence of volume of a non magnetic compound described by the above equation. This anomalous contraction of unit cell volume below T_N is an evidence of magnetoelastic coupling in this sample. This large contraction in volume (ΔV) is found to be proportional to square of magnetic moment in the AFM phase (obtained from refinement of the neutron diffraction data and discussed later). The linear dependence of the lattice strain (ΔV) with square of the ordered moments, albeit with different slopes, below T_N is shown for three samples viz. $YMnO_3$, $Y_{0.8}Ho_{0.2}MnO_3$,$Y_{0.8}Er_{0.2}MnO_3$ in figure 3.7. Chatterji et al. have found similar dependence of the ΔV with order moments for $YMnO_3$ [161]. However, such quadratic relationship between lattice strain and order parameter is expected for single sublattice ferromagnet [213] and simple antiferromagnetic systems [214, 215]. The magnetoelastic coupling, in hexagonal manganites has been shown to arise due to displacement of Mn atoms [126, 150]. However, we do not observe this displacement of Mn (from (x~1/3 0 0) position) plausibly due to limited resolution of the instrument.

The tilting and buckling of MnO_5 bipyramid are important lattice distortion parameters, which are expected to change with doping at Y-site or Mn-site [216-218]. The tilting angle (α) is defined by the angle between the O1-O2 axis of the MnO_5 bipyramid and c axis and the buckling is representedby the angle β between the O3-O4-O4 plane and c axis [153]. The experimentally obtained values of the tilting and buckling angles for $YMnO_3$ are in close agreement with the theoretically obtained values [217]. Substitution of Y with Yb^{3+}, Er^{3+}, Ho^{3+}, and Tb^{3+} changes the tilting of MnO_5 bipyramids. However, the buckling remains constant for all the dopants as shown in figure 3.8(a) and 3.8(b) respectively. For smaller ion dopants, enhancement in tilting of the MnO_5 bipyramid has been observed while it reduces with larger dopant Tb^{3+}. It has been observed in earlier theoretical studies that the tilting and buckling angles of the MnO_5 bipyramid are correlated with the dopant size and valence state of the dopant, respectively [216]. A significant reduction in tilting of MnO_5 bipyramid has been observed for larger size dopants which is similar to our experimentally obtained results. However, Zhang et al., have shown that the incorporation of tetravalent dopants Zr^{4+} and Sn^{4+} into the Y2 (4b) site suppresses the tilting while presence of these dopants in the Y1 (2a) site enhances the tilting [218]. In our case, all the dopants are in 3+ valence state and no preferred site occupancy was observed and therefore, the dopants were evenly distributed between the two Y sites. Similar approach was also adopted in earlier A-site doped studies, in which the dopants with 3+ valence state were evenly distributed [165-168].

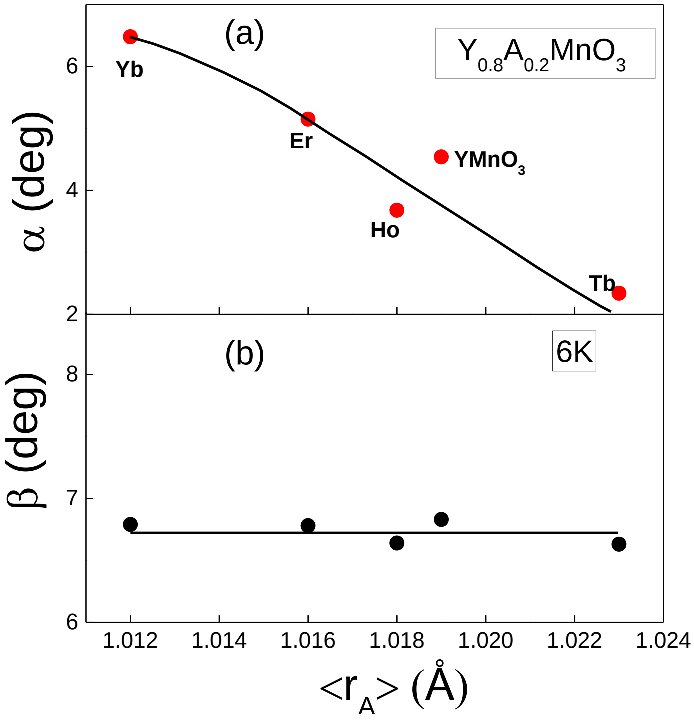

Figure 3.8: (a) Tilting angle for $Y_{0.8}R_{0.2}MnO_3$ (R= Yb, Er, Ho, Tb) samples at 6K. The line is a guide to the eye (b) Buckling angle of MnO_5 trigonal bypiramids for all doped samples at 6K.

3.1.1.2 Magnetic properties

Figure 3.9(a) shows the temperature dependence of magnetization M(T) under an applied magnetic field of 0.1T for all the samples. The magnetic measurements were performed under both zero-field-cooled (ZFC) and field-cooled (FC) conditions. No difference was observed

Table 3.1: Lattice parameters and selected bond lengths at 6K and 300K, Curie-Weiss fit parameters, geometrical frustration parameter (*f*), tilting angle (α), buckling angle (β) and correlation length (*ξ*) for $Y_{0.8x}R_{0.2}MnO_3$ (R= Yb, Er, Tb, Ho).

	$YMnO_3$		**$Y_{0.8}Yb_{0.2}MnO_3$**		**$Y_{0.8}Er_{0.2}MnO_3$**		**$Y_{0.8}Ho_{0.2}MnO_3$**		**$Y_{0.8}Tb_{0.2}MnO_3$**	
	6K	**300K**	**6K**	**300K**	**6K**	**300K**	**6K**	**300K**	**6K**	**300K**
a (Å)	6.1212(4)	6.1402(2)	6.0935 (4)	6.1094 (3)	6.1192 (4)	6.1356 (3)	6.1252 (4)	6.1418 (4)	6.1338 (5)	6.1488 (3)
c (Å)	11.4002 (9)	11.3901 (8)	11.3534 (14)	11.3473 (13)	11.3872 (9)	11.3829 (9)	11.3979 (12)	11.3935 (12)	11.4023 (16)	11.3926 (10)
V (Å^3)	369.93	371.90	365.08	366.79	369.26	371.10	370.33	372.20	371.52	373.02
Mn-O1 (Å)	1.90(2)	1.91(2)	1.90(6)	1.86(5)	1.87(2)	1.86(3)	1.85(3)	1.82(1)	1.85(5)	1.82(2)
Mn-O2 (Å)	1.86(2)	1.84(2)	1.83(6)	1.85 (5)	1.84(3)	1.86(3)	1.86(3)	1.91(2)	1.86(5)	1.89(2)
Mn-O3 (Å)	2.082(3)	2.09(3)	2.09(5)	2.10 (4)	2.126(19)	2.11(4)	2.12(6)	2.09(3)	2.13(3)	2.11(4)
Mn-O4 (Å)	2.039(3)	2.042(15)	2.03(3)	2.03 (2)	2.017(9)	2.030(18)	2.02(3)	2.045(7)	2.018(15)	2.04(2)

α	4.54	4.25	6.48	5.71	5.15	3.3	3.68	2	2.34	2.2
β	6.83	7.02	6.79	7.82	6.78	6.6	6.64	7.12	6.63	7.06
R_{wp} (%)	8.24	8.01	10.0	6.9	9.3	8.43	7.3	6.82	9.0	9.3
R_{exp} (%)	3.96	3.9	2.84	2.23	2.97	3.03	2.71	2.81	2.74	3.01
R_{mag} (%)	14.5	-	17	-	14.7	-	19	-	20.3	-
Θ_{CW} (K)	-421		-373		-84		-61		-70	
μ_{eff} (μ_B) (cal)	4.9		4.98		5.26		5.34		5.27	
μ_{eff} (μ_B) (obs)	4.98		5.80		5.94		6.3		6.04	
f (θ_{CW}/T_N)	5.6		4.9		1.2		0.9		1.07	
ξ (Å)	75K	100K	75K	100K	75K	100K	75K	100K	75K	100K
	33(3)	6(1)	8(1)	5(3)	23(2)	15(1)	19(1)	13(1)	8(1)	7(1)

between the ZFC and FC curves of parent $YMnO_3$ and doped compounds indicating absence of a ferromagnetic component. We note that there is no clear anomaly at the antiferromagnetic transition temperature in the magnetization of all the samples in contrast to the magnetization reported in the case of single crystal sample of $YMnO_3$ [153]. The significant increase in M observed at low temperatures for doped compounds as compared to $YMnO_3$ arises due to the relatively large paramagnetic contribution of the rare earth dopants. In an earlier reported magnetization measurement on single crystal of $Y_{0.8}Tb_{0.2}MnO_3$, two additional transitions at 23K and 3.9K were also observed in addition to the antiferromagnetic transition of Mn^{3+} at 71K [203]. In our case, however, we do not observe any indication of these transitions in the magnetization studies. In the case of Tb doped sample a weak signature of magnetic ordering is observed at ~10K (shown in the inset to figure 3.9(a)) for the Tb doped sample. We associate this to ordering of Tb moments as inferred from neutron diffraction studies (discussed later). The temperature variation of the inverse magnetic susceptibility is shown in figure 3.9(b). A large deviation from the Curie-Weiss behavior starting from $T>>T_N$, characteristic of frustration behavior, is observed only in the case $YMnO_3$ and Yb doped compound clearly indicating that the rare earth dopants with large magnetic moment at the A-site, suppresses the magnetic frustration behavior. The values of the effective Mn moments (μ_{eff}) and θ_{CW} were obtained from a fit of the paramagnetic susceptibility data to the Curie – Weiss (CW) law, given by $\chi = C/T-\theta_{CW}$, where C and θ_{CW} are the Curie constant and Curie-Weiss temperature,respectively. The values of θ_{CW}, and μ_{eff}, obtained for $YMnO_3$ are -421K, and $4.98\mu_B$, respectively. The values of μ_{eff} and θ_{CW} for all the studied $Y_{1-x}R_xMnO_3$ (R= Yb, Er,Tb, Ho; $x \leq 0.2$) samples are given in table 3.1. Theoretically, in all doped samples, effective moments have been calculated as $\mu_{eff}^{cal} = \sqrt{x^2\mu_R^2 + \mu_{Mn}^2}$, where x is the dopant concentration , μ_A and μ_{Mn} are the effective

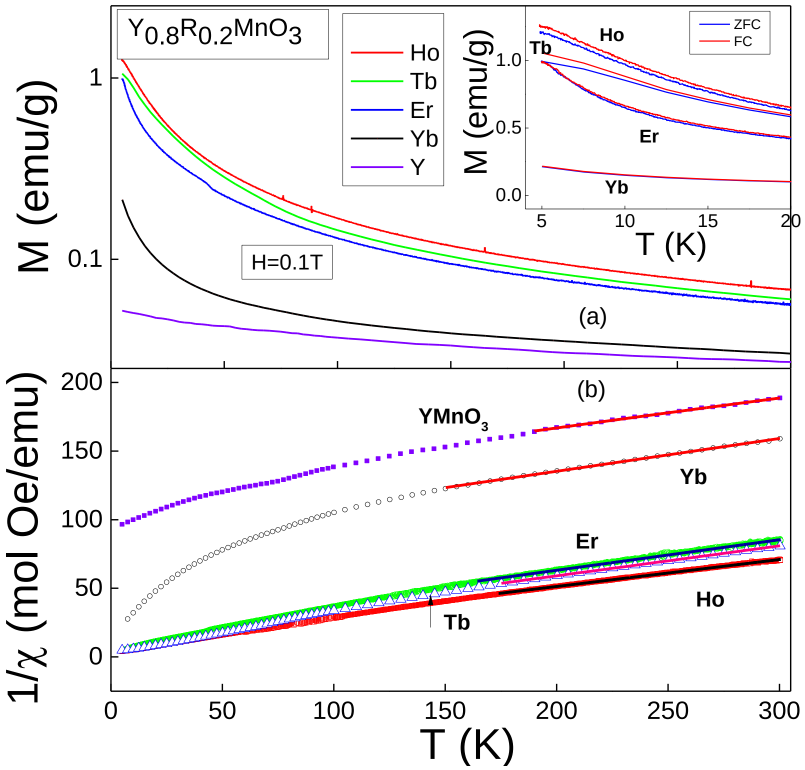

Figure 3.9: (a) The zero field-cooled (ZFC) magnetization (M) versus temperature (T) in field of H = 0.1T for $Y_{0.8}R_{0.2}MnO_3$ (R= Yb, Er, Ho, Tb). Inset shows the enlarged picture of low temperature part of ZFC and FC magnetization (M) versus temperature (T).(b) Shows the inverse of susceptibility as a function of temperature and Curie- Weiss fit (solid line).

magnetic moment of dopants and Mn^{3+} (4.9 μ_B), respectively. The extrapolated paramagnetic temperature (θ_{CW}) in $YMnO_3$ is higher than T_N. This difference in the values of θ_{CW} and T_N is an evidence of the magnetic frustration in these compounds. The frustration parameter ($f = |\theta_{CW}| / T_N$) is found to reduce with doping at the Y-site by a magnetic ion. The value of f is equal to 5.6 for $YMnO_3$ while it reduces to 4.9, 1.2, 0.9, and 1.07 for Yb, Er, Ho, and Tb respectively. For comparison, the value for frustration parameter for fully doped compounds $YbMnO_3$, $ErMnO_3$, and $HoMnO_3$ are 2.5, 1, and, 0.3, respectively [105,166,128]. This indicates that even 20% doping by the magnetic ion at the rare earth site lowers the frustration behaviour, and the decrease is proportional to the moment of the R-ion. In an earlier reported work, doping with Er at Y- site in $YMnO_3$ was found to reduce frustration parameter significantly [166] while with non magnetic Lu dopant the frustration parameter remained constant [167]. However, in Mn site doped compounds, the frustration parameter f changes only slightly with doping [118,219]. In our reported studies on $YMn_{1-x}M_xO_3$ (M = Ti, Fe, Ga; x = 0, 0.1) compounds, we have observed that, doping with Ti (d^0) leads to reduction in frustration behavior whereas Ga (d^{10}) enhances the frustration in the system [219]. It indicates that the magnetic coupling between the magnetic R ion and Mn moments relieves the frustration effects inherent to the quasi-two dimensional Mn moment ordering. This reduction in frustration parameter indicates that even a small amount of magnetic dopant (Yb, Er, Ho, and Tb) is detrimental to the geometrical frustration in this compound.

3.1.1.3 Magnetic Structure

In order to understand the effects of doping on the magnetic structures, neutron diffraction pattern have been recorded for all the studied samples at selected temperatures between 6K and 300K. Thermal evolution of neutron data for $YMnO_3$ is shown in figure 3.10, which shows that the magnetic reflections (100) (101) and (102) together with fundamental reflections gain in intensity with decrease in temperature below 75K. These reflections have been indexed using identical dimensions for the magnetic and chemical cell with propagationvector, $\vec{k}$ = 0 in *P-1* space group. The chemical and magnetic structure refinement has been carried out in $P6_3cm$ and *P-1* space group, respectively. The basis vectors for the propagation vector, $\vec{k}$ = 0 was determined using Sarah program [189]. In $P6_3cm$ space group, six different irreducible representations (IR) ($\Gamma_1 - \Gamma_6$) are possible corresponding to six possible orientations of the Mn spins. The four one-dimensional representations for $YMnO_3$ are shown in figure 3.11. In

YMnO$_3$, the magnetic structure can be described either by Γ_1 or Γ_3 IR, since for both these IRs nearly identical intensities are observed in neutron diffraction studies.

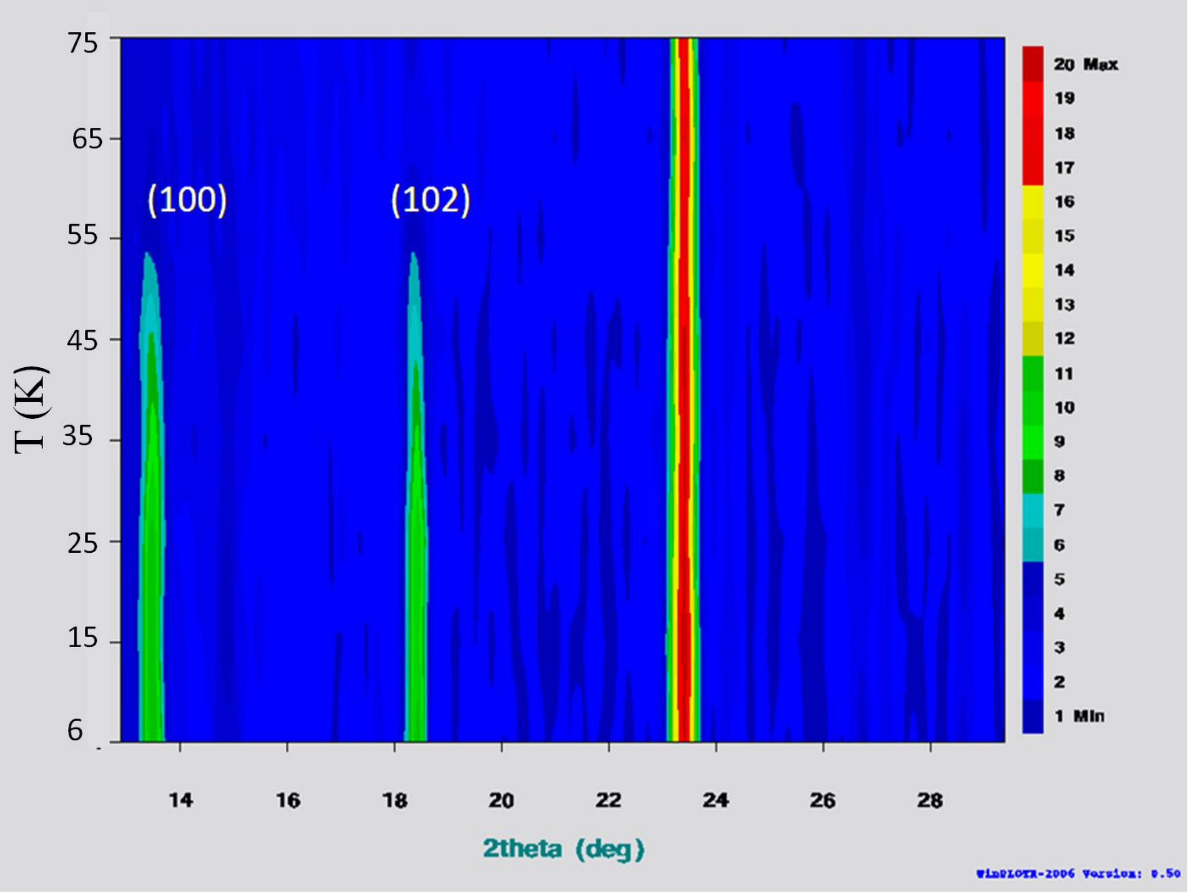

Figure 3.10: Evolution of theselected portion (12° ≤ 2θ ≤ 20°) of neutron diffraction patterns with temperature for YMnO$_3$ in the temperature range 6K - 75K.

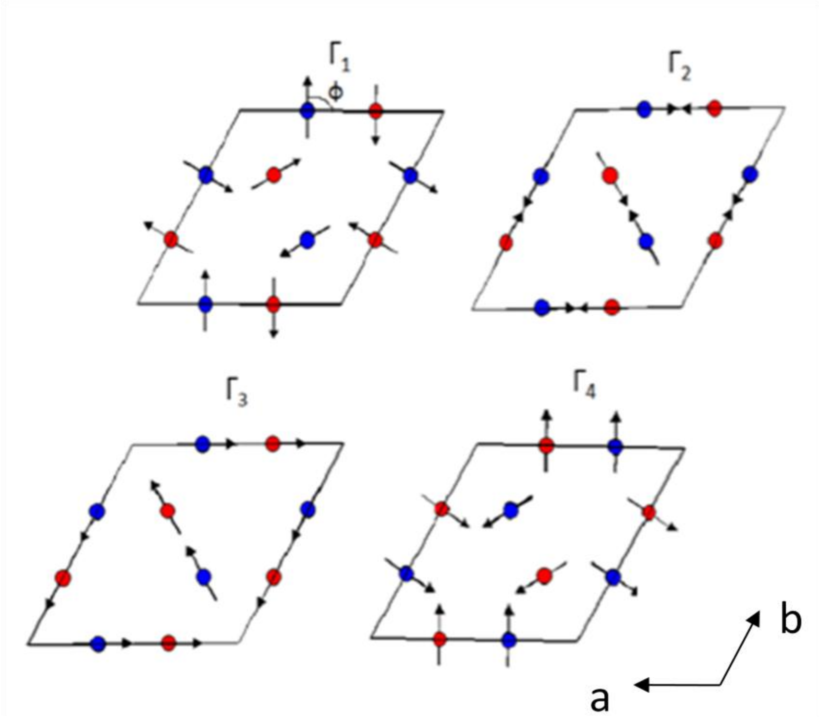

Figure 3.11: One-dimensional irreducible representations for the $YMnO_3$

In Γ_1 representation, the magnetic moment has a component in the xy plane and the spins are oriented perpendicular to the x-axis. The z=0 and z= ½ layers are antiferromagnetically coupled in Γ_1. In Γ_3 representation, the magnetic moment has a component in xy plane and a component along the z axis. The coupling is ferromagnetic for both, the component in xy plane and for the componentalong the z axis. In the theoretical studies it has been shown that Γ_3 IR is stabilized by the next – NN interactions and Γ_1 IR is not an appropriate description for the magnetic structure of $YMnO_3$ [117]. Therefore, we had analyzed our neutron diffraction data by considering Γ_3 IR. However, in earlier reported studies by Park et al [118] and Chatterji et al. [119] the ground state of $YMnO_3$ is best described by a linear combination of Γ_3 and Γ_4 in which Mn moments are aligned at 10.3° and 11.1° to the [100] plane. Figure 3.12 shows Rietveld refinement of neutron diffraction data for $YMnO_3$ at 300K and 6K. The value of the moment on Mn at 6K is $3.24\mu_B$ which is lower than the expected value $4\mu_B$ for Mn^{3+} (S = 2). The observed lower value of Mn moment as compared to the expected value is ascribed to the effect of frustration. Similar reduction in magnetic moment has also been observed on this compound in previous studies [113].

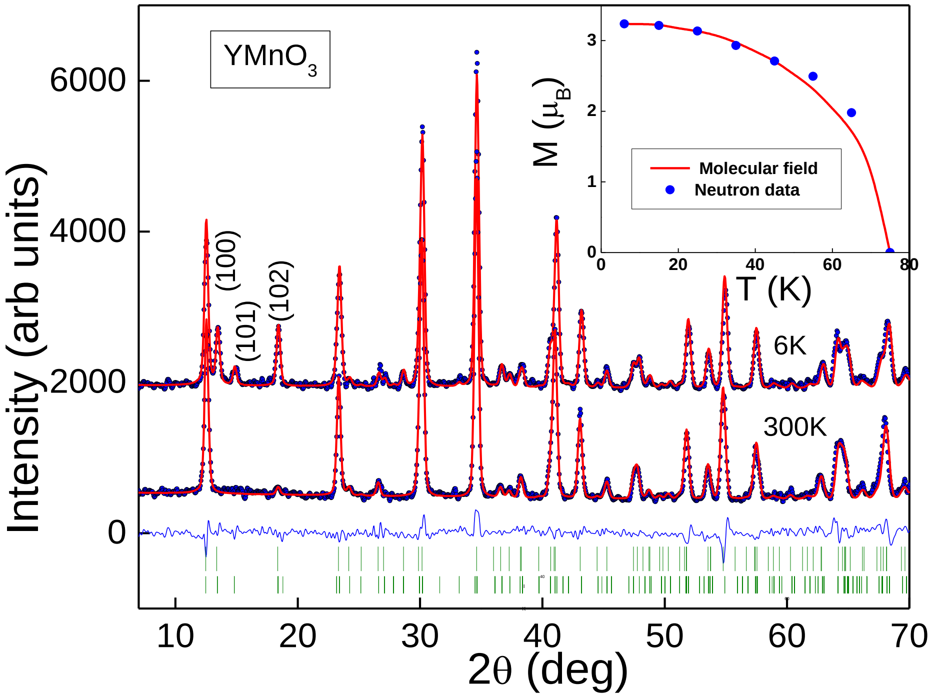

Figure 3.12: The observed (symbols) and calculated (line) neutron diffraction pattern for $YMnO_3$ compound at T = 6K and 300K. Lower solid line is the difference between observed and calculated pattern. The first row of tick marks indicates the position of nuclear Bragg peaks and second row indicate the position of magnetic Bragg peaks. Inset shows the variation of magnetic moment as a function of temperature.

have applied molecular field analysis to describe the thermal variation of Mn magnetic moment. Using the Brillouin description for reduced magnetization, $m_{Mn} = m_{sat}(T)B_2(x)$, where $x = \frac{mN\lambda(gS\mu_B)^2}{k_B T}$, m_{sat} = 3.24 μ_B, S = 2 for Mn^{3+}, T_N = 75K, and molecular field constant $\lambda = \frac{3k_B T_c}{g^2 S(S+1)\mu_B^2}$ = 13.9 T/μ_B [175], we obtained a good fit to the experimental data, as shown in inset of figure 3.12. Here we have used T_N as a parameter in the absence of neutron diffraction data at smaller intervals of temperature. The mean field approximation is found to closely describe the variation of the magnetic moment in this frustrated compound.

The diffraction data for doped samples at room temperature similarly show that the samples are isostructural and crystallize in the hexagonal structure confirming the x-ray diffraction results. Depending on the magnetic structure, superlattice reflections (100) or (101) and enhancement in the intensity of fundamental Bragg reflection (102) is observed, below 75K, indicating the antiferromagnetic nature of the samples. We find partially doping with the magnetic ions (Yb, Er, Ho, Tb) at Y-site changes the magnetic structure significantly. The (100) Bragg peak is purely a magnetic peak in $YMnO_3$ and is only present in Γ_3 (Γ_1) representation (completely absent for Γ_4 (Γ_2) representation), while the other magnetic peak (101) is seen in both Γ_3 and Γ_4 representations but is more pronounced in Γ_4 representation. The (100) reflection which is purely magnetic in $YMnO_3$, is considerably reduced in the Er doped samples but the (101) magnetic reflection is evident as shown in figure 3.13. The emergence of (101) peak in Er doped samples indicates the presence of Γ_4 magnetic symmetry. On doping with Yb^{3+} in $YMnO_3$, the (100) magnetic reflection is completely suppressed while the (101) magnetic reflection is distinctly observed as shown in figure 3.13. We observe that with doping of magnetic ions with smaller ionic radii, the ratio of the intensities of the two strong magnetic reflections are reversed and for the smallest ion (Yb), the (100) magnetic peak is almost suppressed. This change in the ratio of the intensities can be modeled by the change in the mixing ratio of Γ_3 and Γ_4 IR. The increase in the angle of inclination of the moments with doping is shown in the inset of figure 3.13. We do not observe evidence of magnetic ordering of rare earth dopants, except for the case of Tb. For Yb doping, this is because of the small amount of dopant concentration and the small value of ordered moment of Yb^{3+}. However, for Er ions, despite its larger moment, the ordering is not observed because the magnetic contribution for Er doped sample is submerged in the contribution from Mn. In these studied samples, the magnetic structure changes completely as we lower the ionic radii. However, the order moment for Yb (~2.9μ_B) and Er (~2.9μ_B) doped sample remains nearly the same. In pressure dependent studies of $YMnO_3$ [169], it has been observed that the magnetic structure changes continuously from Γ_1 (Γ_1 and Γ_3 are homometric configurations which cannot be distinguished by neutron diffraction) to $\Gamma_1 + \Gamma_2$ (Γ_2 and Γ_4 are also homometric configurations) with pressure, but a complete transition has not been observed up to the maximum achieved pressure, 5GPa at 10K. We have also

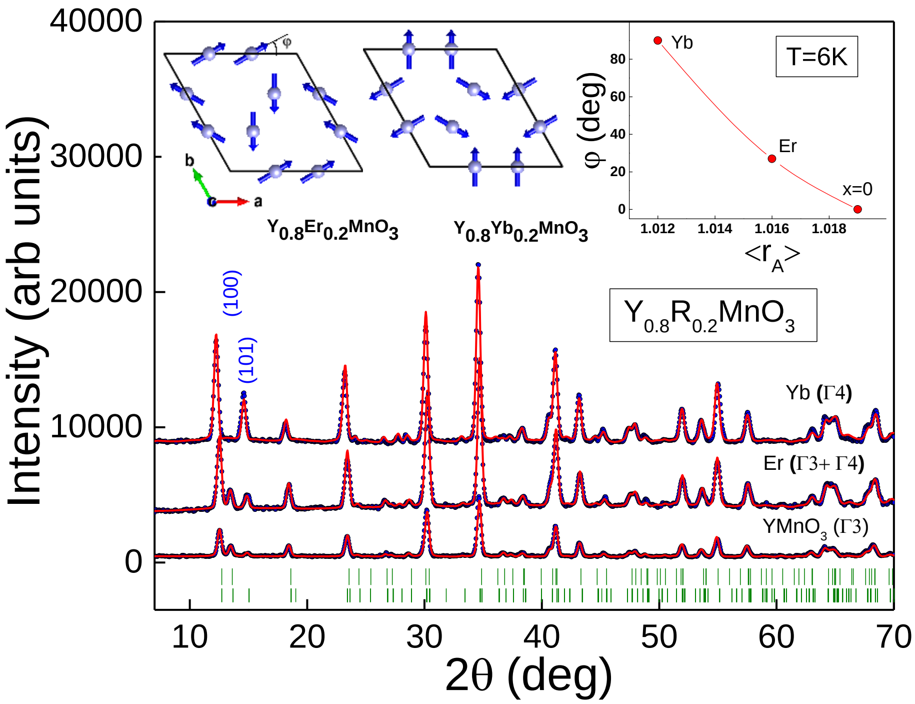

Figure 3.13: The observed (symbols) and calculated (line) neutron diffraction pattern for $YMnO_3$, $Y_{0.8}Er_{0.2}MnO_3$, and $Y_{0.8}Yb_{0.2}MnO_3$ compounds at T = 6K. The first row of tick marks indicates the position of nuclear Bragg peaks and second row indicate the position of magnetic Bragg peaks. Inset (a) shows the variation of tilting angle (φ) as a function of ionic radius and magnetic structures for $Y_{0.8}Er_{0.2}MnO_3$, and $Y_{0.8}Yb_{0.2}MnO_3$.

estimated the equivalent pressure for Yb and Er doped samples by using experimentally obtained compressibility values (k_a= 0.0073GPa^{-1}) [169].

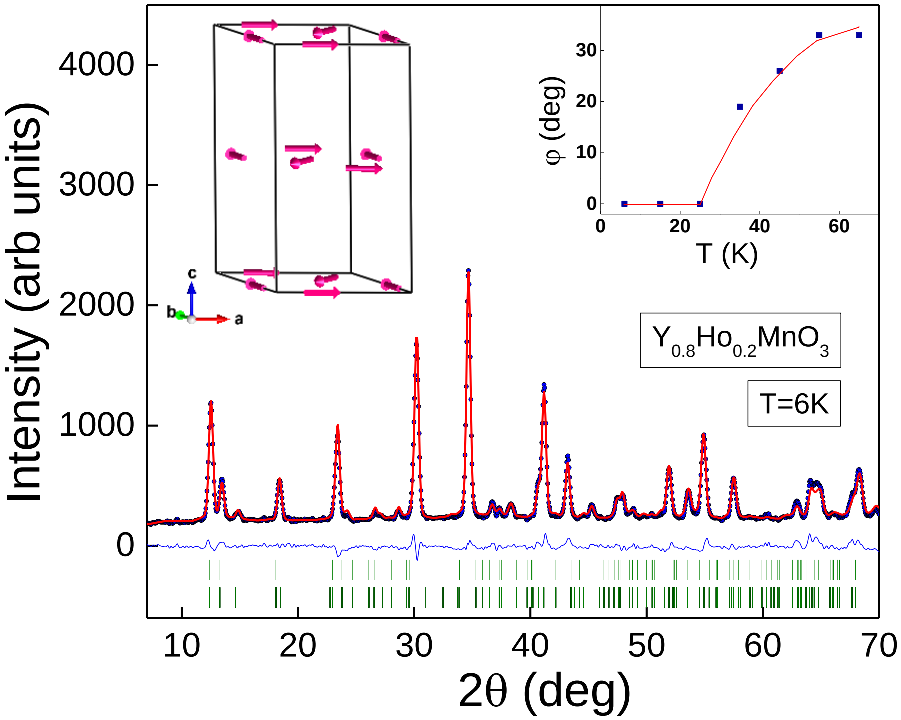

Figure 3.14: The observed (symbols) and calculated (line) neutron diffraction pattern for $Y_{0.8}Ho_{0.2}MnO_3$ compound at T = 6K. Lower solid line is the difference between observed and calculated pattern. The first row of tick marks indicates the position of nuclear Bragg peaks and second row indicate the position of magnetic Bragg peaks. Inset shows the variation of tilting angle (φ) as a function of temperature for $Y_{0.8}Ho_{0.2}MnO_3$, and magnetic structure of $Y_{0.8}Ho_{0.2}MnO_3$ at 6K.

The equivalent pressure for Yb and Er doped sample is 1.59GPa and 0.12GPa, respectively. Thus our study shows that by chemical substitution method, the magnetic structure completely transforms to Γ_4, with a pressure equivalence of ~ 1.6GPa. In comparison, a complete transition has not been observed up to 5GPa in external pressure studies. Therefore, the change in magnetic structure for Yb and Er doped samples cannot be attributed to chemical pressure effects alone. The change in the magnetic structure is a combined effect of R (4*f*)-Mn (3*d*) interactions and chemical pressure effect, which leads to significant changes in the magnetic ground state for these doped compounds. However, in Lu doped $YMnO_3$, the change in magnetic structure has been attributed to chemical pressure effects alone, since both Lu and Y are nonmagnetic [167].

The neutron diffraction pattern for $Y_{0.8}Ho_{0.2}MnO_3$ at 6K is explained by Γ_3 IR and the fit is shown in figure 3.14. With Ho doping at Y site, the magnetic structure is described by Γ_3 for 6K≤ T < 35K. But with increase in temperature (T>35K), the magnetic reflection (101) also starts to appear along with the (100) magnetic peak. In this structure appreciable enhancement in the (101) reflection is an indication of $\Gamma_{2,4}$IR. Therefore, we have modeled the magnetic structure of $Y_{0.8}Ho_{0.2}MnO_3$ at 35K by Γ_3 as well as by mixed Γ_3+ Γ_4 IRs and found that the R_{mag} improves appreciably from Γ_3 (R_{mag} ~28%) to Γ_3+ Γ_4 (R_{mag} ~24%). This indicates that the magnetic structure is best described by mixed IR at T > 35K in this sample. The moment on Mn is inclined at an angle with the a-axis in this case. Therefore, for T>35K, a model with mixed Γ_3 and Γ_4 IR is found to describe the data. A continuous change in intensity of (101) magnetic peak is observed with increase in temperature above 35K, which corresponds to change in the mixing ratio of Γ_4 and Γ_3 IR. The temperature variation of the inclination angle of the moments for $Y_{0.8}Ho_{0.2}MnO_3$ is shown in the inset of figure 3.14. A continuous rather than an abrupt spin reorientation as a function of temperature is observed in this case. The magnetic structure of $Y_{0.8}Ho_{0.2}MnO_3$ at low temperatures (6K≤ T < 35K) is similar to $HoMnO_3$. However, the spin reorientation behavior as a function of temperature is quite different in both these samples. Non-linear optical spectroscopy, neutron scattering experiments, dielectric and specific heat measurements have previously shown the presence of sharp spin reorientation behavior in $HoMnO_3$, in which the magnetic symmetry changes from Γ_3 to Γ_4 IR, while going from low to high temperature (T_{SR}~38K) [108-110]. We have not observed any ordered moments on Ho in $Y_{0.8}Ho_{0.2}MnO_3$ down to 6K. But the change in magnetic structure from Γ_3 + Γ_4 to Γ_3 IR below

35K and reduction in frustration parameter (f) indicates the presence of Ho-Mn interactions in this sample.

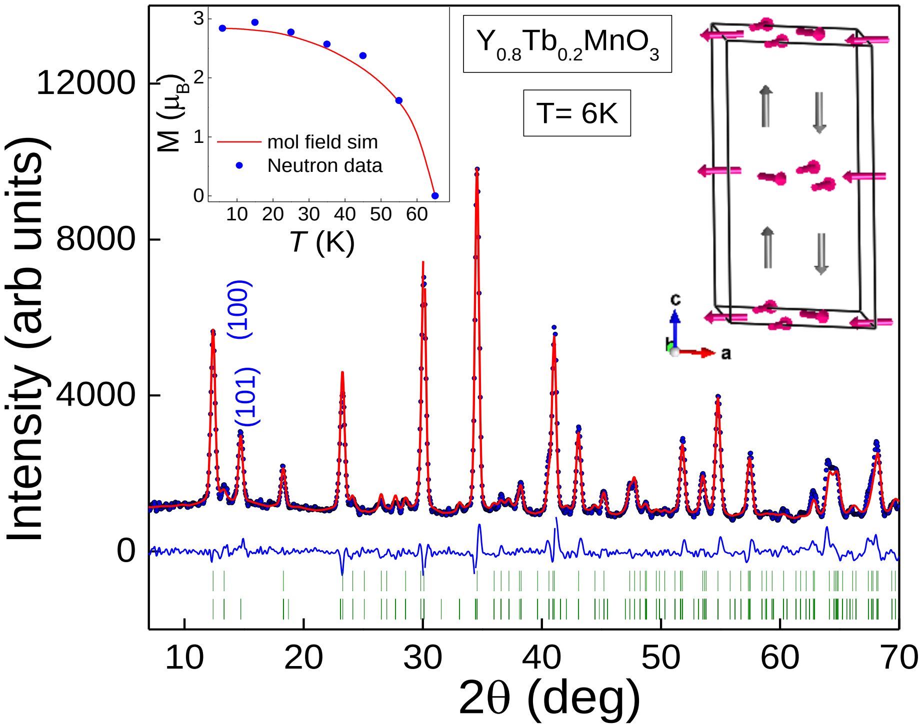

Figure 3.15: The observed (symbols) and calculated (line) neutron diffraction pattern for $Y_{0.8}Tb_{0.2}MnO_3$ compound at T = 6K. Lower solid line is the difference between observed and calculated pattern. The first row of tick marks indicates the position of nuclear Bragg peaks and second row indicate the position of magnetic Bragg peaks. Inset shows the variation of magnetic moment as a function of temperature and magnetic structure at 6K.

The neutron diffraction pattern for $Y_{0.8}Tb_{0.2}MnO_3$ at 6K is shown in figure 3.15. The presence of (101) magnetic reflection indicates the Γ_4 magnetic symmetry of Mn^{3+} ions. But Γ_4 IR does not allow contribution of Mn^{3+} to the (100) peak, which is weakly present in 6K data. With increase in temperature beyond 6K, the (100) magnetic reflection completely disappears. Therefore, the presence of magnetic reflection (100) is attributed to the magnetic ordering of Tb^{3+} ions similar to that observed in $YbMnO_3$ [105]. For magnetic R^{3+} ions, symmetry analysis yields six different irreducible representations. The four one-dimensional representations Γ_1 to Γ_4

correspond to R^{3+} moments aligned parallel/antiparallel to the c axis, and the two dimensional representations Γ_5 and Γ_6 represent magnetic states with R^{3+} moments in the ab plane. Since the IRs Γ_1^R and Γ_3^R do not contribute to the magnetic reflection (100), so, any contribution to this peak has to be attributed to Γ_2^R or Γ_4^R IRs. However, for $Y_{0.8}Tb_{0.2}MnO_3$ the magnetic Mn symmetry Γ_4 IR allows the Γ_4^R alone, in which the intraplane Tb(4b) coupling is AF while the interplane coupling is ferromagnetic. Therefore, the Tb (4b) order must be of Γ_4 type and Γ_2 is discarded. We thus conclude that the magnetic symmetry for $Y_{0.8}Tb_{0.2}MnO_3$ at 6K is $\Gamma_4^{Tb,Mn}$, with order moment for Mn^{3+} is ~2.84 μ_B and for Tb^{3+} is ~1.15 μ_B. With increase in temperature, (100) magnetic peak is completely suppressed, therefore, the magnetic structure for 6K< T ≤ 65K is described by Γ_4 IR without any Tb moment. The change in magnetic structure in Tb doped compound is attributed to the combined effects of the R-Mn interactions and ionic size effects. In earlier magnetization measurement on the single crystal of $Y_{0.8}Tb_{0.2}MnO_3$, spin reorientation behavior similar to $HoMnO_3$ has been suggested. But no such behavior has been seen in our neutron diffraction measurement. The thermal evolution of magnetic moments for $Y_{0.8}Tb_{0.2}MnO_3$ is shown in inset of figure 3.15. We have applied molecular field analysis to describe the thermal variation of Mn magnetic moment. Using the Brillouin description for reduced magnetization $m_{Mn} = m_{sat}(T)B_2(x)$, where $x = \frac{mN\lambda(gS\mu_B)^2}{k_B T}$, $m_{sat} = 2.84\mu_B$, S = 2 for Mn^{3+}, T_N = 65K, and molecular field constant $\lambda = \frac{3k_B T_c}{g^2 S(S+1)\mu_B^2}$ = 12T/μ_B [175], we obtained a good fit to the experimental data, as shown in inset of figure 3.15. This is true for all doped samples studied here. Here we have used T_N as a parameter in the absence of neutron diffraction data at smaller intervals of temperature. The mean field approximation is found to describe well the magnetism in this frustrated compound. The magnetic structure at 6K for both our sample and $YbMnO_3$ are similar. However, in the case of $YbMnO_3$ the moment on Yb appear to persist up to ~40K as against in our case where the T_N^{Tb} appears to be <10K. The absence of the weak (100) reflection at T >6K might be due to the limitations imposed by the instrument as a result of which we are possibly unable to detect it. The similarity of the magnetic structures at 6K between $YbMnO_3$ and Tb doped sample suggests that the mechanism governing the interactions between R and Mn in both the samples could be the same.

Through magnetic ions doping, we find that the magnetic ground state evolve from a frustrated state to one with less frustration and magnetic structure different from that of pure $YMnO_3$. In this study as well as in earlier studies on doped hexagonal manganites it has been observed that the transition between irreducible representations occurs by in phase (moments in adjacent Mn layers rotates with equal direction) or anti phase rotations (Mn moments in adjacent layers rotates with opposite direction).

3.1.1.4 Short range correlations

Hexagonal manganites are geometrically frustrated systems with the 2D network of Mn moments, and the evidence of this frustration can also be seen in the neutron diffraction data around magnetic transition temperature. In addition to the magnetic Bragg peaks, diffuse scattering on the (100) reflection are observed indicating short range magnetic ordering. Figure 3.16(a) and 3.16(b) shows the magnetic diffuse part obtained at 75K and 100K, respectively. The nature of diffuse part is same for the studied doped samples for these two temperatures while it is different for $YMnO_3$, as shown in figure 3.16(a) and 3.16(b). The diffuse part for $YMnO_3$ at 75K is asymmetric, which rises sharply at low angles and fall off slowly towards the high scattering angle. This asymmetric peak shape is the characteristic of the 2D short-range order.

The signature of diffuse scattering is completely absent in the room temperature diffraction data and is pronounced around the magnetic transition temperature which further reduces on lowering of temperature. We observe that the strong diffuse scattering appears for all the studied samples. The diffuse component for these samples has been obtained by subtracting the calculated diffraction pattern assuming a flat background, and this diffuse part is fitted to Warren function valid for a 2D structure [220].

$$I_{hk} \propto \left|F_m\left(Q\right)\right|^2 / \sin\theta \times \int_0^{\pi/2} \exp\left(\frac{-4\pi\xi^2}{\lambda^2}(\sin\theta\cos\phi - \sin\theta_{hk})^2\right) d\phi \ ,$$

where, $F_M\ (Q)$ is the magnetic structure factor, ξ correlation length of the magnetic ions, λ is the wavelength of neutrons, and θ_{hk} is the angular position of the magnetic reflection. Similar signature of diffuse scattering has been also observed in other geometrically frustrated hexagonal manganites indicating the presence of short range spatial correlations. The estimated spin-spin correlation length (ξ) varies with doping. For $YMnO_3$ it is 33Å which reduces to 23Å, 19Å, 8Å and 7Å for Er, Ho, Yb, and Tb doped samples, respectively at 75K. The correlation lengths obtained at 100K are given in table 3.1. In earlier reports the correlation length for the parent $YMnO_3$ varied from 12Å to 22Å. It is also noticeable that the intensity of the diffuse scattering becomes gradually weakened with doping of magnetic ions at the A-site. Similar suppression of diffuse scattering with increase in magnetic ion concentration has been observed in $Y_{1-x}Er_xMnO_3$ samples [166]. However, J. Park et al. have reported a very small change in correlation length with non magnetic Lu doping [168]. The short range ordering in hexagonal manganites have been attributed to geometrical frustration effects. The dynamical nature of these correlations has been brought out in the studies on YMnO3 [165] and InMnO3 [221]. We find that partially substituting with a magnetic ion suppresses the frustration (f) and increases the correlation length

ξ in these compounds in the paramagnetic phase at 100K (Table 3.1). It is observed that compounds with large f have low ξ and vice versa. This brings out the role of frustration and possibly R-Mn interactions on the short range order in these compounds.

To further study the short range correlation in these doped $Y_{1-x}R_xMnO_3$ (R= Yb, Er, Tb, Ho) samples, we have Fourier transformed the diffuse part of the magnetic neutron diffraction data. The radial correlation function, which we obtained after Fourier transformation, is expressed as,

$$g(r) = \int_{Q_1}^{Q_h} I_{mag}(Q)\, f(Q)^{-2} Q \sin(Qr)\, dQ,$$

where, $Q(=4\pi\sin\theta/\lambda)$ is the scattering vector, $I_{mag}(Q)$ is the magnetic scattering intensity, and $f(Q)$ is the magnetic scattering form factor. This gives us the antiferromagnetic and ferromagnetic correlations as a function of distance, *r*. Assuming an isotropic interactions in the system, *g(r)* is related to the spin-spin correlation function by the following expression [222]

$$g(r) = \frac{1}{S(S+1)} \sum_{r'} \langle S_0 . S_{r'} \rangle . \delta\left(|r| - |r'|\right).$$

This expression is a sum of spin-spin correlation function at distance *r*. Figure 3.17 shows the variation in *g(r)* for $Y_{1-x}R_xMnO_3$ (R= Yb, Er, Tb, Ho; x =0, 0.2) series. The arrows in the figure

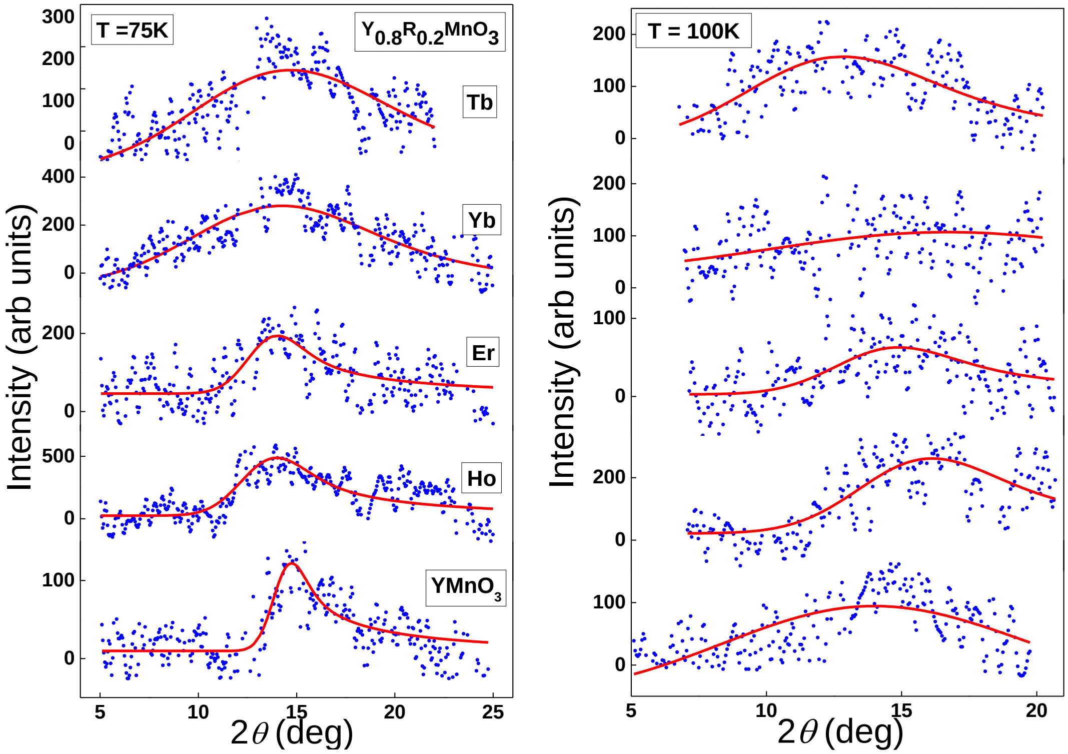

Figure 3.16: The magnetic diffusing scattering for $Y_{0.8}R_{0.2}MnO_3$ (R= Yb, Er, Ho, Tb) and $YMnO_3$, at (a) 75K, (b) 100K. The solid line corresponds to the 2D Warren function fitting results.

indicate the first sixnearest-neighbor bond distances for Mn-Mn pairs. The negative value of *g(r)* for nearest-neighbour Mn-Mn pairs and positive values for next-nearest neighbour Mn-Mn pairs indicate the existence of antiferromagnetic and ferromagnetic magnetic correlations, respectively. It is apparent from the figure that substitution of magnetic ions leads to significant change in the short-range magnetic interactions with nearest neighbours. For third coordination shell, the magnetic correlations changes from antiferromagnetic for $YMnO_3$ to ferromagnetic for A-site doped compounds. Thus, the partial substitution of Y by magnetic ions, not only change the magnetic structure but also effect the short range magnetic correlations, along with the frustrated behavior of the compounds [223].

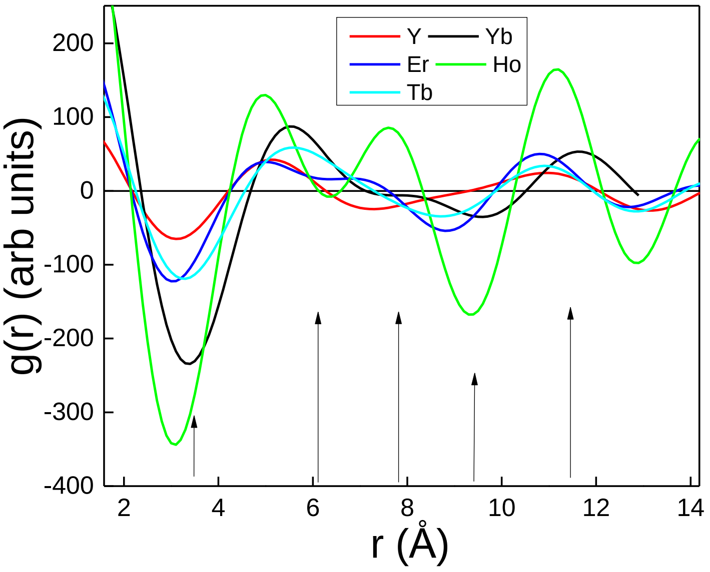

Figure 3.17: Radial correlation function g(r) for $Y_{0.8}R_{0.2}MnO_3$ (R= Yb, Er, Ho, Tb) and $YMnO_3$ at 75K. Arrows indicate the nearest-neighbour bond distances for Mn sublattice.

3.2 Effect of B-site doping on the magnetic properties of $YMnO_3$

3.2. 1 Effect of Mn site substitution on the structural and magnetic properties of $YMn_{1-x}M_xO_3$ (M=Ti, Fe, Ga; x=0, 0.1).

We have studied the effects of Ti^{4+} (d^0), Fe^{3+} (d^5) and Ga^{3+} (d^{10}), doping on the structural and magnetic structure of $YMnO_3$. The dopants have been chosen to study the effect of interaction of the filled and unfilled orbital on the magnetic structure. We find that these three dopants affect the magnetic structure of this compound in contrasting manner. The compositions were limited to 10% doping to remain in the isostructural phase.

3.2.1.1 Crystal structure

The x-ray diffraction patterns and the Rietveld refinement of the studied polycrystalline samples $YMn_{1-x}M_xO_3$ (M = Ti, Fe, Ga; x = 0, 0.1) are shown in figure 3.18. It indicates that all the samples are isostructural and crystallize in hexagonal phase (space group $P6_3cm$). The neutron diffraction data at room temperature confirms the x-ray diffraction result and no structural transition are observed on lowering of temperature [113]. With Fe doping both the lattice parameters a and c increases and the values obtained are similar to the values reported by Zaghrioui et al. [207] while for Ga and Ti doping a increases and c decreases. In the case of Ga doping our result of lower c/a is different from the behavior reported in single crystal studies of $YMn_{1-x}Ga_xO_3$ [129,173], where Ga doping is found to increase the ratio of c/a. The variation of the cell parameters in Ti doped sample are similar to those reported previously where the decrease of c parameter has been ascribed to decrease of the tilting of MnO_5 bypiramids [208].

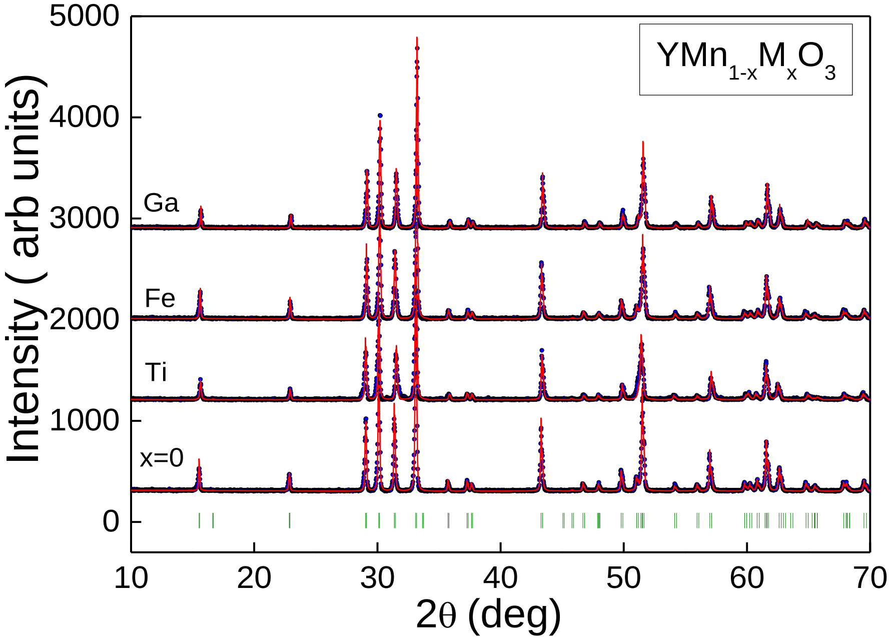

Figure 3.18: Room temperaturepowder X- ray diffraction patterns of $YMn_{1-x}M_xO_3$ (M = Ti, Fe, Ga; x = 0, 0.1). Open circles are observed data points. The solid line represents the Rietveld refinement.

The increase in the cell parameters of Fe doped sample is understood as follows. In trigonal bypiramidal geometry, the d- levels are split into two doublets (d_{xz}, d_{yz}, $d_{x^2-y^2}$ and d_{xy}) and one singlet (d_{z^2}). The four d- electrons of Mn^{3+} occupy lowest lying doublets and no electron is present in d_z^2 orbital. Whereas, Fe^{3+} doping introduces one more electron in the d_z^2 orbital resulting in elongation of the c –axis as argued previously in Fe-doped samples [206,224]. However, it is difficult to explain the behavior of the lattice parameter a in view of the similar ionic radii of Mn^{3+} and Fe^{3+} in five fold coordination (0.58Å). The results of refinement of neutron diffraction data taken at room and low temperature for all the studied compounds are summarized in table 3.2. The apical Mn-O1 and Mn-O2 bond lengths are smaller than the planar Mn-O3 and Mn-O4 bond lengths for all the studied samples and this is consistent with the previous studies [96, 113].

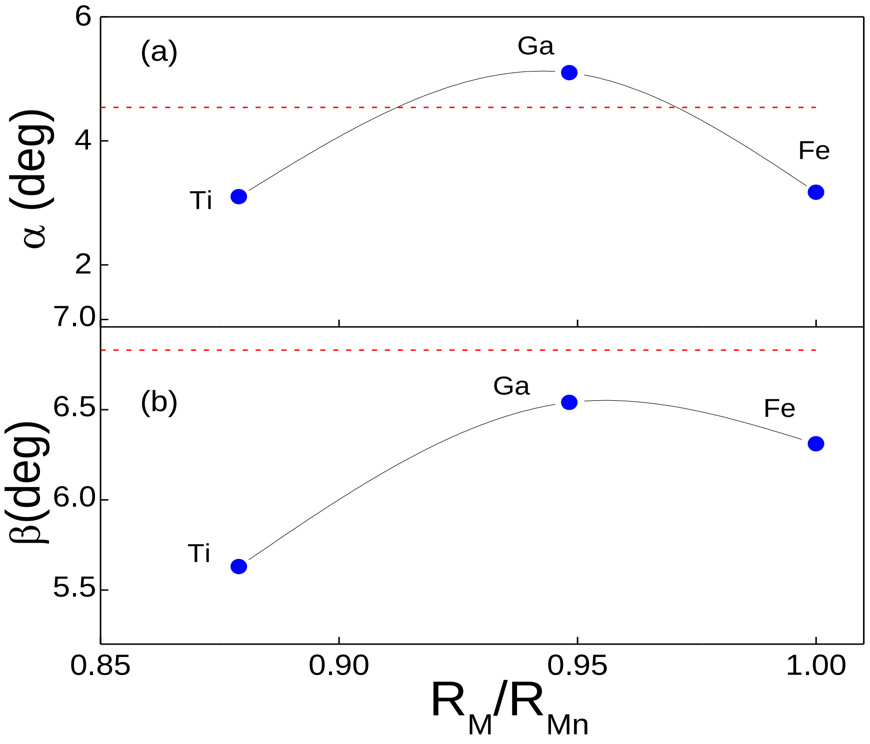

Figure 3.19: Tilting angle for all doped sample at 6K. The dashed line denotes the tilting of YMnO$_3$ (4.5°). (b) Buckling angle of MnO$_5$ trigonal bypiramids for all doped samples at 6K. The dashed line denotes the buckling in YMnO$_3$.

The tilting angle (α) is defined by the angle between the O1-O2 axis of the MnO_5 bipyramid and c axis and the buckling is represented by the angle β between the O3-O4-O4 plane and c axis [216]. Substitution of Mn with Ti^{4+} (d^0), Fe^{3+} (d^5)and Ga^{3+} (d^{10}) changes the tilting and buckling of MnO_5 trigonal bipyramids as shown in figure 3.19(a) and 3.19(b). Substituting Mn with Ti and Fe reduces the tilting and buckling whereas Ga increases the tilting of MnO_5 trigonal bipyramids which is in good accordance with the theoretically calculated values [217]. We find that decrease in buckling, as in the case of Ti doped sample, leads to lowering of frustration.

3.2.1.2 Magnetic properties

The temperature dependence of magnetization M(T) under an applied magnetic field of 0.1T for all the samples is shown in figure 3.20(a). The magnetization increases on lowering of temperature and a distinct anomaly at the transition temperature is observed only in the case of Fe. Similar absence of anomaly at the T_N has been reported previously in $YMnO_3$ [113]. In the case of Ti doped sample the enhancement of M at low temperatures is higher as compared to other samples. We attribute this behavior to the small out of plane ferromagnetic component in the Γ_2 magnetic structure observed in this sample (discussed later). The inverse magnetic susceptibility versus temperature curve is shown in figure 3.20(b). It exhibits a large curvature extending to high temperatures and therefore, we found that it could not be fitted to the Curie – Weiss law. Evidence of short range ordering in the proximity of the T_N has been reported in the parent compound [165-167] and explains the departure from CW behavior in the vicinity of T_N. The doping is found to extend the temperature range above T_N where the short range ordering persists. Diffuse scattering studies in half doped manganites shows evidence of magnetic short range ordering far above their respective magnetic ordering temperatures [165]. We found abetter description of the paramagnetic susceptibility data by fitting the magnetic susceptibility tothe modified Curie – Weiss law, given by $\chi = \chi_0 + C/T\text{-}\theta_{CW}$, where χ_0, C and θ_{CW} are the temperature independent susceptibility, Curie constant and Curie-Weiss temperature, respectively. The values of χ_0, the effective Mn moments (μ_{eff}) and the paramagnetic temperature (θ_{CW}) could be obtained from this fit and is summarized in Table 3.2. The magnetic susceptibility follows a modified Curie – Weiss behavior above 190K for $YMnO_3$, above 175K for $YMn_{0.9}Ti_{0.1}O_3$, above 185K for $YMn_{0.9}Fe_{0.1}O_3$ and above 225K for $YMn_{0.9}Ga_{0.1}O_3$ as shown in figure 3.20(b). The values of θ_{CW} and μ_{eff} obtained for $YMnO_3$ are -421K and $4.98\mu_B$, respectively. With doping of Ti a pronounced reduction in θ_{CW} (-119K) is observed while in the case of Fe and Ga the reduction is marginal (Table 3.2). The effective paramagnetic moment is $4.30\mu_B$, $4.45\mu_B$ and $4.10\mu_B$ for $YMn_{0.9}Ti_{0.1}O_3$, $YMn_{0.9}Fe_{0.1}O_3$ and $YMn_{0.9}Ga_{0.1}O_3$, respectively. Theoretically, μ_{eff} is calculated as, $\mu_{eff}^{cal} = \sqrt{x\mu_{eff}^2(M) + (1-x)\mu_{eff}^2(Mn^{3+})}$, where μ_{eff} for Mn^{3+} (S = 2) is $4.89\mu_B$. According to this equation, μ_{eff}^{cal} values for Ti, Fe and Ga doped compounds are $4.65\mu_B$, $5.0\mu_B$ and $4.65\mu_B$ respectively. With 10% doping of Ti, Fe and Ga at Mn site of $YMnO_3$, Curie - Weiss temperature as well as the effective moment reduces. Substitution of Ti^{4+} at Mn^{3+} site can lead to the formation of Mn^{2+} by introduction of electrons in the system, assuming stoichiometric oxygen. But in magnetization measurement we observe reduction in effective moment value which is inconsistent with the presence of Mn^{2+} in this sample. This suggests that there is a change in the Oxygen stoichiometry in the sample. Previous studies of magnetic susceptibility on samples prepared under reducing atmosphere have shown that at a given temperature the paramagnetic susceptibility decreases for the reduced sample which again suggests the absence of Mn^{2+} [208]. So doping of Ti^{4+} at Mn site changes the stoichiometry

Table 3.2: Results of Rietveld refinement of neutron diffraction pattern at 6K and 300K, Curie – Weiss fit parameters, geometrical frustration parameter, and transition temperature for $YMn_{1-x}M_xO_3$ (M = Ti, Fe, Ga; x = 0, 0.1).

	$YMnO_3$		**$YMn_{0.9}Ti_{0.1}O_3$**		**$YMn_{0.9}Fe_{0.1}O_3$**		**$YMn_{0.9}Ga_{0.1}O_3$**	
	6K	**300K**	**6K**	**300K**	**6K**	**300K**	**6K**	**300K**
a (Å)	6.1212(4)	6.1402(2)	6.1412(4)	6.1579(3)	6.1359(4)	6.1510(4)	6.1378(4)	6.1549(4)
c (Å)	11.4002(9)	11.3901(8)	11.3695(8)	11.3605(8)	11.4289(9)	11.4117(17)	11.3597(14)	11.3560(12)
V (Å^3)	369.93	371.90	371.35	373.07	372.64	373.91	370.61	372.56
Mn-O1 (Å)	1.90(2)	1.91(2)	1.94(3)	1.87(7)	1.88(3)	1.79(5)	1.90(7)	1.87(5)
Mn-O2 (Å)	1.86(2)	1.84(2)	1.79(3)	1.87 (7)	1.82(3)	1.94(5)	1.81(7)	1.87(5)
Mn-O3 (Å)	2.082(3)	2.09(3)	2.12(3)	2.12 (7)	2.08(2)	1.98(5)	2.07(6)	2.11(6)
Mn-O4 (Å)	2.039(3)	2.042(15)	2.023(15)	2.03 (3)	2.043(16)	2.10(3)	2.05(3)	2.03(3)
Y1-O1(×3) (Å)	2.301(20)	2.28(2)	2.33(4)	2.26(6)	2.29(3)	2.41(4)	2.32(5)	2.28(2)
Y1-O2(×3) (Å)	2.286(12)	2.315(16)	2.29(2)	2.31(3)	2.33(2)	2.29(2)	2.31(4)	2.35(2)
Y1-O3 (Å)	2.30(4)	2.32(6)	2.25(7)	2.23(10)	2.39(7)	2.36(7)	2.36(10)	2.37(7)
Y2-O1(×3) (Å)	2.271(12)	2.263(13)	2.28(2)	2.28(3)	2.252(18)	2.25(3)	2.24(3)	2.25(2)
Y2-O2(×3) (Å)	2.276(17)	2.294(17)	2.28(2)	2.32(5)	2.33(3)	2.28(4)	2.30(5)	2.30(3)
Y2 - O4 (Å)	2.45(3)	2.46(3)	2.58(6)	2.56(10)	2.46(6)	2.48(6)	2.44(8)	2.49(6)
Mn-O3-Mn (°)	119.24(12)	119.1 (6)	119.4(6)	118(4)	119 (2)	119.3(10)	119(4)	119 (4)
Mn-O4-Mn (°)	118.51(11)	118.8(7)	119.2(6)	120.0(14)	119.1(6)	119.3(10)	118.5(11)	119.6(11)
θ (K)	- 421		-119		-334		-382	
μ_{eff} (μ_B)	4.98		4.30		4.45		4.10	

χ_0 (emu/mol Oe)	0.001	0.001	0.001	0.0004
$f=(\theta/T_N)$	5.6	2.2	5.6	6.9
T_N (K)	75	55	60	55

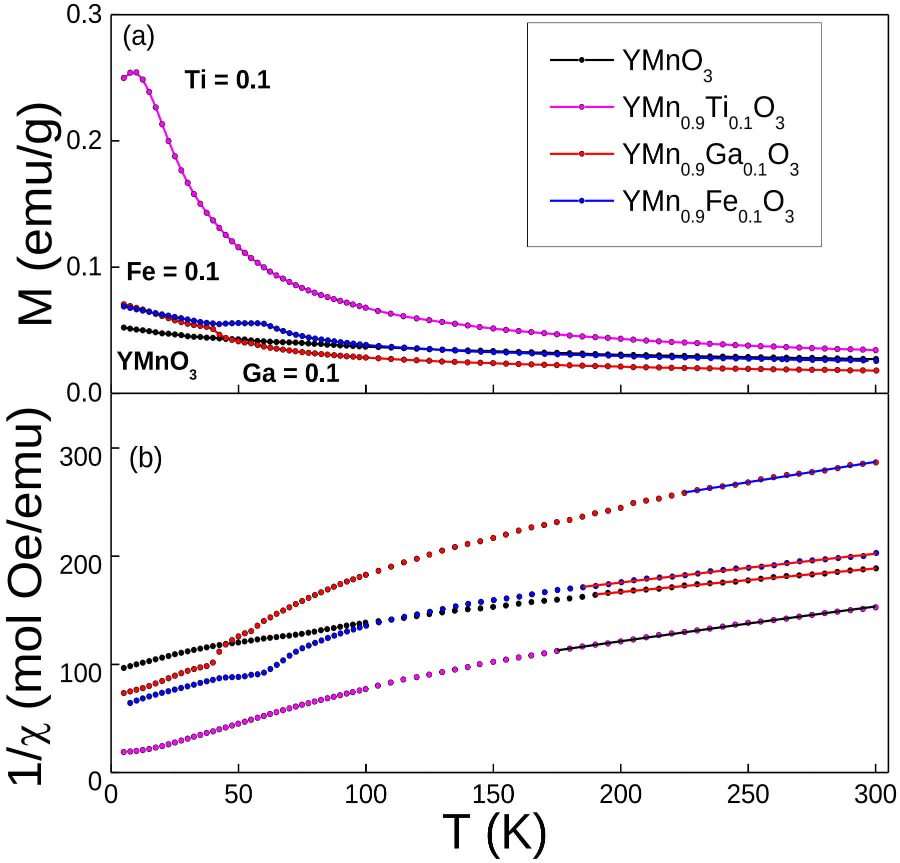

Figure 3.20: The zero field-cooled (ZFC) magnetization (M) versus temperature (T) in field of H = 0.1T for $YMn_{1-x}M_xO_3$ (M = Ti, Fe, Ga; x = 0, 0.1). (b) Shows the inverse of susceptibility as a function of temperature and modified Curie- Weiss fit (solid line).

of oxygen in these samples though, we believe, the change is too small to influence the magnetic structure of the compound. The magnetic structure of $YMnO_{3-\delta}$ ($\delta \sim 0.29$) has been found to be the same as that of $YMnO_3$ albeit, with a different tilt angle [108]. Hence, the oxygen non-stoichiometry does not appear to influence the spin structure, though an enhancement in the transition temperature has been observed in oxygen non- stoichiometric compound $YMnO_{3-\delta}$ [225]. The decrease of effective moment (μ_{eff}) in Fe doped sample is unexpected since Fe^{3+} has one more unpaired electron than Mn^{3+}. The decrease of μ_{eff} in this sample could be explained by the presence of Fe^{2+}. But Mössbauer spectroscopy excludes the presence of Fe^{2+} (discussed below). Therefore, this behavior is explained by considering a competition between ferromagnetic Fe-O-Mn interactions and antiferromagnetic Mn-O-Mn and Fe-O-Fe interactions [207]. The values of θ_{CW} and μ_{eff} for all these samples are given in table 3.2. Using these values of θ_{CW} we have estimated the exchange integral J = 3.0meV between the nearest Mn neighbors using the expression $\theta_{CW} = -z\, J\, S\, (S+1)/3$ [226, 165], where S = 2 for Mn^{3+}, z = 6 is the number of nearest neighbors and θ_{CW} is Curie - Weiss temperature. Doping at Mn site with Ti^{4+} (d^0), Fe^{3+} (d^5) and Ga^{3+} (d^{10}) reduces this exchange integral to 0.93meV, 2.29meV and 2.9meV, respectively.Since Curie – Weiss temperature (θ_{CW})is a measure of AFM coupling strength between Mn ions, the results suggest that doping with Ti suppress the AFM interaction. The extrapolated paramagnetic temperatures (θ_{CW}) in $YMn_{0.9}M_{0.1}O_3$ (M = Ga, Ti and Fe) are much higher than T_N. This difference in the values of θ_{CW} and T_N is an evidence of the magnetic frustration in these compounds. This is expressed by frustration parameter, $f = |\theta_{CW}| / T_N = 5.6$ for $YMnO_3$ while it becomes 2.2, 5.6 and 6.9 for $YMn_{0.9}Ti_{0.1}O_3$, $YMn_{0.9}Ga_{0.1}O_3$ and $YMn_{0.9}Fe_{0.1}O_3$, respectively. Among the three dopants a significant reduction in the frustration parameter is observed in the case of Ti, while it remains same for Fe and increases in the case of

Ga doped sample. Similar behavior has been observed previously in Ga doped $YMnO_3$ [173]. Reduction of frustration has been seen in other doped samples, e.g. on doping with non magnetic ions such as Ru, Al, and Zn at Mn site, frustration parameter reduces. Doping Er at Y- site is also found to reduce frustration in these systems [166].

3.2.1.3 Mössbauer spectrometry

The Mössbauer spectrum of Fe doped sample ($YMn_{0.9}Fe_{0.1}O_3$) was recorded at room temperature to confirm the oxidation state of Fe and is shown in figure 3.21. The spectrum is fitted with three symmetric doublets, indicative of three different chemical environments around Fe atom and all the Fe being paramagnetic. In this structure Mn occupies only one crystallographic site in the unit cell. The three different sites for Fe observed in Mössbauer studies arises due to the random distribution of Fe in lattice having different numbers of Mn^{3+} ion near neighbors. These three different chemical environments around Fe atom could be understood as follows. In this structure

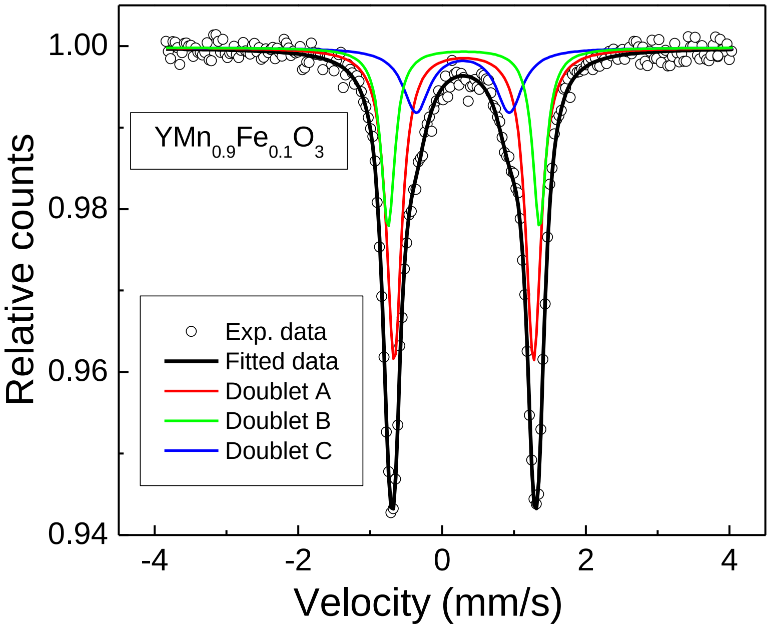

Figure 3.21: Room temperature Mössbauer spectrum of $YMn_{0.9}Fe_{0.1}O_3$.

Mn (or Fe) site has six in-plane nearest neighbors. The system consists of 10% Fe and the rest is Mn. So, the probability of having a Fe atom in the nearest neighbor site is 0.1 (10%) and the probability of Mn is 0.9 (90%). Thus for a given Fe ion, there is 53% chance of having all Mn atoms as nearest neighbors (no Fe atoms), 35% chance of having only one Fe atom (five Mn atoms) and 10% chance of having two Fe atoms. For more than two Fe atoms, probability reduces significantly. The relative area for each doublet is in agreement with the calculated probabilities. However, our results differ from the earlier reported Mössbauer study on the same composition where the Mössbauer data was fitted with two doublets and was ascribed to two different chemical environments around the Fe atom [207]. The hyperfine parameters i.e. isomer shift (δ), quadrupole splitting (ΔE_Q) and line widths (Γ) obtained from the fit are included in table 3.3. The value of isomer shift for all the three doublets is ~ 0.30 mm/s at room temperature and is in agreement with previously reported values for this compound [207]. These value corresponds to the presence of Fe^{3+} in high spin state (S = 5/2) [197]. Quadrupole splitting (ΔE_Q) arises due to interaction between electric quadrupole moment of the nucleus and surrounding electric field gradient and thus give relevant information about the charge symmetry around the nucleus. The large value of quadrupole splitting in this sample is thus attributed to the large distortion of Fe site.

Table 3.3: Mössbauer parameters at room temperature for $YMn_{0.9}Fe_{0.1}O_3$.

x	Iron Sites	^{a}Isomer shift (δ) mm/s	Quadrupole splitting (ΔE_Q) mm/s	Line width (Γ) mm/s	Relative Area R_A (%)
0.1	Doublet 1	0.303 ± 0.002	1.940 ± 0.004	0.256±0.012	53.55
	Doublet 2	0.303 ±0.004	2.109 ±0.008	0.23 ±0.00	27.55
	Doublet 3	0.289 ±0.014	1.295 ±0.028	0.446±0.038	18.90

3.2.1.4 Magnetic Structure

Neutron diffraction pattern has been recorded for all the samples at several temperatures below 300K. The neutron diffraction data for parent $YMnO_3$ has been described above. We have used the Sarah program [189] to carry out the representation analysis and obtain the basis vectors for each of these representations. Doping with Ti^{4+} (d^0), Fe^{3+} (d^5) and Ga^{3+} (d^{10}) at Mn site in $YMnO_3$ reduces T_N significantly. Figure 3.22(a) shows the evolution of integrated intensity of (100) magnetic reflection for parent sample, Ga and Fe doped samples as a function of temperature. The evolution of integrated intensity of (101) magnetic reflection for $YMn_{1-x}M_xO_3$ (M = Ti, Fe, Ga; x = 0, 0.1) is shown in figure 3.22(b). In comparison, doping with Al, Ru, Zn at Mn site is found to show a very small reduction in T_N [118]. This suggests that the present dopants strongly influence the Mn-Mn interactions.

On doping with Ti^{4+} in $YMnO_3$ at Mn site, T_N reduces to 55K. The (100) reflection which is predominately magnetic is absent in this sample but the (101) magnetic reflection is evident as shown in figure 3.23. The magnetic structure in this case could be fitted by both the irreducible representation Γ_2 and Γ_4. In Γ_2 representation, the magnetic moment has a component in xy plane and a component along the z axis. The coupling is antiferromagnetic for the component in xy plane and ferromagnetic for the component along the z axis. In Γ_4 representation the spins are in the xy plane and are oriented perpendicular to the a-axis. The z=0 and z=½ layers are ferromagnetically coupled in Γ_4. In this sample, M(T) shows a significant increase in M on lowering of temperature as compared to other samples in the series. We measured the field dependence of magnetization (M-H curves) at 5K for $YMnO_3$ and for $YMn_{0.9}Ti_{0.1}O_3$. For $YMnO_3$, the magnetization curve do not show any hysteresis phenomenon or saturation magnetization but for $YMn_{0.9}Ti_{0.1}O_3$, M(H) exhibits a hysteresis (shown in the inset to Figure

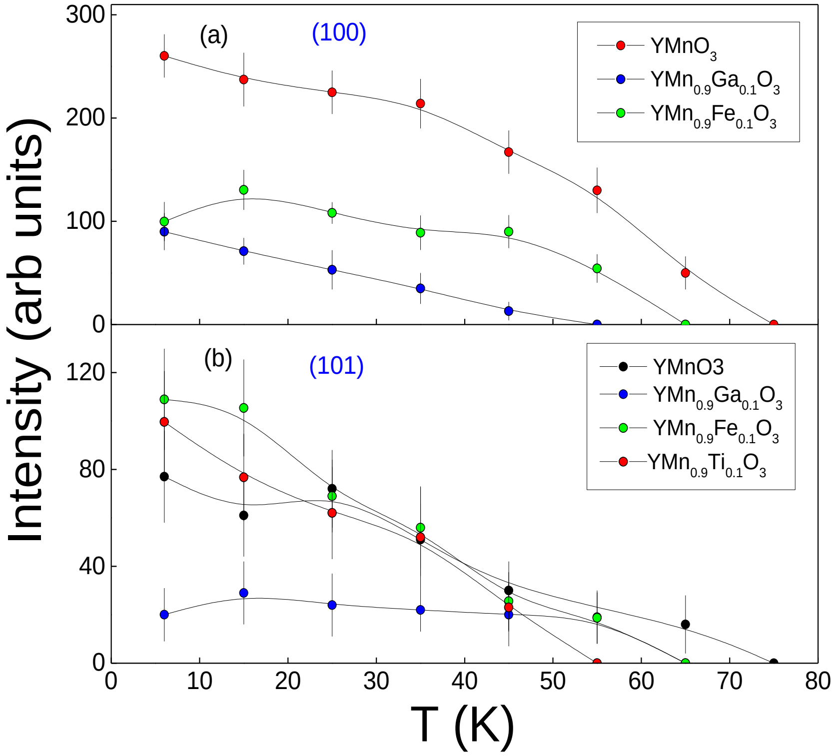

Figure 3.22: Integrated intensity of (100) magnetic reflection for YMn$_{1-x}$M$_x$O$_3$ (M = Ga, Fe; x= 0, 0.1) as a function of temperature. (b) Integrated intensity of (101) magnetic reflection for YMn$_{1-x}$M$_x$O$_3$ (M = Ti, Fe, Ga; x = 0, 0.1) as a function of temperature.

3.23). These two observations suggest the presence of a small ferromagnetic component in the magnetization of Ti doped sample. A ferromagnetic component is supported in Γ_2 and not in Γ_4. Therefore, we have chosen Γ_2 IR. The Rietveld refinement of neutron diffraction data for YMn$_{0.9}$Ti$_{0.1}$O$_3$ at 6K is shown in figure 3.23. Thus, Ti doping leads to the modified magnetic structure for YMn$_{0.9}$Ti$_{0.1}$O$_3$ and is given by Γ_2 representation with moment on Mn being 2.3μ_B at 6K and is oriented along the a-axis. The ferromagnetic component of the moment is lower than that we can detect using neutron diffraction. Therefore, we do not find the out of plane component of moment in the analysis of neutron diffraction data though signatures of this can be found in the magnetization data. The occurrence of weak ferromagnetic component in Ti doped

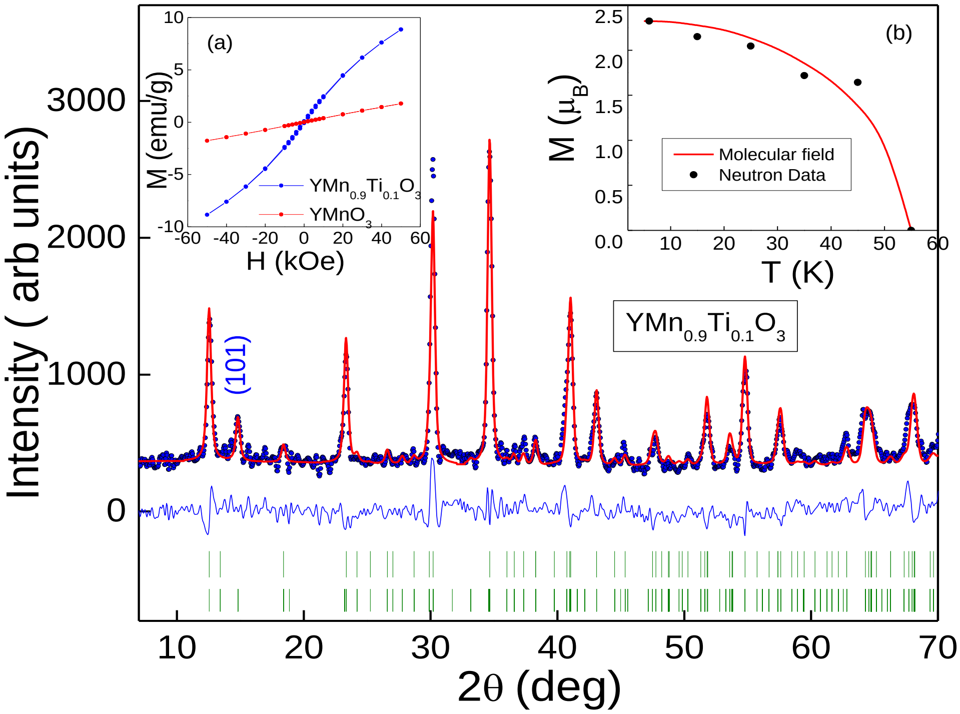

Figure3.23: The observed (symbols) and calculated (line) neutron diffraction pattern for $YMn_{0.9}Ti_{0.1}O_3$ compound at T=6K. Lower solid line is the difference between observed and calculated pattern. The first row of tick marks indicates the position of nuclear Bragg peaks and second row indicate the position of magnetic Bragg peaks. Inset (a) shows the M-H curve at T = 5K. Inset (b) shows the variation of magnetic moment as a function of temperature.

samples can be explained by considering Dzyaloshinskii-Moriya (D-M) type interactions [227]. The thermal evolution of the moments is described by the molecular field analysis using $\lambda = 11.2$ T/μ_B, $T_N = 55K$ and $S = 1.9$. We obtained a good fit to the experimental data as shown in inset of figure 3.23.

As against the previous two samples in the Fe doped sample, spin reorientation as a function of temperature is observed. The neutron diffraction patterns for $YMn_{0.9}Fe_{0.1}O_3$ at T = 55K is shown in figure 3.24. The magnetic phase observed immediately below T_N ~ 55K, is described by considering irreducible representation Γ_3. This compound undergoes a second magnetic transition at T ~ 35K, where the magnetic reflection (101) begins to be observed. In comparison to $YMnO_3$, where the intensity of the (100) and (101) peaks are quite different, in $YMn_{0.9}Fe_{0.1}O_3$ at 6K the intensity of these two peaks is almost same as shown in figure 3.25. So Fe doping at Mn site leads to spin reorientation of Mn magnetic moments and this modified magnetic structure can be described as a linear combination of irreducible representation $\Gamma_3 + \Gamma_4$. With Fe doping the Mn moments are inclined to 28° for $YMn_{0.9}Fe_{0.1}O_3$ at 6K. The spin structures for $YMn_{0.9}Fe_{0.1}O_3$, and $YMn_{0.9}Ti_{0.1}O_3$ at 6K, are shown in figure 3.26. For $YMn_{0.9}Fe_{0.1}O_3$, the spins are coupled ferromagnetically along c-axis from the a-axis. The change in magnetic ground state of $LuMnO_3$ (Γ_4) from $YMnO_3$ (Γ_3) has been ascribed to the behavior of single ion anisotropy which is

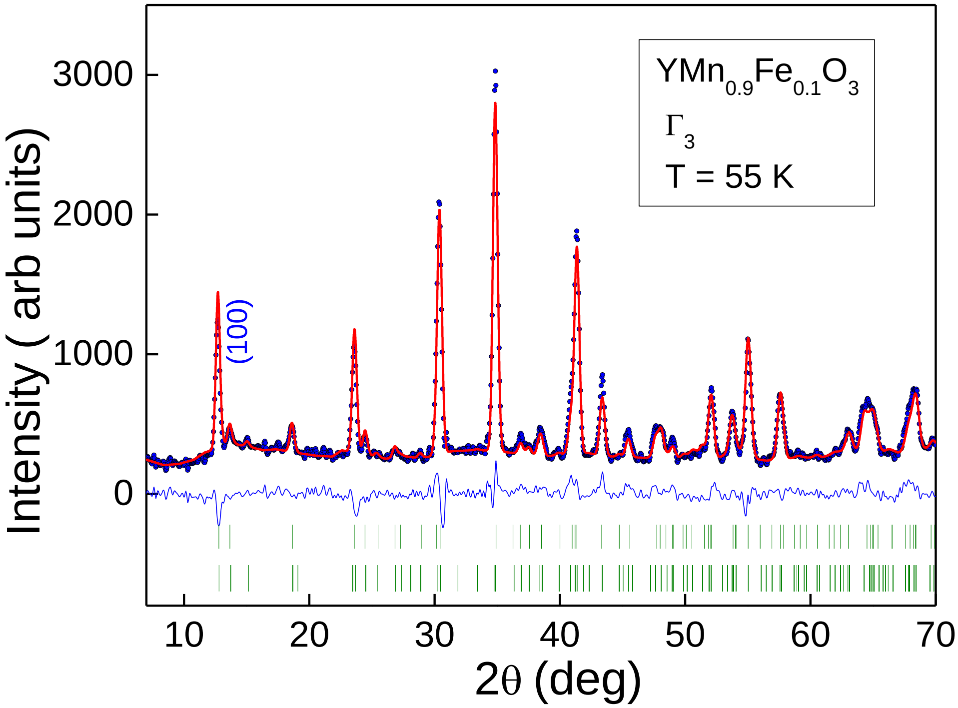

Figure 3.24: The observed (symbols) and calculated (line) neutron diffraction pattern for $YMn_{0.9}Fe_{0.1}O_3$ compound at T = 55K. Lower solid line is the difference between observed and calculated pattern. The first row of tick marks indicates the position of nuclear Bragg peaks and second row indicate the position of magnetic Bragg peaks.

correlated with the distortions of triangular lattice [117]. The presence of d_z^2 orbital in Fe doped $YMnO_3$ influences the anisotropy of the system leading to reorientation of the spins. In earlier studies of Fe doping in $YMnO_3$ it has been seen that Fe doping introduces more magnetic anisotropy in the system [207]. The moment on Mn reduces to 2.93μ_B. For Fe-doped samples, φ angle decreases with increase in temperature. Spin reorientation behavior has also been observed in $HoMnO_3$ below T = 44.6K [226] and in $ScMnO_3$ where the spin reorientation changes the magnetic symmetry from Γ_2 to $\Gamma_1+\Gamma_2$ at low temperature [113]. The thermal variation in Mn magnetic moments for $YMn_{0.9}Fe_{0.1}O_3$ derived from neutron data is shown in inset of figure 3.25.

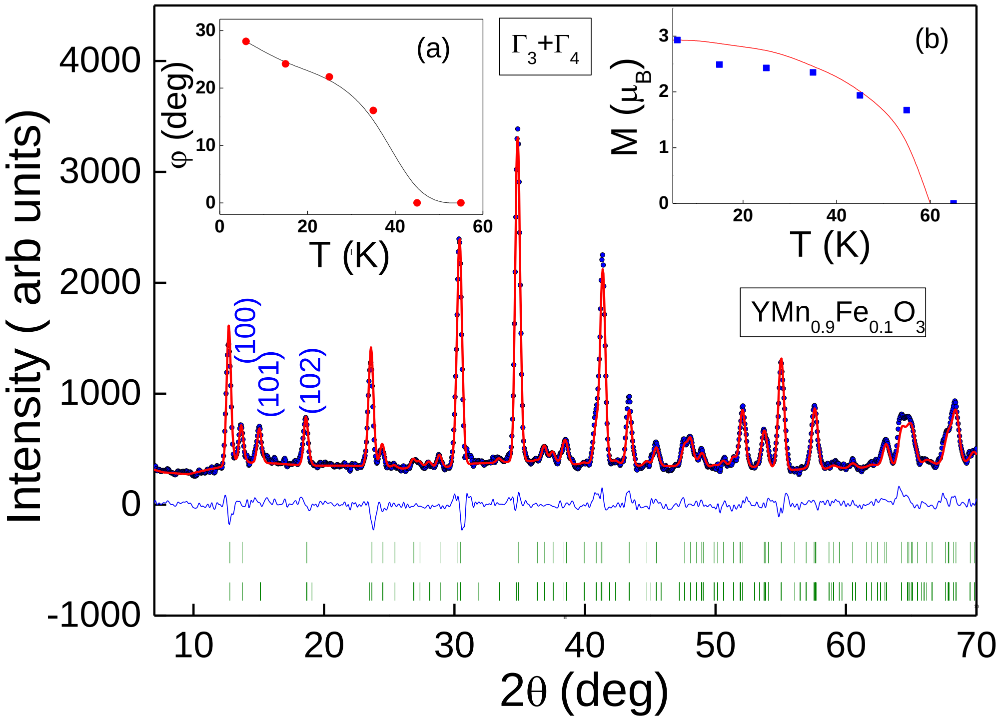

Figure 3.25: The observed (symbols) and calculated (line) neutron diffraction pattern for $YMn_{0.9}Fe_{0.1}O_3$ compound at T=6K. Lower solid line is the difference between observed and calculated pattern. The first row of tick marks indicates the position of nuclear Bragg peaks and second row indicate the position of magnetic Bragg peaks. Inset (a) shows the variation of tilting angle (φ) as a function of temperature. Inset (b) shows the variation of magnetic moment as a function of temperature.

We calculate these thermal variations by applying molecular field model. For these doped sample, we obtained $\lambda = 10.7\ T/\mu_B$ by taking $T_N = 60K$ and $S = 2.05$. We find that the representation remains same on doping with Ga in $YMnO_3$ albeit with a decrease in the value of moment to $2.07\mu_B$ at 6K [219].

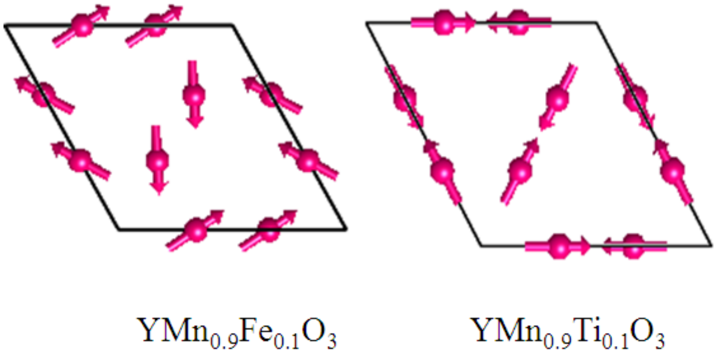

Figure 3.26: Magnetic structures of $YMn_{0.9}Fe_{0.1}O_3$, and $YMn_{0.9}Ti_{0.1}O_3$.

3.2.1.5 Temperature dependent X-ray Absorption Spectroscopy

The local structure of $YMn_{1-x}M_xO_3$ (M = Ti, Fe, Ga; x = 0, 0.1) compounds has been investigated using EXAFS and XANES techniques. Figure 3.27 shows the normalized x-ray absorption near edge spectra (XANES) for Mn K-edge for the $YMn_{1-x}M_xO_3$ (for x=0.1; M= Ti, Fe, and Ga) samples at room temperature. The spectral line shapes are similar for all the studied samples. The XANES spectra of all the samples are plotted together with the reference Mn compounds having formal Mn valence of +2 ($MnCl_2$), +3 (Mn_2O_3), and that of Mn metal with zero oxidation state. The weak pre-edge in the transition metal oxides usually results from the bound state transition. The pre-edge features below the absorption edge are due to 1*s* transition into unoccupied O 2*p*-Mn 3*d* (or Mn 3*d*/4*p*) hybridized states, which have *p* components projected at the Mn site as observed in many transition-metal oxides. It is well known that the XANES is sensitive to oxidation state and small variations in structure [228]. Figure 3.27 clearly shows that the main edge position of $YMnO_3$ and $YMn_{1-x}M_xO_3$ (M = Ti, Fe Ga) samples coincides with Mn_2O_3, indicating that the valence of Mn ion is +3. The two XANES features A and B in figure 3.27 are similar to $YMnO_3$ for $YMn_{1-x}M_xO_3$ (for x=0.1 and M= Ga, Ti and Fe) also indicating that the MnO_5 coordination do not vary with doping. This shows that the substitution of Mn by 10% Ti, Fe and Ga does not lead to any structural transition i.e. structure remain hexagonal at room temperature. These observations are in agreement with our earlier x-ray diffraction and neutron diffraction studies.Similar features are also observed in Zn doped $YMnO_3$ [229]. However, in the case of Ni, Cu and Co doped $YMnO_3$ [230] these features are different from $YMnO_3$ and has been attributed to the MnO_6 octahedron which corresponds to the presence of orthorhombic structure.

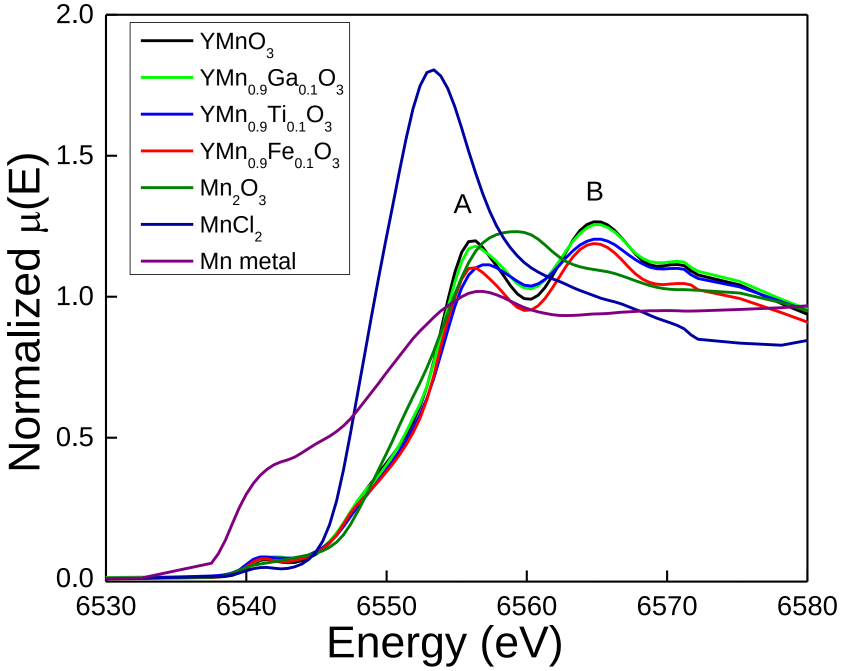

Figure 3.27: Normalised XANES spectra of $YMn_{1-x}M_xO_3$ (for x=0.1 and M=Ga, Ti and Fe) at Mn K-edge with along with reference Mn metal, $MnCl_2$ and Mn_2O_3 sample.

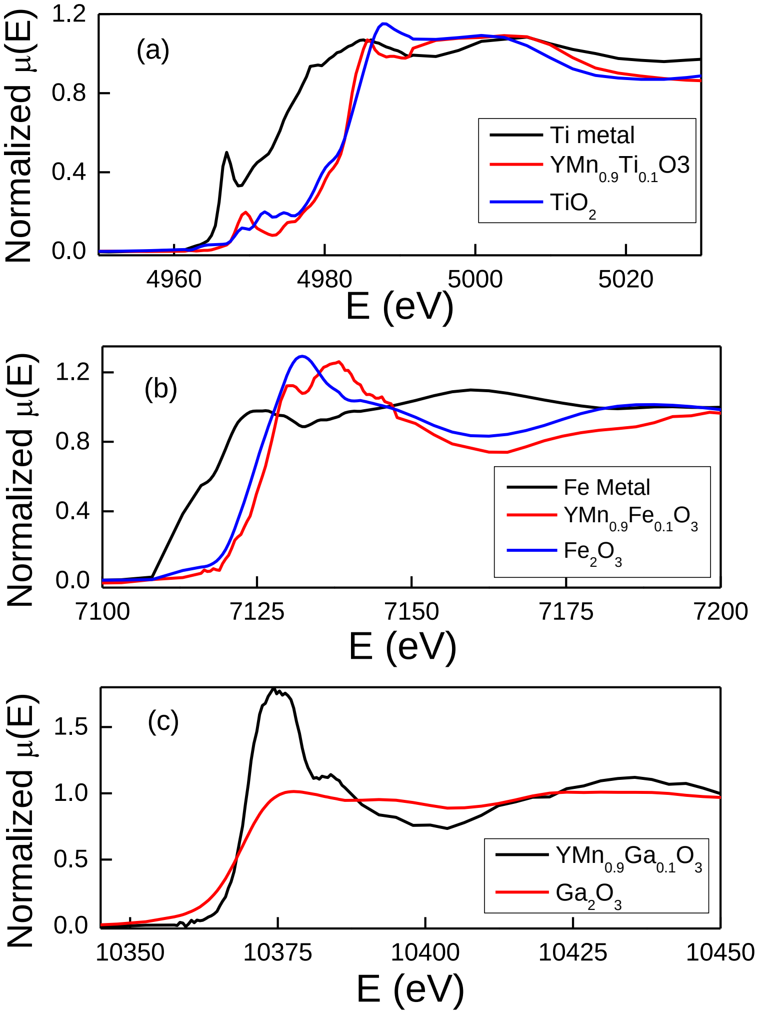

Figure 3.28: Normalised XANES spectra of $YMn_{1-x}M_xO_3$ (for x=0.1 and M=Ga, Ti and Fe) at (a) Ti K-edge with reference Ti metal and TiO_2 (b) Fe K-edge with reference Fe metal and Fe_2O_3, (c) Ga K-edge with reference Ga_2O_3 .

Figure 3.28 (a)-(c) shows the XANES spectra of $YMn_{0.9}Ti_{0.1}O_3$ at Ti K-edge with reference compounds (TiO_2, Ti metal) ,$YMn_{0.9}Fe_{0.1}O_3$ at Fe K-edge with reference compounds (Fe_2O_3, Fe metal), and $YMn_{0.9}Ga_{0.1}O_3$ at Ga K-edge with reference compound Ga_2O_3, respectively. It is shown in figure 3.28(a)-(c) that Ti is in +4 oxidation stateand Ga is in +3 oxidation state as their edge energy coincides with standards TiO_2 and Ga_2O_3 edge energy. In case of Fe doped sample, XANES measurements together with Mössbauer and magnetization measurements indicate the presence of Fe in +3 oxidation state. Similar results have been observed by Harunsani et al [231] for the Fe doped sample. However, these are not in agreement with the results obtained by Namdeo et al.[232]. Room temperature XANES measurements indicate that the structural as well as the oxidation state of Mn remain same for all the doped compounds. We have also performed temperature dependent EXAFS and XANES measurements on some of the selected samples, $YMn_{1-x}M_xO_3$ (for x=0.1 and M=Ti and Fe). Normalized XANES spectrum for Mn K-edge for the $YMn_{1-x}M_xO_3$ (for x=0.1 and M=Ti and Fe) samples is shown in figures 3.29(a)-3.29(c). No appreciable change is observed in the XANES spectra of the samples with temperature.This indicates that structure as well as the oxidation states of Mn remains same with temperature for all doped samples.

EXAFS (Extended X-ray Absorption Fine Structure) spectra correspond to the oscillating part of the X-ray absorption spectrum that extends to about 1000 eV. In order to take care of the oscillations in the absorption spectra $\mu(E)$ has been converted to absorption function $\chi(E)$, defined as $\chi(E) = \frac{\mu(E) - \mu_0(E)}{\Delta\mu_0(E_0)}$, where $E_0, \mu_0(E_0)$, and $\Delta\mu_0(E_0)$ are the absorption edge energy, bare atom background and step in $\mu(E)$ value at the absorption edge, respectively. The energy dependent absorption coefficient $\chi(E)$ has been converted to the wave number dependent absorption coefficient $\chi(k)$ using relation, $K = \sqrt{\frac{2m(E - E_0)}{\hbar^2}}$,where m is the electron mass. $\chi(k)$ is weighted by k^3 to amplify the oscillation at high k and the $\chi(k)k^3$ functions are Fourier transformed in R space to generate the $\chi(R)$ versus R spectra in terms of the real distances from the center of the absorbing atom. The set of EXAFS data analysis available within IFEFFIT software package have been used for analysis [233]. This includes background

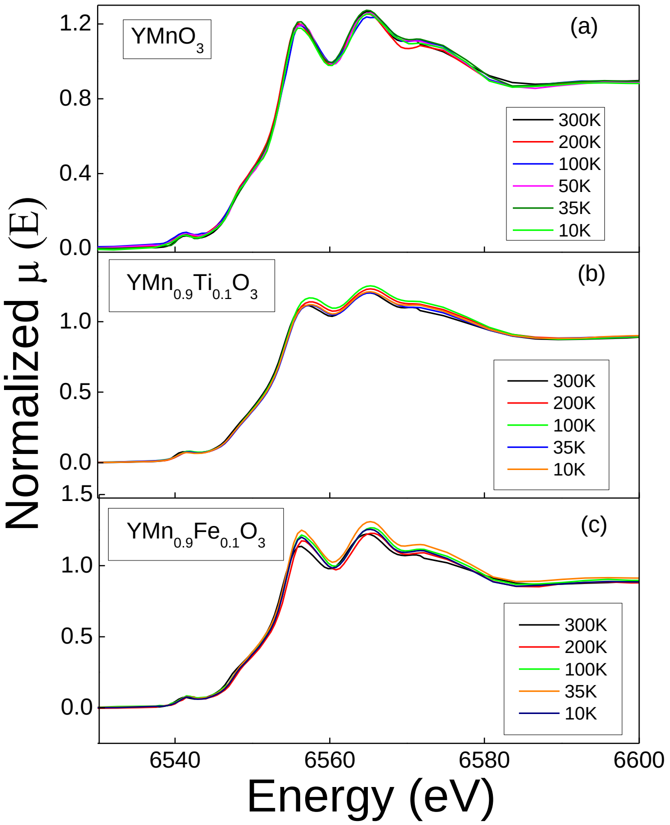

Figure 3.29: Normalised XANES spectra at Mn K-edge for (a) $YMnO_3$, (b) $YMn_{0.9}Ti_{0.1}O_3$, (c) $YMn_{0.9}Fe_{0.1}O_3$ at different temperatures.

reduction and Fourier transform to derive the $\chi(R)$ versus R spectra from the absorption spectra (using ATHENA software), generation of the theoretical EXAFS spectra starting from an assumed crystallographic structure and finally fitting of experimental data with the theoretical spectra using ARTEMIS software. The $\chi(R)$ versus R spectra have been generated (Fourier transform range k=3-10 Å^{-1}) for all the samples from the $\mu(E)$ versus E spectra following the methodology described above. The $\chi(R)$ versus R spectra is shown in figure 3.30(a) for $YMn_{1-x}M_xO_3$ (x = 0.1 and M = Ti, Fe, and Ga) measured at Mn K-edge and in figure 3.30(b) for the samples measured

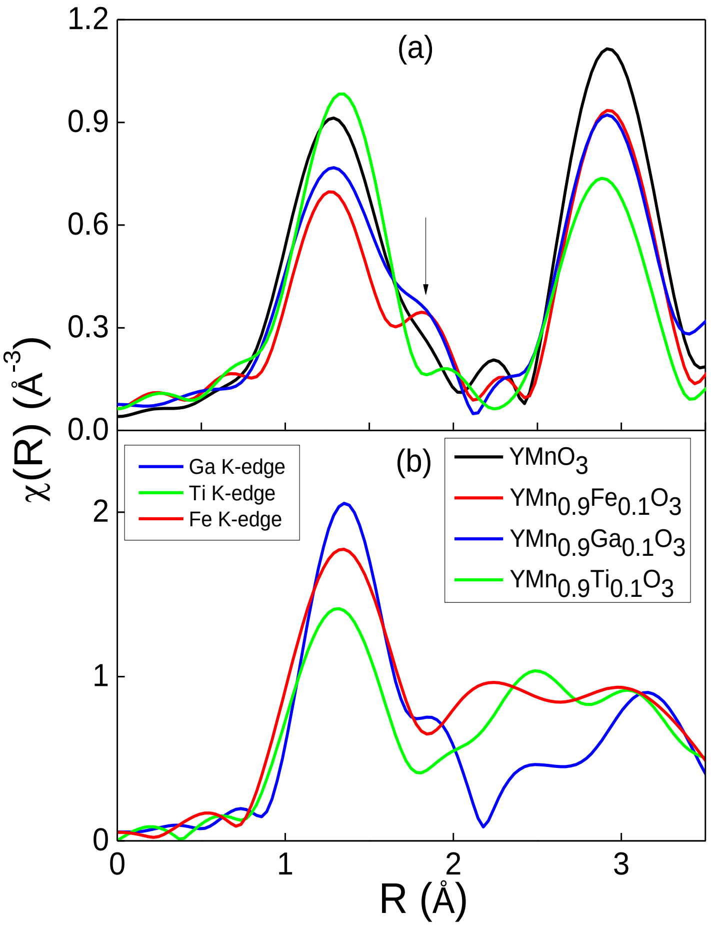

Figure 3.30: Fourier transformed EXAFS spectra of (a) YMn$_{1-x}$M$_x$O$_3$ (for x=0.1 and M=Ga, Ti and Fe) at Mn K-edge, (a) YMn$_{0.9}$Ti$_{0.1}$O$_3$ Ti K-edge (b) YMn$_{0.9}$Fe$_{0.1}$O$_3$ Fe K-edge and (c) YMn$_{0.9}$Ga$_{0.1}$O$_3$ Ga K-edge.

at Ti, Fe and Ga K-edges respectively at room temperature. From figure 3.30(a) and figure 3.30(b) it can be seen that the first peak position in the $\chi(R)$ versus R spectra of doped YMnO$_3$ samples measured at the dopant edges is found to appear at the same position as in the $\chi(R)$ versus R spectra of the samples measured at Mn K-edge. This clearly indicates that dopant atoms go to Mn site in YMnO$_3$ structure. The first peak in the $\chi(R)$ versus R spectrum of YMnO$_3$ at Mn K-edge EXAFS is due to oxygen atoms surrounding the central Mn atoms. It is evident from

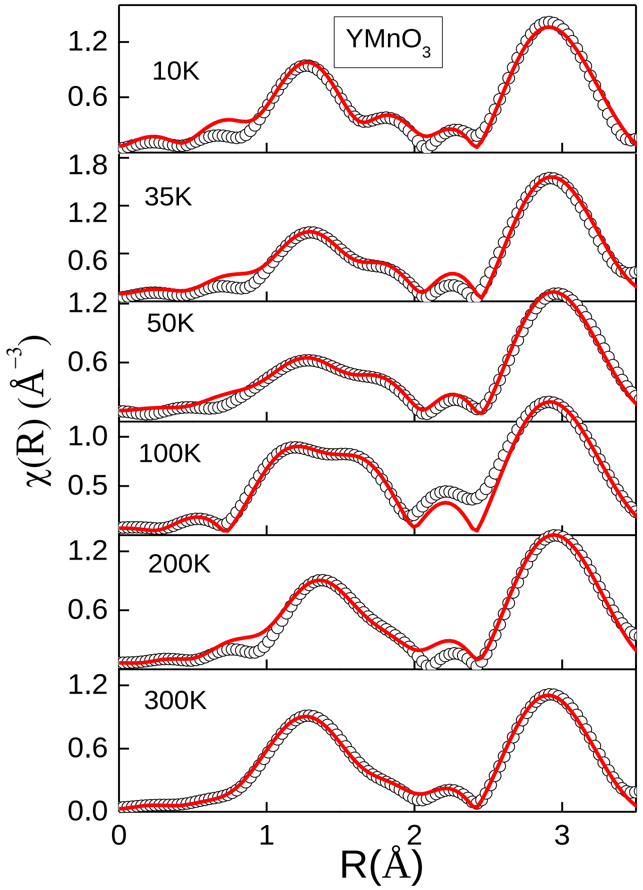

Figure 3.31: Fourier transformed EXAFS spectra of $YMnO_3$ for temperature 300K, 200K, 100K, 50K, 35K and 10K at Mn K-edge (Scatter points) and theoretical fit (Solid line).

the above spectrum that in case of the $YMnO_3$ sample the first peak shows a small shoulder around 1.8Å which is indication of different Mn-O coordination shells having large difference in the bond lengths between the Mn-O_A and Mn-O_P bonds, where O_A and O_P denote the two apical and three planar oxygen atoms, respectively [234-237]. In the hexagonal structure Mn^{3+} (d^4) have D_{3h} symmetry which splits d-levels into two doublets e_{1g} (xz/yz), e_{2g} (xy/x^2-y^2) and one singlet a_{1g} (z^2) in the order of increasing energy. As a result, the four d-electrons of Mn^{3+} occupy the lowest lying doublets e_{1g} and e_{2g} states while leaving the a_{1g} state empty, so that stronger hybridizations occur along the apical Mn-O bonds. Therefore, the characteristic electronic configuration of Mn^{3+} in trigonal geometry leaves the a_{1g} state empty which results in a shorter bond length for the average apical $Mn\text{-}O_A$ bonds than the average planar $Mn\text{-}O_P$ bonds. Similar results have been obtained for all the studied samples here. The initial structural parameters (atomic coordination and lattice parameters) of the studied samples used for simulation of theoretical EXAFS spectra of the samples have been obtained from neutron diffraction results.

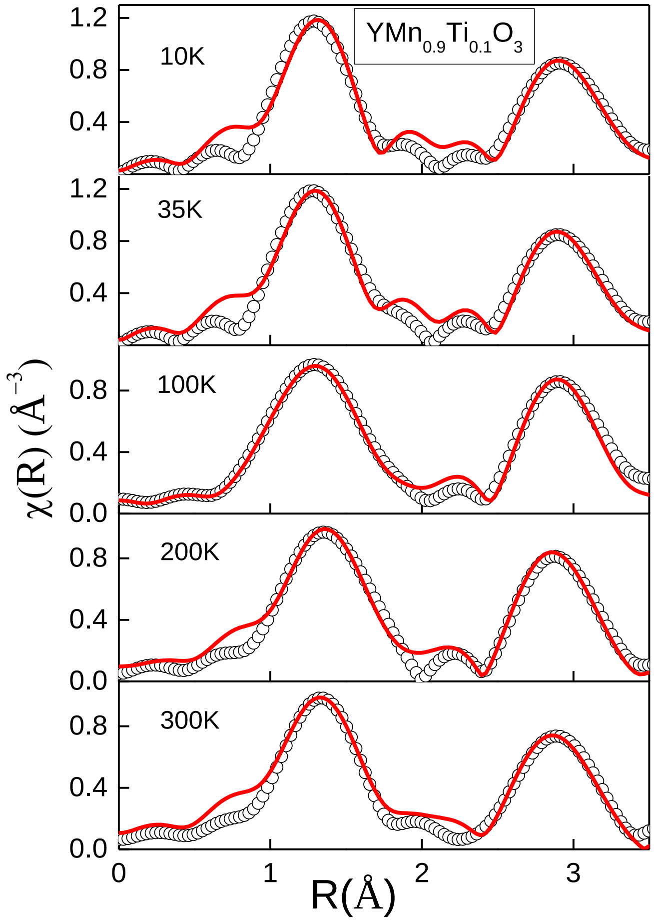

Figure 3.32: Fourier transformed EXAFS spectra of $YMn_{0.9}Ti_{0.1}O_3$ for temperature 300K, 200K, 100K, 35K, and 10K at Mn K-edge (Scatter points) and theoretical fit (Solid line).

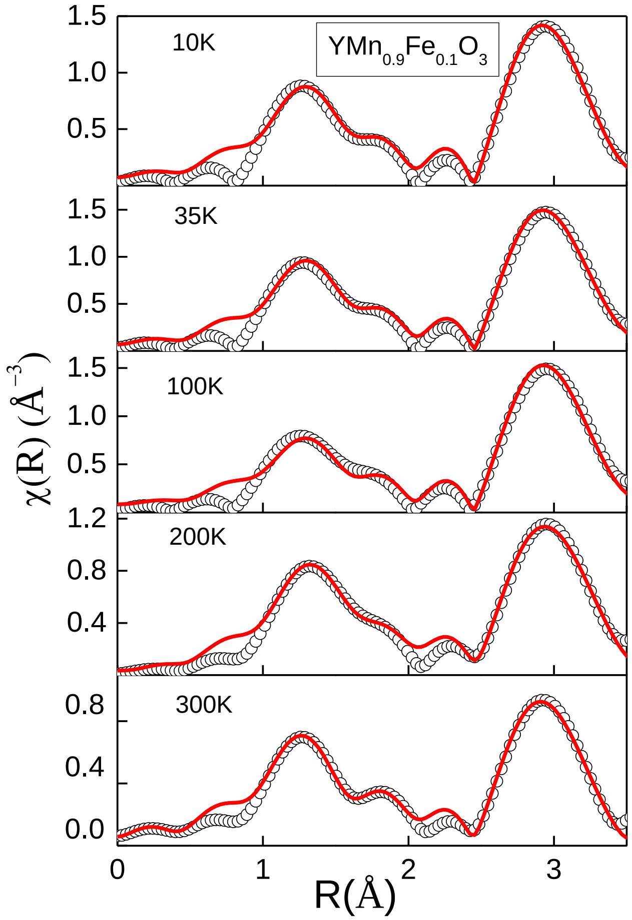

Figure 3.33: Fourier transformed EXAFS spectra of $YMn_{0.9}Fe_{0.1}O_3$ for temperature 300K, 200K, 100K, 35K, and 10K at Mn K-edge (Scatter points) and theoretical fit (Solid line).

The Fourier transform of the EXAFS spectra (fitting range R=1.0-3.5 Å) of the $YMnO_3$, $YTi_{0.1}Mn_{0.9}O_3$, and $YFe_{0.1}Mn_{0.9}O_3$ samples for the measurements carried out at Mn K-edge along with the best fit theoretical plots for different temperatures are shown in figures 3.31, 3.32, and 3.33, respectively. As shown in figure 3.31, the signature of double peak or shoulder has been observed for $YMnO_3$ in all studied temperatures. However, the intensity of the shoulder peak changes with the temperature. The difference between Mn-O_A and Mn-O_P bonds vary slightly with temperature and exhibit maximum value at 10K. Similar temperature dependant behavior is found to be present in the $\chi(R)$ versus R spectrum of the Ti doped sample, as shown in figure

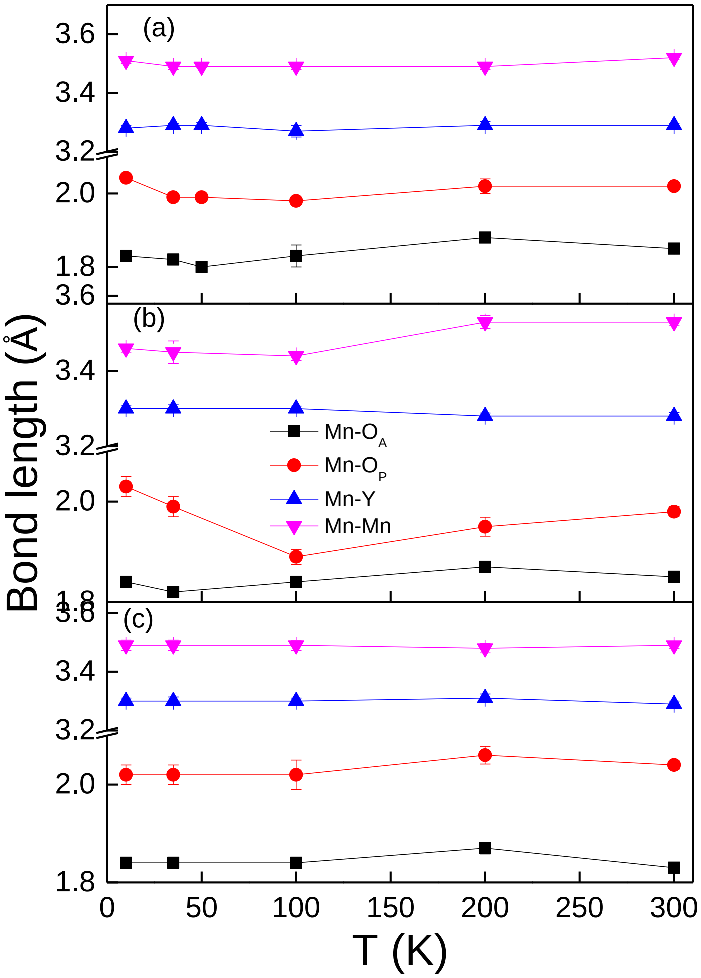

Figure 3.34: Variation of bond length with temperature for (a) $YMnO_3$, (b) $YMn_{0.9}Ti_{0.1}O_3$ and (c) $YMn_{0.9}Fe_{0.1}O_3$.

3.28. However in Fe doped sample, difference between planar Mn-O$_P$ and apical Mn-O$_A$ bond length remain constant with temperature as shown in figure 3.34. The second peak in the fourier transformed spectra is a result of combined contribution of Mn-Y and Mn-Mn bond lengths. It can be seen from figure 3.31-3.33 that the shape of the second fourier transform peak is almost same for all the samples while only their amplitude changes. Since the scattering amplitude of outgoing photoelectron depends on the atomic number, doping with lower Z element than Mn

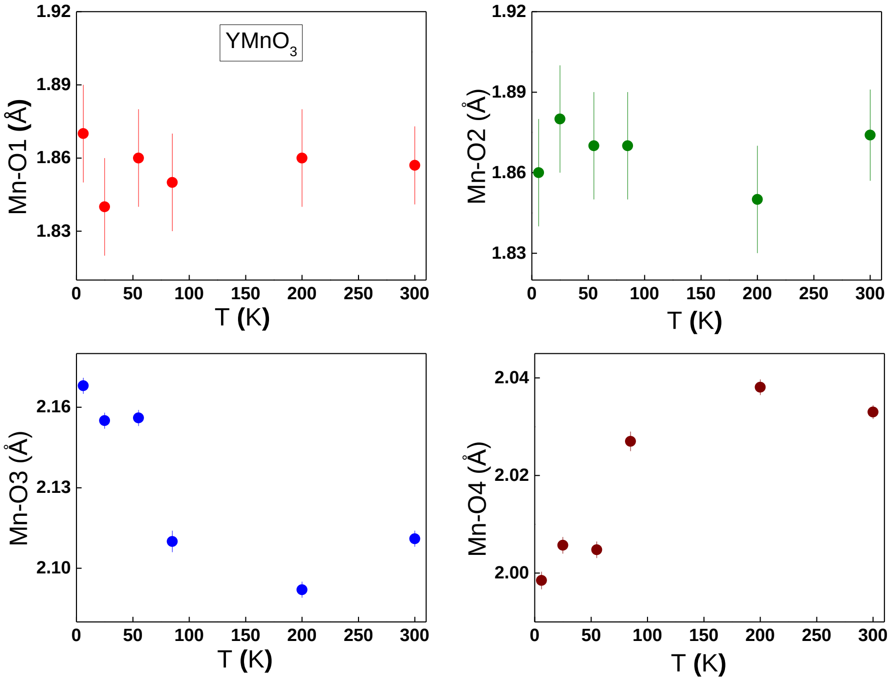

Figure 3.35: Variation of bond lengths (obtained from neutron diffraction) for $YMnO_3$.

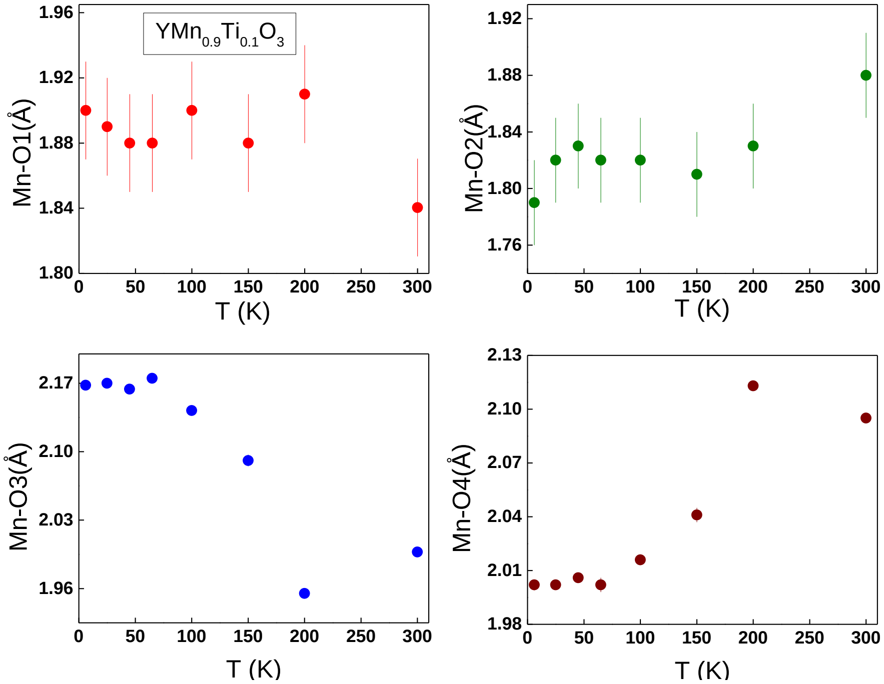

Figure 3.36: Variation of bond lengths (obtained from neutron diffraction) for $YMn_{0.9}Ti_{0.1}O_3$

will result in decrease in peak amplitude as can be seen in case of Ti doped $YMnO_3$. The parameters obtained after fitting are plotted in figure 3.34. The apical bond lengths ($Mn-O_A$) remain constant with temperature but changes have been observed for planar bond lengths ($Mn-O_P$), as shown in figure 3.34. The temperature dependent behavior of bond lengths obtained from EXAFS measurements is in agreement with the bond lengths obtained from neutron diffraction data. The planar bond lengths (Mn-O3 and Mn-O4), for $YMnO_3$ and $YMn_{0.9}Ti_{0.1}O_3$ shows significant changes with temperature, as shown in figure 3.35 and 3.36, respectively. However, no such behavior of bond lengths has been observed in case of Fe doped compound in both EXAFS and neutron diffraction measurements. The difference between apical and average bond lengths obtained from EXAFS measurements in $YMnO_3$ and $YMn_{0.9}Ti_{0.1}O_3$ can also be correlated with the displacement of Mn ions obtained from neutron diffraction measurements as shown in figure 3.37.

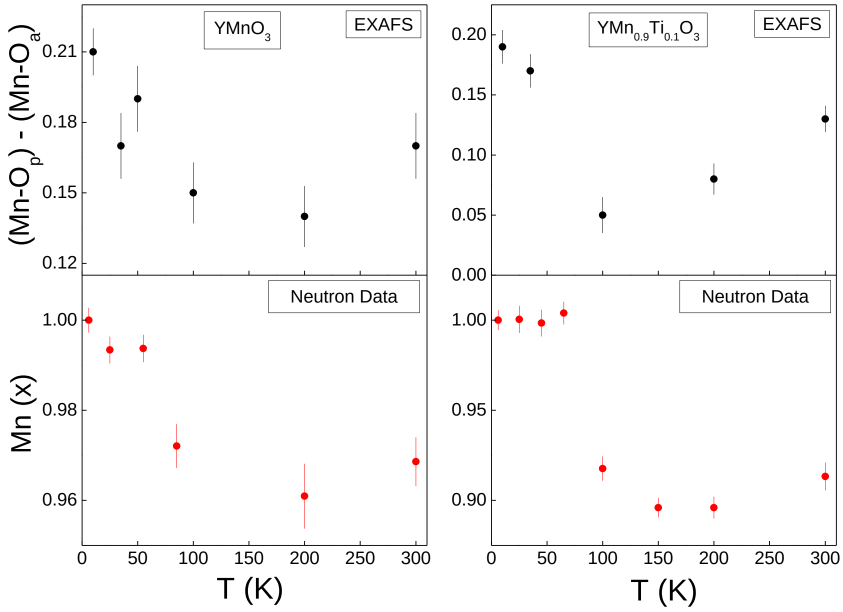

Figure 3.37: Variation of bond lengths for (a)$YMnO_3$, (b) $YMn_{0.9}Ti_{0.1}O_3$

3.2. 2 Magnetic and dielectric behavior in $YMn_{1-x}Fe_xO_3$ ($x \leq 0.5$)

The substitution of Fe by Mn or Mn by Fe is interesting because of the same ionic radii of Fe^{3+} and Mn^{3+} yet different magnetic moment values. Because of the presence of an electron in dz^2 orbital in case of Fe^{3+}, substitution of Fe^{3+} allow us to study the effect of electron doping in the hexagonal $YMnO_3$. In our previous investigation we had reported that Fe doping at Mn site leads to observation of reorientation of Mn magnetic moments as a function of temperature. The modified magnetic structure can be described as a linear combination of Γ_3+Γ_4 IR raising the possibility of observation of dielectric anomalies at the spin reorientation temperatures. In the opposite end, in orthorhombic (*Pnma* space group) $YFe_{1-x}Mn_xO_3$ ($0.10 \leq x \leq 0.45$) it has been found that the magnetic structure changes from Γ_4 ($A_x F_y G_z$) at high temperature to Γ_1 ($G_x C_y A_z$) at low temperature, using magnetic torque measurements [238]. The spin reorientation in Mn substituted orthoferrites has been attributed to the large magnetic anisotropy energy of the Mn^{3+} ion at low temperature. The direction of antiferromagnetic spin axis in $YFeO_3$ is due to the anisotropy energy of the Fe^{3+} ions, but the substitution of Mn at Fe site after the critical concentration overcome the anisotropy energy of the Fe^{3+} ions. This spin reorientation behavior in orthorhombic $YFe_{1-x}Mn_xO_3$ has been recently confirmed by neutron diffraction studies [239]. Dielectric anomaly near the magnetic transition temperature appeared in orthorhombic $YFe_{1-x}Mn_xO_3$ and it has been observed that the dielectric anomaly is more pronounced at higher Mn concentration. However, there is an absence of similar work in the hexagonal rich end of the series, $YMn_{1-x}Fe_xO_3$. The few studies that has been carried out on Fe doping at Mn site, report the concentration range over which the structure changes to orthorhombic [129,206]. In the present work we have synthesized $YMn_{1-x}Fe_xO_3$ ($0.1 \leq x \leq 0.5$) and report the effects of Fe^{3+} (d^5) doping on the structural, dielectric and magnetic properties of frustrated hexagonal $YMnO_3$.

We find that with Fe doping at Mn site, progressive changes in chemical structure and magnetic structure take place as a function of temperature and composition. Large dielectric anomalies are observed coinciding with the magnetic transition temperature in these compounds which we show to scale with sub lattice magnetization obtained from neutron diffraction, in agreement with predictions of Landau theory.

3.2.2.1 Crystal structure

From Rietveld refinement of these diffraction patterns a single hexagonal phase has been observed for $YMn_{1-x}Fe_xO_3$ for $x \leq 0.2$. For $x > 0.2$ the diffraction lines belonging to the orthorhombic phase (space group *Pnma*) characteristic of $YFeO_3$ compound, appear in the x-ray diffraction pattern and therefore analysis with a mixed orthorhombic and hexagonal phase has been carried out for these samples ($0.3 \leq x \leq 0.5$). The parent compound ($YMnO_3$) and the end

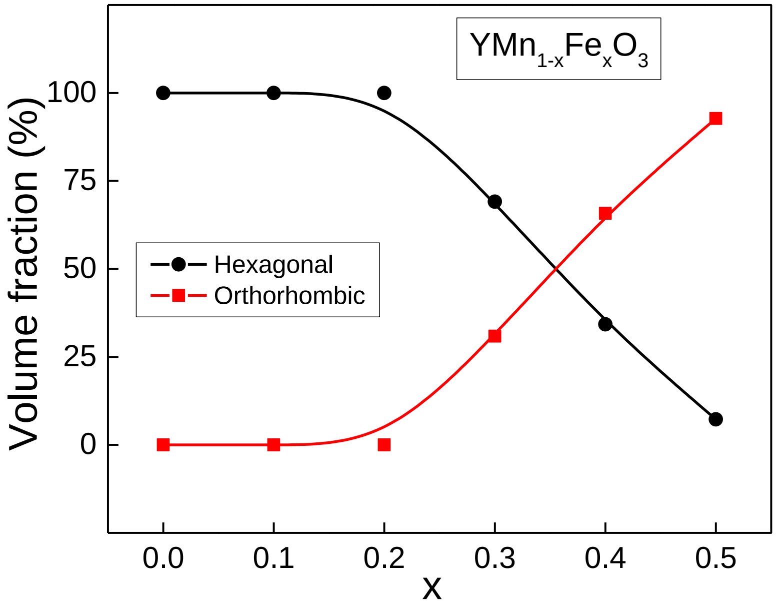

Figure 3.38: The variation of volume fraction of hexagonal and orthorhombic phases of $YMn_{1-x}Fe_xO_3$ with the Fe content x.

compound ($YFeO_3$) of this series have different structures. $YMnO_3$ crystallizes in hexagonal phase with space group *$P6_3cm$* whereas $YFeO_3$ crystallizes in an orthorhombically distorted perovskite structure with space group *Pnma*. All the samples have been characterized by x-ray and neutron diffraction techniques. With increase in Fe doping, there is a progressive increase of the orthorhombic phase as shown in figure 3.38. This is in agreement with previous studies where structural transition in $YMnO_3$ has been observed by doping at Y or Mn site [199, 202,240]. The variation of cell parameters and volume for a single phase hexagonal sample $YMn_{0.8}Fe_{0.2}O_3$ is shown in figure 3.39(a) and 3.39(b), respectively. For hexagonal compounds, it

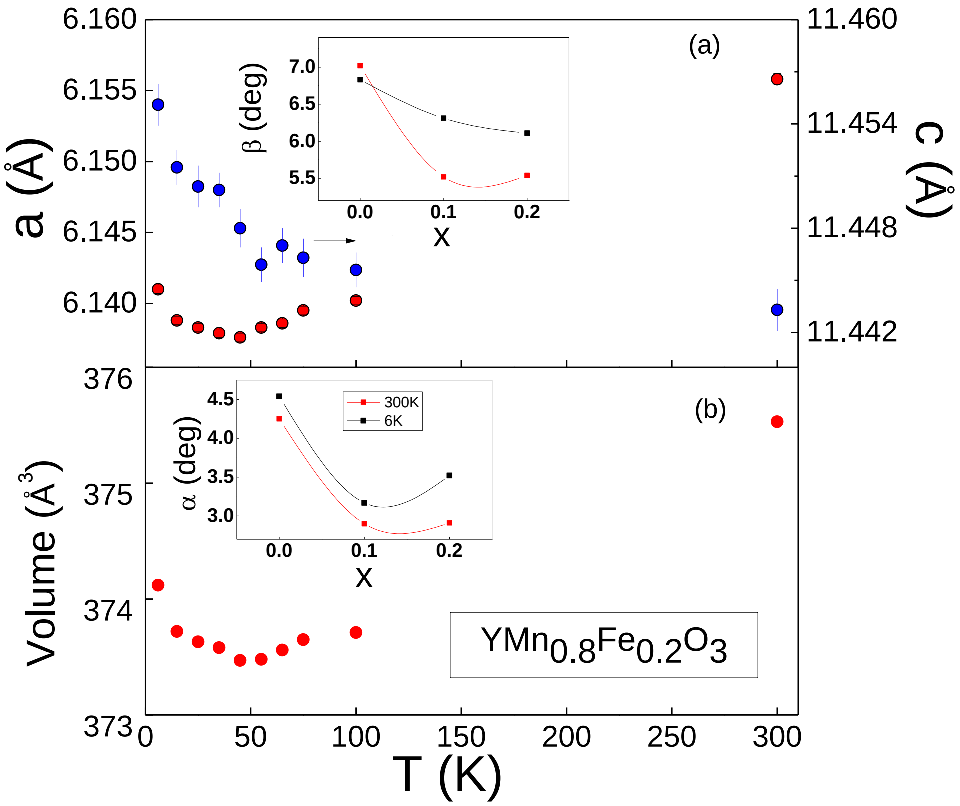

Figure 3.39: Temperature variation of the (a) lattice parameters a and c, (b) unit cell volume for $YMn_{0.8}Fe_{0.2}O_3$. Inset shows the tilting and buckling angles at 6 K and 300K.

has been observed that the lattice parameter a increases and c decreases with increase in temperature and similar behavior of parameters has been observed in all the studied samples in hexagonal phase. The negative thermal expansion of c parameter in hexagonal manganites is explained by the reduction of tilting of MnO_5 bypiramids along with the buckling of Y-planes [100]. The unit cell volume decreases with temperature. However, they exhibit an anomalous behavior in the magnetically ordered state which might be attributed to the magnetoelastic coupling in these hexagonal compounds.

Doping at Y or Mn site is expected to modify the distortion parameters of MnO_5 bypiramid [220]. We find that the distortion parameters (α and β) are suppressed with Fe doping at Mn- site and are shown in inset of figure 3.39(a) and 3.39(b). This reduction of tilting (α) and buckling (β) in Fe doped samples indicates the suppression of average interaction [208] within Mn trimers and this is evidenced in decreased magnetodielctric coupling in Fe doped sample (shown below). Figure 3.40, shows the temperature variation of unit cellvolume of the orthorhombic phase for

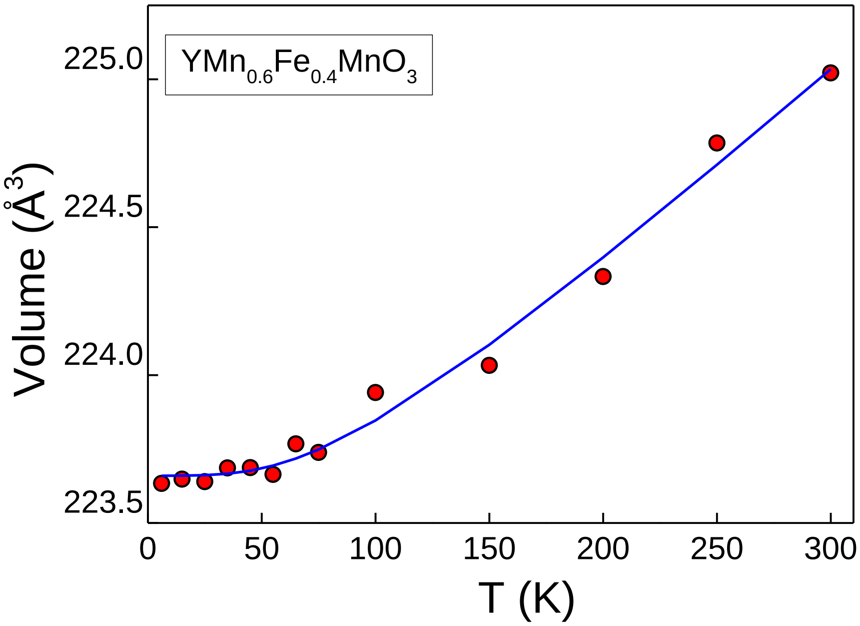

Figure 3.40: Temperature variation of unit cell volume for $YMn_{0.6}Fe_{0.4}O_3$. The solid line is a fit to the Debye - Grüneisen equation.

for $YMn_{0.6}Fe_{0.4}O_3$. The unit cell volume increases continuously with increase in temperature. The temperature dependence of volume has been fitted to Debye model, using Grüneisen approximation (described above) [211]. The blue curve in the figure 3.40 represents the volume obtained by fitting the volume data to the Debye- Grüneisen equation. It is seen from the fit, that the temperature dependence of the volume does not show any anomalous behavior. The refined parameters obtained by neutron diffraction at 6K are given in Table 3.4. With Fe doping, change in Mn-O bond lengths has been observed in hexagonal phase. The Mn-O_1 bond lengths decrease with Fe concentration while enhancement in Mn-O_2 and Mn-O_3 bond lengths is observed.

3.2.2.2 Magnetic properties

Figure 3.41 shows the temperature dependence of magnetization, M(T) for $YMn_{1-x}Fe_xO_3$ (x = 0.1-0.5) under an applied magnetic field of 0.1 T. The parent sample $YMnO_3$ does not exhibit a distinct anomaly at the transition temperature [113]. However, weak anomalies are observed at the T_N in the doped samples. The variation of inverse magnetic susceptibility with temperature is shown in inset of figure 3.41. We found a better description of the paramagnetic susceptibility data by fitting the magnetic susceptibility to the modified Curie – Weiss (CW) law, given by $\chi = \chi_0 + C/T-\theta_{CW}$, where χ_0, C and θ_{CW} are the temperature independent part of the magnetic susceptibility, Curie constant and Curie-Weiss temperature, respectively. The paramagnetic susceptibility follows the Curie – Weiss law in the range 185K to 300K for samples x = 0.1 - 0.4. For x = 0.5 sample, a deviation from this behavior occurs at above 280K as shown in inset offigure 3.41. This curvature is because of the T_N (~ 350K, estimated from reference [239]) of the orthorhombic phase. So for $YMn_{0.5}Fe_{0.5}O_3$ the fitted range has been reduced to 185-250K.

Table 3.4. Results of Rietveld refinement of neutron diffraction pattern at 6K, transition temperature, Curie – Weiss fit parameters, geometrical frustration parameter for $YMn_{1-x}Fe_xO_3$ ($0.1 \leq x \leq 0.5$).

	$YMn_{0.8}Fe_{0.2}O_3$	**$YMn_{0.7}Fe_{0.3}O_3$**		**$YMn_{0.7}Fe_{0.3}O_3$**		**$YMn_{0.5}Fe_{0.5}O_3$**	
		$P6_3cm$	*Pnma*	*$P6_3cm$*	*Pnma*	*$P6_3cm$*	*Pnma*
a (Å)	6.1410(4)	6.1395(4)	5.691(2)	6.1323(11)	5.6797(11)	6.1550(16)	5.6805(8)
b (Å)	6.1410(4)	6.1395(4)	7.4909(20)	6.1323(11)	7.4860(14)	6.1550(16)	7.5015(2)
c (Å)	11.4551(12)	11.4476 (15)	5.2646(15)	11.425(3)	5.2597(8)	11.3540 (21)	5.2666(9)
V ($Å^3$)	374.12	373.68	224.43	372.09	223.63	372.51	224.42
Mn-O1 (Å)	1.81 (6)	1.97(6)	-	2.37(6)	-		
Mn-O2 (Å)	1.90(5)	1.71(9)	-	1.356(19)	-		
Mn-O3 (Å)	2.10(5)	2.18(6)	-	2.477(16)	-		
Mn-O4 (Å)	2.04(2)	2.02(5)	-	1.954(17)	-		
Mn-O3-Mn (°)	119.1(5)	119.9(7)	-	119.49(12)	-		
Mn-O4-Mn (°)	119.2(6)	116.4(7)	-	111.70(20)	-		
Mn-O_1 (Å)	-		1.97(8)	-	1.98(6)		1.989(16)
Mn-O_{21} (Å)	-		2.13(7)	-	2.11(5)		2.107(15)
Mn-O_{22} (Å)	-	-	1.96(8)	-	1.97(7)		1.966(20)
T_N (K)	60	55	250	55	250	250	
θ (K)	-328	-343		-374		-351	
μ_{eff} (μ_B)	5.12	4.87		5.30		5.21	
χ_0 (emu/mol Oe)	0.001	0.001		0.001		0.001	

All the studied samples follow modified Curie – Weiss behavior with negative values of Curie temperature indicating the antiferromagnetic interactions. The values of χ_0, Curie constant and the Curie – Weiss temperature (θ_{CW}) are obtained from this fit and are summarized in table 3.4. From the Curie constant values, we have calculated the effective paramagnetic moment (μ_{eff}) by using eq., $C = \frac{N\mu_{eff}^2\mu_B^2}{3k_B}$. The values of θ_{CW} and μ_{eff}, obtained for $YMnO_3$ are -421K and 4.98μ_B, respectively. The value of θ_{CW} decreases for ($0.0 \leq x \leq 0.2$) and then it start increasingfor higher doped samples ($0.3 \leq x \leq 0.5$). The values of μ_{eff} for x = 0.1, 0.2, 0.3, 0.4 and 0.5 are 4.45μ_B, 4.43μ_B, 4.87μ_B, 5.30μ_B, and 5.23μ_B, respectively.The expected effective moment values were calculated by assuming both Mn and Fe are in trivalent state. Theoretically, μ_{eff} is calculated as,

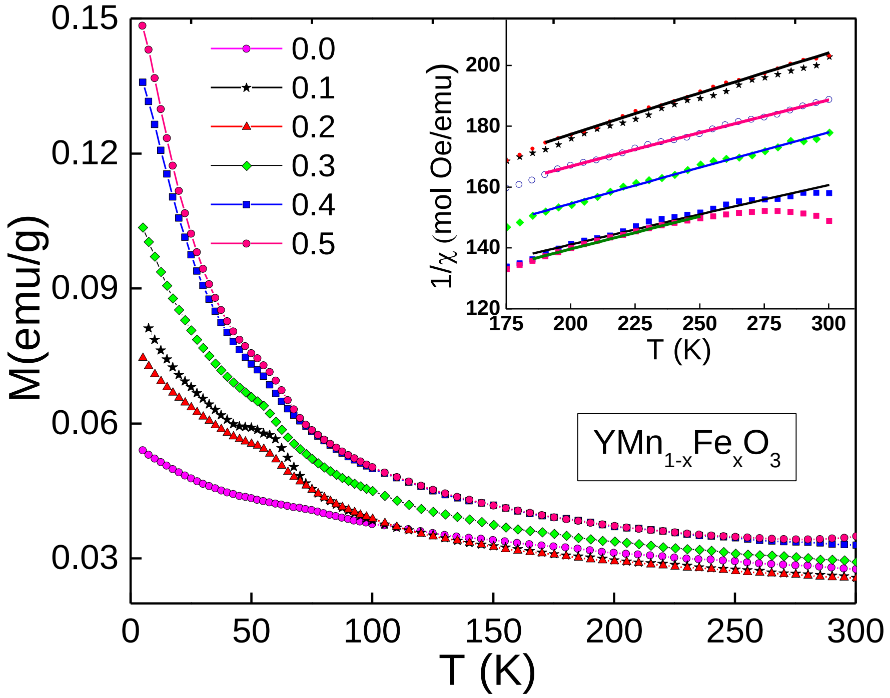

Figure 3.41: The zero field-cooled (ZFC) magnetization (M) versus temperature (T) in field of H=0.1T for $YMn_{1-x}Fe_xO_3$ (x = 0, 0.1, 0.2, 0.3, 0.4, 0.5). Inset shows the inverse of susceptibility as a function of temperature and modified Curie- Weiss fit (solid line).

$\mu_{eff}^{cal} = \sqrt{x\mu_{eff}^{2}(Fe^{3+}) + (1-x)\mu_{eff}^{2}(Mn^{3+})}$ where, μ_{eff} for Fe^{3+} (S= 5/2) and for Mn^{3+} (S=2) are 5.9μ_B and 4.89μ_B respectively. The expected values of μ_{eff} for x = 0.1, 0.2, 0.3, 0.4, and 0.5 are 5.01μ_B, 5.12μ_B, 5.23μ_B, 5.33μ_B, and 5.43μ_B, respectively. The experimentally obtained magnetic moments are close to the expected values for x>0.2.

3.2.2.3 Mössbauer spectrometry

Mössbauer study was carried out to confirm the oxidation state of iron (Fe) in these doped samples. Figure 3.42(a) shows the Mössbauer spectrum for $YMn_{0.8}Fe_{0.2}O_3$ at room temperature. In earlier Mössbauer study of $YMn_{0.9}Fe_{0.1}O_3$, three different sites have been observed for Fe resulting from different chemical environment around Fe ion [219]. The Mössbauer spectrum of $YMn_{0.8}Fe_{0.2}O_3$ which is isostructural with $YMn_{0.9}Fe_{0.1}O_3$ with different Fe content is similarly fitted with three symmetric doublets. These three doublets correspond to three different chemical environments around Fe which are associated with different number of Mn^{3+} ions near neighbors. Explanation for these three different chemical environments around Fe ion has been given in our earlier paper [219]. For higher Fe doped samples, we have obtained a mixed orthorhombic and hexagonal phase. In both these structures, the environment around Fe atom is totally different. In orthorhombic phase, the Fe ion is in six coordinated state while in hexagonal phase, Fe is in 5-fold coordination forming MnO_5 trigonal bypiramids. So the Mössbauer spectra are rather complicated for these mixed phases. For x= 0.5 sample, the main phase is the orthorhombic phase with a small contribution of the hexagonal phase. In Mössbauer spectrum of $YMn_{0.5}Fe_{0.5}O_3$ at room temperature, sextet is observed because of the magnetic contribution of the orthorhombic phase. The Mössbauer spectrum of $YMn_{0.5}Fe_{0.5}O_3$ is fitted with two doublets (related to hexagonal phase) and two sextets (corresponding to the magnetic phase of orthorhombic part) as shown in figure 3.42(b). The hyperfine parameters i.e. isomer shift (δ), quadrupole splitting (ΔE_Q), line widths (Γ) and hyperfine field (H_{hf}) obtained from the fit are included in Table 3.5. The isomer shift (δ) values for all the three doublets in $YMn_{0.8}Fe_{0.2}O_3$ are close to 0.30 mm/s at room temperature and can be attributed to the Fe^{3+} (S = 5/2) in fivefold oxygen coordination. The δ values of both the sextets for $YMn_{0.5}Fe_{0.5}O_3$ are greater that0.30mm/s, and are 0.40mm/s and 0.60mm/s respectively. This could be an indication of octahedrally coordinated Fe^{3+} [197].

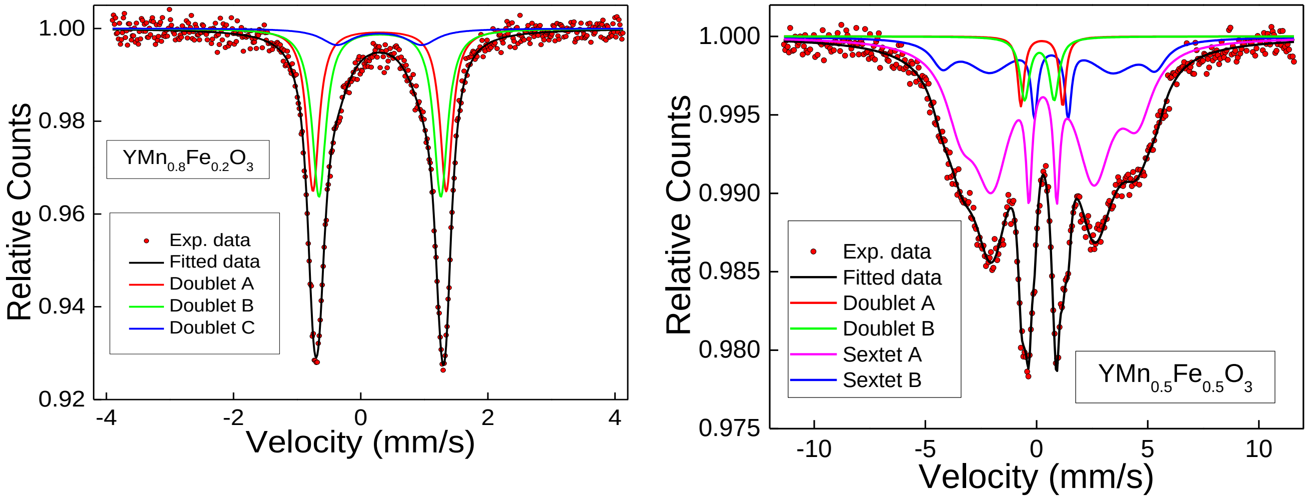

Figure 3.42: The plot of Mössbauer spectrum of (a) $YMn_{0.8}Fe_{0.2}O_3$, (b) $YMn_{0.5}Fe_{0.5}O_3$ at 300K.

Table 3.5: The Mössbauer parameters for $YMn_{1-x}Fe_xO_3$ (x = 0.2, & 0.5) at 300K.

x	**Iron Sites**	**Isomer shift (*δ*) mm/s**	**Quadrupole splitting (ΔE_Q) mm/s**	**Line width (*Γ*) mm/s**	**Hyperfine Field H_{hf} (Tesla)**	**Area R_A (%)**	**Fitting quality (χ^2)**
0.2	Doublet A	0.301±0.002	2.101 ±0.032	0.206 ±0.033	--	28.2	1.031
	Doublet B	0.302±0.001	1.916 ±0.035	0.249 ±0.028	--	52.1	
	Doublet C	0.288±0.009	1.291 ±0.046	0.449 ±0.042	--	19.7	
0.5	Doublet A	0.238±0.046	1.879±0.033	0.352±0.05	--	2.2	1.045
	Doublet B	0.129±0.034	1.33±0.032	0.520±0.046	--	4.4	
	SextetA	0.601±0.02	-0.109±0.05	0.349±0.05	29.71±0.12	24.6	
	Sextet B	0.429±0.012	0.289±0.021	0.329±0.038	24.53±0.16	68.8	

3.2.2.4 Magnetic structure and phase diagram

Neutron diffraction patterns for all studied sample have been recorded at selected temperatures between 6K and 300K. Figure 3.43 shows a section of the diffraction data at 300K and 6K for $YMn_{0.8}Fe_{0.2}O_3$. This is a representative of the samples with $x \leq 0.2$. The refinement of room temperature diffraction data has been carried out in $P6_3cm$ space group. Below 65K superlattice reflections (100) (101) and enhancement in the intensity of fundamental Bragg reflection (102) is observed indicating the antiferromagnetic nature of the samples. The magnetic structure has been refined by representation analysis using Sarah program [189]. The (100) Bragg peak is a pure magnetic peak in $YMnO_3$ and is only present in Γ_3 representation (completely absent for Γ_4 representation), while another magnetic peak (101) is seen in Γ_4 representations.With Fe doping at Mn site, a change in ratio of the intensities of the magnetic reflections is observed. A significant reduction in the intensity of (100) and an enhancement in the intensity of (101) magnetic peaks is seen in 20% Fe doped samples as shown in inset of figure 3.43. With Fe doping, the amount of Γ_4 IR increases for $YMn_{0.8}Fe_{0.2}O_3$ at 6K, with moment 2.35 μ_B. The reorientation of the spins in Fe doped samples (on changing from Γ_3 to Γ_4 IR) may be ascribed to the different magnetic anisotropy of the Fe^{3+} and Mn^{3+} ions [239]. The presence of electron in $d_z{}^2$ orbital in Fe doped $YMnO_3$ influences the anisotropy of the system leading to reorientation of the spins. The thermal variation of the refined Mn/Fe magnetic moments for $YMn_{0.8}Fe_{0.2}O_3$ is shown in the inset of figure 3.43. We calculate the thermal variations of the moment by applying molecular field model. Using the Brillouin description for reduced magnetization, $m_{Mn} = m_{sat}(T)B_2(x)$, where $x = \frac{mN\lambda(gS\mu_B)^2}{k_BT}$, $m_{sat} = 2.35\ \mu_B$, and molecular field constant $\lambda = \frac{3k_BT_c}{g^2S(S+1)\mu_B^2}$ [175], we obtained a good fit to the experimental data, as shown in inset of

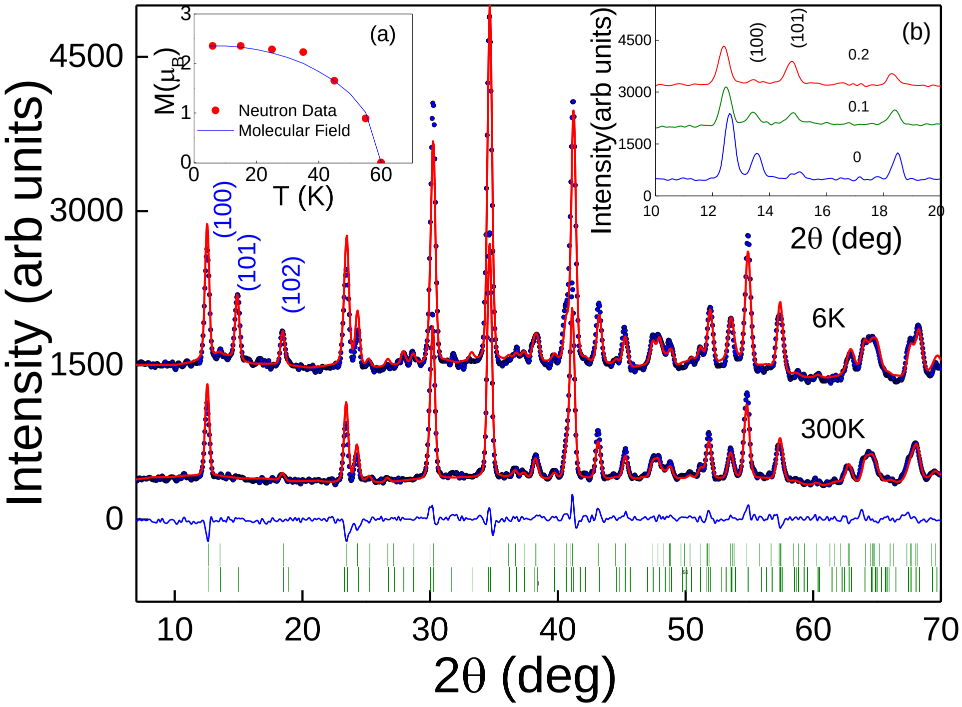

Figure 3.43: The observed (symbol) and calculated (line) neutron diffraction pattern for $YMn_{0.8}Fe_{0.2}O_3$compound at T = 6K and 300K. Lower solid line is the difference between observed and calculated pattern. The first row of tick marks indicates the position of nuclear Bragg peaks and second row indicate the position of magnetic Bragg peaks. Inset (a) shows the variation magnetic moment as a function of temperature. Inset (b) shows the raw neutron data for x= 0, 0.1 and 0.2 samples at 6K.

Figure 3.43. For these doped sample, we obtained $\lambda = 10.2\ T/\mu_B$ by taking T_N = 60K and S = 2.109. Here we are using T_N as a parameter and obtained a good fit by taking T_N = 60K .We do not observe reduction in T_N, because of the absence of neutron diffraction data at smaller intervals of temperature, although small reduction in T_N has been observed in earlier studies [207]. The angle (φ) changes from 28° for $YMn_{0.9}Fe_{0.1}O_3$ to 55° for $YMn_{0.8}Fe_{0.2}O_3$ (moment on Mn is inclined at 55° to the a axis while for $YMn_{0.9}Fe_{0.1}O_3$ it is inclined at 28° to the a axis) at 6K. Enhancement in angle (φ) has been observed as a function of Fe concentration as shown in figure 3.44. In case of Fe doped $YMnO_3$, φ angle decreases with increase in temperature. Similarly,

spin reorientation has also been observed in $HoMnO_3$. But the spin reorientation in $HoMnO_3$ is very abrupt and occurs at a specific temperature unlike in our case where the transition is continuous [134]. The Mn^{3+} spins in $HoMnO_3$ reorient sharply by 90° at thespin reorientation temperature. The spin structures for $YMn_{0.8}Fe_{0.2}O_3$ at 6K, is shown in figure 3.45. In case of $YMn_{0.8}Fe_{0.2}O_3$, the spins are coupled ferromagnetically along c-axis but are more tilted away from the a axis. In contrast, in the case of $YbMnO_3$, enhancement in transition temperature (T_N) has been observed with Fe doping at Mn site [241] and the magnetic structure, though not analyzed by the authors but we infer, remain the same with Fe doping, albeit with an enhancement in the moment values at Mn site.

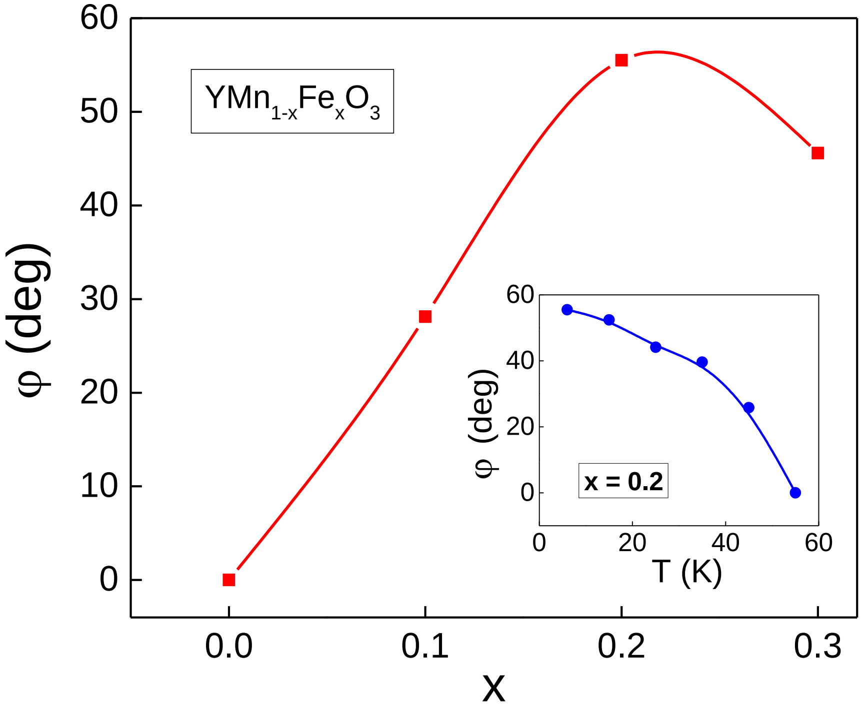

Figure 3.44: The variation of tilting angle (φ) as a function of Fe content at 6K. Inset shows the variation of tilting angle (φ) as a function of temperature for $YMn_{0.8}Fe_{0.2}O_3$.

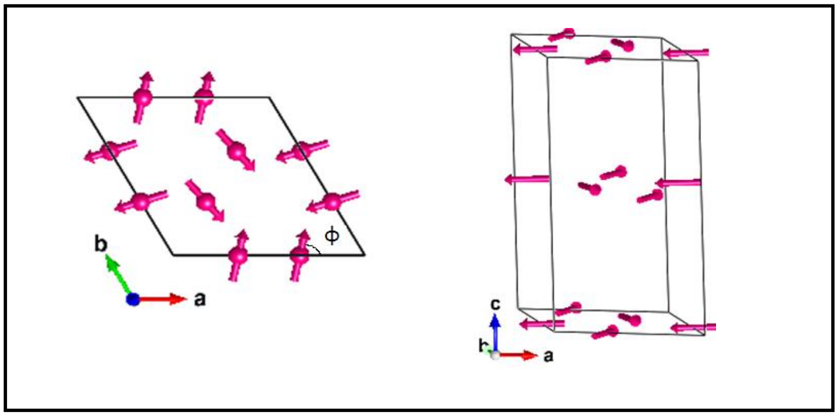

Figure 3.45: The magnetic structure for $YMn_{0.8}Fe_{0.2}O_3$ at 6K.

In higher Fe doped samples i.e. for $0.3 \leq x \leq 0.5$, a two phase refinement of neutron diffraction data has been carried out taking into account orthorhombic (*Pnma*) and hexagonal ($P6_3cm$) phases. Figure 3.46 shows a section of the diffraction data at 300K and 6K for $YMn_{0.7}Fe_{0.3}O_3$. On lowering temperature below 300K, two superlattice reflections (110) and (011) appear in the diffraction pattern. These two reflections are identified with the magnetic peaks corresponding to orthorhombic phase and are similar to the end member of this series i.e $YFeO_3$. To represent the magnetic structure of the orthorhombic phase, Bertaut's notation in the *Pnma* setting is adopted [112, 242]. The spin structure in this temperature range is explained by Γ_1 ($G_xC_yA_z$) in *Pnma* setting. The C_y and A_z components are found to be very small. In addition, for x = 0.3 and 0.4 samples, superlattice reflections (100) and (101) also appears below 65K which are characteristics of the magnetic phase of the $YMnO_3$ compound. For $YMn_{0.7}Fe_{0.3}O_3$ sample, the magnetic structure in hexagonal phase is explained by taking mixed Γ_3 and Γ_4 representations. The magnetic ground state of $YMn_{0.7}Fe_{0.3}O_3$ and $YMn_{0.6}Fe_{0.4}O_3$ is explained by taking $\Gamma_1(G_xC_yA_z)$ representation of *Pnma* setting and $\Gamma_3+\Gamma_4$ representations of $P6_3cm$ symmetry.

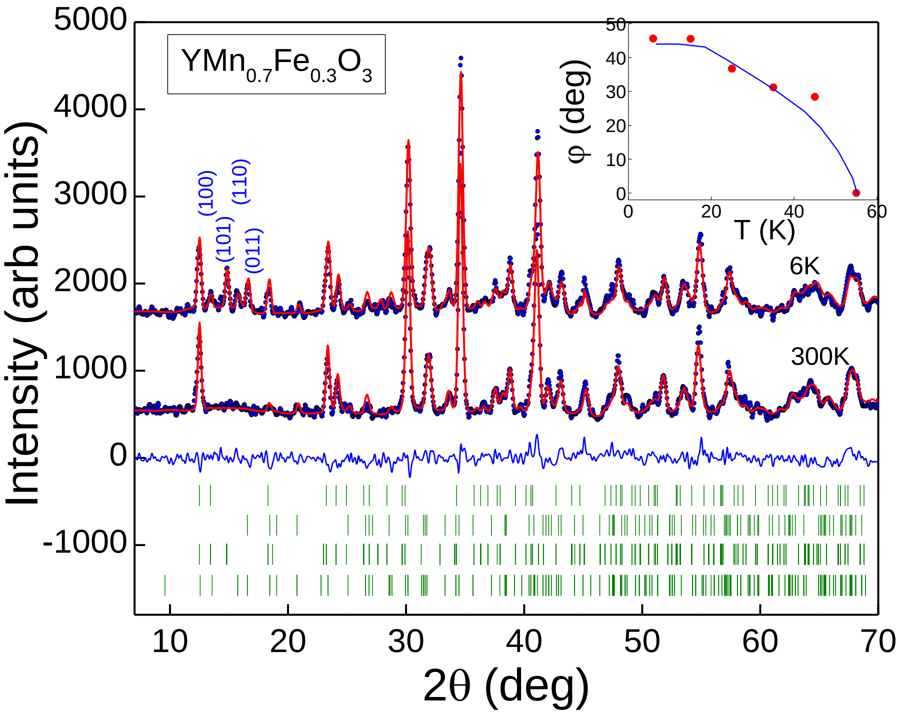

Figure 3.46: The observed (symbol) and calculated (line) neutron diffraction pattern for $YMn_{0.7}Fe_{0.3}O_3$ compound at T = 6K and 300K. Lower solid line is the difference between observed and calculated pattern. The first and second row of tick marks indicates the position of nuclear Bragg peaks for hexagonal and orthorhombic phase respectively. The third and fourth rows indicate the position of magnetic Bragg peaks. Inset shows the variation of tilting angle (φ) as a function of temperature for $YMn_{0.7}Fe_{0.3}O_3$.

In $YMn_{0.5}Fe_{0.5}O_3$, the major phase is the orthorhombic phase with a very small contribution of the hexagonal phase. So the magnetic contribution for this sample is mainly from the orthorhombic phase. Figure 3.47 shows a section of the neutron diffraction data at 300K and 6K for x=0.5 which is representative of these samples. The spin structure in this temperature range is explained by $\Gamma_1(G_xC_yA_z)$ in *Pnma* setting. The moment in the orthorhombic phase for $YMn_{0.5}Fe_{0.5}O_3$ is found to be 2.80 μ_B at 6K, which is lower than the expected value. Similar reduction in ordered moment value has been seen in $YFe_{0.6}Mn_{0.4}O_3$ [239]. The magnetic structure of $YFeO_3$ is described by taking Γ_4 ($A_xF_yG_z$) (IR) where G_z represents the antiferromagnetic arrangement of Fe^{3+} spins along the z-axis and F_y represents the ferromagnetic arrangement of spins along the y-axis due to the canting of G_z spins [14,243]. Doping with Mn is found to change the antiferromagnetic easy axis from z- axis Γ_4 ($A_xF_yG_z$) to x- axis Γ_1 ($G_xC_yA_z$) in $YFe_{1-x}Mn_xO_3$ ($0.10 \leq x \leq 0.45$) and has been ascribed to the different magnetic anisotropy of Fe^{3+} and Mn^{3+}ions [239]. Mn doping also leads to enhancement in T_{SR} (spin reorientation temperature) and reduction in T_N. For $YFe_{0.55}Mn_{0.45}O_3$ sample, T_{SR} is 330K, which means the antiferromagnetic easy axis changes from z- axis Γ_4 ($A_xF_yG_z$) to x- axis Γ_1 ($G_xC_yA_z$) at

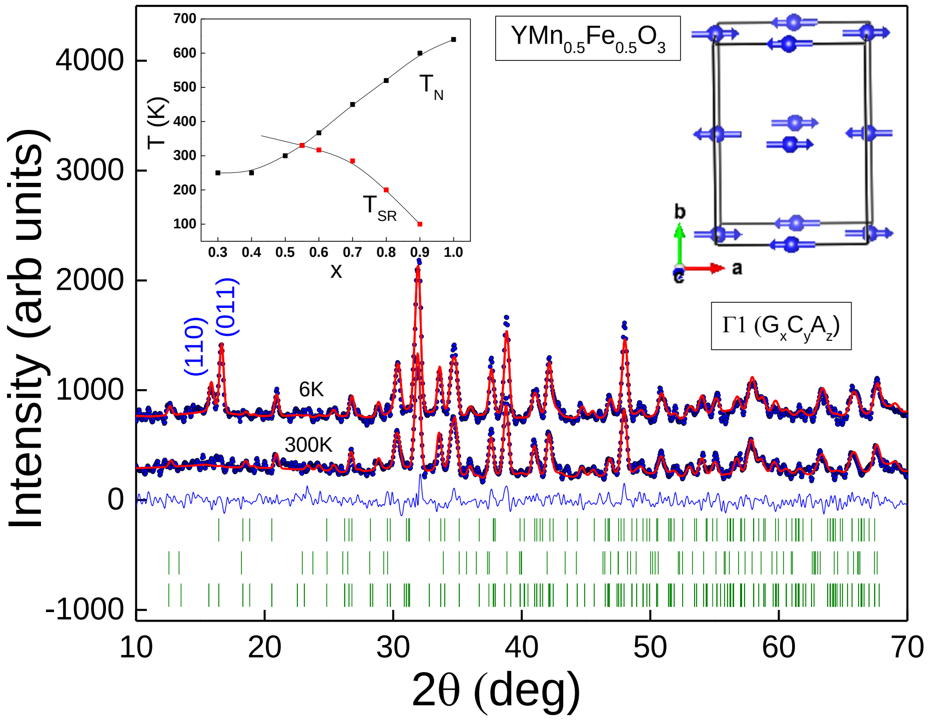

Figure 3.47: The observed (symbol) and calculated (line) neutron diffraction pattern for $YMn_{0.5}Fe_{0.5}O_3$compound at T=6K and 300K. Lower solid line is the difference between observed and calculated pattern. The first row of tick marks indicates the position of nuclear Bragg peaks and second row indicate the position of magnetic Bragg peaks. Inset shows the magnetic structure of the compound at 6K and variation of T_{SR} and T_N as a function of Fe concentration (x).

this temperature. Extrapolating T_{SR} to higher compositions of Mn indicates that T_{SR} would be above 300K for x=0.5 sample. A plot for T_{SR} and T_N as a function of Fe concentration (x) is shown in inset of figure 3.47. This explains the absence of T_{SR} in the studied samples and the magnetic structure at 300K is already Γ_1.

The above results are summarized in phase diagram for the series $YMn_{1-x}Fe_xO_3$ and are shown in 3.48. The structure remains hexagonal for $x \leq 0.2$, above which the mixed orthorhombic and hexagonal phase has been observed. The antiferromagnetic transition temperature changes slightly with Fe concentration [244].

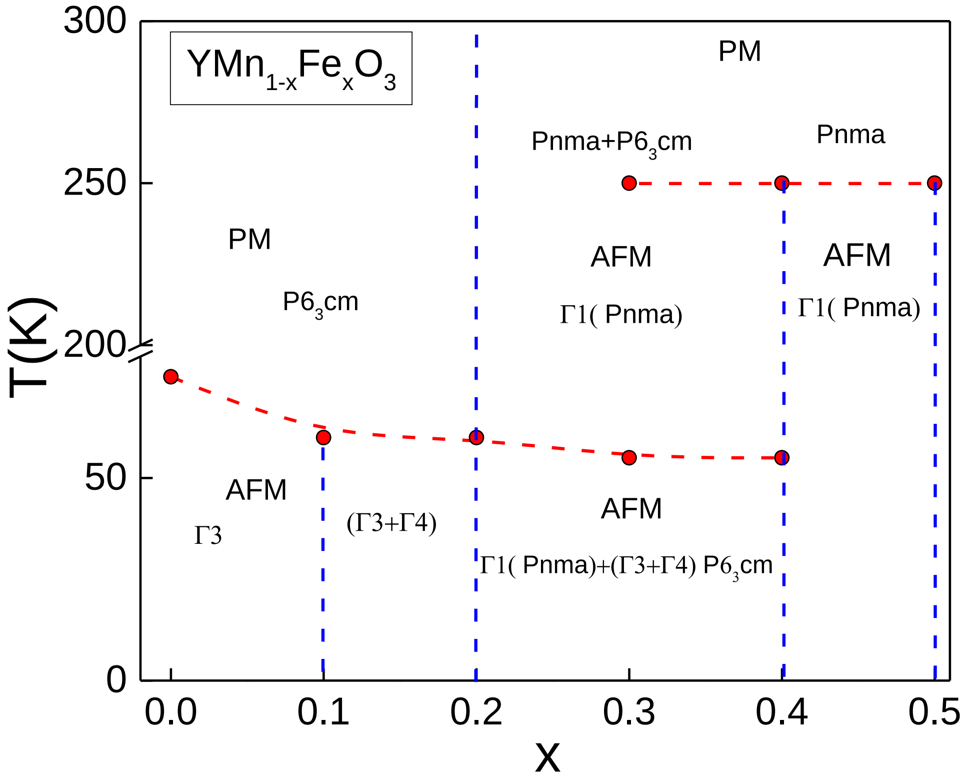

Figure 3.48: Phase diagram of $YMn_{1-x}Fe_xO_3$ $(0.0 \leq x \leq 0.5)$.

3.2.2.5 Dielectric properties

The dielectric constant (ε′) as a function of temperature (behavior is same for all frequencies, for clarity only 10 kHz data shown) is shown in figure 3.49. A distinct anomaly is observed in dielectric constant and tanδ for $YMnO_3$ near Néel temperature (T_N) as shown in figure 3.49(a). This behavior is similar to that reported earlier for the same compound [149,155, 232]. For a detailed investigation of magnetoelectric effect in Fe doped $YMnO_3$, we chose two compositions, one with the hexagonal structure (x = 0.2) and one with the orthorhombic phase (with a small contribution of the hexagonal phase, x = 0.5) as shown in figure 3.49(b) and 3.49(c). With Fe doping, the anomaly is observed to be diminished as shown in figure 3.49(b). Below T_N, however, no further discontinuity in ε′ is observed in the x=0.2 doped sample, in which we observe a spin reorientation behavior as a function of temperature. This is in contrast to dielectric measurement of single crystal of $HoMnO_3$, where a peak has been observed at the spin reorientation temperature [129,154], where the Mn^{3+} spin reorient sharply by 90°. No such anomalyis observed in the case of $YMnO_3$ and Fe doped samples and instead in these samples, the orientation of the spin changes continuously with temperature. This is in agreement with the progressive suppression of the spin reorientation behavior observed in the case of $Ho_{1-x}Y_xMnO_3$ samples [128]. The coupling of ferroelectric and magnetic order in a ferroelectromagnets in the absence of an external applied field occurs by the electron-phonon interactions [91, 149]. Here in case of an antiferromagnetic $YMnO_3$, in the absence of an external electric and magnetic field, isostructural phase transition at antiferromagnetic transition temperature (T_N) and atomic displacements of atoms below T_N are likely to be responsible for observed magnetoelectric effect [149]. The displacement of Mn from its x~1/3 position at T_N and below has been observed in previously reported neutron diffraction experiments [150]. The suppression of dielectric anomaly in Fe doped samples may be correlated with the change in coupling between spin correlation and electric polarization. In earlier studies of Fe doping at Mn-site of $YbMnO_3$, it has been observed that increase in Fe content leads to weakening of ferroelectricity in the system [241]. For the ferroelectric distortion to occur, the d orbitals in the direction of electric polarization must be empty. The ferroelectric distortion in hexagonal manganites is induced by the hybridization between unoccupied d_z^2 orbital of Mn and p_z orbital of oxygen atom. The weakening of ferrolectricity in Fe doped $YbMnO_3$ has been attributed to the presence of partially filled dz^2 orbital which lowers the degree of hybridization between d_z^2 orbital of Mn/Fe and p_z orbital of oxygen atom.

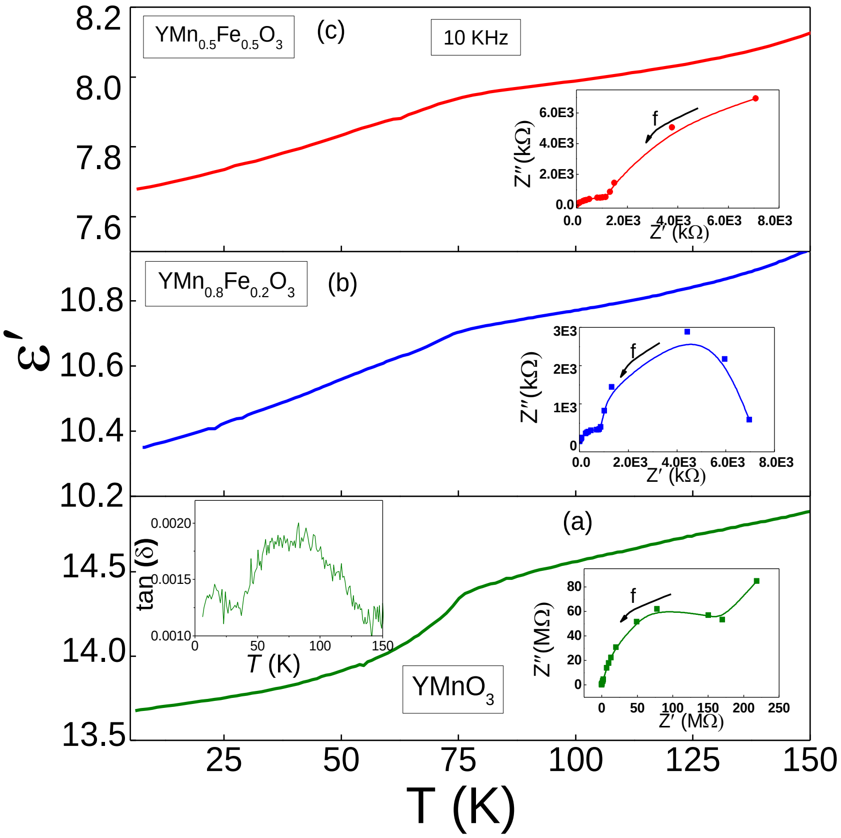

Figure 3.49: The variation of dielectric constant (ε') with temperature (T) for (a) $YMnO_3$ (b) $YMn_{0.8}Fe_{0.2}O_3$ and (c) $YMn_{0.5}Fe_{0.5}O_3$. Inset shows the complex impedance (Z'') plane plot versus real part of impedance (Z'). Dielectric loss (tan(δ)) versus temperature (T) is shown in the inset of a.

In $YMn_{0.5}Fe_{0.5}O_3$, the main phase is the orthorhombic phase with a very small contribution from the hexagonal phase (~ 7%), so the dielectric anomaly in this compound might be related with the remnant hexagonal phase of the $YMnO_3$. As shown in the inset of figure 3.49(a), two semicircle arcs can be seen in the impedance plane. Similar kind of two semicircular arcs has been seen in case of $HoMnO_3$ ceramic samples [245]. These two arcs in different frequency regions correspond to contribution from sample electrodes interface as well as from sample.The arc in the lower frequency region (away from the origin) corresponds to the dielectric response from electrodes, whereas the dielectric response from grain and grain boundary is represented by the arc in high frequency region (towards the origin). The complex impedance can be defined as

$$Z^* = Z' + jZ'' = \frac{R}{1+(\omega CR)^2} + j\frac{\omega CR^2}{1+(\omega CR)^2},$$

Where Z^*, R and C are the complex impedance, resistance and capacitance of the studied samples. Two semicircular arcs are also observed in Fe doped samples as shown in inset of figure 3.49(b) and figure 3.49(c).

The anomaly in dielectric constant at Néel temperature (T_N) for x=0, 0.2 & 0.5 ($YMn_{1-x}Fe_xO_3$) samples is evidenced by a decrease in ε below the T_N. In order to analyze this dielectric anomaly at T_N, we have obtained the value of dielectric constant at 0K, ε′(0) using a exponential function similar to that done before [148]. Then we subtract off the lattice contribution from the observed dielectric constant below T_N and this difference Δε is shown in inset of figure 3.50 for these three samples. We find a different behavior of dielectric difference as a function of temperature for parent and Fe doped samples. With Fe doping, the difference between lattice contribution and the observed dielectric constant decreases. This behavior of dielectric anomaly below T_N may be attributed to the different spin structure for parent and Fe doped sample. To understand the magnetoelctric effect of ferroelectric antiferromagnet, we have considered the free energy expansion in the Landau theory [148].

$$F = F_0 + \frac{a_1}{2}L^2 + \frac{a_2}{2}L^4 + \frac{b_1}{2}P^2 + \frac{c_1}{2}P^2L^2 + \frac{c_2}{2}P^2H^2 - EP$$

where E, H, P and L are the electric field, magnetic field, polarization and antiferromagnetic vector, respectively. The minimum of the free energy defines the equilibrium state of the system.

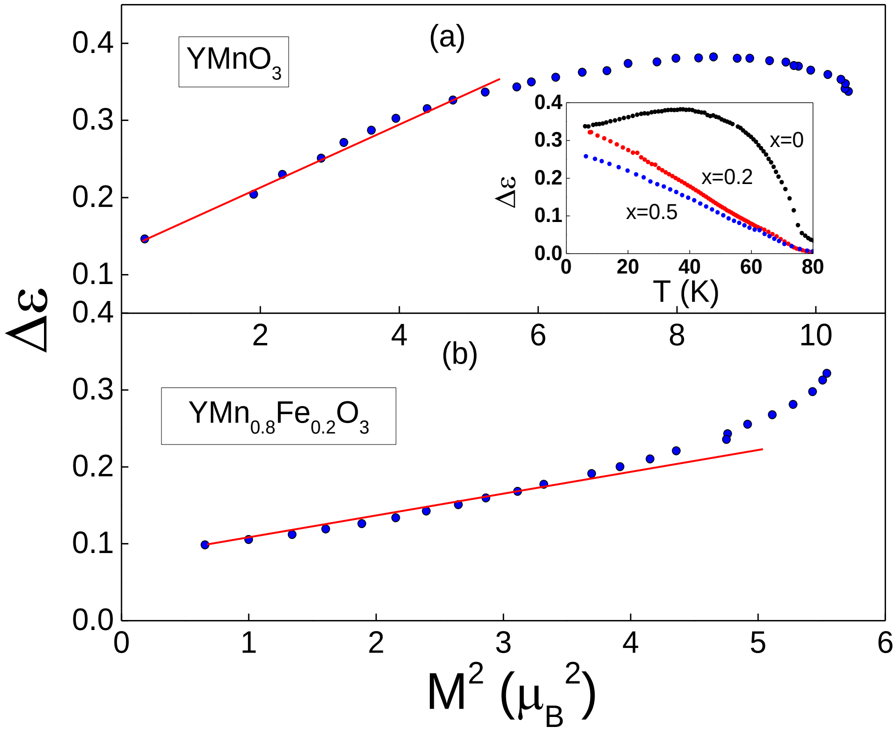

Figure 3.50: The variation of Δε (ε'(T) - ε'(0)) as a function of M^2(T) for (a) YMnO3 and (b) YMn$_{0.8}$Fe$_{0.2}$O$_3$. Inset shows the thermal variation of Δε for YMnO$_3$ (x=0), YMn$_{0.8}$Fe$_{0.2}$O$_3$ (x=0.2), and for YMn$_{0.5}$Fe$_{0.5}$O$_3$ (x=0.5).

By considering the equilibrium condition, we find

$$\frac{\partial F}{\partial P} = 0, \qquad \frac{\partial F}{\partial L} = 0$$

$$\frac{\partial F}{\partial P} = b_1 P + c_1 P L^2 + c_2 P H^2 - E = 0 .$$

dielectric constant of a medium can be defined as, $\varepsilon = 1 + \frac{P}{\varepsilon_0 E}$, where ε_0 is the permittivity of the free space. Using above equation in the absence of any external magnetic field (H=0), for small values of L the dielectric constant can be written as, $\varepsilon \approx 1 + \frac{1}{b_1} - \frac{c_1 L^2}{b_1^2}$. We can rewrite this equation as $\varepsilon = a + bL^2$. Therefore, the temperature dependence of dielectric permittivity near T_N is expected to be proportional to the $L^2(T)$. This antiferromagnetic vector (L) is equal to the magnetic moment (M) below T_N. In figure 3.50 we show a plot of $\Delta\varepsilon$ as a function of M^2. A clear linear region is observed for low M values demonstrating a coupling of the two order parameters in the absence of field. Earlier, a similar suppression of dielectric behavior in the magnetically ordered state and a linear dependence of $\Delta\varepsilon$ versus M^2 had been observed in $BaMnF_4$ [246] and attributed to presence of weak ferromagnetic character in the sample. Similar behavior has also been reported in the case of non-centrosymmetric ferromagnet $BiMnO_3$ [247]. In contrast to the previous observations, the present results bring out a correlation between ε and M in the case of a frustrated antiferromagnet in the absence of a magnetic field and ferromagnetic behavior.

3.2.2.6 X-ray Absorption Spectroscopy

In the present study we have performed XANES and EXAFS measurements on $YMn_{1-x}Fe_xO_3$ ($0.1 \le x \le 0.5$) samples to probe the local structure surrounding the Mn and Fe sites. Figure 3.51 shows the normalized XANES spectra measured at Mn K-edge for the $YMn_{1-x}Fe_xO_3$ (for x = 0.0, 0.1, 0.2, 0.3, 0.4 and 0.5) samples along with that of Mn metal foil and commercial Mn_2O_3 powder. The extended part of pre edge region denoted by A is shown in the inset of figure 3.51. It can be seen from figure 3.51 that the pre edge feature around ~6540 eV changes with increase in Fe concentration. Firstly the peak intensity increases upto 20% on Fe doping and then it starts decreasing with increase in Fe concentration. Also the pre edge peak for higher Fe ($0.3 \leq x \leq 0.5$) concentration starts to flatten out. The intensity of the pre edge depends on the coordination geometry. The presence of centre of symmetry for octahedral coordination would yield lower intensity pre-edge peak compared to tetragonal coordination geometry [248]. As it is observed by x-ray and neutron diffraction study on this system, for up to 20% of Fe doping, the samples are predominantly hexagonal where Mn coordination is fivefold without any centre of symmetry and this gives rise to an intense pre edge peak as shown in figure 3.51. However, beyond 20% Fe doping, a second orthorhombic phase appears where Mn is coordinated by six oxygen atoms (octahedral coordination) resulting in the decrease in the pre edge intensity. The Mn K-edge positions in $YMnO_3$ and $YMn_{1-x}Fe_xO_3$ samples coincide with that of Mn_2O_3, and hence Mn ion should have avalence or effective chargeof +3 in the samples. The XANES measurements performed by Namdeo et. al [232] on similar systems have showed the presence of mixed

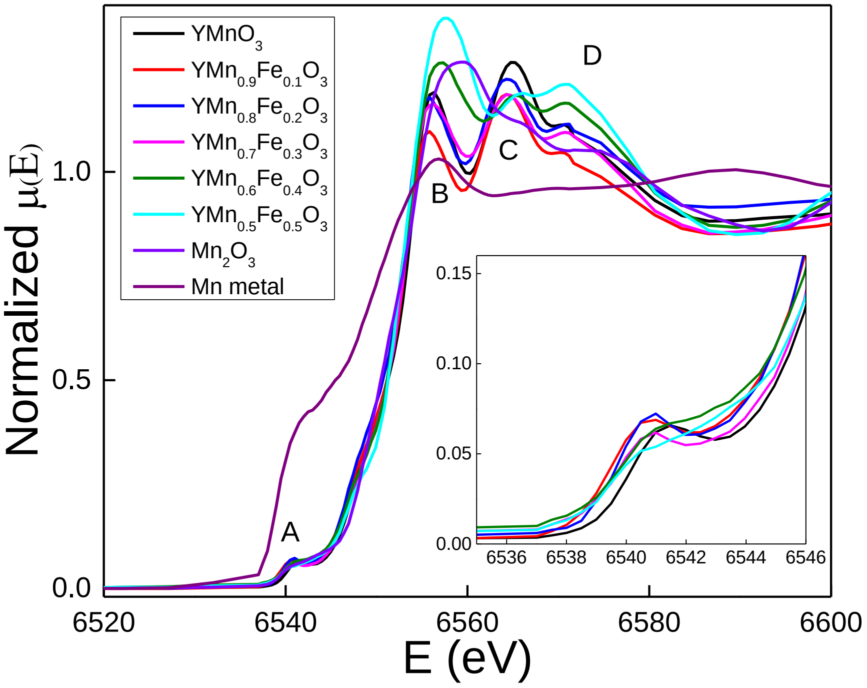

Figure 3.51: Normalised XANES spectra of $YMn_{1-x}Fe_xO_3$ ($0.0 \leq x \leq 0.5$) at Mn K-edge.

oxidation states of Mn in Fe doped $YMnO_3$ samples. However, in our case no shift in the Mn edge position is observed and it is concluded that Mn is present in +3 oxidation state in all of the samples. The XANES features B and C in figure 3.51 are similar for undoped and 10% Fe doped $YMnO_3$ samples suggesting that MnO_5 coordination remains intact upon Fe doping, however the intensity ratio is changed slightly for 10% doped samples compared to pure $YMnO_3$ sample. Similar features are also observed in Zn doped $YMnO_3$[229], however in case of Ni, Cu and Co doped $YMnO_3$ [230], these features are different from $YMnO_3$ and are attributed to structural transition to orthorhombic phase. It can be seen from figure 3.51 that for other samples also, the peak positions are same though the relative peak intensities of B and C change with increase in Fe concentration which manifests drastic change in local structure of the samples. Along with the change in intensity of the peaks at B and C, as Fe concentration in the samples is increased, one new peak appears at D.

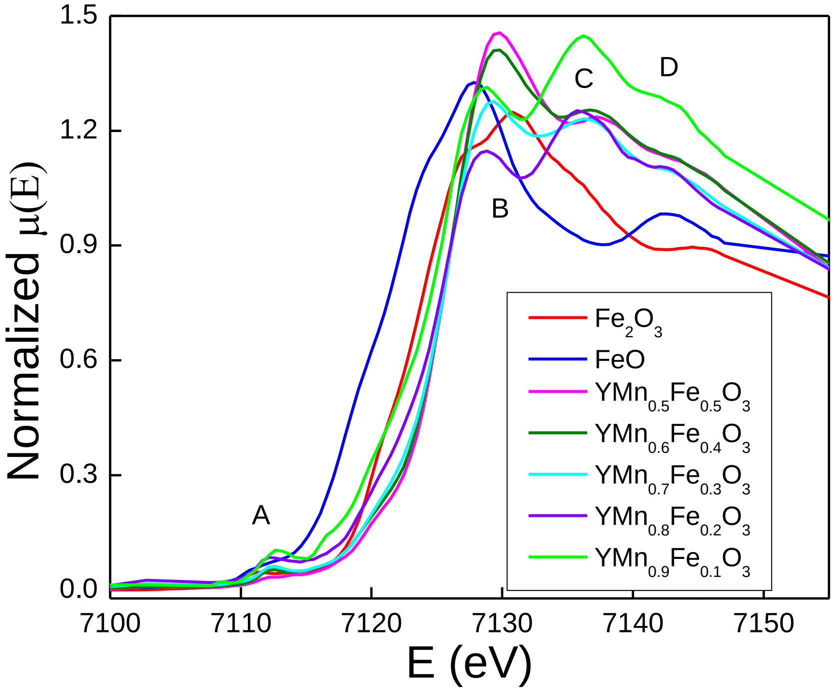

Figure 3.52: Normalised XANES spectra of $YMn_{1-x}Fe_xO_3$ ($0.0 \leq x \leq 0.5$) at Fe K-edge.

Figure 3.52 shows the XANES spectra of $YMn_{1-x}Fe_xO_3$ samples measured at Fe K-edge along with that of commercial Fe_2O_3 sample. The Fe K-edge energies in the Fe doped samples show a small shift towards higher energy side than that in the Fe_2O_3 standard sample manifesting an oxidation state higher than +3 in the Fe doped samples.The edge position taken from the maxima of first derivative ate listed in Table 3.6. However, such small change in oxidation state of Fe has been not observed in Mössbauer spectroscopy and magnetization measurements. It is clearly visible that the pre edge (denoted by A) intensity decreases with increase in Fe content. The changes are also observed at B, C and D positions. With increase in Fe concentration, intensity at B is found to increase while it decreases at C and D.

Table 3.6: Fe K-edge energy of reference (Fe_2O_3) and $YMn_{1-x}Fe_xO_3$ samples.

Sample	Energy (E_0) (eV)
Fe_2O_3	7123.91
$YMn_{0.9}Fe_{0.1}O_3$	7125.91
$YMn_{0.8}Fe_{0.2}O_2$	7125.93
$YMn_{0.7}Fe_{0.3}O_3$	7125.99
$YMn_{0.6}Fe_{0.4}O_3$	7126.42
$YMn_{0.5}Fe_{0.5}O_3$	7126.56

Figure 3.53 and 3.54 shows the $\chi(R)$ versus R spectra at Mn K-edge and Fe K-edge for varying Fe concentration, respectively. The changes in the coordination peaks are clearly visible. The second peak in $YMnO_3$ at ~3 Å (phase uncorrected spectra) is contribution of Mn-Y and Mn-Mn shell at 3.29 Å and 3.52 Å respectively which is the signature of hexagonal coordination. As Fe concentration increases, the peak starts decreasing and another peak at 3.25 Å starts appearing

from x=0.3 and becomes significant for x=0.4 and x=0.5. Similar changes are also observed in XANES spectra (discussed above) and this shows contribution from another crystalline phase in the samples as obtained from x-ray and neutron diffraction measurements also. Thus the FT-EXAFS spectra forthe samples with x=0.3, 0.4 and 0.5 are fitted with two types of crystal structures, hexagonal and orthorhombic phase. The ratio of the contribution of the two phases has been taken from the x-ray and neutron diffraction results and the coordination number is kept fixed while fitting. The values of Fe-O bond lengths obtained after fitting are comparable to Mn-O bond length for haxagonal structure showing substitution of Mn atoms by Fe in the $YMn_{1-x}Fe_xO_3$ samples.

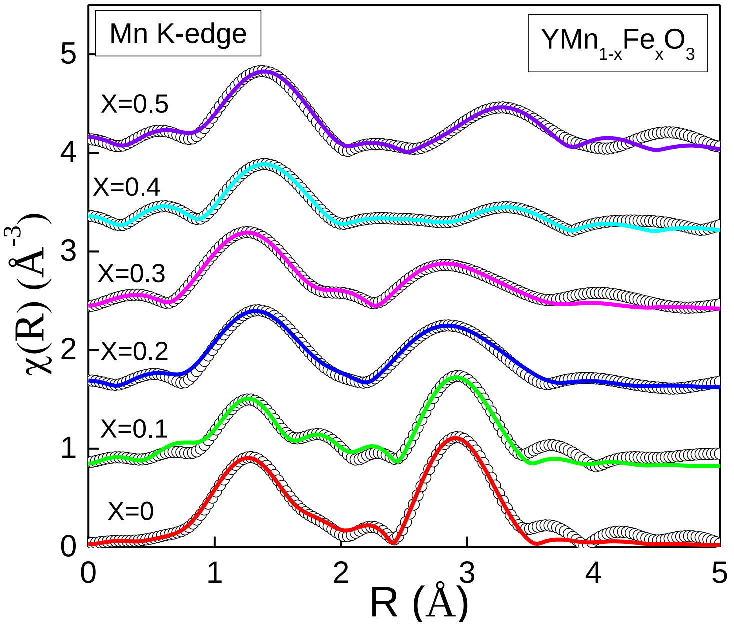

Figure 3.53: Fourier transformed EXAFS spectra of $YMn_{1-x}Fe_xO_3$ at Mn K-edge (Scatter points) and theoretical fit (Solid line).

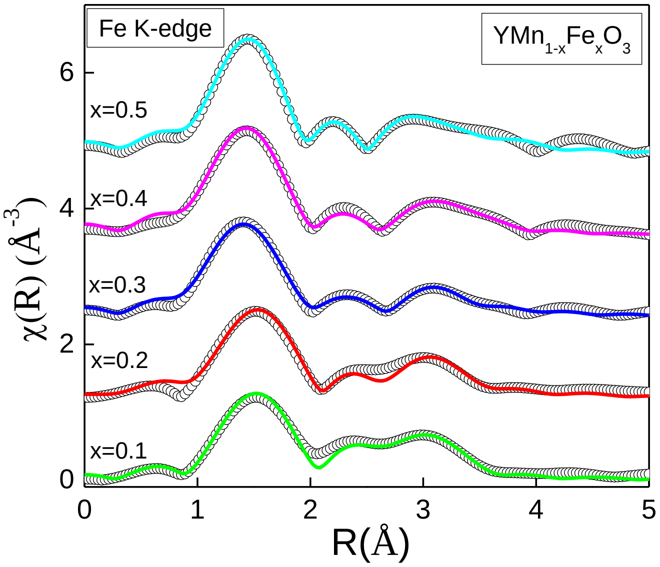

Figure 3.54: Fourier transformed EXAFS spectra of $YMn_{1-x}Fe_xO_3$ at Fe K-edge (Scatter points) and theoretical fit (Solid line).

3.3 Computational studies on $YMnO_3$

The first principle calculations described in this thesis were performed using a plane wave pseudopotential implementation of density functional theory (DFT) within the local density approximation (LDA) [249]. Density functional theory (DFT) is most popular method available in condensed matter physics for determination of electronic properties and other ground state properties of matter. It is called a functional theory as the energy is a function of the density, E(ρ), which in turn is a function of the position, ρ(r). The basic idea of DFT is to describe a many-body interacting system via its electron density.It is based on the Hohenberg-Kohm theorems [250-252]. The first Hohenberg-Kohm theorem states that the properties of the ground state of a many-electron system are uniquely determined by the electron density. It reduces the 3N degrees of freedom of the N-body system to only three spatial coordinates through the use of density functional. The second theorem establishes that the groundstate energy can be obtained variationally (the density that minimizes the total energy is the exact groundstate density).

Within these DFT formalisms, the energy is split up as follows, $E(\rho) = T(\rho) + \int V_{ext}(r)\rho(r)dr + V_H(\rho) + E_{xc}(\rho)$, where, $T(\rho)$ is the electronic kinetic energy, V_{ext} is potential on electron due to the nuclei, and last term is the exchange-correlation energy. It is this Kohn-Sham equation which is solved using the QUANTUM ESPRESSO (QE) package in order to determine the properties of our system [253]. This package contains two codes in addition with some auxiliary codes for the study of calculation of electronic structure properties within density functional theory, using the plane wave basis set and peudopotentials. The two codes are (i) PWscf (plane wave self consistent field), (ii) CP/ FPMD (variable cell Car Parinello molecular dynamics). The PWscf code can perform different calculations such as, structural relaxation, electronic structure, molecular dynamics etc.

All the DFT calculations in the present work were performed with the QUANTUM ESPRESSO (QE) by using PWscfcode. These calculations were performed with the Hubbard correction (U).The exchange-correlation potential utilized in these calculations was the Perdew-Zunger (PZ) version of the local density approximation (LDA) [254]. In hexagonal $YMnO_3$, calculations were performed with a grid of 12×12×12 reciprocal lattice points. In all calculations, the electronic self-consistent cycles were made to converge until the variation of the total energy was less than 10^{-8}eV. The pseudopotentials used in the calculation were taken from the database provided in the QE package. In these pseudopotentials, the total number of valence states is 7 for Mn, 3 for Y and 6 for oxygen. An energy cutoff of 120 Ry on the plane wave basis was used in representation of Kohn-Sham wave-functions. Structural optimization was carried out with Broyden–Fletcher–Goldfarb–Shanno (BFGS) algorithm.

The starting values of structural parameters (lattice parameters, coordinates) were taken from our neutron data at 6K. In our calculations, we imposed an A-type antiferromagnetic order and did the structural relaxation. The calculations were performed with Hubbard correction (U=8eV). The relaxed lattice parameters and unit cell volume obtained are summarized in table 3.7 and compared with experimental structures. The calculated bond lengths are reported intable 3.8. All calculations were performed at 0 K for a A-type AFM order. The relaxed structure is in excellent agreement with the experimental data. The cell parameter is slightly overestimated while the a parameter is in good agreement with the experimental value. The calculated atomic positions are also in good agreement with the experimental data. The simulation results of QE are also compared with the results obtained by using Vienna ab-initio simulation package (VASP). By using VASP, relaxed structure parameters were obtained within both the local density approximation (LDA) and the generalized gradient approximation (GGA) [255]. The structural parameters and the bond lengths obtained using QE code are in agreement with the experimental as well as with the simulations results of VASP (LDA).

Table 3.7: Comparison between the calculated and experimental (6K) structural parameters of $YMnO_3$ (Hexagonal phase, space group $P6_3cm$). The experimental structure (space group $P6_3cm$) consists of Y1 and O3 atoms at the position 2a(x,y,z), Y2 and O4 at 4b(x,y,z), and Mn, O1, and O2 at 6c(x,y,z) Wyckoff site.

			VASP [255]		**QE**
		Expt.	**GGA**	**LDA**	**LDA**
	a (Å)	6.1212	6.2527	6.0952	6.0651
	b (Å)	6.1212	6.2527	6.0952	6.0651
	c (Å)	11.4002	11.6441	11.4159	11.6400
O1	x	0.30764	0.3080	0.3057	0.3066
	y	0.0000	0.0000	0.0000	0.0000
	z	0.16565	0.1652	0.1641	0.1754
O2	x	0.64087	0.6416	0.6398	0.63997
	y	0.0000	0.0000	0.0000	0.0000
	z	0.33743	0.3348	0.3360	0.32433
O3	x	0.0000	0.0000	0.0000	0.0000
	y	0.0000	0.0000	0.0000	0.0000
	z	0.48449	0.4751	0.4760	0.4600
O4	x	0.3333	0.3333	0.3333	0.3333
	y	0.6666	0.6666	0.6666	0.6666
	z	0.02164	0.0208	0.0207	0.0391
Mn	x	0.33884	0.3334	0.3334	0.33231
	y	0.0000	0.0000	0.0000	0.0000
	z	0.0000	0.0000	0.0000	0.0000
Y1	x	0.0000	0.0000	0.0000	0.0000
	y	0.0000	0.0000	0.0000	0.0000
	x	0.28168	0.2740	0.2753	0.22825
Y2	x	0.6666	0.6666	0.6666	0.6666
	y	0.3333	0.3333	0.3333	0.3333
	z	0.23650	0.2319	0.2311	0.23189

Table 3.8: Comparison between the calculated and experimental bond lengths in YMnO$_3$ (Hexagonal phase, space group P6$_3$cm).

		VASP [255]		**QE**
Bond (Å)	**Exp**	**GGA**	**LDA**	**LDA**
Mn-O1	1.90	1.93068	1.8805	2.028
Mn-O2	1.862	1.92888	1.8796	2.035
Mn-O3	2.082	2.10500	2.0508	2.069
Mn-O4	2.039	2.09802	2.0451	2.075
Y1-O1	2.301	2.30498	2.2550	1.960
Y1-O2	2.286	2.35047	2.3021	2.453
Y1-O3	2.30	2.34124	2.2903	2.698
Y2-O1	2.271	2.30279	2.2550	2.208
Y2-O2	2.276	2.34065	2.2923	2.223
Y2-O4	2.45	2.45812	2.4026	2.244
Mn-Mn	3.505	3.60947	3.51855	3.507
Mn-Y1	3.240	3.35726	3.27232	3.335
Mn-Y2	3.371	3.41139	3.68071	3.374

3.4 Conclusion

In this chapter, we have investigated the influence of Y- and Mn-site substitutions on the structural, magnetic and frustrated behavior of the hexagonal YMnO$_3$. The Y-site doped compounds are found to be isostructural and crystallize in hexagonal structure in $P6_3cm$ space group. The Mn-site doped compounds are also found to be isostructural except for the case of higher Fe concentration.

The partial substitution of magnetic ions (Yb, Er, Ho, Tb) at Y-site changes the magnetic structure significantly, while the transition temperature is suppressed slightly. The magnetic structure of YMnO$_3$ is described by Γ_3 below T_N ~ 75K. The magnetic structure changes gradually from $\Gamma_3 + \Gamma_4$ to Γ_4 IR by Er and Yb doping, while the moments at 6K remain almost unchanged with doping. Temperature dependent spin reorientation behavior has been observed in

Ho doped sample, in which the magnetic structure changes from Γ_3 IR to $\Gamma_3 + \Gamma_4$ with increase in temperature for $T \geq 35K$. However, in Tb doped sample, the magnetic structure at 6K has been explained by $\Gamma_4^{Tb,Mn}$ IR. The moment on Tb has been observed only at 6K. The partial substitution of Y by magnetic ions not only change the long range Mn order but also effect the short range magnetic correlations, along with the frustrated behavior of the compounds. The magnetic coupling between the magnetic R ion and Mn moments plays an important role here and relieves the frustration effects inherent to the quasi-two dimensional Mn moment ordering.

Doping with these three ions, Ga^{3+} (d^{10}), Ti^{4+} (d^0) and Fe^{3+} (d^5) reduces T_N significantly and they influence the magnetic structure differently. The magnetic structure remains same on doping with nonmagnetic ion Ga^{3+} (d^{10}). However, the magnetic structure is modified on doping with Ti^{4+} (d^0) and is described by the basis vectors of the Γ_2 IR with moment $2.3\mu_B$ at 6 K. In Fe doped samples, the magnetic structure is described as a mixture of Γ_3 and Γ_4 irreducible representation (IR) in the hexagonal phase and the ratio of these two IRs is found to vary with Fe doping ($x \leq 0.2$). The magnetic ground state in the orthorhombic phase of the higher doped samples ($x \geq 0.3$) is explained by taking Γ_1 ($G_xC_yA_z$) representation of *Pnma* setting. The ordered moments are found to be reduced from the expected value for a Mn^{3+} ion in all these compounds indicating the frustrated nature of these compounds. In $YMnO_3$, suppression of dielectric constant ε' is observed below T_N indicative of magnetoelectric coupling. This anomalous behavior reduces in Fe doped samples. The dielectric constant is found to be correlated with the magnetic moment (M) obtained from neutron diffraction experiments and follows a M^2 behavior close to T_N in agreement with Landau theory.

Computational first principle calculations were performed on pure hexagonal-$YMnO_3$.These calculations were performed with the Hubbard correction. All the DFT calculations were performed with the QUANTUM ESPRESSO (QE) code. In our calculations, we imposed an A-type antiferromagnetic order and did the structural relaxation. The relaxed structural parameters obtained by QE code are reported. They are in agreement with the experimental as well as with the simulations results of VASP.

Chapter 4

Effect of A-site and B-site doping on the magnetic properties of orthorhombic $CaMnO_3$

In perovskite manganites, electrical charge, spin, and lattice degrees of freedom which are strongly coupled, is a source of unique and intriguing properties. Some important properties include colossal magnetoresistance, ferroelectricity, phase separation, orbital and charge ordering etc. These materials offer a degree of chemical flexibility that permits the relation between the structural, electronic and magnetic properties of these oxides to be examined in a systematic way.The perovskite manganites have been extensively studied in view of the existence of large variety of physical phenomena.

Recently, there is overwhelming evidence that these compounds with high chemical homogeneity can show spatially inhomogeneous structures, i.e. regions showing different magnetic and electronic phases [41-46]. In particular, attention was paid to the unexpected behavior observed for the low doped-regime, where a ferromagnetic (FM) component develops together with G-type antiferromagnetic structure. This is observed in both hole doped and electron doped manganites. However, in contrast with the hole-doped systems, there have been very few attempts to understand the electron-doped (Mn (IV)- rich) systems theoretically as well as experimentally. The role of spin canting and/or phase separation leading to FM behavior in these compounds has been a subject of discussion in literature.

The doping in the $CaMnO_3$ leads to the presence of mixed valent Mn ions, which is responsible for the different electronic and magnetic properties. The debate over phase separation versus canted magnetic structure in the electron doped manganites (Mn^{4+} rich region of the phase diagram) continues to be of interest. In the Ca-site substituted studies both phase separation and canted behavior has been observed. In the introduction, we have discussed about the presence of phase inhomogeneities in doped orthorhombic calcium manganites. In electron doped regions of $A_{1-x}Ca_xMnO_3$ (A = Sm, Pr) for x=0.9 a mixture of G-type AFM and ferromagnetic component has been observed i.e phase separation has been confirmed for these compounds [54]. In $Pr_{0.1}Ca_{0.9}MnO_3$, 6-7% of C-type monoclinic phase also has been seen which is considered as a minority phase [65]. In the case of $Ho_{0.1}Ca_{0.9}MnO_3$,canted $C_XF_YA_Z$ magnetic ordering has been observed, and with further Ho doping canting decrease and it vanishes for ≈ 17.5% of Ho doping [66].

The effect of substituting at the Mn site in $CaMnO_3$ has been previously investigated by various authors. It has been found that the introduction of pentavalent or hexavalent ion (Nb,Ta,W,Mo) in $CaMnO_3$ at Mn^{4+} site generates Mn^{3+} ion and consequently leads to colossal magnetoresistance (CMR)[256]. This doping also induces ferromagnetic (FM) double – exchange interactions and a quasi - semimetallic behavior. Doping at Mn site with Ru leads to the development of long-range ordered ferromagnetic phase which co-exist with the AFM phase of $CaMn_{1-x}Ru_xO_3$ system with $x \geq 0.10$ [67]. However, doping of $CaMnO_3$ at Mn site with Mo induces FM interactions just for low Mo concentrations (~ 6%) while with increase in Mo concentration FM interactions are suppressed and leads to a C-type AFM state [68]. For 4% Mo concentration, $A_XF_yG_Z$ magnetic structure has been observed and it is seen that around 110K all the three components appear simultaneously, but the neutron diffraction study is not able to distinguish between phase separation and spin canting behavior in this compound. This particular magnetic structure in turn modifies the magnetic and electrical properties of the compound. It has also been found that partial substitution of Mn^{4+} with an ion of same valence (eg. Ti^{4+}) does not induce colossal magnetoresistance (CMR) [257]. In the series of samples, $CaMn_{1-x}Ti_xO_{3-\delta}$ it is observed that samples with x = 0 and 0.1 exhibits weak ferromagnetic behavior due to spin canting and further increase in concentration of Ti^{4+} suppresses the weak ferromagnetic component.

4.1 Effect of A-site doping on the magnetic properties of $CaMnO_3$

4.1.1 Studies on Yttrium doped $CaMnO_3$

Hole doped managnites $La_{1-x}Ca_xMnO_3$ exhibit a complex magnetic phase diagram. Doping $CaMnO_3$ with Y^{3+} ion which is non magnetic and similar to La^{3+}, albeit with lower ionic radii, it was expected, that an equally complex magnetic phase diagram would emerge [258-259]. However, the previous study on Y doped $CaMnO_3$ could not establish the presence of either phase-separation or homogeneous canted AFM magnetic structure [258]. We have investigated these isostructural $Ca_{1-x}Y_xMnO_3$ ($0\leq x \leq 0.2$) compounds and show that a phase separated behavior, with coexisting short range ferro- and long range antiferromagnetic ordering describes the magnetic state of x = 0.1 compound. At higher doping (x = 0.2), the orthorhombic phase partially transforms to a monoclinic phase. Antiferromagnetic ordering of type G_z for the orthorhombic structure and C-type ordering for the monoclinic structure is observed in this case.

4.1.1.1 Crystal structure

The Rietveld refinement of the room temperature x-ray diffraction pattern confirms the single – phase nature of the studied samples $Ca_{1-x}Y_xMnO_3$($x \leq 0.2$) and is shown in figure 4.1. The samples are in single phase and can be indexed according to the orthorhombic structure with space group *Pnma*, as observed in $CaMnO_3$ (x=0). The cell parameters for $CaMnO_3$ exhibits a > c> b/√2 identified with the O'-orthorhombic structure [260] arising due to the superimposition of JT distortion on O-orthorhombic structure. The presence of Jahn-Teller distortion is due to the high spin d^4 configuration of Mn^{3+} ions in $CaMnO_3$ as also reported in oxygen deficient samples of $CaMnO_3$ [261]. The oxygen non-stoichiometry (δ) in parent $CaMnO_3$ indicates the presence of mixed oxidation states of Mn. The cell parameters of $Ca_{0.9}Y_{0.1}MnO_3$ sample follow the relation $a>b/\sqrt{2}>c$ in the temperature range $6K \leq T \leq 300K$, which corresponds to an O-type orthorhombic structure. This structure results from a cooperative buckling of the corner shared octahedral [260]. No evidence of monoclinic phase is found in this compound. Therefore, for x=0.1, we have analyzed the neutron diffraction data in the *Pnma* space group alone. However, analysis of the x-ray and neutron diffraction data at 12K for $Ca_{0.8}Y_{0.2}MnO_3$ sample shows that this sample exhibits a monoclinic phase with *$P2_1/m$* symmetry in addition to the orthorhombic

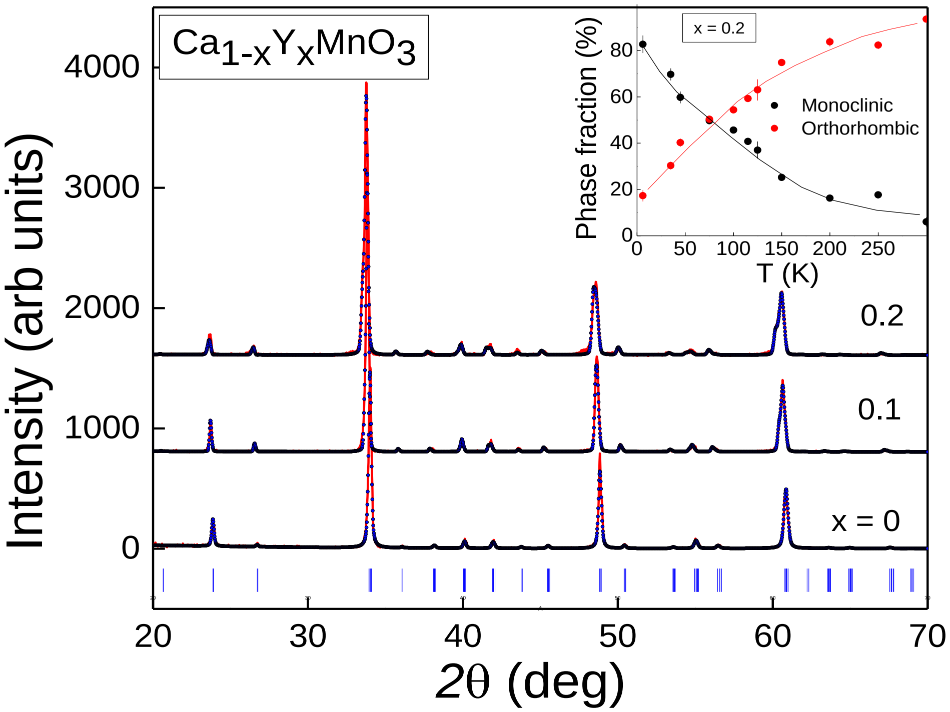

Figure 4.1: Room temperaturepowder X- ray diffraction patterns of $Ca_{1-x}Y_xMnO_3$ ($0 \leq x \leq 0.2$). Open circles are observed data points. The solid line represents the Rietveld refinement. The tick marks indicates the position of nuclear Bragg peaks. The plots for x=0.1 and 0.2 are offset vertically for clarity. Inset shows the temperature variation of the monoclinic and orthorhombic

phase. Therefore, a two phase refinement, with both orthorhombic and monoclinic has been carried out for this sample. At 6K the monoclinic phase is dominant with 82% volume fraction. The fraction of monoclinic phase gradually decreases with increase in temperature and at 300K the fraction of monoclinic phase is very small (~ 6%), as shown in the inset of figure 4.1. In this sample, the orthorhombic cell parameters exhibits a $>b/\sqrt{2} > c$ at 300K. The unit cell volume, increases with Y substitution despite the lower ionic radius of Y^{3+} (1.07Å) as compared to Ca^{2+} (1.18Å). The observed increase in volume, therefore, is ascribed to the larger ionic radius of Mn^{3+} (0.645 Å) in comparison to Mn^{4+} (0.530 Å) in six coordinated state which overcomes the difference of ionic radii between Ca^{2+} and Y^{3+} ions [210]. The difference in ionic radii of Ca^{2+} and Y^{3+} leads to ionic-size disorder which is quantified by the A-cation radius distribution expressed as $\sigma^2 = \sum x_i r_i^2 - \langle r \rangle^2$, where x_i is the fractional occupancy of the A-site ion and r_i is the corresponding ionic radius and $\langle r \rangle$ is the average A-site ionic radius [262-263]. The $\langle r \rangle$ decreases with increase of the Y^{3+} content because of the lower ionic size of Y ion. This reduction in $\langle r \rangle$ induces the tilt of MnO_6 which results in the localization and ordering of Mn^{3+}/Mn^{4+}cations.The disorder σ^2 values are given in Table 4.1. Previously, the structural changes in Y doped $CaMnO_3$ reported by Vega et al [259] as a function of doping and temperature show a complete transition from O- orthorhombic to O´ as a function of composition. This behavior is not in agreement with our studies where we find for x=0.1 sample the structure remains O- orthorhombic (*Pnma* space group) in the whole temperature range while a transition from orthorhombic phase to monoclinic phase is observed in x=0.2 sample. Similar transition to monoclinic phase has been observed in some of the earlier studies on electron doped manganites [264-266]. Moreover, the presence of monoclinic phase has been shown to be related with the nature of magnetic ordering [55-56, 264].

4.1.1.2 Transport and magnetic properties

The temperature dependence of resistivity for these samples is shown in figure 4.2(a). The resistivity data for all the samples were collected during heating and cooling cycles. The value of resistivity (ρ_{300}) at 300K for $CaMnO_3$ is ~1.7Ω cm and is in agreement with the value reported by Yuh Murano et al [267]. On doping with Y, the value of ρ_{300} decreases (Table 4.1). This resistivity behavior is consistent with earlier studies onY doping reported by Aliaga et al [258] and Sudheendra et al. [268]. The resistivity values at 300K for these samples are found to decrease with increase in Y^{3+} concentration. However, the doping does not lead to a metal-insulator transition at low temperatures. When Y^{3+} is substituted for Ca^{2+} in $CaMnO_3$, Mn^{3+} ions are introduced in the system as a result of charge compensation. The decrease in the value of resistivity in Y doped samples has been attributed to the presence of Mn^{3+} ions which introduces ferromagnetic double exchange between Mn^{3+} and Mn^{4+} ions. Similar decrease in the resistivity with doping by a trivalent ion at A-site has been previously reported in $Ca_{1-x}A_xMnO_3$ (A= La, Gd, Nd, Tb Ho, Y) systems [53, 54, 66, 269]. An insulator to metal transition has been observed in Ho^{3+} and Ce^{4+} doped $CaMnO_3$ albeit, in the high temperature region (300-900K) [269-270]. Semiconductor like behavior is observed for all these studied samples. A departure from semiconducting behavior is observed in the case of x=0.1 sample for T < 125K which coincides with the magnetic ordering temperature of this sample and therefore, this behavior may be correlated with the magnetic nature of the sample. Short range ferromagnetic correlations are observed for x=0.1 sample in the magnetically ordered ($T < T_N$) as well as in the paramagnetic region (discussed later) which possibly explains the reduction in resistivity, ρ(0). However, the compound continues to remain insulating indicating that the size of the FM

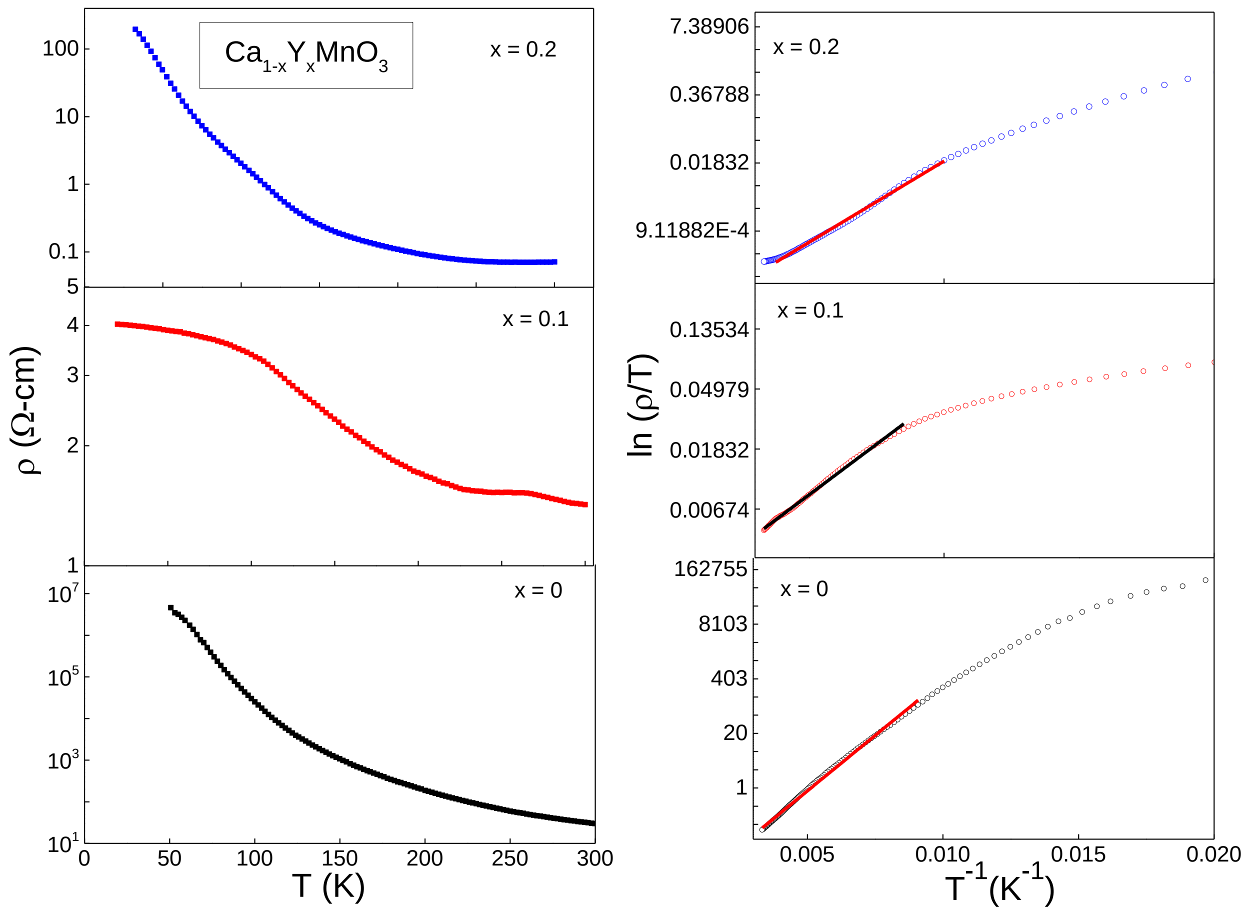

Figure 4.2: (a) Electrical resistivity (ρ) versus temperature (T) for $Ca_{1-x}Y_xMnO_3$(x = 0.0, 0.1, 0.2). (b) The variation of ln (ρ/T) with inverse of temperature. The solid line through the data is the fit to the small polaron model.

clusters in the magnetically ordered state are below the percolation threshold. The temperature dependence of resistivity in the temperature region ($T_N \leq T \leq 300K$) is found to be described by small polaron model as shown in figure 4.2(b). The resistivity due to small polarons is expressed as $\rho(T) = AT\exp(W/k_BT)$, where W represents the activation energy. The variation of W with x is shown in figure 4.3. A significant reduction in the activation energy is observed in the case of x=0.1 sample. The variation of W and resistivity at 50K (ρ_{50K}) with x is shown in figure 4.3. A significant reduction in both the activation energy and ρ_{50K} is observed in the case of x=0.1 sample. These reductions are attributed to the presence of ferromagnetic clusters in this sample.

With further increase in Y concentration, the value of activation energy increases from 29 meV for x=0.1 sample to 61meV for x=0.2 sample as shown in figure 4.3. The increase in the value of activation energy for x > 0.1 could be correlated with the increase in tendency to form small polarons when the concentration of Y^{3+} increases (concentration of Mn^{3+} ions increases) [271]. Similar transport behavior has been previously reported in Sb doped $CaMnO_3$ where the value of activation energy is found to increase gradually with increase in Sb concentration in spite of a monotonous decrease in the resistivity at high temperature region [267].

Table 4.1 Results of Rietveld refinement of neutron diffraction pattern at 6K, resistivity values, Curie – Weiss fit parameters, and variance (σ^2) for $Ca_{1-x}Y_xMnO_3$.

	x = 0	**x = 0.1**	**x = 0.2**	
			Pnma (18%)	*P2₁/m* (82%)
a (Å)	5.2771(10)	5.2895 (8)	5.3059(3)	5.3456(2)
b (Å)	7.4404(14)	7.4572(14)	7.4512(14)	7.4225(20)
c (Å)	5.2616(11)	5.2508(8)	5.2687(9)	5.2821(2)
Volume (Å^3)	206.6	207.1	208.3	209.5
β (°)	-	-	-	91.1(3)
ρ_{300K} (Ω-cm)	1.7 ± 0.4	1.4 ± 0.2	0.0708 ± 0.01	
θ(K)	-510	-69	-96	
μ_{eff}(μ_B)	4.18	4.13	4.65	
$\sigma^2\times10^{-3}$	-	1	1.7	

Figure 4.4 shows the temperature dependence of magnetic susceptibility for $Ca_{1-x}Y_xMnO_3$ (x = 0, 0.1, 0.2) samples. For temperature below 110K, a significant enhancement in the magnetic susceptibility is observed for $Ca_{0.9}Y_{0.1}MnO_3$, indicating the presence of a magnetic transition with FM component. A strong ferromagnetic moment of ~1.2μ_B is observed for the x=0.1 sample as shown in the M(H) curve in the inset of figure 4.4. The inset (b) of figure 4.4 shows the inverse of susceptibility (χ^{-1}) as a function of temperature for the samples (x= 0.1, 0.2).

In the paramagnetic regime, the inverse susceptibility follows the Curie-Weiss law, given by $\chi = C/(T-\theta)$, where χ, C and θ are the magnetic susceptibility, Curie constant and Curie-Weiss temperature, respectively. However, for the x=0.1 sample, χ^{-1} (T) shows a deviation from Curie-Weiss law in the paramagnetic region. The deviation of (χ^{-1}) from a linear dependence with temperature well above transition temperature is the characteristic of a Griffiths phase [272-274].

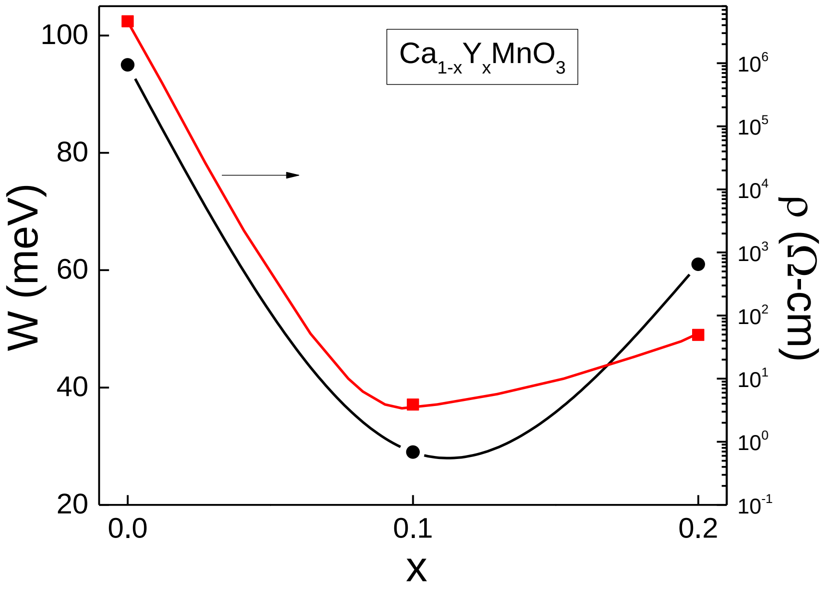

Figure 4.3: The variation of activation energy (W) and resistivity at 50K (ρ_{50K}) as a function of composition. The solid line is a guide to the eye.

The temperature dependence of susceptibility for Griffiths model is given by $\chi^{-1} = (T - T_C)^{1-\lambda}$, where λ is susceptibility exponent and 0<λ<1. A fit to Griffiths model is also shown in the inset of figure 4.4 with λ~ 0.12. The presence of Griffiths like phase in x=0.1 sample, suggests the presence of short range ferromagnetic (FM) clusters in the paramagnetic region. The Griffiths like behavior has been observed in various systems like intermetallics, hole doped manganites, layered manganites and in few electron doped manganites also [275-278]. The emergence of Griffiths phase is mainly associated with the presence of competing ferromagnetic double exchange and antiferromagnetic superexchange interactions in the system. A fit to the Curie – Weiss behavior yields a negative Curie temperature of -69K and -96K for samples x=0.1 and 0.2, respectively (Table 4.1). The negative value of Curie temperature indicates the antiferromagnetic interactions in the system which is in agreement with the neutron diffraction studies (discussed later). In previously studied $Ca_{1-x}Y_xMnO3$ compounds, positive values for Curie temperature were reported for x=0.1, 0.2, indicating FM interactions in the system [258]. From the Curie constant values, we have calculated the effective paramagnetic moment (μ_{eff}). As a result of trivalent doping, the Mn site is occupied by a mixture of Mn^{4+} and Mn^{3+} ions. So for these doped samples, μ_{eff} is calculated as $\mu_{eff}^{cal} = \sqrt{x\mu_{eff}^2(Mn^{3+}) + (1-x)\mu_{eff}^2(Mn^{4+})}$, where, μ_{eff} for Mn^{4+}

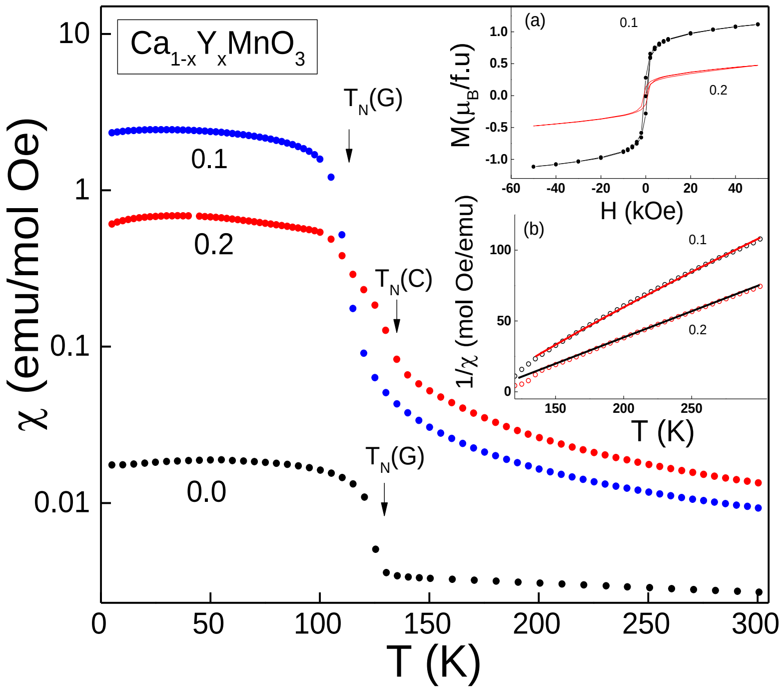

Figure 4.4: The temperature variation of the magnetic susceptibility for $Ca_{1-x}Y_xMnO_3$ ($0 \leq x \leq 0.2$).Inset (a) shows the variation of M with magnetic field at T=5K. Inset (b) shows the inverse of susceptibility as a function of temperature and fit to Griffiths model (x=0.1) and Curie- Weiss law.

(S =3/2) and for Mn^{3+} (S = 2) is 3.87μ$_B$ and 4.89 μ$_B$ respectively. According to this equation, the expected values of μ_{eff}^{cal} for x= 0.0, 0.1, and 0.2 are 3.87 μ$_B$, 3.99 μ$_B$, and 4.10 μ$_B$, respectively, which are close to the experimentally obtained values given in table 4.1. This indicates that the crystal field of Mn has not been influenced by the substitution of Y in $CaMnO_3$. In the parent compound, the calculated value obtained by considering Mn^{4+} alone is different from that obtained experimentally, this difference in value of paramagnetic moment between observed and calculated in $CaMnO_3$ is explained by taking into account the presence of Mn^{3+}.

4.1.1.3 Magnetic structure

Neutron diffraction patterns for all the samples have been recorded at various temperatures between 6K and 300K. In the case of x= 0 and 0.1 sample, superlattice reflections at low angles are observed on lowering of temperature below 125K. These reflections could be indexed with $\vec{k}$=0 propagation vector in P-1 space group. The strong enhancement in the intensity of (011) reflection indicate a purely magnetic contribution as the nuclear contribution is absent in this reflection. Additionally, we do not observe any enhancement in the intensity of the fundamental Bragg reflections. This indicates the absence of long range ferromagnetic component in this sample. The basis vectors have been determined by using BASIREPS program [188] with propagation vector $\vec{k}$ =0. To represent the magnetic structure of these compounds Bertaut's notation in the *Pnma* setting is adopted. The magnetic structure is found to be G_Z – type for x = 0 sample in which each Mn^{4+} is coupled antiferromagnetically with its near neighbors. The moment on Mn at 6K is 2.84 μ$_B$ which is close to the expected value of 3μ$_B$ for Mn^{4+}. This is in agreement with the earlier reported value ≈ 2.64 μ$_B$ on stoichiometric $CaMnO_3$ by Yudin et al. [279], and 2.45μ$_B$ in oxygen deficient $CaMnO_{3-\delta}$ (δ = 0.11) [280]. The neutron diffraction pattern for x=0.1 sample is shown in figure 4.5. For x = 0.1 sample, at 6K the magnetic structure is found to be G_Z (Γ_4) type with spins coupled antiferromagnetically along the z-axis (crystallographic c-axis). The moment on Mn is found to be $2.1\mu_B$ at 6K, which is lower than the expected value of $3.1\mu_B$ for this compound. The thermal variation of the magnetic moment exhibits Brillioun-type temperature dependence and is shown in the inset of figure 4.5. However, the temperature dependence of susceptibility (figure 4.4), shows a rapid increase below 110K, indicating the presence of ferromagnetic correlations in x=0.1 sample. The presence of ferromagnetic behavior in magnetization studies of $Ca_{0.9}Y_{0.1}MnO_3$ raises an important question whether there is a canting of the G-type AFM structure, as originally proposed by deGennes

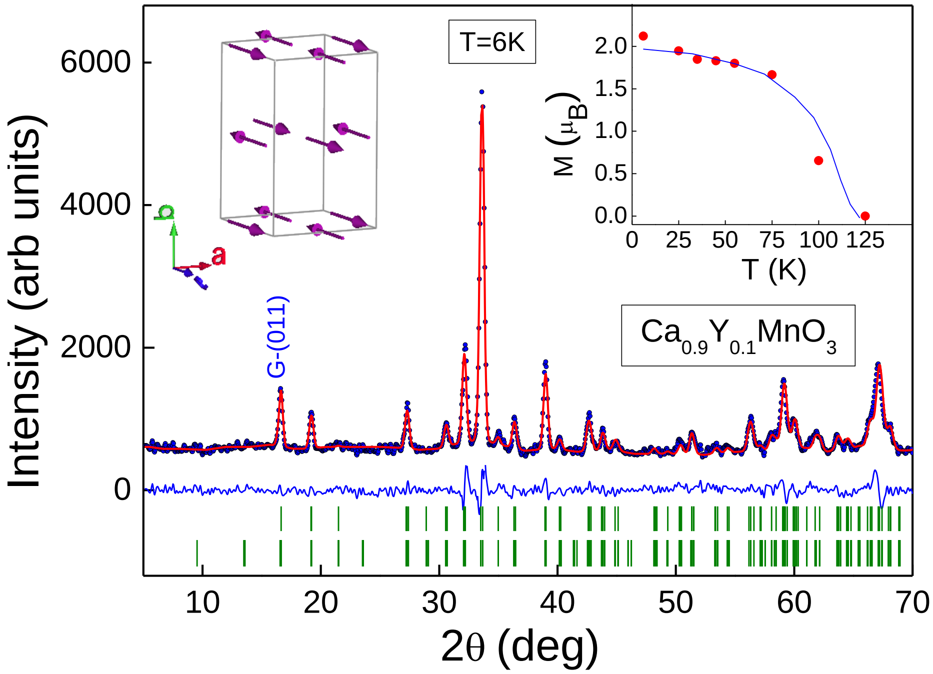

Figure 4.5: The observed (symbols) and calculated (line) neutron diffraction pattern for $Ca_{0.9}Y_{0.1}MnO_3$ compound at T = 6K. Lower solid line is the difference between observed and calculated pattern. The first row of tick marks indicates the position of nuclear Bragg peaks and second row indicate the position of magnetic Bragg peaks. Inset shows the thermal variation of magnetic moments. The obtained magnetic structure is drawn in the inset.

[37], or a coexistence of magnetic phase separation to form domains of AFM and FM ordering. The absence of any magnetic contribution in the form of enhancement in the intensity of the low angle fundamental reflections in our neutron diffraction results rules out the presence of canted AFM. The magnetic structure of this compound is similar to the G_Z-type magnetic ordering we had reported earlier in the parent compound, $CaMnO_3$. However, the site moment $2.1\mu_B$ for x=0.1 is lower than $2.84\mu_B$ for x=0 sample (expected value of $3\mu_B$ for Mn^{4+}). Similar low value of moments has been observed in other doped samples [54-56]. The lower value of the moment previously has been attributed to the Mn (3d) - O(2p) hybridization. It could also be an indication of incomplete ordering of the Mn ions, below the T_N, in this sample.

Figure 4.6 shows a section of the neutron diffraction data at 300K and 6K for $Ca_{0.8}Y_{0.2}MnO_3$. As shown in the inset of figure 4.1, this sample exhibits a structural transition to a monoclinic phase on cooling below 300K and both these phases coexist over a large temperature region. For T<125K, superlattice reflections in addition to those corresponding to G-type magnetic ordering are observed. This strong reflection could be indexed as (100) in the $P2_1/m$ space group.The neutron diffraction pattern has been analyzed taking into account both the monoclinic ($P2_1/m$ space group) and orthorhombic (*Pnma* space group) phases. The basis vectors have been determined by using BASIREPS program with propagation vector $\vec{k} = (\frac{1}{2}\ 0\ \frac{1}{2})$ for $P2_1/m$ space group and $\vec{k} = (0\ 0\ 0)$ for *Pnma* space group. The magnetic structure is found to be C-type AFM corresponding to monoclinic phase and G-type AFM for orthorhombic phase. The value of the moment on Mn at 6K is found to be $2\mu_B$ for both the phases, which is lower than the expected value of $3.2\mu_B$. The lower value of moments in this sample too indicates that parts of the Mn moments are not completely ordered below T_N. The C-AFM structure is characterized by a ferromagnetic ordering of the magnetic moments of Mn ions in chains and by anantiferromagnetic coupling between neighboring chains suggesting double-exchange interactions along the chains and superexchange interactions (SE) between neighboring chains. Therefore, in the presence of C-type AFM, 1D FM correlations leads to the $d_{3z^2-r^2}$ orbital polarization and hence it further leads to lowering of the symmetry from orthorhombic (*Pnma*) to monoclinic ($P2_1/m$) [55]. The T_N (C-type) is found to be higher (125K $<T_N$(C) <150K) than T_N (G-type) (~100K). Similar behavior has been found in the case of $Ca_{1-x}La_xMnO_3$ ($0 \le x \le 0.2$) [55]. However, there is no evidence of ferromagnetic behavior in this sample. In earlier reported studies on single electron doped $Ca_{1-x}A_xMnO_3$ systems, a canted G-type structure was observed only up to x~0.1, which then changed to C-type structure [39, 53, 55, 265, 281-282] for higher values of x, which is similar to our results on Y doped $CaMnO_3$. Similar, crystallographic and magnetic phase diagram has been observed in case of two electron doped $Ca_{1-x}Ce_xMnO_3$ ($x \ge 0.075$) system [84]. Eventually, the studied system tends to stabilize in the C-type AFM structure which is comprised of FM chains. The absence of ferromagnetic behavior has also been observed in the case of $Ca_{0.85}Sm_{0.15}MnO_3$ [58]. The low temperature crystallographic and magnetic phase, in this compound is described by C-$P2_1$/m and G-Pnma. However, application of magnetic field is found to result in F-Pnma phase together with G-Pnma. This result therefore, bridges our observations between 10% and 20% doping levels. The evolution of this long range magnetic ordering in electron doped systems is supported by previously published theoretical work [27, 283-284]. Theoretically it has been observed that the systematics of the phase diagram in manganites changes considerably as a function of J_H (Hund's coupling), J_{AF} (superexchange coupling) and (W) band width. Pai et al. has summarized the magnetic phase diagram for electron doped manganites for different electron concentration as a function of J_H and J_{AF} [285]. For low electron concentration, the SE (superexchange) interaction dominates over Hund's coupling and leads to G-type structure. With further electron doping, the kinetic energy starts dominating over the SE coupling. The competition between effective kinetic energy (determined by J_H) and SE leads to transition from G-type to C-type. The electron doping concentration and competition between J_H and J_{AF} leads to different magnetic structures (G-C-A-F).

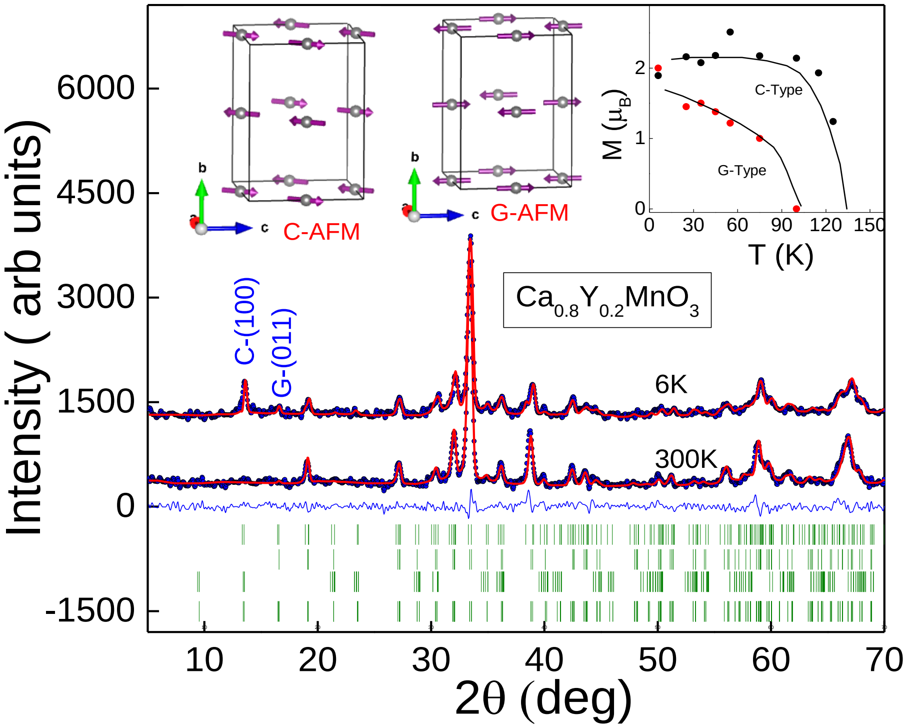

Figure 4.6: The observed (symbols) and calculated (line) neutron diffraction pattern for $Ca_{0.8}Y_{0.2}MnO_3$ compound at T = 6K and 300K. Lower solid line is the difference between observed and calculated pattern. The first and second row of tick marks indicates the position of nuclear Bragg peaks for $P2_1/m$ and *Pnma* space group, respectively. The third and fourth row indicates the position of magnetic Bragg peaks for C-type and G-type AFM, respectively. Inset shows the thermal variation of magnetic moments. The obtained magnetic structures are drawn in the inset.

4.1.1.4 Neutron depolarization studies

Unlike, in the case of x = 0.2 compound where no evidence of ferromagnetic correlations are observed, in x = 0.1 we had observed that the magnetization increases rapidly below 110K, indicating the presence of ferromagnetic correlations. However, it was inconclusive from neutron diffraction experiments. Therefore, this behavior has been further studied using neutron depolarization measurements. In this experiment, we measured the flipping ratio R (ratio of transmitted intensities for two spin states of the incident neutron spin) which is a measure of the transmitted beam polarization. The flipping ratio can be expressed in the form $R = \frac{1 - P_i D P_A}{1 + (2f - 1) P_i D P_A}$ [286] where, P_i is the incident beam polarization, P_A is the efficiency of the analyzer crystal, f is the efficiency of the DC flipper and D is the depolarization coefficient (due to the sample under investigation). Figure 4.7 shows the temperature dependence of flipping ratio for x = 0.1 and 0.2 samples. For x=0.1 sample, flipping ratio remain constant up to ~ 110K , below which, the flipping ratio decreases rapidly, reaching a minimum at ~ 90K and after that remains constant down to 2K. This decrease in flipping ratio below 110K indicates the presence of ferromagnetic correlations which correlates well with our magnetization study on this compound. An estimate of the domain size in the ferromagnetic region is obtained using the expression $P_f = P_i \exp[-\alpha (d/\delta) \langle \phi_\delta \rangle^2]$,where P_f and P_i are the transmitted beam and incident beam polarization, respectively, α is a dimensionless parameter (=1/3), *d* is the sample thickness, δ is a typical domain length and the precession angle $\phi_\delta = (4.63 \times 10^{-10} Oe^{-1} A^{-2}) \lambda \delta B$ [190]. The domain magnetization, B is obtained from the bulk magnetization. This expression is valid in the limit where domains are randomly oriented and the Larmor precession of the neutron spin due to the internal magnetic field of sample is small fraction of 2π, over the typical domain length scale

[190]. The estimated domain size for x=0.1 sample is ~ 7 µm. This measurement therefore, gives a clear evidence of the existence of the ferromagnetic domains. Similar micrometer size clusters have been observed in LPCMO system by Uehara et al [78]. In the case of x = 0.2, the flipping ratio remain constant down to the lowest temperature indicating absence of ferromagnetic domains in this sample. In an antiferromagnet, since there is no net magnetization, depolarization is not expected. This is in agreement with the magnetization and neutron diffraction studies on this sample, where no evidence of enhancement in the intensity of fundamental Bragg reflections (101) (020) is observed. Since neutron depolarization measurements provide information on the magnetic inhomogeneity in a length scale > 1µm we rule out the presence of ferromagnetic correlation at this length scale in x= 0.2 sample.

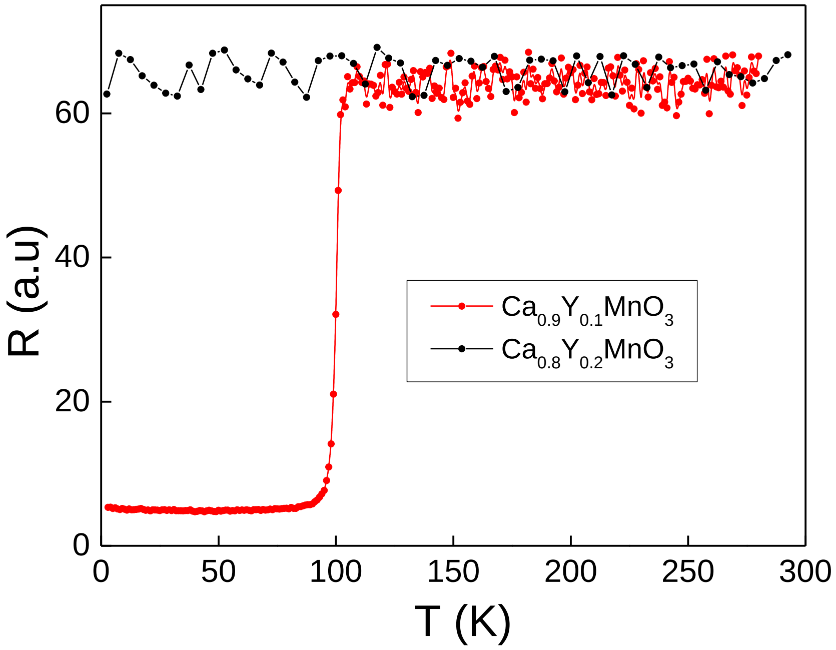

Figure 4.7: The flipping ratio (R) versus temperature for $Ca_{1-x}Y_xMnO_3$ (x=0.1, 0.2).

Monte Carlo simulations on the manganites have shown the generation of the large FM clusters in the antiferromagnetic phase, when the densities of ferromagnetic and antiferromagnetic phases are equal [27, 77]. The variation in the size of clusters has been explained by Moreo et al. [77] on the basis of disorder in the system. They find that introducing disorder into AFM matrix leads to growth of FM clusters. The size of the clusters eventually shrinks on increasing the disorder. We attribute the absence of ferromagnetic clusters (of micrometer length scale) in x=0.2 to increase in disorder. For x=0.1 sample, the magnetic ground state is explained by considering phase separated state, which consists of short range FM clusters embedded in the G-type AFM matrix. Similar behavior has been observed before in the case of half doped manganites [287]. Its presence at different length scales in doped manganites has been discussed by Shenoy et al. [73].

Phase separation (coexistence of FM and AFM) behavior has been observed experimentally in single electron doped systems such as $Ca_{1-x}La_xMnO_3$ for $0<x\leq0.09$, $Ca_{1-x}Pr_xMnO_3$ for $x\leq0.1$, and $Ca_{0.9}Tb_{0.1}MnO_3$ [83]. However, in two electron doped $Ca_{1-x}Ce_xMnO_3$ for $0<x\leq0.075$ system, the magnetic ground state is better described by canted AFM model. The origin of weak ferromagnetism in doped manganites, in term of spin canted state was originally proposed by deGennes [37]. However, later theoretical studies have shown that the phase separated state in doped manganites is the more stable phase [59-62]. We attribute the phase separated behavior with varying coexisting magnetic structures in the studied $Ca_{1-x}Y_xMnO_3$ to the disorder in the system [288].

4.2 Effect of Mn-site doping on the magnetic properties of $CaMnO_3$

4.2.1 Effect of Fe doping on the transport and magnetic properties of $CaMnO_3$

In the present work, we describe the effect of doping Fe at Mn site of $CaMnO_3$ and its influence on the crystal structure, magnetic properties and transport behavior and compare our results with other electron doping effects observed in this compound. Unlike in the case of Ca-site doping we find that doping with Fe at Mn site leads to an insulating canted AFM structure as predicted by deGennes [37]. In a recent study on Fe^{4+} doping effects in $CaMnO_3$, on the basis of magnetization measurements, the authors proposed a mixed AFM+FM ground state for doped samples and the T_N of the compounds is found to decrease with Fe doping [289]. As a result of the identical electronic configuration of Mn^{3+} and Fe^{4+}, it's doping in effect results in electron doping. However, as opposed to other dopants at the Mn site, doping with Fe does not induce metallicity. Further, the Fe^{4+} ions in $CaFeO_3$ undergo charge disproportionation to Fe^{3+} and Fe^{5+} at 290K [290]. These studies necessitate understanding the true nature of the ground state in the Fe doped compounds. Partial substitution of Mn^{4+} with isovalent Fe^{4+} having electronic configuration $t_{2g}^3e_g^1$, similar to Mn^{3+} ion, raises the possibility of influencing magnetotransport behavior.

4.2.1.1 Crystal structure

Figure 4.8 shows the xrd patterns of the compounds of the series $CaMn_{1-x}Fe_xO_{3-\delta}$ with $x \leq 0.3$. The samples are in single phase and can be indexed according to the orthorhombic structure with space group *Pnma,* as observed in $CaMnO_3$(x=0). The variation of lattice parameters and unit cell volume as a function of Fe concentration x is shown in figure 4.9. It is observed that lattice parameters and unit cell volume monotonically increases with Fe concentration. The unit cell volume at 300K increases from 206.6 (x=0) to 210.3Å^3 (x=0.3) arising from the higher ionic radius of Fe^{4+} (0.585 Å) as compared to Mn^{4+} (0.530 Å) in six coordination state [210]. So the partial substitution of Fe in $CaMnO_3$ at Mn site induces lattice expansion. We have obtained the oxygen non-stoichiometry (δ) in our samples from refinement of the neutron diffraction patterns. For x=0 sample the valueof δ ~0.14 and with Fe doping this value reduces to 0.05 for x = 0.3. This implies that with Fe doping in $CaMnO_{3-\delta}$ the concentration of Mn^{3+} is suppressed, which is in agreement with the relation of the cell parameters. The cell parameters for $CaMnO_3$ exhibits a > c > b/√2, which accounts for the O'- orthorhombic structure. But in the case of Fe doped samples, cell parameters exhibit a > b/√2 > c which accounts for the O-orthorhombic structure, due to the pure rotation of the octahedral. The oxygen non-stoichiometry (δ) in our samples indicates the presence of mixed oxidation states of Mn, which is further studied by another complementary technique.

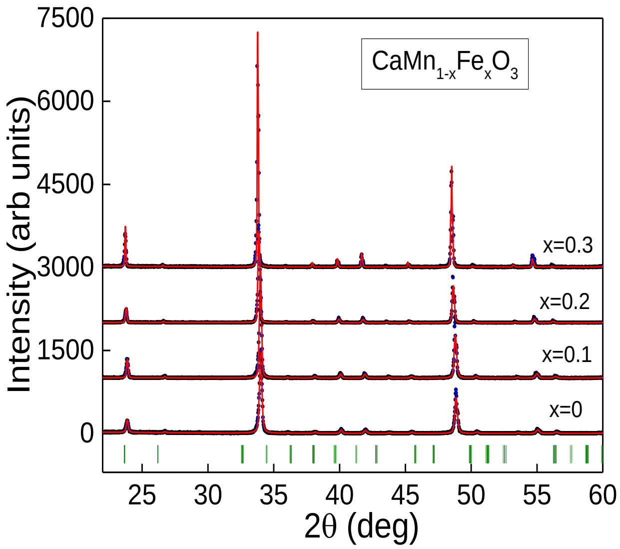

Figure 4.8

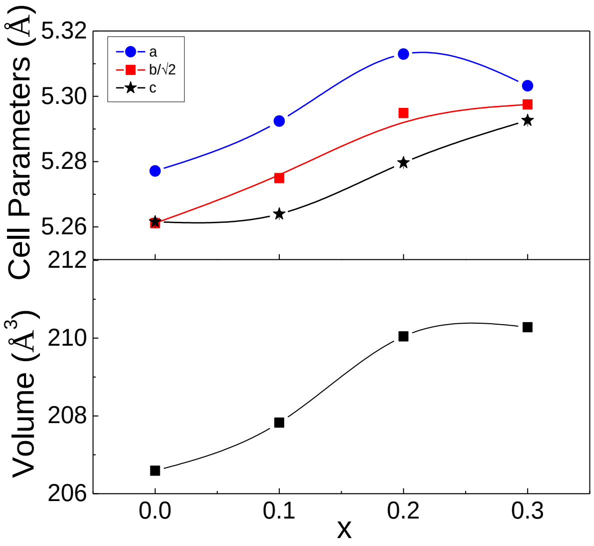

Figure 4.9

Figure 4.8: Room temperaturepowder X- ray diffraction patterns of $CaMn_{1-x}Fe_xO_3$ ($0 \leq x \leq 0.3$). Open circles are observed data points. The solid line represents the Rietveld refinement. The tick marks indicates the position of nuclear Bragg peaks. The plots for x=0.1, 0.2 and 0.3 are offset vertically for clarity.

Figure 4.9: (a) Lattice parameters a, b/√2, c and, (b) cell volume as a function of x for $CaMn_{1-x}Fe_xO_{3-\delta}$.

Table 4.2: Results of Rietveld refinement of neutron diffraction pattern at 6K, resistivity values at room temperature, Curie – Weiss fit parameters, exchange integral values, ferromagnetic component (F_Y) and antiferromagnetic component (G_Z) of moment for $CaMn_{1-x}Fe_xO_{3-\delta}$.

	x = 0	**x = 0.1**	**x = 0.2**	**x = 0.3**
a(Å)	5.2771(10)	5.2924(7)	5.3129(8)	5.3032(8)
b(Å)	7.4404(14)	7.4599(12)	7.4881(12)	7.4918(12)
c(Å)	5.2616(11)	5.2640(7)	5.2797(8)	5.2926(8)
Volume ($Å^3$)	206.590	207.827	210.045	210.277
$Mn-O_1$ (Å)	1.8824(3)	1.8977(3)	1.9033(3)	1.9020(3)
$Mn-O_{21}$ (Å)	1.8826(3)	1.9104(18)	1.9086(2)	1.9172(2)
$Mn-O_{22}$ (Å)	1.9491(3)	1.9038(18)	1.9137(2)	1.8918(2)
$Mn-O_1-Mn$ (°)	162.35(4)	158.70(4)	159.21(4)	159.93(4)
$Mn-O_2-Mn$ (°)	153.01(3)	156.21(2)	156.92(3)	159.16(3)
ρ_{300K} (Ω-cm)	1.7 ± 0.4	1082±165	330±73	325±79
θ(K)	-510	-163	-83	-90
J(meV)	2.93	0.94	0.48	0.51
C(emu K mol^{-1})	2.18	2.46	2.16	2.33
μ_{eff}(μ_B)	4.18	4.038	4.161	4.32
F_Y (μ_B)	0	0.3(4)	0.9(1)	0.35(1)
G_Z (μ_B)	2.85(5)	2.47(4)	1.86(5)	1.23(4)

4.2.1.2 XANES study

This XANES study has been mainly done to know about the valence state of Mn in our compounds. Normalized XANES spectra ($\mu(E)$ versus E) at the Mn K-edge for $CaMn_{1-x}Fe_xO_{3-\delta}$ samples with x = 0, 0.1 and 0.2 is shown in figure 4.10 along with the spectra for two standard Mn compounds viz., Mn_2O_3 and MnO_2 oxide having Mn oxidation state +3 and +4, respectively.

By comparing the edge position of $CaMnO_3$ with that of reference compounds of Mn_2O_3 and MnO_2, it is found that the oxidation state of Mn in $CaMnO_3$ is in between the +3 and +4. In x = 0.1 and x = 0.2 samples the energy edges shift towards higher energy side as shown in the inset of figure 4.10, which is due to the fact that electronegativity of Fe being more than Mn, replacement of Mn by Fe would increase the effective positive charge at the Mn site to maintain the effective positive charge at the cationic site unaffected. This in turn cause shifts of the edge energy of Mn to higher energy. Similar shifts in X-ray absorption edges due to change in Chemical environment of the absorbing species have been observed in different other systems [291-293]. A similar systematic shift of edge peak with the doping concentration has been observed in experimental studies in related perovskite systems, $LaMn_{1-x}Co_xO_3$ [294], $LaMn_{1-}$

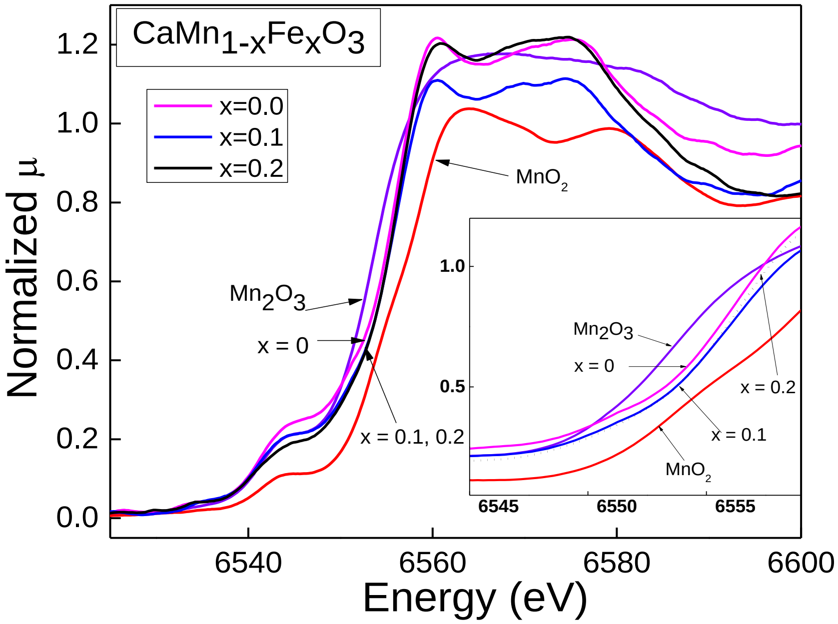

Figure 4.10: XANES spectra of the $CaFe_xMn_{1-x}O_{3-\delta}$ samples for x = 0, 0.1 and 0.2 at Mn K-edge along with that of reference compounds Mn_2O_3 and MnO_2.

${}_xGa_xO_3$ [295], $LaMn_{1-x}Ni_xO_3$ [296] systems. XANES measurements indicate the presence of mixed oxidation states of Mn, which is in agreement with our neutron diffraction results.

4.2.1.3 Mössbauer spectra

In order to confirm the valence state of Fe in the doped compounds, Mössbauer spectra was recorded. Figure 4.11 shows the Mössbauer spectra (MS) for x = 0.1 and x=0.2 samples at room temperature.The hyperfine parameters i.e isomer shift (δ), quadrupole splitting (Δ) and line widths (Γ) obtained from the fit are included in table 4.3. The Mössbauer spectra of both these samples are fitted with two symmetric doublets. The two doublets are indicative of two different sites for Fe i.e. two different types of surroundings around Fe nucleus in both the samples and both Fe sites are paramagnetic. These two different sites for Fe arise due to the random distribution of Fe in lattice with equal probability of having either Fe or Mn as the nearest neighbor.The increase in the quadrupole splitting values with Fe content suggests an increase in local distortion at the Mn/Fe site leading to a higher asymmetry in the system. From the observed values of isomer shift for both the doublets in both the compounds we infer that Fe is more closer to 4+ valence state since isomer shift for Fe^{3+}(S = 3/2) is between ~ 0.2 and 0.4 mms^{-1} and for Fe^{4+}(S = 2) it is between ~ -0.1 and 0.1mms^{-1}[197]. In these Fe doped compounds, Mössbauer results indicate the presence of Fe^{4+} in studied samples.

Table 4.3: Mössbauer parameters at room temperature for CaMn$_{1-x}$Fe$_x$O$_{3-\delta}$.

x	Iron Sites	^{a}Isomer shift (δ) mm/s	Quadrupole splitting (Δ) mm/s	Line width (Γ) mm/s	Area R_A (%)
0.1	Doublet 1	0.127(3)	0.409(20)	0.345(13)	82
	Doublet 2	0.144(7)	0.138(20)	0.200(50)	18
0.2	Doublet 1	0.154 (5)	0.634(26)	0.365(30)	44
	Doublet 2	0.125(3)	0.206(17)	0.357(50)	56

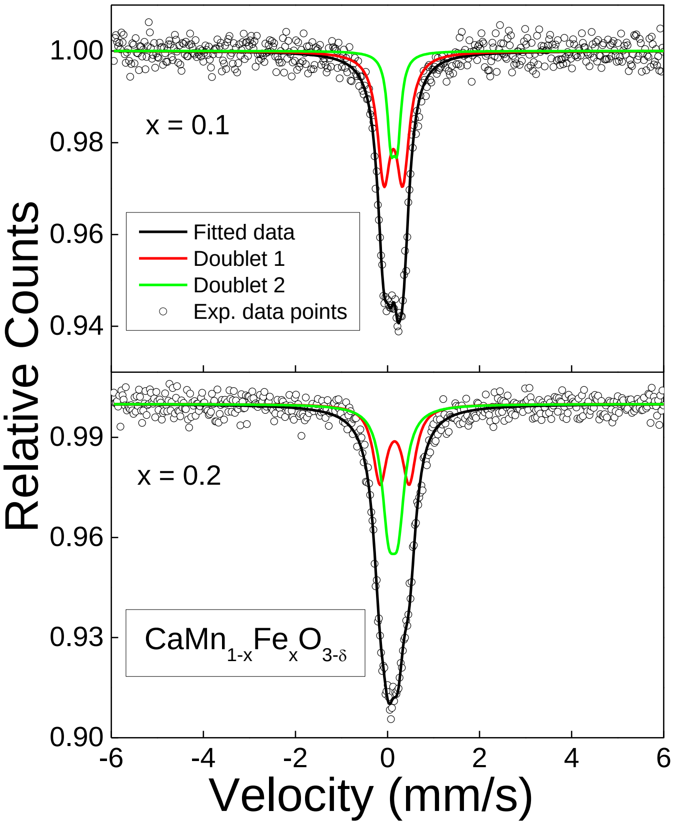

Figure 4.11: Room temperature Mössbauer spectra of CaMn$_{1-x}$Fe$_x$O$_3$ for x=0.1 and 0.2 samples.

4.2.1.4 Transport and magnetic properties

The temperature dependence of resistivity for these samples is shown in figure 4.12(a). The resistivity data for all the samples were collected during heating and cooling cycles. For all the samples ρ(T) decreases as the temperature increases in the measured temperature range between 5K and 300K. On doping with Fe, ρ_{300} shows large enhancement as compared to that of pure sample as is evident from Table 4.2. This resistivity behavior is consistent with earlier Fe doping behavior as reported by X.J. Liu et al [289]. This increase in the value of resistivity in Fe doped samples can be explained by considering band picture of transition metal cations. Based on studies on the conductivity of $La_{0.85}Ba_{0.15}Mn_{1-x}Fe_xO_3$ [297] and $La_{1-x}Ca_xFe_{1-x}MnO_3$ [298], a band picture of Fe and Mn has been proposed by K.H.Ahn et.al [299]. According to this band picture, bottom of the Mn $e_{g\uparrow}$ band is at the same level or higher than the top of the Fe $e_{g\uparrow}$ band. In our

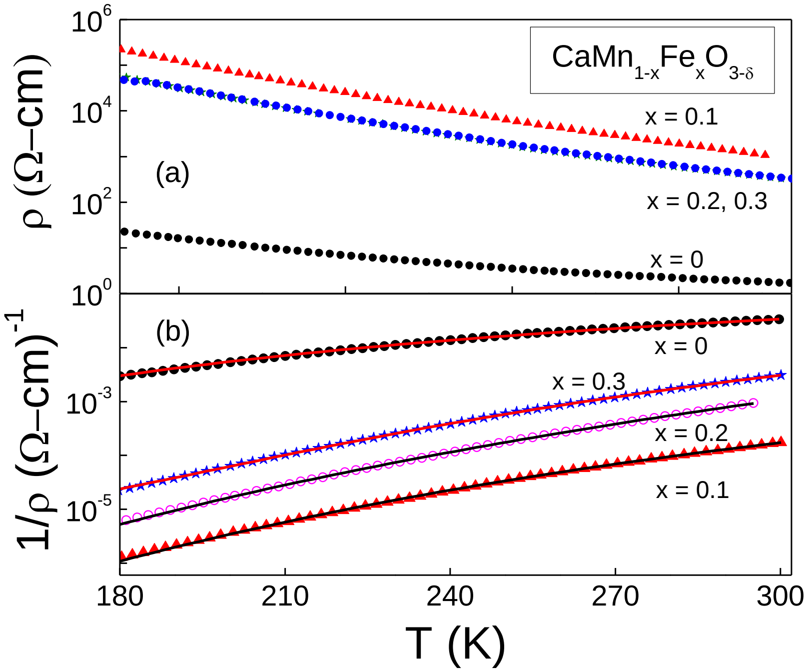

Figure 4.12: (a) Electrical resistivity (ρ) versus temperature (T) for $CaMn_{1-x}Fe_xO_{3-\delta}$(x = 0.0, 0.1, 0.2, 0.3) . (b) The variation of 1/ ρ with temperature. The continuous line through the data is the fit (discussed in the text).

compounds, Mn and Fe, both are in 4+ valence state having electronic configuration t_{2g}^3 and $t_{2g}^3 e_g^1$ respectively i.e Mn e_g band is empty and e_g band of Fe is less than half-filled. So hopping of electron between Fe e_g band and Mn e_g band is energetically forbidden. This results in enhancement of resistivity with doping of Fe. For the parent sample, resistivity behavior in the temperature region (175K-300K) is found to be described by small polaron hopping model [300]. In this model ρ(T) is expressed as, $\rho(T) = AT\exp(W/k_BT)$, for which, the fitting parameters are given below in table 4.4. In oxygen deficient $CaMnO_{3-\delta}$ ($\delta = 0.11$) the reported value of W is ~ 22meV [301] and this increases to 94 meV for $\delta = 0.14$ in our case. In the Fe doped sample (x = 0.1), conduction mechanism is found to bebetter described by variable range hopping (VRH) model [302]. In the VRH model ρ(T) is expressed as, $\rho(T) = \rho_0 \exp(T_0/T)^{0.25}$ where, T_0 is Mott's activation energy and is defined as $T_0 \approx 21/k_B N(E_F)\zeta^3$. In this equation, k_B is Boltzmann's constant, $N(E_F)$ is the density of states (DOS) at Fermi level E_F, and ζ is the localization length [302]. The characteristic temperature T_0 is inversely proportional to the electronic density of states at Fermi level. To describe the resistivity behavior in higher Fe doped samples i.e for x=0.2,0.3 we find that a parallel combination of variable range hopping and small polaron models best describes the data in the same temperature range. For this parallel combination, resistivity is described as, $\frac{1}{\rho} = \frac{1}{\rho_1} + \frac{1}{\rho_2}$,where ρ_1 is the resistivity from variable range hopping model and ρ_2 from small polaron model. The fit described by this parallel combination is shown in fig 4.12(b). The fitting parameters are included in table 4.4. The range of these T_0 values that we obtained from the fit are very similar to those reported in other manganites $La_{1-x}Ca_xMnO_3$ (x=0.5) and $La_{0.5}Ca_{0.5-x}Ba_xMnO_3$ (x=0.05,0.10,0.15) [303-304].

Table 4.4: The parameters obtained from fitting the resistivity data for $CaMn_{1-x}Fe_xO_{3-\delta}$ in the paramagnetic region.

X	T_0(K)	W(meV)
0	-	94.2
0.1	$7.06X\ 10^8$	-
0.2	$5.076X10^8$	206.98
0.3	$2.862X10^7$	225.36

Figure 4.13 shows the temperature dependence of the magnetization M(T) for $CaMn_{1-x}Fe_xO_{3-\delta}$samples (x=0,0.1,0.2,0.3) under an applied field of 1T. Small discontinuities are observed in the region between 100K and 125K, and are identified with T_N of these compounds. There is a small reduction in T_N with Fe doping which is in agreement with earlier reported behavior [292]. The inset of figure 4.13 shows the inverse of susceptibility as a function of temperature for all these samples (x=0.0,0.1,0.2,0.3). In the paramagnetic regime, the inverse susceptibility follows the Curie-Weiss law, given by $\chi = C/(T-\theta)$, where χ is the susceptibility, C is the Curie constant and θ is the paramagnetic Curie temperature. The reciprocal susceptibility for these compounds shows a linear dependence above 150K and is shown in the inset of figure 4.13. The value of Curie constant is calculated for all these samples by inverse susceptibility plot. From these Curie constant values, we have calculated the effective paramagnetic moment (P_{eff}) by using eq., $C = NP_{eff}^2 \mu_B^2 / 3K_B$. Theoretically, $\mu_{eff}$is calculated as, $\mu_{eff}^{cal} = \sqrt{xP_{eff}^2(Fe^{4+}) + (1-x)P_{eff}^2(Mn^{4+})}$, where, P_{eff} for Mn^{4+} (S=3/2) and for Fe^{4+} (S=2) is $3.872\mu_B$ and $4.89\mu_B$ respectively [305]. According to this equation, P_{eff}^{cal} values for x=0.0, 0.1, 0.2, 0.3 are 3.87 μ_B, 3.98 μ_B, 4.09 μ_B, and $4.20\mu_B$ respectively, which are close to the experimentally obtained values given in table 4.2. This indicates the presence of Fe^{4+} (S=2) in doped samples. In these Fe doped compounds,

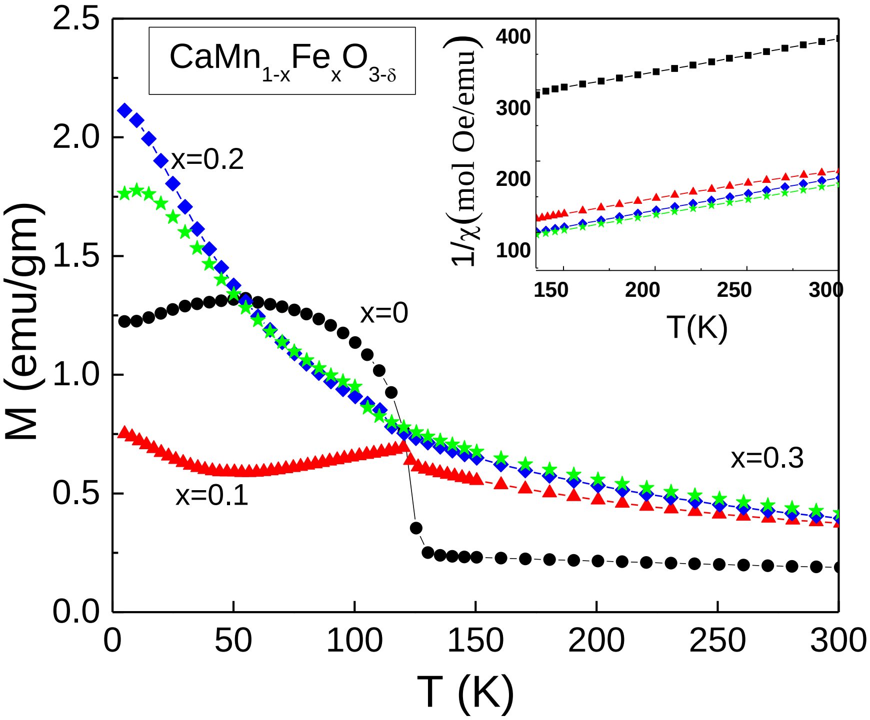

Figure 4.13: The zero field-cooled (ZFC) magnetization (M) versus temperature (T) in field of H = 1T for $CaMn_{1-x}Fe_xO_{3-\delta}$(x = 0.0,0.1,0.2,0.3) .Inset shows the inverse of susceptibility as a function of temperature.

Mössbauer results indicates the presence of Fe in 4+ valence state which together with magnetization results confirms the presence of Fe^{4+} in studied samples. In the parent compound, the calculated value obtained by considering Mn^{4+} alone is different from that obtained experimentally, but in the doped samples there is an agreement between the observed and calculated values. This difference in value of paramagnetic moment between observed and calculated in $CaMnO_3$ is explained by taking into account the presence of Mn^{3+}. The percentage of Mn^{3+} in the parent sample is 27% and it reduces with Fe doping. For x = 0.1, 0.2 and 0.3 the percentage of Mn^{3+} reduces to 4.6%, 5.8% and 10% respectively. This also indicates that oxygen deficiency is suppressed with Fe doping. The extrapolated paramagnetic temperatures are negative for all our studied compounds indicating that the dominant interactions are antiferromagnetic in all these compounds. This is in contrast to $CaMn_{1-x}Ru_xO_3$ ($0.04 \leq x \leq 0.08$) and $CaMn_{1-x}Mo_xO_3$($0.02 \leq x \leq 0.04$) compounds where doping gives rise to positive Curie-Weiss temperature (θ) [300]. The values of θ for $CaMn_{1-}xFexO_3$ are given in table 4.2. Using these values of θ, we have estimated theexchange integral J between the nearest Mn neighbors, by employing the nearest- neighbor (NN) model [226],

$$2J/k_B = \frac{3\theta}{zs(s+1)}$$

where, z=6 is the number of nearest neighbors of Mn in the orthorhombic structure, θ is Curie-Weiss temperature and S =3/2 for Mn^{4+}. It is found that J decreases with Fe doping indicating that antiferrromagnetism is gradually suppressed with increasing Fe concentration.

4.2.1.5 Magnetic structure

Neutron diffraction pattern has been recorded for all the samples at 6K and 300K. Fig 4.14 shows a typical Rietveld refinement pattern for $CaMn_{0.8}Fe_{0.2}O_{3-\delta}$ at 300K and 6K. On lowering the temperature below T_N to 6 K, enhancement in the intensity of (0 1 1) reflection and relatively weakly in the case (101) (020) is observed. The enhancement in the intensity of (011) reflection indicate G-type AFM ordering while the increase in the intensity of (101) (020) reflections indicate presence of a ferromagnetic component. The magnetic cell is same as the chemical cell. The magnetic structure has been refined by representation analysis using BASIREPS [188]. The magnetic structure of $CaMnO_3$ is G-type as described above. In the case of x=0.1 a very small canting of moments is observed. Enhancement in intensity of (1 0 1) (0 2 0) in addition to (0 1 1) is found indicating a canted AFM structure in x=0.1, 0.2, 0.3 samples. The magnetic structure for x=0.1, 0.2 and 0.3 is analyzed by taking Γ_4 irreducible representation. The magnetic structure is found to be F_YG_Z type having ferromagnetic order along Y-axis (crystallographic b-axis) and antiferromagnetic along Z-axis (crystallographic c-axis). A similar type of magnetic configuration, A_YF_Z type has also been found in lightly doped (La, A)MnO_3 (A=Ca, Sr) [306]. The weak ferromagnetic component in lightly doped $LaMnO_3$ is attributed to D-M interactions.The canted magnetic structure in Fe doped samples can also be explained by considering D-M interactions. According to Dzyaloshinsky, combination of low symmetry and spin orbit coupling give rise to antisymmetric exchange interaction, and this interaction favours

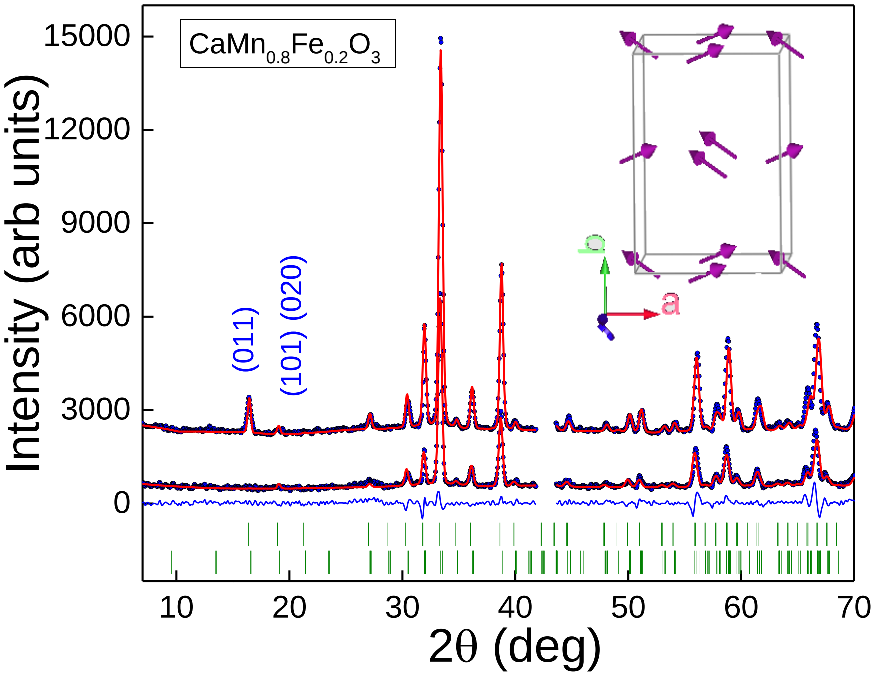

Figure 4.14: The observed (symbols) and calculated (line) neutron diffraction pattern for $CaMn_{0.8}Fe_{0.2}O_3$compound at T = 6K and 300K. Lower solid line is the difference between observed and calculated pattern. The first and second row of tick marks indicates the position of nuclear Bragg peaks and magnetic Bragg peaks for*Pnma* space group, respectively. The obtained magnetic structures are drawn in the inset.

the canted spin arrangement. This antisymmetric exchange interaction is expressed as, **D**.[$\mathbf{S}_i$x$\mathbf{S}_j$], where D is a constant vector. The vector D does not vanish in general case but it vanishes when the crystal field surrounding the magnetic ion has inversion symmetry [227]. In this case the Mn ions in the magnetic cell occupy non centrosymmetric positions. For all these samples (x=0.0, 0.1, 0.2, 0.3) the ferromagnetic and antiferromagnetic components of moments are given in table 4.2. The ferromagnetic component is maximum for the concentration x=0.2. The antiferromagnetic moments reduces with Fe doping, although the T_N reduces only marginally [310]. Unlike in the case of other dopants we find that doping with Fe leads to an insulating canted AFM structure as predicted by deGennes [37].

4.2.1.6 Dielectric study

The temperature dependence of real part of dielectric permittivity ε' for $CaMn_{1-x}Fe_xO_{3-\delta}$ with $x \leq 0.2$ for various applied frequencies is shown in figures 4.15 - 4.17. The dielectric constant shows the presence of dominant frequency-dependent dielectric relaxations, though it is small and relatively frequency independent below 50K for x = 0, 0.1 and below 150K for x = 0.2 sample. The peak temperature at which maximum dielectric constant occurs is found to be frequency-dependent and shifts to higher temperatures with frequency. This is characteristic property of dielectric relaxor. Also, the maximum value of dielectric permittivity decreases with increase in frequency. The variation in $\varepsilon'(T)$ exhibits a strong temperature dependence for x=0.1 and x=0.2 as compared to parent $CaMnO_3$. The presence of strong dielectric relaxations is also seen in the corresponding loss (tanδ) for the samples studied here. In all the studied samples ε' reaches to very large values in low frequency region, however, the ε' decreases with increase in frequency. In $CaMn_{1-x}Fe_xO_{3-\delta}$ compounds, the oxygen non-stoichiometry (δ) indicates the presence of mixed oxidation states of Mn. Therefore, the polarization in these compounds is via a conduction mechanism, i.e., electron-hopping between Mn^{3+} and Mn^{4+} ions. This electron-hopping appears to be favorable at lower applied ac electric field frequencies; the dielectric constant has therefore a maximum value at lower frequencies [308]. However, with Fe doping, δ decrease, which implies that with Fe doping in $CaMnO_{3-\delta}$ the concentration of Mn^{3+} is suppressed, which further, reduces the value of ε' for Fe doped compounds. In some of the materials giant dielectric constant values has been attributed to the Maxwell–Wagner polarization [309-315], some attributed it to the electron-relaxation-mode coupling [316] mechanism in which carriers are coupled with existing dielectric modes and some suggested that the motion of carriers (or polaron hopping) is responsible for this behavior. In our case, the large value of dielectric constant values can be explained by electron hopping mechanism along with Maxwell-Wagner relaxation. Maxwell-Wagner polarization generally refers to interfacial polarization occurring in inhomogeneous systems and is responsible for a giant dielectric constant in many dielectric inhomogeneous materials [309]. In Maxwell-Wagner relaxation the sample consists of conducting grains and poorly conducting grain boundaries. When an electric current passes through interfaces between these two different regions, because of their different conductivities, surface charges carriers accumulated at the interfaces, and give rise to a Debye-like relaxation process under an applied alternating voltage [312, 317]. The Debye-like relaxation behavior observed in these studied samples can arise from heterogeneity of the sample. The intrinsic contribution is due to the material's bulk response, observed at medium and high frequencies. The extrinsic contribution to ε' is associated with interfacial polarization produced in grain boundaries and sample-electrode contacts. In thin films of $Ca_{1-x}La_xMnO_3$, giant dielectric constant has been attributed to an internal barrier-layer capacitor composed of insulating layers between semiconducting grains [318].

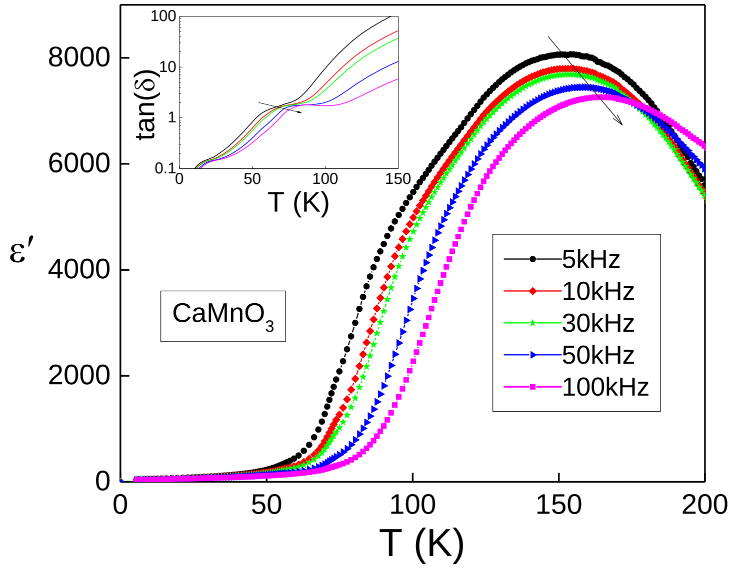

Figure 4.15: Real part of dielectric permittivity ε' as a function of temperature at different frequencies for $CaMnO_3$. Inset shows the variation of loss (tanδ) with temperature.

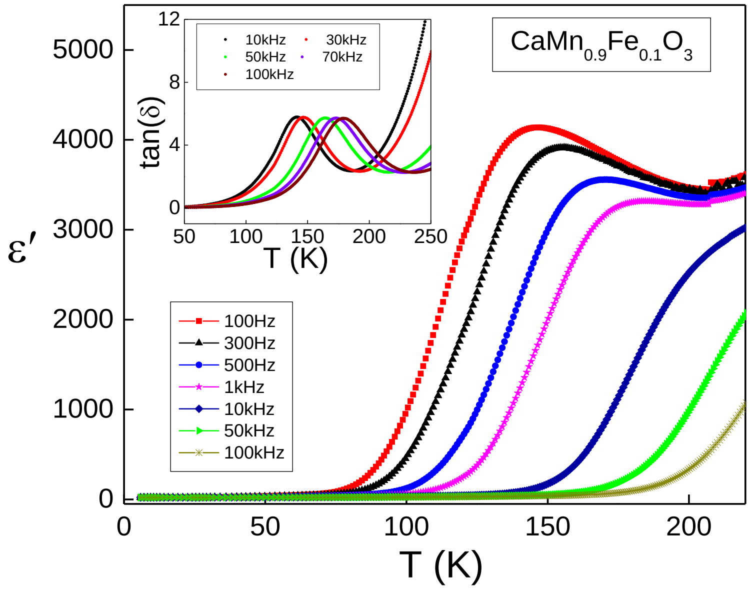

Figure 4.16: Real part of dielectric permittivity ε' as a function of temperature at different frequencies for $CaMn_{0.9}Fe_{0.1}O_3$. Inset shows the variation of loss (tanδ) with temperature.

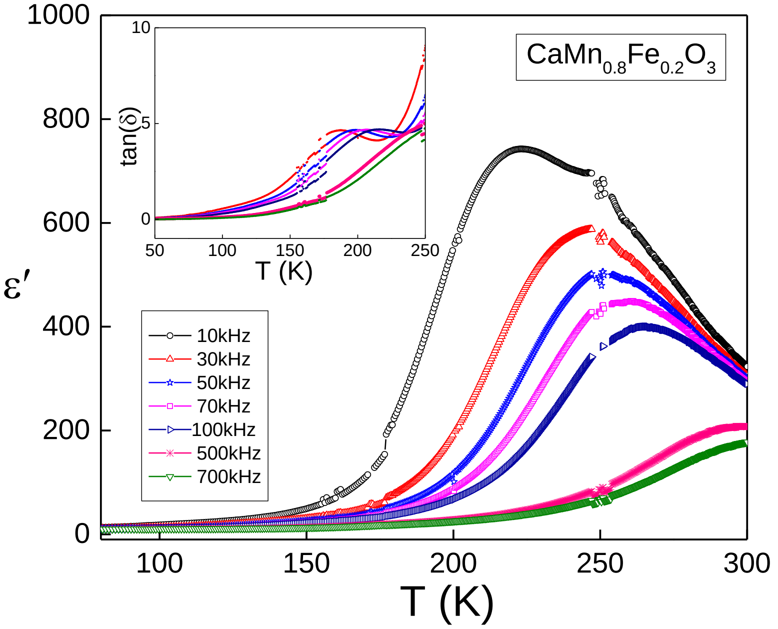

Figure 4.17: Real part of dielectric permittivity ε' as a function of temperature at different frequencies for $CaMn_{0.8}Fe_{0.2}O_3$. Inset shows the variation of loss (tanδ) with temperature.

The frequency dependence of the ε' can be represented by Cole-Cole equation with conductivity term, expressed as [312],

$$\varepsilon^*(\omega) = \varepsilon'(\omega) - i\varepsilon''(\omega) = \varepsilon_\infty + \frac{\varepsilon_s - \varepsilon_\infty}{1+\left(i\omega\tau\right)^{1-\alpha}} - \frac{\sigma_{dc}}{\omega\varepsilon_0}$$

where, ε_s and ε_∞ are the respective values of the dielectric constant at low and high frequency, $\omega(=2\pi f)$ is the angular frequency, τ is the relaxation time, σ_{dc} is ohmic conductivity, α is a measure of the distribution of relaxation time with values between 0 and 1. $\alpha < 1$ implies that the relaxation has a distribution of relaxation times, leading to a broader peak shape than a Debye peak. The last term dominates at low and moderate frequency region. The relaxation time τ is obtained by fitting ε' to above mentioned equation and is plotted as a function of 1000/T in figure 4.18(a)-4.18(c). The thermal variation of the τ is Arrhenius-like in the accessible temperature ranges, $\tau = \tau_0 \exp\left(E_A/k_B T\right)$, where, τ_0 is a constant, and E_A is the activation energy. The values of activation energy for x = 0, x = 0.1, and x = 0.2 are 0.07eV, 0.05eV, and 0.048eV, respectively. The values of activation energy are similar to that obtained for electron doped $Ca_{0.97}La_{0.03}MnO_3$ (~0.03eV) [318]. However, in an earlier report on oxygen deficient $CaMnO_{2.5}$, the estimated activation energy is found to be ~ 0.33eV [319].

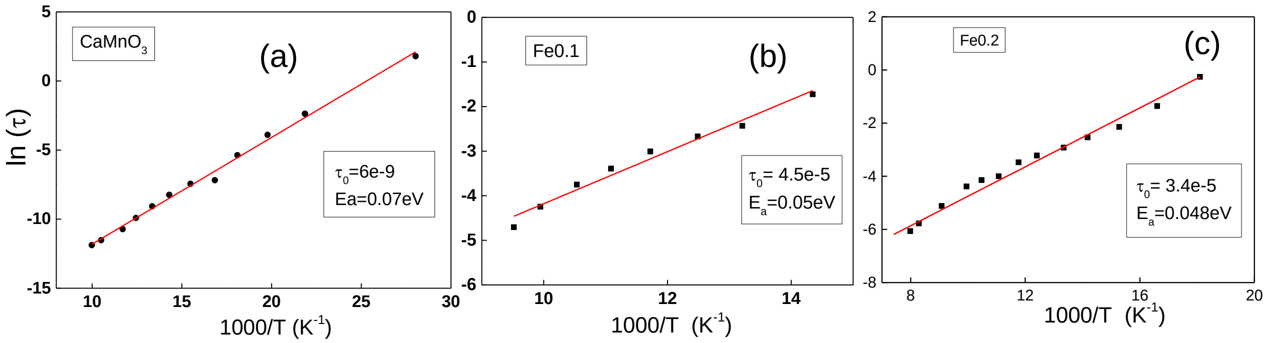

Figure 4.18: Arrheniuos plot of relaxation times for (a) $CaMnO_3$ (b) $CaMn_{0.9}Fe_{0.1}O_3$ (c) $CaMn_{0.8}Fe_{0.2}O_3$

4.3 Computational results

In this part we discuss our first-principle calculations on the parent compound $CaMnO_3$. The first-principle calculations were performed according to the density functional theory scheme (DFT) within the local spin density approximation (LDA) using a standard plane-wave code Quantum ESPRESSO (QE). The pseudopotentials used in the calculation were taken from the database provided in the QE package. In these pseudopotentials the 3s and 3p orbitals were treated as valence states for Mn and Ca atoms and 2s and 2p orbitals were considered as valence states for O atoms.The total number of valence states is therefore 15 for Mn, 10 for Ca and 6 for oxygen. The calculations were performed with a grid of 8×4×8 reciprocal lattice points. In this study, A-type, G-type, C-type antiferromagnetic states are considered.The relative stabilities of these magnetic states are determined by the comparison of their total energies (or enthalpy). In all calculations, the electronic self-consistent cycles were made to converge until the variation of the total energywas less than 10^{-8}eV. An energy cutoff of 60 Ry on the plane wave basis was used in representation of Kohn-Sham wave-functions.Structural optimization was carried out with Broyden–Fletcher–Goldfarb–Shanno (BFGS) algorithm.

These calculations were performed by stabilizing the structure of $CaMnO_3$, including lattice parameters and atomic coordinates. The starting values of structural parameters (lattice parameters, coordinates) were taken from our neutron data at 6K. The calculations were performed with different Hubbard correction (U). The relax lattice parameters and unit cell volume obtained are summarized in table 4.5 and compared with experimental structures. Note that the calculations correspond to a temperature of 0 K. Looking at the cell volumes, it is clear that the calculations with different values of Hubbard correction (U = 4eV, 5eV, 6eV) give optimised structures that are close to the experimental structure. The structural parameters changes slightly with U values. According to neutron powder diffraction, the most stable structure for $CaMnO_3$ is G-type AFM. In agreement with the experimental results, we find that for all the Hubbard approximation, the most stable configuration (lowest total energy) is obtained for the known G-type AFM configuration. The values of enthalpy for different magnetic structures calculated for different values of U are tabulated in table 4.6. The value of U does not change the relative stability of the magnetic structure. However increasing U increases the energy differences between the different structures.

Table 4.5: Structural parameters for CaMnO$_3$ obtained for three different values of Hubbard corrections compared with our experimental results.

Parameters	U=4eV			U=5eV			U=6eV			Exp
	G-type	C-type	A-type	G-type	C-type	A-type	G-type	C-type	A-type	G-type
a (Å)	5.1730	5.1710	5.1971	5.1889	5.1899	5.2144	5.2080	5.2119	5.2383	5.2771 (10)
b (Å)	7.2761	7.2909	7.2712	7.2922	7.3055	7.2917	7.3093	7.3235	7.3119	7.4404 (14)
c (Å)	5.1318	5.1323	5.1316	5.1417	5.1425	5.1422	5.1529	5.1529	5.1546	5.2616 (11)
Vol (Å^3)	193.2	193.5	193.9	194.55	194.98	195.5	196.15	196.68	197.43	206.59

Table 4.6: Values of total enthalpy for CaMnO$_3$calculated for three differentvalues of Hubbard corrections (U).

	U=4	U=5	U=6
	Enthalpy	Enthalpy	Enthalpy
G-type	-2302.54	-2597	-2443.70
C-type	-2300.03	-2569	-2406.86
A-type	-2261.02	-2505	-2333.25

4.4 Conclusion

The effect of electron doping on the structural, transport, and magnetic properties of Mn (IV) -rich ($Ca_{1-x}Y_xMnO_3$ ($x \leq 0.2$) and $CaMn_{1-x}Fe_xO_{3-\delta}$ ($0.0 \leq x \leq 0.3$)) samples have been investigated. Electron doping studies at Ca-site and Mn-site substitution leads to different magnetic and structural properties. The $Ca_{1-x}Y_xMnO_3$ ($x \leq 0.2$) compounds crystallize in orthorhombic structure for $x \leq 0.1$ while a coexistence of monoclinic (space group *$P2_1/m$*) and orthorhombic (space group *Pnma*) phase is observed at low temperatures in the case of x=0.2. However, in case of $CaMn_{1-x}Fe_xO_{3-\delta}$ ($0.0 \leq x \leq 0.3$), the compounds are found to be isostructural and crystallize in orthorhombic structure (space group *Pnma*). Doping with trivalent ion (Y^{3+}) at Ca^{2+} site or tetravalent Fe^{4+} substitution at Mn-site is found to give rise to ferromagnetic (FM) behavior in these compounds. The magnetic structure changes from G_z-type collinear AFM structure for x = 0.0 to canted AFM structure G_ZF_Y-type for Fe doped compounds. However, the phase separated magnetic ground state has been found for $Ca_{1-x}Y_xMnO_3$ compounds. A phase separated magnetic ground state consisting of ferromagnetic domains (~7μm) embedded in G-type antiferromagnetic matrix is observed in the sample, $Ca_{0.9}Y_{0.1}MnO_3$. The transition to the long-range magnetically ordered state in this sample is preceded by a Griffith's phase. The ferromagnetic behavior in the case of $Ca_{0.8}Y_{0.2}MnO_3$ is suppressed and the antiferromagnetic ordering is described by coexisting C-type and G-type magnetic structures corresponding to the monoclinic and orthorhombic phases, respectively.

Chapter 5

Summary and Conclusions

In the present thesis, we have investigated the effect of A-site and B-site doping on the magnetic structures of hexagonal $YMnO_3$ and orthorhombic $CaMnO_3$. The polycrystalline samples of doped manganites, studied in this thesis were prepared by solid state reaction method. Experimental techniques such as X-ray diffraction, neutron diffraction, dc magnetization, neutron depolarization, resistivity, dielectric, EXAFS, XANES and Mössbauer spectroscopy, were employed to investigate the structural, electronic and magnetic properties of these compounds. Rietveld refinement technique has been used to refine the crystal structures and to determine the magnetic structures. Bertaut's representation theory has been applied to find the possible models of magnetic structures for particular space group. This chapter presents the concise summary and conclusions based on the studies described in chapter 3 and 4.

5.1 Effect of A-site and B-site doping on the magnetic properties of hexagonal $YMnO_3$

Hexagonal manganites are currently under intensive investigations because of their interesting multiferroic behavior. Apart from the multiferroic phenomenon, there is another interesting aspect in hexagonal manganites: they have a natural two-dimensional structure with a triangular arrangement of the manganese atoms, which makes them an ideal system to explore the 2D magnetism. Among the hexagonal manganites, Yttrium manganite ($YMnO_3$) has an antiferromagnetic transition at T_N~75K and a ferroelectric transition at T_C~950K. The magnetic structure and frustrated behavior of this compound is found to be strongly influenced by chemical substitution or under the influence of external pressure.

5.1.1 Effect of A-site doping on the magnetic properties of $YMnO_3$

We have partially doped $YMnO_3$ with magnetic ions (Yb, Er, Ho, Tb) and studied its effect on the long range and short range magnetic behavior of these compounds. Doping by magnetic ions at Y-site influences the average A-site ionic radius and introduces additional R-Mn interactions in addition to Mn-Mn interactions in the system which is found to have significant influence on the magnetic properties and frustrated behaviour.

The A-site doped $Y_{1-x}R_xMnO_3$ (R= Yb, Er, Tb, Ho; $x \leq 0.2$) compounds are isostructural, and crystallize with hexagonal structure in *$P6_3cm$* space group. In this structure, Mn occupies 6c (x, 0, 0) site, O occupies 6c (x, 0, z), 2a (0, 0, z) and 4b (1/3, 2/3, z) sites, and Y occupies 2a (0, 0, z) and 4b (1/3, 2/3, z) sites. The dopants are evenly distributed between the two Yttrium sites. The unit cell volume shows a linear dependence with average A-site ionic radii, $<r_A>$. No significant change in T_N (within 10K) is observed on doping. The temperature variation of the volume indicates an anomalous reduction in volume at T_N which is found to be correlated with the square of the antiferromagnetic Mn moment. The anomaly exists irrespective of the moment of the dopant. Substitution of Y with Yb^{3+}, Er^{3+}, Ho^{3+}, and Tb^{3+} changes the tilting of MnO_5 trigonal bipyramids. The tilting angle (α) is defined by the angle between the O1-O2 axis of the MnO_5 bipyramid and c axis, and the buckling is represented by the angle β between the O3-O4-O4 plane and c axis . The tilting angle of the MnO_5 polyhedron decreases linearly with increase in $<r_A>$, whereas the buckling angle remains constant. No significant influence of this change is observed on the magnetic nature of these samples. By substituting Y with 20% of Er and Yb, the magnetic structure changes gradually from Γ_3 to Γ_4 irreducible representation (IR), while the moments at 6K remain almost unchanged with doping. With Ho doping at Y site, the magnetic structure is explained by taking Γ_3 alone for $5K \leq T < 35K$ and a mixture of Γ_3 and Γ_4 IR for $T \geq$

35K. However, in Tb doped sample, the magnetic structure has been explained by Γ_4 IR with moment on Tb. Geometrical frustration effect reduces significantly in all the doped samples. It is also noticeable that the intensity of the diffuse scattering becomes gradually weakened with doping of magnetic ions at the Y-site. The short range correlations in these doped samples have also been studied by Fourier transforming the diffuse part of the magnetic neutron diffraction data. The magnetic coupling between the magnetic R ion and Mn moments plays an important role here and relieves the frustration effects inherent to the quasi-two dimensional Mn moment ordering. We find the results can be explained by combining the effect of R-Mn interactions and ionic size of the dopants. These studies conclude that the partial substitution of Y by magnetic ions, not only change the long range Mn order but also effect the short range magnetic correlations, along with the frustrated behavior of the compounds.

5.1.2 Effect of B-site doping on the magnetic properties of $YMnO_3$

The effect of B-site substitution in $YMn_{1-x}M_xO_3$ (M = Ti, Fe, Ga; x = 0, 0.1) and $YMn_{1-x}Fe_xO_3$ ($x \leq 0.5$) series have been investigated. We find that these dopants affect the magnetic structure of this compound in contrasting manner.

The polycrystalline compounds of $YMn_{1-x}M_xO_3$ (M = Ti, Fe, Ga; x = 0, 0.1) are isostructural and crystallize with hexagonal structure in *P6₃cm* space group. We find that doping with these three ions, Ti^{4+} (d^0), Fe^{3+} (d^5) and Ga^{3+} (d^{10}), influences both the T_N and magnetic structure, unlike other Mn-site dopants reported previously. The magnetic structure of $YMnO_3$ is described by Γ_3 IR below T_N ~ 75K. The magnetic structure remains same with Ga doping. However, the magnetic structure is modified on doping with nonmagnetic ion Ti^{4+} (d^0). It is modeled by the basis vectors of the Γ_2 IR with moment $2.3\mu_B$ at 6K. On doping with Fe^{3+} (d^5) the magnetic structure immediately below T_N is explained by considering the Γ_3 IR.On further lowering of temperature, a spin reorientation at ~ 35K is observed. Below this temperature, the magnetic structure of $YMn_{0.9}Fe_{0.1}O_3$ is explained by considering mixed Γ_3 and Γ_4 representations. The ordered moments are found to be reduced from the expected value for a Mn^{3+} ion in all these compounds indicating the frustrated nature of these compounds. However, the frustration parameter, f is significantly reduced in the case of Ti doped compound with Γ_2 representation. This reduction might be due to the out of plane interaction allowed in Γ_2 IR.

We have investigated the local structure of hexagonal $YMn_{1-x}M_xO_3$ (M = Ti, Fe, Ga; x = 0, 0.1) compounds by x-ray absorption spectroscopy measurements. The x-ray absorption near edge spectra (XANES) show that the valence state of Mn atom remain essentially unaltered on doping. The dopants substitute at the Mn-site preserving the trigonal bipyramidal geometry. This shows that the substitution of Mn by 10% Ti, Fe and Ga does not lead to any structural transition i.e. structure remain hexagonal and is therefore, in agreement with our earlier x-ray diffraction and neutron diffraction studies.XANES spectra of $YMn_{0.9}Ti_{0.1}O_3$ at Ti K-edge,$YMn_{0.9}Ga_{0.1}O_3$ at Ga K-edge, indicates Ti is in +4 oxidation state and Ga is in +3 oxidation state, respectively. XANES measurements together with Mössbauer and magnetization measurements indicate the presence of Fe in +3 oxidation state. No appreciable change is observed in the XANES spectra of the samples with temperature.This indicates that structure as well as the oxidation states of Mn remains same with temperature for all doped samples. The EXAFS measurements indicate the presence of a double peak or shoulder for all the studied samples at all studied temperatures. The presence of double peak is an indication of different Mn-O coordination shells having large difference in the bond lengths between the $\langle Mn\text{-}O_A \rangle$ and $\langle Mn\text{-}O_P \rangle$ bonds, where O_A and O_P denote the two apical and three planar oxygen atoms, respectively. This difference in $\langle Mn\text{-}O_A \rangle$ and $\langle Mn\text{-}O_P \rangle$ bonds is also observed in neutron diffraction data. The temperature dependent behavior of bond lengths obtained from EXAFS measurements is in agreement with the neutron diffraction data in all studied samples.

Further, we have investigated the role of doping Fe on the structural, magnetic and dielectric properties of frustrated antiferromagnet $YMn_{1-x}Fe_xO_3$ ($x \leq 0.5$). We find that with Fe doping at Mn site progressive changes in chemical structure and magnetic structure as a function of temperature and composition. The neutron diffraction analysis shows that the structure of these polycrystalline samples changes from hexagonal phase (space group $P6_3cm$) to orthorhombic phase (space group *Pnma*) for $x > 0.2$. The frustration parameter decreases with Fe substitution. All the compounds are antiferromagnetic and the magnetic structure belongs to a mixture of Γ_3 and Γ_4 (IR) in the hexagonal phase and the ratio of these two IRs is found to vary with Fe doping ($x \leq 0.2$). The angle (φ) the spin makes with the a-axis changes from 28° for $YMn_{0.9}Fe_{0.1}O_3$ to 55° for $YMn_{0.8}Fe_{0.2}O_3$ at 6K. A continuous spin reorientation as a function of temperature is observed in these samples. The magnetic ground state in the orthorhombic phase of the higher doped samples ($x \geq 0.3$) belongs to Γ_1 ($G_xC_yA_z$) representation of *Pnma* setting. In $YMnO_3$ suppression of dielectric constant ε' is observed below T_N indicative of magnetoelectric coupling. This anomalous behavior reduces in Fe doped samples. Large dielectric anomalies are observed coinciding with the magnetic transition temperature in these compounds which we show to scale with sub lattice magnetization obtained from neutron diffraction and follows a M^2 behavior close to T_N in agreement with predictions of Landau theory. XANES measurements at Mn K-edge demonstrate that the valence state of Mn atom remain essentially unaltered by doping. The dopants substitute the Mn-site, preserving the trigonal bipyramidal geometry for $x \leq 0.2$. For higher doping region ($0.3 \leq x \leq 0.5$), a second orthorhombic phase appears where Mn is coordinated by six oxygen atoms (hexagonal coordination). These observations are in agreement with our earlier x-ray diffraction and neutron diffraction studies.

The first-principle calculations on $YMnO_3$ were performed according to the density functional theory scheme (DFT) within the local spin density approximation (LDA) using a standard plane-wave code Quantum ESPRESSO (QE). The exchange-correlation potential utilized in these calculations was the Perdew-Zunger (PZ) version of the local density approximation (LDA). The pdseudopotentials used in the calculation were taken from the database provided in the QE package. These calculations were performed incorporating the Hubbard correction.The A-type antiferromagnetic ordering was adopted in the magnetic calculations. The relaxed structural parameters obtained by QE code are in agreement with the experimental as well as with the simulations results of VASP.

5.2 Effect of A-site and B-site doping on the magnetic properties of orthorhombic $CaMnO_3$

$CaMnO_3$ is the end member of the (La,Ca)MnO_3 system. It has the perovskite related $GdFeO_3$-type orthorhombic structure and exhibits a G-type antiferromagnetic (AFM) structure (T_N ~125 K) with a weak ferromagnetic component in its ground state. Doping with trivalent ions at Ca^{2+} site or tetravalent or pentavalent substitution at Mn site is found to give rise to ferromagnetic (FM) behavior in these compounds. In particular, attention was paid to the unexpected behavior observed for the low doped-regime, where a ferromagnetic (FM) component develops together with G-type antiferromagnetic structure. The role of spin canting and/or phase separation leading to FM behavior in these compounds(Mn (IV)- rich) has been a subject of discussion in literature.

5.2.1 The effect of A-site doping on the magnetic properties of $CaMnO_3$

The effect of electron doping on the structural, transport, and magnetic properties of Mn(IV)-rich $Ca_{1-x}Y_xMnO_3$ ($x \leq 0.2$) samples have been investigated. The compounds crystallize in orthorhombic structure for $x \leq 0.1$ while a coexistence of monoclinic and orthorhombic phase is observed at low temperatures in the case of x=0.2. The temperature dependence of the resistivity exhibits a semiconducting behavior and is described by small polaron model. The activation energy exhibits a minimum at x=0.1 and is ascribed to presence of ferromagnetic clusters in this sample. The magnetic structure for x=0.1 sample, at 6K is found to be G_Z type similar to the parent compound. The rapid increase in magnetization and decrease in flipping ratio below 110K, indicates the presence of ferromagnetic correlations (~7μm). These studies together indicate a phase separated state with FM clusters embedded in the AFM matrix in x=0.1 sample. The transition to the long-range magnetically ordered state in this sample is preceded by a Griffith's phase. Neutron diffraction and neutron depolarization studies rule out the presence of ferromagnetic correlations in x=0.2 sample. The ferromagnetic behavior in this case is suppressed and the antiferromagnetic ordering is described by coexisting C-type and G-type magnetic structures. For x=0.2, the orthorhombic phase partially transforms to a monoclinic phase. An antiferromagnetic ordering of the type G_z for the orthorhombic phase and C-type ordering for the monoclinic phase is observed in x=0.2 sample.

5.2.2 The effect of B-site doping on the magnetic properties of $CaMnO_3$

The B-site substitutional effects have been investigated in $CaMn_{1-x}Fe_xO_{3-\delta}$ ($0.0 \leq x \leq 0.3$) compounds by using resistivity, magnetization, and neutron powder diffraction techniques. The compounds are found to be isostructural and crystallize in $GdFeO_3$-type orthorhombic structure (space group *Pnma*). With Fe doping, no change in structure is observed although it induces lattice expansion. Mössbauer and paramagnetic susceptibility measurements show that Fe substitutes in 4+ valence state and XANES measurements indicate the presence of mixed oxidation states of Mn. The compounds exhibit insulating behavior in the studied temperature range. An increase in resistivity is observed with Fe doping, and this is explained by taking into consideration the band structure of Fe^{4+} and Mn^{4+}. The temperature dependence of resistivity is found to be described by small polaron model in x=0 sample. But for x=0.1 sample resistivity behavior is better described by variable range hopping mechanism rather than small polaron model. With further increase in Fe doping a parallel combination of variable range hoping model and small polaron model is used to describe the resistivity behavior. A small reduction in T_N from 120K (x = 0) to 100K (x = 0.2) with increase in x is found. The magnetic structure changes from G_z-type collinear AFM structure for x=0.0 to canted AFM structure G_ZF_Y-type for Fe doped compounds. The AFM component of the moment progressively decreases with x while FM component exhibits a maximum at x = 0.2.

First principle calculations on orthorhombic-$CaMnO_3$ were performed using the QE code to establish the magnetic ground state of this compound. The PZ version of the LDA for the exchange-correlation potential was utilized in these calculations. The Hubbard corrections were incorporated. For orthorhombic $CaMnO_3$, the calculations were performed with a grid of 8×4×8 reciprocal lattice points. In this study, A-type, G-type, C-type antiferromagnetic states were considered. The relative stabilities of these magnetic states were determined by comparing their total energies (or enthalpy). These calculations show that for $CaMnO_3$, G-type magnetic structure is the most stable among the three antiferromagnetic configurations, which is in agreement with the experimental results.

5.3 Scope of the work

The nature of manganites and their strong correlations, offer a wide range of electronic properties, magnetic properties, and cross coupling of electric and magnetic properties (multiferroics). In particular, these compounds provide a stage to study the cooperative ordering of strongly coupled charge, spin, lattice and orbital degrees of freedom. In the present work the effect of substituting with magnetic and non magnetic ions, at the A- and B-site, on the magnetic properties, electronic properties and variation in crystal structure of hexagonal $YMnO_3$ orthorhombic $CaMnO_3$ have been investigated.

Our neutron scattering studies on both Y-site doping and Mn-site doping on $YMnO_3$ have shown different magnetic ground states. These studies showed that the phase transition from one magnetic phase to other and the mechanism that drives these transitions is complicated. The multiferroic properties (ferroelectric polarization) of these hexagonal mangnaites can be controlled by changing the magnetic ground state. Therefore, doping at Y-site and Mn-site could possibly improve the multiferroic properties. Thus, different types of doping need to be investigated to understand the mechanism that governs the magnetic phase transitions and also to improve the multiferroic properties of hexagonal manganites. In $CaMnO_3$, the Ca-site as well as Mn-site substituted studies showed both phase separation and canted behavior. We have observed that the electron doping studies at Ca-site and Mn-site substitution leads to different magnetic ground state. The debate over phase separation versus canted magnetic structure continues to be of interest. The $Ca_{1-x}Y_xMnO_3$ and $CaMn_{1-x}Fe_xO_3$ are not conclusive of the whole magnetic phase diagram of the electron doped system. Therefore, a continuation of compositional exploration is necessary to understand the magnetic structure of these electron-doped (Mn (IV)- rich) systems.

References:

[1] J. H. van Santen and G. H. Jonker, Physica **16**, 599 (1950).

[2] G. H. Jonker and J. H. van Santen, Physica **16**, 337 (1950).

[3] Littlewood P.B., Principles of Quantum Condensed Matter Physics, Lecture notes, 2002. Available at http://www.tcm.phy.cam.ac.uk/~pbl21.

[4] M. V. Mostovoy, Phys. Rev. Lett. **96**, 067601 (2006).

[5] J. J. Betouras, G. Giovannetti and J. van den Brink, Phys. Rev. Lett. **98**, 257602, (2007).

[6] S.-W. Cheong and M. Mostovoy, Nature Mater. **6**, 13 (2007).

[7] M.A. Gilleo, Acta Crystallogr. **10**, 161 (1957).

[8] H. L. Yakel, W. Koehler, E. F. Bertaut and E. F. Forrat, Acta Crystallogr. **16**, 957 (1963).

[9] M. N. Iliev, M. V. Abrashev, H. G. Lee, V. N. Popov, Y. Y. Sun, C. Thomsen, R. L. Meng, and C. W. Chu, Phys. Rev. B **57**, 2872 (1998).

[10] W. C. Yi, C. S. Seo, S. I. Kwun, and J. G. Yoon, Appl. Phys. Lett. **77**, 1044 (2000).

[11] H. N. Lee, Y. T. Kim, and S. H. Choh, Appl. Phys. Lett. **76**, 1066 (2000).

[12] S. Imada, T. Kuraoka, E. Tokumitsu, and H. Ishiwara, Jpn. J. Appl. Phys. **40**, 666 (2001).

[13] S. Geller, and E. A. Wood, Acta Cryst. **9**, 563 (1956); S. Geller, J. Chem. Phys. **24**, 1236 (1956).

[14] R. L. White, J. Appl. Phys. **40**, 1061 (1969).

[15] G. Demazeau, M. Pouchard and P. Hagenmuller, J. Solid State Chem. **9**, 202 (1974).

[16] A. J. Millis, P. B. Littlewood and B. I. Shraiman, Phys. Rev. Lett. **74**, 5144 (1995).

[17] A. Urushibara, Y. Moritomo, T. Arima, A. Asamitsu, G. Kido and Y. Tokura, Phys. Rev. B **51**, 14103 (1995).

[18] H. Röder, J. Zang and A. R. Bishop, Phys. Rev. Lett. **76**, 1356 (1996).

[19] A. V. Boris, N. N. Kovaleva, A. W. Bazhenov, P. J. M. van Bentum, Th. Rasing, S.-W. Cheong, A. V. Samoilov and N.-C. Yeh, Phys. Rev. B **59**, R697 (1999).

[20] M. Quijada, J. Cerne, J. R. Simpson, H. D. Drew, K. H. Ahn, A. J. Millis, R. Shreekala, R. Ramesh, M. Rajeswari and T. Venkatesan, Phys. Rev. B **58**, 16093 (1998).

[21] A. J. Millis, B. I. Shraiman and R. Mueller, Phys. Rev. Lett. **77**, 175 (1996).

[22] H. L. Ju, H.-C. Sohn and K. M. Krishnan, Phys. Rev. Lett. **79**, 3230 (1997).

[23] V. Ferrari, M. Towler and P. B. Littlewood, Phys. Rev. Lett. **92**, 227202 (2003).

[24] A. S. Moskvin and I. L. Avvakumov, Physica B **322**, 371 (2002).

[25] H. Jahn and E. Teller, Proc. R. Soc. Lond. A **161**, 5220 (1937).

[26] C. Zener, Phys. Rev. **118**, 141 (1960).

[27] E. Dagotto, T. Hotta, A. Moreo, Phys. Rep. **344**, 1 (2001);

[28] T. Hotta, Rep. Prog. Phys. **69,** 2061 (2006).

[29] H. F. Kay, and P. C. Bailey, Acta. Cryst. **10**, 219 (1957).

[30] V. M. Goldschmidt, Naturwissenschaften **14**, 477 (1926); V. Goldschmidt Skrifer Norske Videnskaps-Akad. Oslo, I. Mat.-Nat. Kl. 8, (1926)

[31] J. B. Goodenough, Rep. Prog. Phys. **67**, 1915 (2004).

[32] A. M. Glazer, Acta Cryst. B **28**, 3384 (1972); A. M. Glazer, Acta Cryst. A **31**, 756 (1975).

[33] J. B. Goodenough, and J. M. Longo in Landolt-Börnstein Tabellen; New Series III/4a; Springer-Verlag: Berlin, 1970; J. B. Goodenough, Prog. Solid State Chem. **5**, 145 (1975).

[34] G. Maris, V. Volotchaev, and T. M. Palstra, New J. Phys. **6**, 153 (2004).

[35] C. Zener, Phys. Rev. **82**, 403 (1951).

[36] P. W. Anderson and H. Hasegawa, Phys. Rev. **100**, 675 (1955).

[37] P. G. de Gennes, Phys. Rev. **118**, 141 (1960).

[38] H. A. Kramers, Physica **1**, 182 (1934).

[39] J. B. Goodenough, Phys. Rev. **100**, 564 (1955).

[40] J. Kanamori, J. Phys. Chem. Solids **10**, 87 (1959).

[41] E. O. Wollan and W. C. Koehler, Phys. Rev. **100**, 545 (1955).

[42] H. L. Ju, H.-C. Sohn and K. M. Krishnan, Phys. Rev. Lett. **79**, 3230 (1997).

[43] M. Fath, S. Freisem, A. A. Menovsky, Y. Tomioka, J. Aarts, and J. A. Mydosh, Science **285**, 1540 (1999).

[44] P. A. Algarabel, J. M. De Teresa, J. Blasco, M. R. Ibarra, Cz. Kapusta, M. Sikora, D.Zajac, P. C. Riedi, and C. Ritter, Phys. Rev. B **67**, 134402 (2003).

[45] S. von Molnar, and J. M. D. Coey, Curr. Opin. Solid State Mater. Sci. **3**, 171 (1998).

[46] J. van den Brink and D. Khomskii, Phys. Rev. B **63**, R140416 (2001).

[47] AP. Schiffer, A.P. Ramirez, W. Bao, S.-W. Cheong, Phys. Rev. Lett. **75**, 3336 (1995).

[48] K. R. Poeppelmeier, M. E. Leonowicz, J. C. Scanlon, J. M. Longo, and W. B. Yelon, J. Solid State Chem. **45**, 71 (1982).

[49] C. Martin, A.Maignan, M. Hervieu and B. Raveau, Phys. Rev. B **60**, 12191 (1999).

[50] H. Taguchi, Phys. Status Solidi A **88**, K79 (1985).

[51] I. O. Troyanchuk, N. V. Kasper, N. V. Samsonenko, H. Szymczak, and A. Nabialek, J. Phys.: Condens. Matter **8,** 10627 (1996).

[52] J. Blasco, C. Ritter, J. García, J. M. de Teresa, J. Pérez-Cacho, and M. R. Ibarra, Phys. Rev. B **62**, 5609 (2000).

[53] A. Maignan, C. Martin, F. Damay, and B, Raveau, Chem. Mater. **10**, 950 (1998).

[54] C. Martin, A. Maignan, M. Hervieu, B. Raveau, Z. Jirák, M. M. Savosta, A. Kurbakov, V. Trounov, G. André, and F. Bourée, Phys. Rev. B **62**, 6442 (2000).

[55] C. D. Ling, E. Granado, J. J. Neumeier, J. W. Lynn, and D.N. Argyriou, Phys. Rev. B **68**, 134439 (2003).

[56] E. Granado, C. D. Ling, J. J. Neumeier, J. W. Lynn, and D. N. Argyriou, Phys. Rev. B **68**, 134440 (2003).

[57] N. Imamura, M. Karppinen, and T. Motohashi, H. Yamauchi, Phys. Rev. B **77**, 024422 (2008).

[58] P. A. Algarabel, J. M. De Teresa, B. García- Landa, L. Morellon, M. R. Ibarra, C. Ritter, et al., Phys. Rev. B **65**, 104437 (2002).

[59] M. Yu. Kagan, D. I. Khomskii, and M. V. Mostovoy, Eur. Phys. J. B **12**, 217 (1999).

[60] S. Yunoki, and A. Moreo, Phys. Rev. B **58**, 6403 (1998).

[61] H. Yi, and J. Yu, Phys. Rev. B **58,** 11123 (1998).

[62] S. Yunoki, J. Hu, A. L. Malvezzi, A. Moreo, N. Furukawa, and E. Dagotto, Phys. Rev. Lett. **80**, 845 (1998).

[63] A. Moreo, S. Yunoki and E. Dagotto, Science **283**, 2034 (1999a).

[64] S. K. Mishra, S. Satpathy, F. Aryasetiawan, O. Gunnarsson, Phys. Rev. B **55**, 2725 (1997).

[65] M. M. Savosta, P. Novák, M. Maryško, Z. Jirák, J. Hejtmánek, J. Englich, J. Kohout, C. Martin, and B. Raveau, Phys. Rev. B **62**, 9532 (2000).

[66] K. Hagdorn, D. Hohlwein, J. Ihringer, K. Knorr, W. Prandl, H. Ritter, H. Schmid, Th. Zeiske, Eur. Phys. J. B **11**, 243 (1999).

[67] A. Maignan, C. Martin, M. Hervieu, B. Raveau, Solid State Commun. **117**, 377 (2001).

[68] C. Martin, M. Miclau, S. Hébert, M. Giot, A.Maignan, G. André, F. Bouree-Vigneron, J. Magn. Magn. Mater. **321**, 3938 (2009).

[69] N. D. Mathur,& P. B. Littlewood, Phys. Today **56**, 25 (2003).

[70] C. N. R. Rao, A. K. Kundu, M. M. Seikh, L. Sudheendra, Dalton Trans. 3003 (2004).

[71] E. Dagotto, Nanoscale phase separation and colossal magnetoresistance. Berlin,Germany: Springer, 2003; E. Dagotto, Science **309**, 257 (2005).

[72] V. B Shenoy, D. D. Sarma, C. N. R. Rao, Chem. Phys. Chem. **7**, 2053 (2006).

[73] Vijay B. Shenoy, and C. N. R. Rao, Phil. Trans. Royal Soc. London A **366**, 63 (2008).

[74] C. Ritter, R. Mahendiran, M. R. Ibarra, A. Maignan, B. Raveau, C. N. R. Rao, Phys. Rev. B **61**, R9229 (2000).

[75] J. M. Tranquada, B. J. Sternlieb, J. D. Axe, Y. Nakamura, and S. Uchida, Nature (London) **375**, 561 (1995).

[76] J. M. Tranquada, P. Wochner, and D. J. Buttrey, Phys. Rev. Lett. **79**, 2133 (1997).

[77] A. Moreo, M. Mayr, A. Feiguin, S. Yunoki, E. Dagotto, Phys. Rev. Lett. **84**, 5568, (2000).

[78] M. Uehara, S. Mori, C. H. Chen, S.-W. Cheong, Nature **399**, 560 (1999).

[79] J. B. MacChesney, H. J. Williams, J. F. Potter, and R. C. Sherwood, Phys. Rev. **164**, 779 (1967).

[80] J. Briatico, B. Alasciao, R. Allub, A. Butera, A. Caneiro, M. T. Causa, and M. Tovar, Phys. Rev. B **53**,14020 (1996).

[81] Y. Zhou, I. Matsubara, R. Funahashi, G. Xu, and M. Shikano, Mater. Res. Bull. **38**, 341 (2003).

[82] E. Dagotto, T. Hotta, and A. Moreo, Phys. Rep. **344**, 1 (2001).

[83] A. Machida, Y. Moritomo, S. Mori, N. Yamamoto, K. Ohoyama, E. Nishibori, M. Takata, M. Sakata. T. Otomo, and A. Nakamura, J. Phys. Soc. Jpn., **71**, 27 (2002).

[84] El’ad N. Capsi, M. Avdeev, S. Short, J. D. Jorgensen, M. V. Lobanov, Z. Zeng, M. Greenblatt, P. Thiyagarajan, C. E. Botez, P. W. Stephens, Phys. Rev. B **69**, 104402 (2004).

[85] H. L. Yakel, W. Koehler, E. F. Bertaut and E. F. Forrat, Acta Cryst. **16**, 957 (1963).

[86] N. A. Spaldin, and M. Fiebig, Science **309** (2005) 391.

[87] S. –W Cheong and M. Mostovoy, Nature Mater. **6,** 13 (2007).

[88] H. Schmid, Ferroelectrics **162**, 317 (1994).

[89] T. Kimura, T. Goto, H. Shintani, K. Ishizaka, T. Arima, Y. Tokura, et al. Nature **426**, 55 (2003).

[90] N. Hur, S. Park, P.A. Sharma, J. S. Ahn, S. Guha, and S. –W Cheong. Nature **429**, 392 (2004).

[91] G. A. Smolenskii and V. A. Bokov, J. Appl. Phys., **35**, 915 (1964).

[92] K. H. Hellwege, A. M. Hellwege, Numerical data and Functional Relationship group III 16a, (1981)

[93] E. F. Bertaut, M. Mercier, and R. Pauthenet, Phys. Lett. **5**, 27 (1963).

[94] B. B. van Aken, Structural response to electronic transition in hexagonal and ortho-manganites, PhD Thesis, University of Gronigen (2001).

[95] K. Lukaszewicz and J. Karut-Kalicinska, Ferroelectrics **7**, 81 (1974).

[96] T. Katsufuji, M. Masaki, A. Machida, M. Moritomo, K. Kato, E. Nishibori, M. Takata, M. Sakata, K . Ohoyama, K. Kitazawa and H. Takagi, Phys. Rev. B **66**, 134434 (2002).

[97] I.-K. Jeong, N. Hur, and T. Proffen, J. of App. Crystallogr. **40**, 730 (2007).

[98] C. J. Fennie and K. M. Rabe, Phys. Rev. B **72**, 100103 (2005).

[99] T. Lonkai, D. G. Tomuta, U. Amann, J. Ihringer, R. W. A. Hendrikx, D. M. Többens, and J. A. Mydosh, Phys. Rev. B **69**, 134108 (2004).

[100] A. S. Gibbs, K. S. Knight, and P. Lightfoot, Phys. Rev. B **83**, 094111 (2011).

[101] A. P. Ramirez, in Handbook of Magnetic Materials, edited by K. H. J. Buschow, Vol 13 (North-Holland, Amsterdam, 2001).

[102] B. B. Van Aken, J. W. G. Bos, R. A. de Groot, and T. T. M. Palstra, Phys. Rev. B **63**,125 (2001).

[103] W. C. Koehler, H. L. Yankel, E. O. Wollan, and J. W. Cable, Phys. Lett. **9**, 93 (1964).

[104] F. Yen, C. de la Cruz, B. Lorenz et al., J. Mater. Res, **22** 2163 (2007).

[105] X. Fabréges, I. Mirebeau, P. Bonville, S. Petit, G. Lebras-Jasmine, A. Forget, G. André, and S. Pailhès, Phys. Rev. B **78**, 214422 (2008).

[106] M. Fiebig, C. Degenhardt, and R. V. Pisarev, Phys. Rev. Lett.**88**, 272031 (2002).

[107] M. Fiebig, D. Fröhlic, K. Kohn, St. Leute, Th. Lottermoser, V. V. Pavlov ,and R. V. Pisarev, Phys. Rev. Lett. **84**, 24. (2000).

[108] T. Lonkai, D.Hohlwein, J. Ihringer, and W. Prandl, Appl. Phys. A **74**, S843 (2002).

[109] M. Fiebig, Th. Lottermoser, and R. V. Pisarev, J. Appl. Phys. **93**, 8194 (2003).

[110] O. P. Vajk, M. Kenzelmann, J. W. Lynn, S. B. Kim, and S.-W. Cheong, Phys. Rev. Lett. **94**, 087601, (2005).

[111] D. Meier, H. Ryll, K. Kiefer, B. Klemke, J. –U. Hoffmann, R. Ramesh, and M. Fiebeg, Phys. Rev. B **86**, 184415 (2012).

[112] E. F. Bertaut, Magnetism, edited by G. T. Rado and H. Shul (Academic, New York, 1963), Vol III.

[113] A. Muñoz, J. A. Alonso, M. J. Martínez-Lope, M. T. Casáis, J. L. Martínez and M. T. Fernández- Diáz Phys. Rev. B **62,** 9498 (2000).

[114] J. Reif, C. Rau, and E. Mitthias, Phys. Rev. Lett. **71**, 1931 (193).

[115] V. V. Pavalov, R. V. Pisarev, A. Kirilyuk, ans T. Rasing, Phys. Rev. Lett. **78** 2004 (1997)

[116] R. R. Birss, Symmetry and Magnetism (North-Holland, Amsterdam, 1966*).*

[117] I. V. Solovyey, M. V. Valentyuk and V. V. Mazurenko, Phys. Rev. B **86**, 054407 (2012).

[118] J. Park, M. Kang, J. Kim, S. Lee, K -H Jang, A. Pirogov, and J –G Park, Phys. Rev. B **79**,064417 (2009).

[119] T. Chatterji and T. C. Hansen J. Phys.: Condens. Matter **23**, 276007 (2011).

[120] D. G. Tomuta, S. Ramakrishnan, G. J. Niewenhuys, and J. A.Mydosh, J. Phys.: Condens. Matter **13**, 4543 (2001); N. Iwata, J. Phys. Soc. Jpn. **67**, 3318 (1998).

[121] H. J. Lewtas, A. T. Boothroyd, M. Rotter et al. Phys. Rev. B **82**, 184420 (2010).

[122] B. Lorenz, ISRN Cond. Mat. Phys. **2013**, 497073 (2013).

[123] D. P. Kozlenko, S. E. Kichanov, S. Lee, J. G. Park, and B. N. Savenko, J. Phys.: Condens. Matter **19**, 156228 (2007).

[124] M. Bieringer, J. E. Greedan, and A. S. Wills, Appl. Phys. A **74**, S601 (2002).

[125] M. Bieringer and J. E. Greedan, J. Solid State Chem. **143**, 132 (1999).

[126] X. Fabréges, S. Petit, I. Mirebeau, L. Pinsard, A. Forget, M. T. Fernández-Diáz, and F. Porcher, Phys. Rev. Lett. **103**, 067204 (2009).

[127] M. Fiebig, D. Fröhlich, T. Lottermoser, and K. Kohn, Appl. Phys. Lett. **77**, 4401 (2000).

[128] H. D. Zhou, J. Lu, R. Vasic, B. W. Vogt, J. A. Janik et al., Phys. Rev. B **75**, 132406, (2007)

[129] H. D. Zhou, J. C. Denyszyn, and J. B. Goodenough, Phys. Rev. B **72,** 224401 (2005).

[130] P. A. Sharma, J. S. Ahn, N. Hur et al., Phys. Rev. Lett. **93**, 177201 (2004).

[131] N. Hur, I. K. Jeong, M. F. Hundley, S. B. Kim, and S.W. Cheong, Phys. Rev. B **79**, 134120 (2009).

[132] B. Lorenz, F. Yen, M. M. Gospodinov, and C. W. Chu, Phys. Rev. B **71**, 014438 (2005).

[133] H. D. Zhou, J. A. Janik, B. W. Vogt et al., Phys. Rev. B **74**, 094426 (2006).

[134] A. Muñoz, J. A. Alonso, M.J. Martínez-Lope, M. T. Casáis, J. L. Martínez, M. T. Fernández-Diáz, Chem. Mater. **13**, 1497 (2001).

[135] M. Fiebig, C. Degenhardt, and R. V. Pisarev, J. Appl. Phys. **91**, 8867 (2002).

[136] S. Nandi, A. Kreyssig, L. Tan et al., Phys. Rev. Lett. **100**, 217201 (2008).

[137] P. J. Brown and T. Chatterji, J. Phys.: Condens. Matter **18**, 10085 (2006).

[138] J. Park, U. Kong, A. Pirogov, S. I. Choi, J.-G. Park, Y. N. Choi, C. Lee, and W. Jo, Appl. Phys. A: Mater. Sci. Process. **74**, S796 (2002).

[139] J. Park, U. Kong, S. I. Choi, J.-G. Park, C. Lee, and W. Jo, Appl. Phys. A **74**, 802 (2002).

[140] M. C. Sekhar, S. Lee, G. Choi, C. Lee and J. –G. Park Phys. Rev. B **72,** 014402 (2005).

[141] S. Lee and J.-G. Park, Neutron News **17**, 24 (2006).

[142] E. F. Bertaut, E. F. Forrat and P. Fang, C. R. Acad. Sci. **256**, 1958 (1963).

[143] B. B. Van Aken, T.T.M. Palstra, A. Filippetti, and N.A. Spaldin, Nature Mater.**3**, 164 (2004).

[144] N. A. Hill, J. Phys. Chem. B **104**, 6694 (2000).

[145] M. Fiebig, J. Phys. D: Appl. Phys. **38**, R123 (2005).

[146] R. Ramesh and N. A. Spaldin, Nature Mater. **6**, 21 (2007).

[147] L. D. Landau and E. M. Lifshitz. Elektrodinamika sploshnykh sred (Electrodynamics of Continuous Media), gostekhizdat, 1957, 1959.

[148] G. Nènert, U. Adem, E. M. Bauer, C. Bellitto, G. Righini, and T. T. M. Palstra, Phys. Rev. B **78**, 054443 (2008).

[149] Z. J. Huang, Y .Cao, Y. Y. Sun, Y. Y. Xue, and C. W. Chu Phys. Rev. B **56**, 2623 (1997).

[150] S. Lee, A. Pirogov, M. Kang, K.-H. Jang, M. Yonemura, T. Kamiyama, S.-W. Cheong, F. Gozzo, N. Shin, H. Kimura, Y. Noda, and J.-G. Park, Nature **451**, 06507 (2008).

[151] S. Lee, A. Pirogov, J. H. Han, J.-G. Park, A. Hoshikawa, and T. Kamiyama, Phys. Rev. B **71**, 180413 (R) (2005).

[152] A. K. Singh, S. Patnaik, S. D. Kaushik, and V. Siruguri, Phys. Rev. B **81,** 184406, (2010).

[153] T. Katsufuji, S. Mori, M. Masaki, Y. Moritomo, N. Yamamoto, and H. Takagi, Phys. Rev. B **64**, 104419 (2001).

[154] B. Lorenz, A. P. Litvinchuk, M. M. Gospodinov, and C. W. Chu, Phys. Rev. Lett. **92**, 087204 (2004).

[155] H. Sugie, N. Iwata, and K. Kohn, J. Phys. Soc. Jpn. **71,** 1558 (2002).

[156] M. Fiebig, D. Fröhlich, S. Leute, and R. V. Pisarev, J. Appl. Phys. **83**, 6560 (1998).

[157] M. Fiebig, T. Lottermoser, D. Fr¨ohlich, A. V. Goltsev, and R. V. Pisarev, Nature **419**, 818 (2002).

[158] E. Hanamura, K. Hagita, and Y. Tanabe, J. Phys.: Condens. Matter **15**, L103 (2003).

[159] A. V. Goltsev, R. V. Pisarev, T. Lottermoser, and M. Fiebig, Phys. Rev. Lett. **90**, 177204 (2003).

[160] M. Fiebig, A. V. Goltsev, T. Lottermoser, and R. V. Pisarev, J. Magn. Magn. Mater. **353**, 272 (2004).

[161] T. Chatterji, B. Ouladdiaf, P. F. Henry and D. Bhattacharya J. Phys.: Condens. Matter **24,** 336003 (2012).

[162] Y. T. Wang, C. W. Luo, T. Kobayashi, Adv. Condens. Mater. Phys. **2013**, 104806 (2013).

[163] H. Fukumura, S. Matsui, H. Harima, K. Kisoda, T. Takahashi, T. Yoshimura and N. Fujimura, J. Phys.: Condens. Matter **19,** 365239 (2007).

[164] J.Vermette, S. Jandl, A. A. Mukhin, et al., J. Phys.: Condens. Matter **19,** 365239 (2007).

[165] J. Park, J. –G. Park, G. S. Jeon, H. –Y. Choi, C. Lee, W. Jo, R. Bewley, K. A. McEwen and T. G. Perring, Phys. Rev. B **68**, 104426 (2003).

[166] M. C. Sekhar, S. Lee, G. Choi, C. Lee and J. –G. Park Phys. Rev. B **72,** 014402 (2005).

[167] J. Park, S. Lee, M. Kang, K. –H. Jang, C. Lee, S. V. Streltsov, V. V. Mazurenko Phys. Rev. B **82,** 054428 (2010).

[168] J. Park, M. Kang, J. Kim, S. Lee, K -H Jang, A. Pirogov, and J –G Park, Phys. Rev. B **79**, 064417 (2009).

[169] D. P. Kozlenko, S. E. Kichanov, S. Lee, J –G Park, V. P. Glazkov, and B. N. Savenko, JETP Lett. **82**, 193 (2005).

[170] D. P. Kozlenko, S. E. Kichanov, S. Lee, J –G Park, and B. N. Savenko, J. Phys.: Condens. Matter **19**, 156228 (2007).

[171] D. P. Kozlenko, I. Mirebeau, J. –G. Park, I.N. Goncharenko, S. Lee, J. Park, an B. N. Savenko, Phys. Rev. B **78,** 054401 (2008).

[172] S. Mori, J. Tokunaga, Y. Horibe, Y. Aikawa, T. Katsufuji, Phys. Rev. B **72**, 224434 (2005).

[173] A. A. Nugroho, N. Bellido, U. Adem, G. Nénert, Ch. Simon, M. O. Tjia, M. Mostovoy, T. T. M. Palstra, Phys. Rev. B **75**, 174435 (2007).

[174] E. M. Engler, Chem. Technol. **17**, 542 (1987).

[175] Charles Kittel, Introduction to Solid State Physics, John-Wiley and Sons (2004).

[176] W. Ashcroft and N. D. Mermin, Solid State Physics 2nd edn., Thomson-Cole (2003).

[177] B.D. Cullity, Elements of X-Ray Diffraction, Addison - Wesley (1978).

[178] Robert E. Dinnebier and Simon J. L. Billinge, Powder Diffraction-Theory and Practise, (2008).

[179] J. Als-Nielsen and D. McMorrow, Elements of Modern X-ray Physics (John Wiley & Sons, Ltd., 2001).

[180] G. E. Bacon, Neutron Diffraction, Clarendon Press, Oxford (1962).

[181] J. Schweizer in Neutron Scattering from Magnetic Materials, edited by T. Chatterji Elsevier B.V., Amsterdam, (2006).

[182] A. Sequeria, Proc. Neutron dffraction Conf., Petten, RCN-**234**, 454, (1975).

[183] S. K. Paranjpe and Y. D. Dande, Pramana-J. Phys. **32**, 793 (1989).

[184] O. Halpern and M. H. Johnson, Phys. Rev. **55**, 898 (1939).

[185] Booklet on ‘National Facility for Neutron Beam Research’, available at http://www.barc.ernet.in/publications/tb/nfnbr-book-R.pdf. Published by Bhabha Atomic Research Centre, Mumbai

[186] H. M. Rietveld, J. Appl. Cryst. **2**, 65 (1969).

[187] The Rietveld Method, edited by R. A. Young, Oxford University Press, Oxford (1993.

[188] J. Rodríguez-Carvajal, Physica B **192**, 55 (1993).

[189] A. S. Wills, Physica B **276**, 680 (2000).

[190] G. Halperin and T. Holstein, Phys. Rev. **59**, 960 (1941), R. W. Erwin, J. Appl. Phys. **67**, 5229 (1990).

[191] S. M. Yusuf and L. M. Rao, Pramana-J. Phys. **47**, 171 (1996).

[192] L. M. Rao, S. M. Yusuf, and R. S. Kothare, Indian J. Pure Appl. Phys. **30**, 276 (1992).

[193] D. C. Jiles, Introduction to Magnetism and Magnetic Materials, Routledge Chapman & Hall, (1998).

[194] Scott Calvin, XAFS for Everyone, CRC Press, 2013.

[195] http://www.rrcat.gov.in/technology/accel/srul/beamlines/index.html.

[196] R. L. Mossbauer, Z. Physik **151**, 124 (1958).

[197] N. N. Greenwood and T. C. Gibb Mössbauer Spectroscopy (Chapman and Hall Ltd., London,) 1971.

[198] M. D. Dyar, Geochemical instrumentation and analysis: Mossbauer spectroscopy, retrievedmarch20,2012,from*http://serc.carleton.edu/research−education/geochemsheets/techniques/mossbauer.html*.

[199] A. G. Razumnaya, A. G. Rudskaya, M. F. Kupriyanov and Yu. V. Kabirov, Phys. Solid State **51,** 2304 (2009).

[200] S. M. Dlouhá,. Z. Vratislav, J. Jirák, K. Hejtmánek, D. Sedmidubský, Appl. Phys. A **74,** S673 (2002).

[201] A. Atulraj, R. Gundakaram, A. Biswas, N. Gayathri, A. K. Raychaudhuri and C. N. R. Rao, J. Phys.: Condens. Matter **10** 447 (1998).

[202] S. Chatterjee and A. K. Nigam, Phys. Rev. B **66,** 104403 (2002).

[203] H. N. Li, J. W. Haung, L. X. Xiao, L. P. Peng, Y. Y. Wu, G. H. Du, Z. W. Ouyang, B. R. Chen, and Z. C. Xia, J. Appl. Phys. **111,** 083913 (2012).

[204] W. R. Chen, F. C. Zhang, J. Miao, B. Xu, L. X. Cao, X. G. Qiu and B. R. Zhao, J. Phys.: Condens. Matter **17,** 8029 (2005).

[205] Y. J. Yoo, Y. P. Lee, J. S. Park, J.–H. Kang, J. Kim, B. W. Lee, and M S. Seo, J. Appl Phys. **112,** 013903 (2012).

[206] S L Samal, W Green, S E Lofland, K V Ramanujachary, D Das, A K Ganguly, J. Solid State Chem. **181,** 61 (2008) .

[207] M. Zaghrioui, J. M. Grenèche, C. Autret- Lambert, M. Gervais, J. Magn. Magn. Mater. **323,** 509 (2011).

[208] Y.Aikawa, T.Katsufuji, T.Arima, and K.Kato, Phys. Rev. B **71**, 184418 (2005).

[209] L.Jeuvrey, O.Peña, A.Moure, and C.Moure, J. Magn. Magn. Mater. **324**, 717 (2012).

[210] R. D. Shannon, Acta Crystallogr. A **32**, 751 (1976).

[211] T. Chatterji and T. C. Hansen, J. Phys.: Condens. Matter **23,** 276007 (2011).

[212] D.C. Wallace, *Thermodynamics of Crystals* (New York: Wiley, 1972).

[213] A. V. Andreev, *Handbook of Magnetic Materials,* edited by K. H. J. Buschow, Vol 8 (Amsterdam: Elsevier, 1995).

[214] T. Chatterji, B. Ouladdiaf, T. C. Hansen, J. Phys.: Condens. Matter **22,** 096001 (2010).

[215] T. Chatterji, G. N. Lies, B. Ouladdiaf, and T. C. Hansen, J. Phys.: Condens. Matter **22,** 316001 (2010).

[216] U. Adem, A. A. Nugroho, A. Meetsma, and T. T. M. Palstra, Phys. Rev. B **75,** 014108 (2007).

[217] N. Jiang and X. Zhang, J. Phys.: Condens. Matter **24**, 235402 (2012).

[218] C. Zhang, X. Zhang, Y. Sun, S. Liu, Phys. Rev. B **83,** 054104 (2011).

[219] Neetika Sharma, A. Das, C. L. Prajapat, and S. S. Meena, J. Magn. Magn. Mater.**348**, 120 (2013).

[220] B.E. Warren, Phys. Rev. **59**, 693 (1941).

[221] X. Fabréges, I. Mirebeau, S. Petit, P. Bonville, and A. A. Belik, Phys. Rev. B **84**, 054455 (2011).

[222] J. N. Reimers, J. E. Gredan, R.K. Kremer, E. Gmelin, and M. A. Subramanian, Phys. Rev. B **43**, 3387 (1991).

[223] Neetika Sharma, A. Das, C. L. Prajapat, M. R. Singh (under review).

[224] A. M. Zhang, W. H. Zhu, X. S. Wu, B. Qing, J. Crystal Growth **318,** 912 (2011).

[225] D P Chen, Y Du, X L Wang, Z X Cheng, S X Dou, Lin Z W, J G Zhu, J. Appl. Phys.**111**, 07D913 (2012).

[226] J. Spalek, A. Lewicki, Z. Tarnawski, J. K. Furdyna, R. R. Galazka, and Z.Obuszko, Phys. Rev. B **33**, 3407 (1986).

[227] K. Yosida, Theory of Magnetism, Springer Series in Solid-State Sciences (1996).

[228] X-Ray Absorption: Principles, Applications, Techniques of EXAFS, SEXAFS and XANES, edited by D.C. Konigsberger and R. Prince (Wiley, New York, 1988).

[229] Deok-Yong Cho, Junghwan Park, Jiyeon Kim, and Je-Geun Park,Appl. Phys. Lett. **99**, 031906 (2011).

[230] K. Asokan, Y. S. Chen, C. W. Pao, H. M. Tsai, C. W. O. Lee, C. H. Lin, H. C. Hsueh, D. C. Ling, W. F. Pong, J. W. Chiou, M.-H. Tsai, O. Peña and C. Moure, Appl. Phys. Lett. **95**, 131901 (2009).

[231] M.H. Harunsani, J. Li, Y. B. Qin, H.T. Tian, J. Q. Li, H. X. Yang, and R. I. Walton, Appl. Phys. Lett. **107**, 062905 (2015).

[232] S. Namdeo, A.K.Sinha, M. N. Singh, and A. M. Awasthi, J. Appl. Phys. **113**, 104101 (2013).

[233] M. Newville, B.Ravel, D. Haskel, J.J. Rehr, E.A. Stern and Y. Yacoby, Physica B **154,** 208 (1995).

[234] D.-Y. Cho, J. Y. Kim, B. G. Park, K. J. Rho, J. H. Park, H. J. Noh, B. J. Kim, S. J. Oh, H. M. Park, J. S. Ahn, H. Ishibashi, S. W. Cheong, J. H. Lee, P. Murugavel, T. W. Noh, A. Tanaka, and T. Jo, Phys. Rev. Lett. **98**, 217601 (2007).

[235] D.-Y. Cho, S.-J. Oh, D. G. Kim, A. Tanaka, and J. H. Park, Phys. Rev. B **79**, 035116 (2009).

[236] W. S. Choi, D. G. Kim, S. S. A. Seo, S. J. Moon, D. Lee, J. H. Lee, H. S. Lee, D.-Y. Cho, Y. S. Lee, P. Murugavel, J. Yu, and T. W. Noh, Phys. Rev. B **77**, 045137 (2008).

[237] J. Kim, K. C. Cho, Y. M. Koo, K. P. Hong, and N. Shin, Appl. Phys. Lett. **95**, 132901 (2009).

[238] Yujiro Nagata, Keizo Ohta, J. Phys. Soc. Jpn., **44**, 1148 (1978).

[239] P. Mandal, C. R. Serrao, E. Suard, V. Caignaert, B. Raveau, A. Sundaresan, and C. N. R. Rao, J. Solid State Chem. **197**, 408 (2013).

[240] C. Maure, D. Gutierrez, O. Peña, P. Duran, J. Solid State Chem. **163**, 377 (2002).

[241] S. L. Samal, T. Magdaleno, K. V. Ramanujachary, S. E. Lofland, and A. K. Ganguly, J. Solid State Chem. **183**, 643 (2010).

[242] E. Bertaut, J. Phys. IV, France**07**, C1-11 (1997).

[243] T. Yamaguchi, J. Phys. Chem. Solids **35**, 479 (1974).

[244] Neetika Sharma, A. Das, S. K. Mishra, C. L. Prajapat, M. R. Singh, and S. S. Meena, J. Appl Phys. **115**, 213911 (2014).

[245] W. Wang, Baolong Xu, Ping Gao, Wei Zhang, and Yuming Sun, Solid State Commun. **177**, 7 (2014).

[246] D. L. Fox, D. R. Tilley, J. F. Scott, and H. J. Guggenheim, Phys. Rev. B **21**, 2926 (1980).

[247] T. Kimura, S. Kawamoto, I. Yamada, M. Azuma, M. Takano, and Y. Tokura, Phys. Rev. B **67**, 180401 (R) (2003).

[248] L. A. Grunes, Phys. Rev. B **27**, 2111 (1983).

[249] R. G. Parr and W. Yang, Density-functional theory of atoms and molecules (Oxford University Press, New York, 1989).

[250] P. Hohenberg and W. Kohn, Phys. Rev. **136**, B864 (1964).

[251] W. Kohn and L. J. Sham, Phys. Rev. **140**, A1133 (1965).

[252] W. Kohn, Rev. Mod. Phys. **71**, 1253 (1999).

[253] Paolo Giannozzi et al., J. Phys.: Condens. Matter **21**, 395502 (2009).

[254] J. P. Perdew, A. Zunger, Phys. Rev. B **23**, 5048 (1981).

[255] Mayank gupta, Ranjan Mittal, Mohamed Zbiri, Neetika Sharma, Stéphane Rols, Helmut Schober, S.L. Chaplot, J. mater. Chem C (in press).

[256] B. Raveau,Y.M.Zhao,C.Martin, M.Hervieu, and A.Maignam, J. Solid State Chem. **149**, 203 (2000).

[257] K. Nakade, K. Hirota, M. Kato, and H. Taguchi, Mater. Res. Bull. **42**, 1069 (2007).

[258] H. Aliaga, M. T. Causa, H. Salva, M. Tovar, A. Butera, B. Alascio, D. Vega, G. Polla, G. Leyva, and P. Konig, arXiv: cond-mat/0010295v5 (2001); H. Aliaga, M. T. Causa, B. Alascio, H. Salva, M. Tovar, D. Vega, G. Polla, G. Leyva, and P. Konig, J. Mag. Magn. Mater. **226**, 791 (2001).

[259] D. Vega, G. Leyva, G. Polla, P. Konig, H. Lonza, A. Esteban, H. Aliaga, M. T. Causa, M. Tovar, and B. Alascio, J. Solid State chem.**156**, 458 (2001).

[260] J.B. Goodenough, A. Wold, R. J. Arnott, and N. Menyuk, Phys. Rev. **124**, 373 (1961).

[261] B. Singh, S.S. Manoharan, Materials Letters **65**, 2029 (2011).

[262] L. M. Rodriguez-Martinez and J. P. Attfield, Phys. Rev. B **54**, R 15622 (1996).

[263] L. M. Rodriguez-Martinez and J. P. Attfield, Phys. Rev. B **58**, 2426 (1998).

[264] Th. Zeiske, K. Hagdorn, D. Hohlwein, J. Ihringer, W. Prandl, H. Ritter, Physica B **624**, 276 (2000).

[265] P. N. Santhosh, J. Goldberger, P. M. Woodward, T. Vogt, W. P. Lee, and A. J. Epstein, Phys. Rev. B **62**, 14928 (2000).

[266] R. Mahendiran, A. Maignan, C. Martin, M. Hervieu, and B. Raveau, Phys. Rev. B **62**, 11644 (2000).

[267] Y. Murano, M. Matsukawa, S. Ohuchi, S. Kobayashi, S. Nimori, R. Suryanarayanan, K. Koyama, and N. Kobayashi, Phys. Rev. B **83**, 054437 (2011).

[268] L. Sudheendra, A. R. Raju, and C. N. R. Rao, J. Phys.: Condens. Matter **15**, 895 (2003).

[269] D. Sousa, M. R. Nunes, C. Silveira, I. Matos, A. B. Lopes, M. E. Melo Jorge, Mater. Chem. Phys. **109**, 311 (2008).

[270] M. E. Mole Jorge, M. R. Nunes, R. Silva Maria, and D. Sousa, Chem. Mater. **17**, 2069 (2005).

[271] A. Maignan, C. Martin, F. Damay, and B. Raveau, J. hejtmanek, Phys. Rev. B **58**, 2758 (1998).

[272] Robert B. Griffiths, Phys. Rev. Lett. **23**, 17 (1969).

[273] A. J. Bray, Phys. Rev. Lett. **59**, 586 (1987).

[274] A. J. Bray and M. A. Moore, J. Phys. C: Solid State Phys. **15**, L765 (1982).

[275] Julia Herrero-Albillos, Luis Miguel Garcia, and Fernando Bartolomé, J. Phys.: Condens. Matter **21**, 216004 (2009).

[276] S. M. Zhou, Y. Li, Y. Q. Guo, J. Y. Zhao, X. Cai, and L. Shi, J. Appl. Phys. **114**, 163903 (2013).

[277] Wanjun Jiang, XueZhi Zhou, Gwyn Williams, Y. Mukovskii, and K. Glazyrin, Phys. Rev. B **77**, 064424 (2008).

[278] J. Deisenhofer, D. Braak, H. –A. Krug von Nidda, J. Hemberger, R. M. Eremino, V. A. Ivanshin, et al., Phys. Rev. Lett. **95**, 257202 (2005).

[279] V. M. Yudin, A. I. Govrilishina, M. V. Artem’eva, M. F. Bryzhina, Soviet Phys., Solid State **7**, 1856 (1966).

[280] C. R. Wiebe, J. E. Greedan, J. S. Gardner, Z. Zeng, and M. Greenblatt, Phys. Rev. B **64**, 064421 (2001)

[281] M. Respand, J. M. Broto, H. Rakoto, J. Vanacken, P. Wagner, C. Martin, A. Maignan, and B. Raveau, Phys. Rev. B **63**, 144426 (2001).

[282] T. Qian, P. Tong, Bongju Kim, Sung-Ik Lee, Namsoo Shin, S. Park, and Bog G. Kim, Phys. Rev. B **77**, 094423 (2008).

[283] S. M. Dunaevsky and V. V. Deriglazov, Phys. Rev. B **67**, 014409 (2003).

[284] I. V. Solovyev and K. Terakura, Phys. Rev. B **63**, 174425 (2001).

[285] G. Venketeswara Pai, Phys. Rev. B **63**, 064431 (2001).

[286] A. Das, S. K. Paranjpe, S. Honda, S. Murayama, and Y. Tsuchiya, J. Phys.: Condens. Matter **11**, 5209 (1999).

[287] A. Das, P. D. Babu, Sandip Chatterjee, and A. K. Nigam, Phys. Rev. B **70**, 224404 (2004).

[288] Neetika Sharma, A. Das, C. L. Prajapat, Amit Kumar, M. R. Singh, (under review).

[289] X. J. Liu, Z.Q. Li, P. Wu, H. L. Bai, and E. Y. Jiang, Solid State Commun. **142**, 525 (2007).

[290] P. M. Woodward, D. E. Cox, E. Moshpoulou, A.W. Sleight, and S. Morimoto, Phys. Rev. B **62**, 844 (2000).

[291] S. K. Pandey, A. R. Chetal and P. R. Saroda, J. Phys. Soc. Jpn. **59**, 1848 (1990).

[292] H. K. Hinge, S. K. Joshi, B. D. Shrivastava, J. Prasad, and K. Srivastava, Ind. J. Pure & Appl. Phys. **49**,168 (2011).

[293] D. Joseph, S. Basu, S. N. Jha and D. Bhattacharyya, Phys. Res. B **274**, 126 (2012).

[294] M. Sikora, Cz. Kapusta, K. Knížek, Z. Jirák, C. Autret, M. Borowiec, C. J. Oates, V. Procházka, D. Rybicki, and D. Zajac, Phys. Rev. B **73**, 94426 (2006).

[295] M. C. Sánchez, G. Subías, J. García, and J. Blasco, Phys. Rev. B **69**, 184415 (2004).

[296] M. C. Sánchez, J. García, J. Blasco, G. Subías, and J. Perez-Cacho, Phys. Rev. B **65**, 14440 (2002)

[297] G. H. Jonker, Physica **20**, 1118 (1954).

[298] E. Banks and N. Tashima, J. Appl. Phys. **41**, 1186 (1970).

[299] K. H. Ahn, X.W. Wu, K. Liu, and C. L. Chien, J. Appl. Phys. **81**, 5505 (1997).

[300] L. Pi, S. Hebert, C. Martin, A. Maignan, and B. Raveau, Phys. Rev. B **67**,024430 (2003).

[301] Z. Zeng, M. Greenblatt, and M. Croft, Phys. Rev. B **59**, 8784 (1999).

[302] N. F. Mott and E. A. Davis, Electronic Processes in Noncrystalline Material (Oxford:Clarendon, 2nd edition,1979).

[303] H. D Zhou, R. K. Zheng, G. Li, S. J. Feng, F. Liu, X. J. Fan, and X. G. Li, Eur. Phys. J. B **26**, 467 (2002).

[304] I. Dhiman, A. Das, and A. K. Nigam, J. Phys.: Condens. Matter. **21**, 386002 (2009).

[305] H. Taguchi, Physica B **311**, 298 (2002).

[306] A. A. Mukhin, M. Biberacher, A. Loidl, Journal of Magnetic Resonance **170**, 8 (2004).

[307] Neetika, A. Das, I. Dhiman, A. K. Nigam, A. K. Yadav et al. J. Appl. Phys. **112**, 123913 (2012).

[308] A. K. Jonscher, Dielectric Relaxation in Solids (Chelsea Dielectrics, London, 1983).

[309] A. R. von Hippel, Dielectrics and Waves (MIT Press, Cambridge, MA, 1966).

[310] O. Bidault, P. Goux, M. Kchikech, M. Belkaoumi, and M. Maglione, Phys. Rev. B **49**, 7868 (1994).

[311] G. M. Tsangaris, G. C. Psarras, and N. Kouloumbi, J. Mater. Sci.**33**, 2027 (1998).

[312] J. Liu, C. G. Duan, W. G. Yin, W. N. Mei, R. W. Smith, and J. R. Hardy, Phys. Rev. B **70**, 144106 (2004).

[313] I. P. Raevski, S. A. Prosandeev, A. S. Bogatin, M. A. Malitskaya, and L. Jastrabik, J. Appl. Phys. **93**, 4130 (2003).

[314] E. Billig and K. W. Plessner, Proc. Phys. Soc. London B **64**, 361 (1951).

[315] I. Ahmad, M. J. Akhtar, M. Younas, M. Siddique, and M. M. Hasan, J. Appl. Phys. **112**, 074105 (2012).

[316] M. Maglione and M. Belkaoumi, Phys. Rev. B **45**, 2029 (1992).

[317] P. Lunkenheimer, V. Bobnar, A. V. Pronin, A. I. Ritus, A. A. Volkov, and A. Loidhl, Phys. Rev. B **66**, 052105 (2002).

[318] J. L. Cohn, M. Peterca, and J. J. Neumeier, J. Appl. Phys. **97**, 034102 (2005).

[319] N. Pandey, A. K. Thakur, and R. N. P. Choudhary, Ind. J. Eng. Mater. Sci. **15**, 1919 (2008).